Dipl.-Ing. Martin Jakob Ganahl

Dynamics of Strongly Correlated One-Dimensional Quantum Systems using Matrix Product States

DOCTORAL THESIS

For obtaining the academic degree of
Doktor der technischen Wissenschaften
Doctoral Programme of Technical Sciences
Technical Physics

Graz University of Technology

Supervisor:

Prof. Dr.rer.nat. Hans Gerd Evertz
Institute for Theoretical Physics - Computational Physics
Graz University of Technology

Graz, April 2014

Abstract

The subject of this thesis is the investigation of the dynamics of strongly correlated 1-dimensional quantum lattice models using Matrix Product States techniques. In the first chapter, we give a concise description of the numerical implementation of the employed algorithms. Our results are divided into three main parts: in chapter two, we apply the described methods to the XXZ Heisenberg model, where we investigate the time evolution of different initial states following a local quantum quench. Depending on the particular type of quenching, we observe strong signatures of many-body bound states of two-, three- and more spins, also known as string-states. We find that string states occur in the ferromagnetic as well as in the anti-ferromagnetic phase with finite magnetization m. To validate our results, we compare the numerically determined propagation speed of these states with analytically exact results from Bethe ansatz, and find perfect agreement. We also investigate the effect of a harmonic confinement potential and of integrability breaking perturbations. In both cases, the signatures are seen to persist. In chapter four, we investigate the dynamics following the scattering of a single particle with momentum k from large cluster of interacting particles, in different lattice models. We consider spinless fermions, Fermi and Bose Hubbard models. For the integrable models we observe lack of backscattering of the incoming particle. In all cases the impinging particle shifts the cluster by an amount of two particles, contrary to the classical expectation. Inside the cluster, the particle signal is transformed into a hole-like signal. For non-integrable models, the dynamics splits up into a linear superposition of a backscattering and a transmission event. Chapter five is devoted to the dynamics of quantum impurity models and contains two parts. In the first part, we develop the Chebyshev expansion technique for Matrix Product States combined with linear prediction to calculate the impurity spectral function of the interacting Single Impurity Anderson Model (SIAM). We benchmark our results with analytical results for the non-interacting case and with results from dynamical Density Matrix Renormalization Group in the interacting case. For both we obtain very good agreement. We further propose a modification of the existing algorithm which reduces the number of auxiliary parameters. We apply the method as an impurity solver within the Dynamical Mean Field Theory. In the second part of chapter five we apply the Time Evolving Block Decimation technique to obtain quasi steady state currents of the SIAM. To this end we investigate three different ways (quenches) of obtaining steady state currents. We show current-voltage characteristics for different interactions and discuss interaction and band-edge effects. Our results compare very well with existing data where available.

Kurzfassung

Das Thema der vorliegenden Arbeit ist die theoretische Untersuchung der Dynamik stark korrelierter, eindimensionaler Quantensysteme am Gitter. Zur Lösung der entsprechenden Gleichungen wird die Methode der Matrix Produkt Zustände verwendet. Kapitel zwei gibt eine Einführung in die Grundlagen dieser numerischen Methode. Die Resultate sind auf drei Kapitel verteilt. Kapitel drei widmet sich der Untersuchung der Zeitevolution lokaler Anregungen im Heisenberg XXZ Modell. Abhänging vom Typus der lokalen Anregung lässt sich die Ausbreitung von gebundenen Vielteilchenzuständen, so genannten "string-states" beobachten. Diese Zustände treten sowohl bei lokalen Anregungen des ferromagnetischen Zustandes auf, als auch bei Anregungen aus dem antiferromagnetischen Grundzustand mit endlicher Magnetisierung m. Der Vergleich der numerisch ermittelten Ausbreitungsgeschwindigkeiten mit analytischen Ergebnissen des Betheansatzes zeigt hervorragende Übereinstimmmung. Die Resultate sind robust gegen integrabilitätsbrechende Störungen wie ein harmonisches Fallenpotential und nächste Nachbar Wechselwirkung. In Kapitel vier wird die Dynamik der Streuung eines Teilchens mit vorgegebenem Impuls k an einer großen Gruppe von gebundenen, wechselwirkenden Teilchen in verschiedenen Gittermodellen untersucht. Bei den Modellen handelt es sich um spinlose Fermionen, das Fermi- und das Bose-Hubbard Modell. In allen Fällen lässt sich ein Verschiebung des Teilchenkonglomerats um zwei Teilchen beobachten, was im Gegensatz zum klassisch erwarteten Verschiebung um ein Teilchen steht. Beim Auftreffen auf die Teilchengruppe wandelt sich das einfallende Teilchensignal in ein Lochsignal um. Im Falle von nicht-integrablen Modellen besteht die Dynamik aus einem reflektierten und einem transmittierten Anteil in linearer Superposition. Kapitel fünf beschäftigt sich mit der Dynamik von Störstellen und ist in zwei Teile gegliedert. Im ersten Teil wird ein Verfahren zur Berechnung der Störstellenspektralfunktion für ein Single Impurity Anderson Modell (SIAM), basierend auf der Methode der Chebyshev Entwicklung für Matrix Produkt Zustände und linearer Vorhersage, entwickelt. Für den nicht-wechselwirkenden Fall werden die Resultate mit analytischen Ergebnissen verglichen, im wechselwirkenden Fall mit Ergebnissen der Dynamischen Dichte Matrix Renormierungsgruppe. In beiden Fallen ist die Übereinstimmung hervorragend. Es wird weiters eine Modifizierung der Chebyshev Methode eingeführt, die die Zahl der Hilfsparameter der Methode reduziert. Die Chebyshev Methode wird weiters als "impurity solver" für die Dynamische Molekularfeld Theorie verwendet. Im zweiten Teil des Kapitels fünf wird die "Time Evolving Block Decimation" Technik verwendet um quasi-Gleichgewichtsströme für das SIAM zu berechnen. Es werden drei unterschiedliche Arten dies zu bewerkstelligen untersucht und verglichen. Die berechneten Strom-Spannungs-Kennlinien zeigen starke Abhängigkeit von der Wechselwirkungsstärke. Es werden Korrelations-und Bandeffeckte diskutiert. Die Ergebnisse sind in bester Übereinstimmung mit existierenden Daten aus der Literatur.

Contents

Chapter 1

Introduction

At very small length scales, and very short times, the dynamics of atoms and molecules is governed by quantum mechanics. In this regime, matter behaves (most unintuitively) like waves. Many classical experimental observations, like metallic, semi-conducting and insulating states of matter can only be properly understood from such a perspective. The theoretical treatment of such materials involves the quantum mechanical description of electronic motion inside a regular array of atoms, a crystal. Most interestingly, one can in many cases completely omit any interaction between the electrons and still get an accurate description of experimental results. Already for these cases the theoretical derivation of experimentally measureable quantities is rather non-trivial. However, not all states of matter can be described by such non-interacting electrons. The most prominent example are classical BCS superconductors where electrons indirectly interact with each other by exchanging lattice phonons, or the famous Mott-Hubbard insulator, which is fundamentally different from conventional band insulators and can only be explained by taking into account electron-electron interactions. The inclusion of such interactions considerably complicates the analytical treatment, in many cases it renders it impossible, even for the most simple theoretical models like the Hubbard model, where electrons interact locally by an interaction U, or the Heisenberg model of spins, where neighboring, localized spin degrees of freedom interact via a magnetic exchange interaction Δ. Typically, one is interested in static groundstate properties (e.g. correlation functions) of these materials, since they already contain important information about their properties. In such cases, the only remedy is to employ approximate numerical techniques. The most popular ones are Quantum Monte Carlo (QMC) [1, 2], Exact Diagonalization (ED) [3], the Numerical Renormalization Group (NRG) [4], Density Matrix Renormalization Group (DMRG) [5] and Dynamical Mean Field Theory (DMFT) [6]. The appropriate choice is often dictated by the particular model. QMC can in principle be applied to any quantum many body system, but in many cases suffers from the so called sign problem. ED is in principle exact, but it can handle only small system, when one is typically interested in the thermodynamic limit of an infinitely large system. The NRG can only handle interacting impurities coupled to a bath of free electrons. DMRG is highly accurate for non-critical systems of large sizes, typically several hundred lattice sites, but it can only handle 1d systems; and DMFT yields exact results for local observables, but only in the limit of an infinite dimensional lattice. Nevertheless, all methods have fundamentally contributed to our understanding of the properties of many different kinds of strongly

correlated materials.

A further complication arises when considering dynamical properties of many-body quantum systems, because in this case a large number of eigenstates of the system is expected to contribute to observables. Two different viewpoints on this subject have emerged during the last decades. The first and more traditional one is the question as to how systems in equilibrium (i.e. at a given temperature and chemical potential) react to external perturbations, e.g when irradiating them with light or particle-radiation. Typical quantities of immediate interest are the single particle spectral function $A(\omega)$ or spin and charge suszeptibilities. Such dynamics are typically related to groundstate properties, since the system can be expected to move "not too far away" from its initial state if the perturbation is sufficiently weak or localized. These quantities are notoriously hard to compute, and major efforts have been made in the last decades to invent efficient techniques for their evaluation. For 1d systems, the first attempts involving the DMRG method, known as Correction Vector Method (CVM) [7] and Dynamical DMRG (DDMRG) [8], were already very successful and have become a standard tool in condensed matter physics. Major breakthroughs followed in 2004 with the invention of efficient techniques for real time evolution on the basis of Matrix Product States (MPS) [9] and DMRG, and only recently there have been several proposals, on the basis of MPS technology, for new, efficient methods to access Greens and spectral functions of 1d quantum systems.

The second, more recent viewpoint on dynamics of correlated quantum systems is concerned with initial states which are "far away" from the groundstate. Here, the emphasis lies on investigations of thermalization, and effects of integrability on the dynamics. The interest in such topics is fueled by the recent progress in control and manipulation of cold atoms in optical traps, where non-equilibrium setups of strongly correlated spin- and electron models are now accessible in experiments.

This thesis investigates non-equilibrium dynamics of different many-body quantum lattice models using the DMRG and the Time Evolving Block Decimation (TEBD) [10, 11] technique. The numerical details of the methods are explained in Chap.2 and largely follow the reviews in Refs. [9, 12, 13, 14, 15]. The results of this thesis are divided into three parts. Chap. 3 adresses local quantum quenches in the Heisenberg XXZ model. For certain types of quenches we find strong contributions of two-string and three-string excitations to the dynamics. Our results suggest that local quenches are an ideal setting for experimental investigations of the properties of these many-body states, which for a long time have eluded convincing experimental observation. Our predictions were confirmed in a recent cold-atom experiment [16].

In Chap.4 we investigate the dynamics of collisions of single particles with large, immobile clusters of interacting particles for three different lattice models, a spinless fermion model and the Bose and the Fermi Hubbard model. We find intruiging and unexpected effects like a shift of the clusters by two particles, even though only one particle impinges, and particle hole transformations. We analyze the effect of integrability breaking onto reflection properties of the incoming particle from the clusters.

Chap. 5 deals with applications of Matrix Product State (MPS) methods to quantum impurity problems. In the first part of this chapter, we use the Chebyshev expansion technique for MPS to calculate the impurity spectral function $A(\omega)$. We combine it with the linear prediction technique to obtain highly accurate results, and benchmark

it with the most precise data available up to date, where we obtain perfect agreement. We further propose a modification of the method which reduces the number of auxiliary parameters. We also show that the method can be applied as an impurity solver within the Dynamical Mean Field Theory. The second part of Chap.5 is concerned with current-voltage characteristics of an interacting quantum dot. We compare three different ways of obtaining the steady state currents, and present results over broad parameter ranges. We find very good agreement with existing data, where available.

Chapter 2

Methods

2.1 Introduction

Since its invention more than two decades ago [5, 17], the Density Matrix Renormalization Group (DMRG) has emerged as the method of choice to tackle strongly correlated one dimensional (1d) quantum systems. It was developed out of a modification of Wilson's Numerical Renormalization Group Method (NRG) [18, 19]. The following chapter introduces the basic tools needed when working with Matrix Product States (MPS). Starting with a short introduction to the DMRG in its original formulation [17], it introduces the concept of Matrix Product States, how they are manipulated and how they can be used for numerics. The chapter largely follows the definitive reviews on MPS by Schollwöck [9, 12], Verstraete [13] and Noack [14] as well as an introductory paper by McCulloch [15].

2.2 Density Matrix Renormalization Group

In the following, we will introduce the concepts of DMRG [5] for the isotropic Heisenberg spin 1/2 model with N sites and open boundary conditions (obc), defined by

$$H = J \sum_{i=1}^{N} (S_i^x S_{i+1}^x + S_i^y S_{i+1}^y + S_i^z S_{i+1}^z) \tag{2.1}$$

where $S_i^{x,y,z}$ are spin operators in at site i, and J is the coupling strength between neighboring spins. The local Hilbert space dimension of a single site will be denoted d. For the Heisenberg spin 1/2 model, $d = 2$.

The main problem one faces when trying to solve the Schrödinger equation for a system of interacting particles is that the computational effort grows *exponentially* which the size of the system under consideration. For example, for a system of N spins, the relevant basis set contains 2^N states (if no symmetries are incorporated). Using massive parallel computation with highly optimized algorithms, largest systems solved by exact diagonalization using the Lanczos method (see chapter 1) contain about $N = 32 - 35$ sites for a spin 1/2 Heisenberg system [20] and $N = 20$ for a single band Hubbard model with 12 electrons [21]. These numbers are not likely to be pushed much further.

DMRG on the other hand is an iterative and approximate, though highly accurate method for calculation of groundstates and low lying exited states of large (i.e. $N \approx$

$100 - 10000$), 1d quantum system (early calcuations already gave ground-state energies with 8 digits accuracy for the $N = 60$ sites Heisenberg system [17]). The approximate nature of DMRG enters through a truncation procedure by which the full Hilbert space of the problem is reduced to a smaller (effective) number of states. These states are chosen such that the groundstate (or low-lying exited state) wave function is (in some sense) optimally described within this set. The DMRG algorithm comes in two flavors, the infinite and the finite system DMRG. We will first describe the infinite system algorithm, since it is conceptually easier to understand.

2.2.1 Infinite system DMRG (iDMRG)

Our goal is to find an effective set of states which describes the properties of the ground-state of our system in the limit $N \to \infty$. To this end, iDMRG considers chains of increasing length N, and the groundstate for a chain of length $N+2$ is obtained from the groundstate of a chain of length N. A key ingredient is the splitting of the system into four parts: a left "system" block L of length l, a right "environment" block R (of length r) and two local sites i, j in between. We assume that blocks L and R are completely described by a set of D states $|\alpha\rangle$ and $|\gamma\rangle$. All operators (including H) living on block L thus have a representation in this set, e.g. S^z_m, with $m \in$L having a representation $\langle\alpha| S^z_m |\alpha'\rangle = (S^z_m)_{\alpha\alpha'}$ (and similar for block R, with γ instead of α). In practical implementations, the environment R is taken to be the same as L. In the next step, we want to find a similar basis for the enlarged system $L\bullet$, where the bullet represents the single physical site i. To find such a basis, we construct a *super-block*-system L$\bullet\bullet$R and solve for the groundstate $|\psi\rangle$ of this super-block using a sparse eigensolver like Lanczos 1 or Davidson-Liu:

$$|\psi\rangle = \sum_{\alpha ij\gamma} \psi_{(i\alpha)(j\gamma)} |\alpha ij\gamma\rangle , \tag{2.2}$$

where $(i\alpha)$ means that two indices have been combined into a single one. To construct the super-block Hamiltonian, we use the representations of the operators living on L and R: the super-block Hamiltonian can be decomposed into

$$\begin{aligned} H = {} & H_L \mathbb{1}_i \mathbb{1}_j \mathbb{1}_R + \mathbb{1}_L \mathbb{1}_i \mathbb{1}_j H_R \\ & + J \sum_\sigma ((S^\sigma_{i-1})_L S^\sigma_i \mathbb{1}_j \mathbb{1}_R + \mathbb{1}_L \mathbb{1}_i S^\sigma_j (S^\sigma_{j+1})_R + \mathbb{1}_L S^\sigma_i S^\sigma_j \mathbb{1}_R) \end{aligned} \tag{2.3}$$

where $(S^\sigma_{i-1})_L = (S^\sigma_{i-1})_{\alpha\alpha'}, (S^\sigma_{j+1})_R = (S^\sigma_{j+1})_{\gamma\gamma'}, H_L = (\sum_{i=1}^{l-1} \vec{S}_i \vec{S}_{i+1})_{\alpha\alpha'}, H_R = (\sum_{i=1}^{l-1} \vec{S}_i \vec{S}_{i+1})_{\gamma\gamma'}$ are operator representations on the blocks of size $N/2$. From $|\psi\rangle$, we compute the reduced density matrix

$$\rho_{L\bullet} = \mathrm{tr}_{\bullet R} |\psi\rangle \langle\psi| = \sum_{i\alpha i'\alpha'} \underbrace{\sum_{j\gamma} \psi_{(i\alpha)(j\gamma)} \psi^*_{(i'\alpha')(j\gamma)}}_{\rho_{(i\alpha)(i'\alpha')}} |i\alpha\rangle \langle i'\alpha'| \tag{2.4}$$

for system $L\bullet$ and diagonalize it:

$$\begin{aligned}\rho_{L\bullet} &= \sum_{i\alpha,i'\alpha'} \rho_{(i\alpha)(i'\alpha')} \left|i\alpha\right\rangle \left\langle i'\alpha'\right| \\ &= \sum_{i\alpha,i'\alpha',\beta} U_{(i\alpha)\beta}\lambda_\beta^2 U^*_{\beta(i'\alpha')} \left|i\alpha\right\rangle \left\langle i'\alpha'\right| \\ &= \sum_\beta \lambda_\beta^2 \left|\beta\right\rangle \left\langle\beta\right|\end{aligned} \tag{2.5}$$

where

$$\left|\beta\right\rangle = \sum_{i\alpha} U_{(i\alpha)\beta} \left|i\alpha\right\rangle . \tag{2.6}$$

The states $|\beta\rangle$ now form the *new effective basis set* for system L$\bullet$. However, because we added a single site to the system, the number of states within this new set is dD, where d is the local Hilbert space dimension of the added site i. To make the algorithm feasible for iteration, the basis set has to be truncated: we keep only D eigenstates belonging to the D largest eigenvalues of $\rho_{L\bullet}$, by which we introduce an approximation, the nature of which will be discussed below. We can infer the quality of this approximation by considering the truncated weight

$$\epsilon_{tw} = \sum_{i=D+1}^{dD} \lambda_i^2 = 1 - \sum_{i=1}^{D} \lambda_i^2 \tag{2.7}$$

where we made use of the normalization $\sum_{i=1}^{dD} \lambda_i^2 = 1$. The smaller ϵ_{tw} is, the better the approximation. Typical values of ϵ_{tw} during DMRG simulations range from 10^{-6} down to machine precision. We now can close the iteration loop by taking $L' = L\bullet$ as new system block with length $N/2+1$ and $R' = \bullet R$ as new environment block. The iteration proceeds until convergence of the groundstate energy obtained from the eigensolver is reached.

At every step, one obtains a *local* representation of the groundstate wave function, $\psi_{(i\alpha)(i'\alpha')}$, of the many-body system of size $N+2$. Many properties of interest, like local observables and also correlation functions can be computed using the corresponding representations of the operators.

2.2.2 Finite system DMRG

From infinite system DMRG, it is only a small step towards finite system DMRG. The main difference is that now one allows the system L and environment R to be of different sizes. Given a system of N spins, the sizes s of the blocks have to obey

$$s(L) + s(R) + 2 = N. \tag{2.8}$$

The procedure starts with an iDMRG run until Eq.2.8 is obeyed. For all intermediate system sizes of the blocks L and R, all operator representations have to be stored for later use. The next step, i.e. finding optimal basis set for L$\bullet$, now differs from the infinite

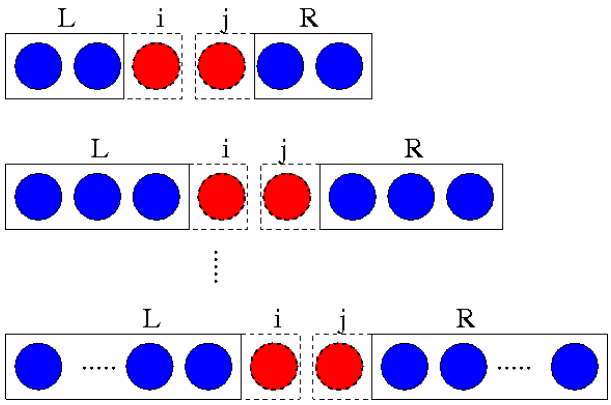

Figure 2.1: Visualization of the infinite system DMRG algorithm. At every iteration, the size of the blocks L and R is increased by one additional site. Red dots are the single sites by which L,R are enlarged.

DMRG algorithm: Instead of taking the environment block R to be of the same size as L, one uses the block of size s(L)-2 from a previous iteration, thus the total length of the system (including the two single sites between the blocks) is N. In the same fashion, one iterates the procedure until s(L)=$N-2$, and s(R)=0, using as environment blocks R the system blocks L from the previous iteration, decreasing in size. At this point, the direction is reversed, and the blocks *L and R switch their character*, i.e. L now serves as environment and R as system. After having found the groundstate $|\psi\rangle$ for this partitioning, one now calculates the reduced density matrix *for system R* instead of L (see Eq.2.4):

$$\rho_{\bullet R} = \mathrm{tr}_{L\bullet} |\psi\rangle \langle\psi| = \sum_{j\gamma j'\gamma'} \underbrace{\sum_{i\alpha} \psi_{(i\alpha)(j\gamma)} \psi^*_{(i\alpha)(j'\gamma')}}_{\rho_{(j\gamma)(j'\gamma')}} |j\gamma\rangle \langle j'\gamma'| \tag{2.9}$$

Note that at this stage (i.e. at the right side of the system) states $|\gamma\rangle$ are an empty set (dummy variables). $\rho_{\bullet R}$ is again diagonalized,

$$\begin{aligned} \rho_{\bullet R} &= \sum_{j\gamma, j'\gamma'} \rho_{(j\gamma)(j'\gamma')} |j\gamma\rangle \langle j'\gamma'| \\ &= \sum_{j\gamma, j'\gamma', \delta} U_{(j\gamma)\delta} \lambda^2_\delta U^*_{\delta(j'\gamma')} |j\gamma\rangle \langle j'\gamma'| \\ &= \sum_\delta \lambda^2_\delta |\delta\rangle \langle\delta| \end{aligned} \tag{2.10}$$

with

$$|\delta\rangle = \sum_{j\gamma} U_{(j\gamma)\delta} |j\gamma\rangle \,. \tag{2.11}$$

After truncation of the set to the states with the D largest eigenvalues λ^2 one obtains the new effective basis for the system block R'=•R. One now moves one site to the *left*, using the block L' of size s(L')=$N - s$(R')-2 from the previous iteration as new environment

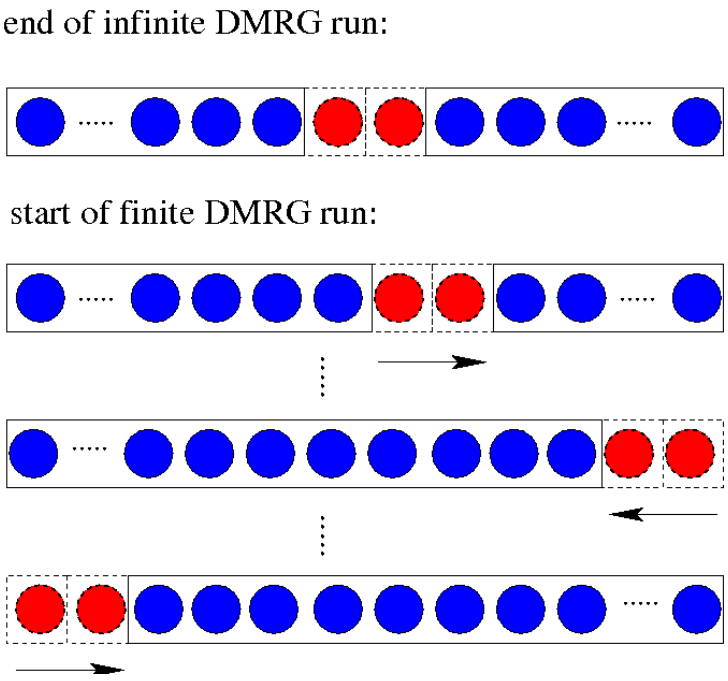

Figure 2.2: Visualization of the finite system DMRG algorithm.

block. In this fashion, one sweeps back and forth through the system until convergence of the groundstate energy is obtained (after typically 5-10 sweeps). It is worth noting that for any bi-partition of the system, the eigenvalues of the left and right reduced density matrix are the same.

2.3 Matrix Product States

One of the reasons why the DMRG methods works so well lies in the fact that it implicitly creates a special form of the ground state wave function [22, 23, 9], dubbed Matrix Product State (MPS) representation. The concept of MPS turned out to be an incredibly versatile tool in condensed matter physic and quantum information theory and quickly sparked off a whole new area of research. The following sections will give a short and basic introduction to the concept of MPS.

2.3.1 Definition and notations

we will start this section with the formal definition of a matrix product state. For concreteness, let us consider a chain of N spins 1/2 in the z-basis, $|\sigma\rangle \in \{|\uparrow\rangle, |\downarrow\rangle\}$, with obc., i.e. our computational basis has a product structure $|\{\sigma_i\}\rangle \equiv |\sigma_1 \cdots \sigma_N\rangle$. A many-body quantum state $|\psi\rangle$ is said to be in a matrix product state form if it can be written in the following way:

$$|\psi\rangle = \sum_{\{\sigma_i\}} \vec{X}^{\sigma_1,[1]} X^{\sigma_2,[2]} \cdots X^{\sigma_{N-1},[N-1]} \vec{X}^{\sigma_N,[N]} |\{\sigma_i\}\rangle \tag{2.12}$$

$X^{\sigma_i,[i]} \equiv X^{\sigma_i,i}_{\alpha_{i-1}\alpha_i}$ are $D \times D$ matrices (i.e. for every σ, α_{i-1} and α_i run from 1 to D) living at site i of the system. The leftmost and the rightmost X^σ are $1 \times D$ and $D \times 1$ matrices, respectively, indicated by vector-arrows in Eq.2.12, which is a consequence of the use of open boundary conditions. The single index in brackets ($[i]$) is a site index. It is a reminder that matrices at different sites can be different from each other. In the following we will omit this index.

For periodic boundary conditions, we can impose translational symmetry using the form

$$|\psi\rangle = \sum_{\{\sigma_i\}} \mathrm{tr}\left(X^{\sigma_1} X^{\sigma_2} \cdots X^{\sigma_{N-1}} X^{\sigma_N}\right) |\{\sigma_i\}\rangle\,, \tag{2.13}$$

with only a *single* matrix $X^{\sigma_n}_{\alpha_{n-1},\alpha_n}$. Translational symmetry, i.e. invariance under the shift operator T^n, with

$$T^n\,|\sigma_1 \cdots \sigma_N\rangle = |\sigma_{1+n} \cdots \sigma_{N-1+n}\sigma_{N+n} = \sigma_n\rangle \tag{2.14}$$

(where $n \in 1, 2, \cdots, N$ and $\sigma_{i+n} = \sigma_{\mathrm{mod}(i+n,N)}$) then follows from the cyclic property of the trace operation. The fact that only a single set of matrices $M^\sigma_{\alpha\beta}$ is needed in this case can be used to increase efficiency of MPS-algorithms. More generally, if the state under consideration is known to have certain symmetry properties (i.e. it is an eigenstate of the corresponding symmetry operator), then conserved quantum numbers can be used to label the matrix-indices, which in many cases yields considerable speed up in computation time and decrease in memory consumption [24, 15, 25].

2.3.2 DMRG produces Matrix Product States

A very remarkable property of the DMRG-algorithm first noticed by Östlund and Rommer [23, 22] is that it implicitly creates a matrix product state representation of groundstates. Consider again the infinite DMRG algorithm for the toy-model Eq.2.1. Let us start the algorithm using a system block L small enough for full diagonalization, with basis states $|\alpha_0\rangle$ (and vice versa for environment R, with a basis $|\gamma_0\rangle$). After completion of the first iteration step, we obtain a groundstate wave function $|\psi\rangle$

$$|\psi\rangle = \sum_{\alpha_0\sigma_i\sigma_{i+1}\gamma_0} \psi_{\alpha_0\sigma_i\sigma_{i+1}\gamma_0}\,|\alpha_0\sigma_i\sigma_{i+1}\gamma_0\rangle\,, \tag{2.15}$$

from which we compute the reduced density matrix $\rho_{L\bullet} = \rho_{(\alpha_0\sigma_i)(\alpha'_0\sigma'_i)}$ by tracing out the right site + environment $\bullet$R. After diagonalization of $\rho_{(\alpha_0\sigma_i)(\alpha'_0\sigma'_i)} = U_{(\alpha_0\sigma_i)\alpha_1}\lambda^2_{\alpha_1}U^*_{\alpha_1(\alpha'_0\sigma'_i)}$, we get the new effective basis for L$\bullet$ via

$$|\alpha_1\rangle = \sum_{\alpha_0\sigma_i} U_{(\alpha_0\sigma_i)\alpha_1}\,|\alpha_0\sigma_i\rangle\,. \tag{2.16}$$

Iterating, we find that after n steps, the effective basis $|\alpha_n\rangle$ has the structure

$$|\alpha_n\rangle = \sum_{\{\alpha_i\}\{\sigma_i\}} U_{(\alpha_0\sigma_1)\alpha_1}U_{(\alpha_1\sigma_2)\alpha_2}\cdots U_{(\alpha_{n-1}\sigma_n)\alpha_n}\,|\alpha_0\{\sigma_i\}\rangle \tag{2.17}$$

Figure 2.3: AKLT state: filled blue circles are auxiliary spin 1/2 degrees of freedom, which are combined into a larger local degree of freedom (black boxes). Green wiggly lines represent a singlet shared by two auxiliary spin 1/2 system of adjacent sites.

which, by simple relabeling, yields

$$|\alpha_n\rangle = \sum_{\{\alpha_i\}\{\sigma_i\}} U^{\sigma_1}_{\alpha_0\alpha_1} U^{\sigma_2}_{\alpha_1\alpha_2} \cdots U^{\sigma_n}_{\alpha_{n-1}\alpha_n} |\alpha_0\{\sigma_i\}\rangle \,, \tag{2.18}$$

which is exactly a matrix product state representation of the effective basis. Because the U's originate from a basis transformation, they must satisfy the left-unitarity condition

$$\sum_{\alpha_{i-1}\sigma_i} U^{\sigma_i}_{\alpha_{i-1}\alpha_i} U^{*\sigma_i}_{\alpha_{i-1}\alpha'_i} = \delta_{\alpha_i\alpha'_i} \tag{2.19}$$

which reflects the orthonormality property of the effective basis $|\alpha_i\rangle$. Note that due to truncation, the opposite relation does not hold, i.e.

$$\sum_{\alpha_i} U^{\sigma_i}_{\alpha_{i-1}\alpha_i} U^{*\sigma'_i}_{\alpha'_{i-1}\alpha_i} \neq \delta_{\alpha_{i-1}\alpha'_{i-1}} \delta_{\sigma_i\sigma'_i}$$

2.3.3 The AKLT groundstate is an MPS

We introduced the concept of matrix product states in a rather ad hoc fashion. In 1987, during a period of intense research on anti-ferromagnetic systems due to the discovery of high TC superconductivity, Affleck, Kennedy, Lieb and Tasaki (AKLT) [26] in fact showed that MPS appear quite naturally as groundstates of certain (relevant) Hamiltonians. This section follows closely the reviews by Schollwöck [9] and Verstraete [13]. AKLT were interested in the so called valence bond state (VBS) of a chain of spin 1 particles. In this state, a pair of neighboring spins is connected by a valence bond. The character of this state is best understood by splitting up each spin 1 particle into two (virtual) spin 1/2 particles (see Fig.2.3) and considering the spin 1 Hilbert space as being obtained from the symmetric subspace of two spin 1/2 particles [9, 13]:

$$\begin{aligned} |1\rangle &= |\uparrow\uparrow\rangle \\ |0\rangle &= \frac{|\uparrow\downarrow\rangle + |\downarrow\uparrow\rangle}{\sqrt{2}} \\ |-1\rangle &= |\downarrow\downarrow\rangle \end{aligned} \tag{2.20}$$

By definition of the VBS, each of the spin 1/2 particles now is in a singlet state with one spin 1/2 particle from a neighboring spin 1 site (blue lines in Fig.2.3). AKLT asked if there exists a Hamiltonian with the VBS as the exact groundstate, and constructed it by observing that the total spin of a pair of spin 1 sites can *not* be 2, because two of the

four spin 1/2 form a spin 0 singlet, and the other pair can then only be either in a triplet (spin=1) or singlet (spin=0). By observing that the projection operator

$$\vec{S}_i\vec{S}_{i+1} + \frac{1}{3}(\vec{S}_i\vec{S}_{i+1})^2 + \frac{2}{3} \tag{2.21}$$

projects onto the 5-dimensional spin 2 subspace of two spin 1 particles, this Hamiltonian is then

$$H = \sum_i \vec{S}_i\vec{S}_{i+1} + \frac{1}{3}(\vec{S}_i\vec{S}_{i+1})^2 + \frac{2}{3}. \tag{2.22}$$

It has a groundstate energy $E_0 = 0$ (because the VBS is completely annihilated)

The construction of the state $|VBS\rangle$ proceeds as follows (we use pbc): Using $|\{\sigma\}\rangle \equiv |\sigma_1 \cdots \sigma_N\rangle$ and $|\{\delta\}\rangle \equiv |\delta_1 \cdots \delta_N\rangle$ as basis states for the $2N$ spin 1/2's, the state with singlet bonds in the auxiliary space of $2N$ spin 1/2 has the form

$$|\psi\rangle = \sum_{\{\sigma\}\{\delta\}} \Sigma_{\delta_1\sigma_2}\Sigma_{\delta_2\sigma_3} \cdots \Sigma_{\delta_N\sigma_1} |\{\sigma\}\{\delta\}\rangle \tag{2.23}$$

with

$$\Sigma = \begin{pmatrix} 0 & \frac{1}{\sqrt{2}} \\ -\frac{1}{\sqrt{2}} & 0 \end{pmatrix}. \tag{2.24}$$

To get the VBS $|VBS\rangle$, the local state of the two spin 1/2 at each spin 1 site has to be mapped to the computational basis of a spin 1 particle. This is achieved using the following projection operator (see [9]) $\mathcal{P}_i$ at each site i:

$$\mathcal{P}_i = |1_i\rangle \langle\uparrow_i\uparrow_i| + |-1_i\rangle \langle\downarrow_i\downarrow_i| + |0_i\rangle \frac{\langle\uparrow_i\downarrow_i| + \langle\downarrow_i\uparrow_i|}{\sqrt{2}} \tag{2.25}$$

which can be written as

$$\begin{aligned} \mathcal{P}_i &= \sum_{\alpha_i\sigma_i\delta_i} X^{\alpha_i}_{\sigma_i\delta_i} |\alpha_i\rangle \langle\sigma_i\delta_i| \qquad (2.26) \\ X^{1_i}_{\sigma_i\delta_i} &= \begin{pmatrix} 1 & 0 \\ 0 & 0 \end{pmatrix} \\ X^{-1_i}_{\sigma_i\delta_i} &= \begin{pmatrix} 0 & 0 \\ 0 & 1 \end{pmatrix} \\ X^{0_i}_{\sigma_i\delta_i} &= \begin{pmatrix} 0 & \frac{1}{\sqrt{2}} \\ \frac{1}{\sqrt{2}} & 0 \end{pmatrix}, \end{aligned}$$

and $|\alpha_i\rangle \in \{|1\rangle, |0\rangle, |-1\rangle\}$. The full projection operator $\mathcal{P}$ is

$$\mathcal{P} = \prod_i \mathcal{P}_i = \sum_{\{\alpha\}\{\sigma\}\{\delta\}} X^{\alpha_1}_{\sigma_1\delta_1} \cdots X^{\alpha_N}_{\sigma_N\delta_N} |\{\alpha\}\rangle \langle\{\sigma\}\{\delta\}| \tag{2.27}$$

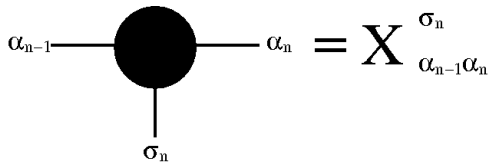

Figure 2.4: Representation of an MPS matrix $X^{\sigma_i}_{\alpha_{i-1}\alpha_i}$.

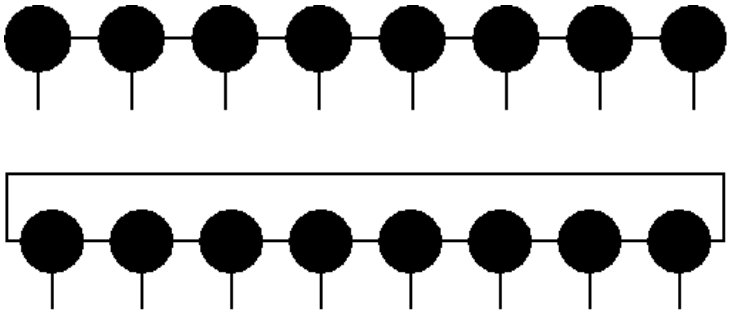

Figure 2.5: Representation of a matrix product state. Upper figure: MPS for obc, lower figure: MPS for pbc. Lines connecting different dots denote matrix multiplications. In the lower figure, the outer line is the trace operation (see Eq.2.13)

from which we get

$$|VBS\rangle \equiv \mathcal{P}\,|\psi\rangle = \sum_{\{\alpha\}} \sum_{\{\sigma\}\{\delta\}} \underbrace{X^{\alpha_1}_{\sigma_1\delta_1}\Sigma_{\delta_1\sigma_2}}_{\tilde{X}^{\alpha_1}_{\sigma_1\sigma_2}} X^{\alpha_2}_{\sigma_2\delta_2}\Sigma_{\delta_2\sigma_2}\cdots X^{\alpha_N}_{\sigma_N\delta_N}\Sigma_{\delta_N\sigma_1}\,|\{\alpha\}\rangle$$
$$= \sum_{\{\alpha\}} \mathrm{tr}\left(\tilde{X}^{\alpha_1}\cdots\tilde{X}^{\alpha_N}\right)|\{\alpha\}\rangle\,. \tag{2.28}$$

This is a matrix product state representation for a chain with periodic boundary conditions.

2.3.4 Graphical representations for MPS-calculus

From the previous section it should have become clear that dealing with MPS involves a great deal of tedious index manipulations. Fortunately, most of the mathematical operations (which involve simple linear algebra) can be done using a graphical representation, considerably simplifying evaluation of equations and allowing for intuitive manipulation of mathematical expressions. The formalism uses graphical representations of the matrices $X^{\sigma_i}_{\alpha_{i-1}\alpha_i}$, shown in Fig.2.4.

The matrices (or rather, the tensor) are symbolized by a black dot with three legs sticking out. Every leg stands for one of the indices of $X^{\sigma_i}_{\alpha_{i-1}\alpha_i}$. The indices α_{n-1} and α_n are called auxiliary indices, and σ_n is the physical index of X. The full MPS of length N is then simply obtained by drawing N dots in a line and connecting each right-auxiliary index of a dot with the left-auxiliary one of the right-next dot to denote contraction of this index, i.e. matrix multiplication. This is shown in Fig.2.5) for both open and periodic boundary conditions. In the following chapters, we will introduce several special forms of MPS by imposing constraints on the matrices $X^{\sigma_i}_{\alpha_{i-1}\alpha_i}$. These special forms will be

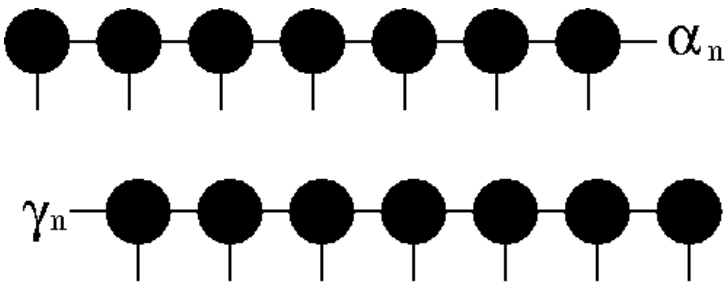

Figure 2.6: Representation of a set of left-orthonormal MPS $|\alpha_n\rangle$ (upper figure) and right-orthonormal MPS $|\gamma_n\rangle$ (lower figure)

needed to rephrase the DMRG in MPS-language and when dealing with non-equilibrium dynamics of many-body quantum systems.

2.3.5 Orthonormality, Schmidt's decomposition, canonical forms and the reduced density matrix

So far, the matrices of an MPS were completely arbitrary. We will now introduce special forms of MPS by imposing conditions on the matrices [9, 15]

Orthonormal MPS

When discussing the connection of MPS and DMRG in section 2.3.2, we saw that the DMRG at every iteration step produces a set of orthonormal MPS $|\alpha_n\rangle$. Orthonormality follows immediately from the fact that the states $|\alpha_n\rangle$ are obtained from a basis transformation (i.e. diagonalization of the reduced density matrix). Let us now consider such an effective basis set in MPS form (see Fig.2.6, upper figure):

$$|\alpha_n\rangle = \sum_{\{\alpha_i\}\{\sigma_i\}} X^{\sigma_1}_{\alpha_0\alpha_1} X^{\sigma_2}_{\alpha_1\alpha_2} \cdots X^{\sigma_n}_{\alpha_{n-1}\alpha_n} |\alpha_0\{\sigma_i\}\rangle \tag{2.29}$$

where in the sums over $\{\alpha_i\}$ the index α_n is excluded. The set $|\alpha_n\rangle$ forms an orthonormal set if two conditions are satisfied: first, the set $|\alpha_{n-1}\rangle$,

$$|\alpha_{n-1}\rangle = \sum_{\{\alpha_i\}\{\sigma_i\}} X^{\sigma_1}_{\alpha_0\alpha_1} \cdots X^{\sigma_{n-1}}_{\alpha_{n-2}\alpha_{n-1}} |\alpha_0\{\sigma_i\}\rangle \tag{2.30}$$

has to be an orthonormal basis set:

$$\langle\alpha_{n-1}|\alpha'_{n-1}\rangle \stackrel{!}{=} \delta_{\alpha_{n-1}\alpha'_{n-1}} \tag{2.31}$$

and second, the matrix $X^{\sigma_n}_{\alpha_{n-1}\alpha_n}$ has to obey

$$\sum_{\alpha_{n-1}\sigma_n} X^{\sigma_n}_{\alpha_{n-1}\alpha_n} X^{*\sigma_n}_{\alpha_{n-1}\alpha'_n} \stackrel{!}{=} \delta_{\alpha_n\alpha'_n} \tag{2.32}$$

where * denotes complex conjugation. Throughout this work (and also in many other scientific publications), a matrix satisfying Eq.2.32 will be reserved its own letter: $X^{\sigma_n}_{\alpha_{n-1}\alpha_n} \to A^{\sigma_n}_{\alpha_{n-1}\alpha_n}$.

A similar consideration applies to the case when the dangling bond is on the left side (see Fig.2.6, lower figure). In this case, the states $|\gamma_n\rangle$ form an orthonormal set if the states at the next bond, $|\gamma_{n+1}\rangle$, are orthonormal ($\langle\gamma_{n+1}|\gamma'_{n+1}\rangle = \delta_{\gamma_{n+1}\gamma'_{n+1}}$) and the matrices $X^{\sigma_{n+1}}_{\alpha_n\alpha_{n+1}}$ obey

$$\sum_{\alpha_{n+1}\sigma_{n+1}} X^{\sigma_{n+1}}_{\alpha_n\alpha_{n+1}} X^{*\sigma_{n+1}}_{\alpha_{n'}\alpha_{n+1}} \stackrel{!}{=} \delta_{\alpha_n\alpha'_n}. \tag{2.33}$$

Matrices obeying Eq.2.33 will be reserved the letter B: $X^{\sigma_{n+1}}_{\alpha_n\alpha_{n+1}} \to B^{\sigma_{n+1}}_{\alpha_n\alpha_{n+1}}$. Eq.2.32 and 2.33 are graphically represented in Fig.2.7, where red dots symbolize left-orthonormal A-matrices, and blue ones right-orthonormal B-matrices. Note that an MPS-matrix can be either left-orthonormal or right-orthonormal, *but not both*. Thus, the states $|\alpha_n\rangle$ are orthonormal if *all* matrices X^{σ_k} are *left orthonormal* for $k \leq n$, and similar all states $|\gamma_n\rangle$ are orthonormal if *all* matrices X^{σ_l} with $l \geq n$ are *right orthonormal*. The states

$$\begin{aligned} |\alpha_n\rangle &= \sum_{\{\alpha_i\}\{\sigma_i\}} A^{\sigma_1}_{\alpha_0\alpha_1} A^{\sigma_2}_{\alpha_1\alpha_2} \cdots A^{\sigma_n}_{\alpha_{n-1}\alpha_n} |\{\sigma_i\}\rangle \\ |\gamma_n\rangle &= \sum_{\{\gamma_i\}\{\sigma_i\}} B^{\sigma_{n+1}}_{\gamma_n\gamma_{n+1}} B^{\sigma_{n+2}}_{\gamma_{n+1}\gamma_{n+2}} \cdots B^{\sigma_N}_{\gamma_{N-1}\gamma_N} |\{\sigma_i\}\rangle \end{aligned} \tag{2.34}$$

are called left ($|\alpha_n\rangle$) and right ($|\gamma_n\rangle$) orthonormal basis states (note that in the sums $\{\alpha_i\}$ and $\{\gamma_i\}$, α_n and γ_n are excluded).

To bring a matrix $X^{\sigma_n}_{\alpha_{n-1}\alpha_n}$ into left- or right-orthonormal form, one uses either a *singular value decomposition* (SVD) or *QR-factorization*. From a computational point of view, using the latter is favorable because it is a less expensive operation. The SVD of a complex $m \times n$ matrix M is given by the decomposition

$$M = U\lambda V^\dagger \tag{2.35}$$

with U an $m \times m$ unitary matrix and V an $n \times n$ unitary matrix. λ is a $m \times n$ diagonal matrix with real, positive entries. For our purpose, it is sufficient to use an "economic" version of the SVD where λ is reduced to a $m \times m$ matrix and $V^\dagger$ is reduced to an $m \times n$ matrix. Similarly, a QR decomposition of M is given by

$$M = QR \tag{2.36}$$

where Q is unitary ($Q^\dagger Q = \mathbb{1}$) and R is an upper triagonal matrix. An RQ decomposition is defined analogously. All results in this work were obtained using an SVD.

Let us first consider the case of left-orthonormalization. First, one combines the indices σ_n and α_{n-1} into a single index $(\alpha_{n-1}\sigma_n)$. The resulting matrix $X_{(\alpha_{n-1}\sigma_n)\alpha_n}$ is then SV decomposed:

$$X_{(\alpha_{n-1}\sigma_n)\alpha_n} = \sum_{\beta_n} U_{(\alpha_{n-1}\sigma_n)\beta_n} \lambda_{\beta_n} (V^\dagger)_{\beta_n\alpha_n} \tag{2.37}$$

The matrix $U_{(\alpha_{n-1}\sigma_n)\beta_n}$ is left unitary ($U^\dagger U = \mathbb{1}$). By index-splitting and relabeling $\beta_n \to \alpha_n$, the matrix U becomes $A_{(\alpha_{n-1}\sigma_n)\alpha_n}$ which thus obeys Eq.2.32. To bring a given MPS into a fully left-orthonormal form (i.e. all matrices are left-orthonormal), one starts at the leftmost matrix and applies Eq.2.37. The product $\lambda V^\dagger$ is then multiplied onto the matrix to the right,

$$\begin{aligned} X_{(\alpha_0\sigma_1)\alpha_1} &= \sum_{\beta_1} U_{(\alpha_0\sigma_1)\beta_1}\lambda_{\beta_1}(V^\dagger)_{\beta_1\alpha_1} \\ X^{\sigma_2}_{\alpha_1\alpha_2} &\to \sum_{\alpha_1\beta_1} \lambda_{\beta_1}(V^\dagger)_{\beta_1\alpha_1}X^{\sigma_2}_{\alpha_1\alpha_2}, \end{aligned} \tag{2.38}$$

and one moves one site to the right (using a QR decomposition, the product $\lambda V^\dagger$ is replaced by R). This way, one proceeds to the rightmost matrix. After having done the SVD of this rightmost matrix, the product $\lambda V^\dagger$ contains the norm of the MPS (i.e. it is a single number). If this norm is disregarded, the resulting left-orthonormal MPS is *normalized*, i.e. $\langle\psi|\psi\rangle = 1$.

Right-orthonormalization is done in a similar fashion. One starts at the right hand side with matrix $X^{\sigma_N}_{\alpha_{N-1}\alpha_N}$, and now combines σ_N and α_N into a single index $(\alpha_N\sigma_N)$. The resulting matrix is SV-decomposed,

$$X_{\alpha_{n-1}(\alpha_N\sigma_N)} = \sum_{\beta_{N-1}} U_{\alpha_{N-1}\beta_{N-1}}\lambda_{\beta_{N-1}}(V^\dagger)_{\beta_{N-1}(\alpha_N\sigma_N)} \tag{2.39}$$

and the product $U\lambda$ is multiplied to the *left* (using a RQ decomposition, $U\lambda$ is replaced by R)

$$X^{\sigma_{N-1}}_{\alpha_{N-2}\alpha_{N-1}} \to \sum_{\alpha_{N-1}\beta_{N-1}} X^{\sigma_{N-1}}_{\alpha_{N-2}\alpha_{N-1}}U_{\alpha_{N-1}\beta_{N-1}}\lambda_{\beta_{N-1}}. \tag{2.40}$$

When having reached the leftmost site, the resulting $U\lambda$ expression again contains the state norm, and upon disregarding it, the state is then normalized.

Both these operations can be used to reduce the dimension of the MPS-matrices from dimension D to dimension $D' < D$, an operation usually called *truncation* (see Sec. 2.9). Truncation is done by disregarding a certain number of singular values λ_β (usually the smallest ones), and thus reducing the size of the U and $V^\dagger$ matrices. This of course introduces an approximation, since the state after truncation is not the same one as before. The quantity which usually quantifies this approximation is the truncated weight $\epsilon_{tw} = \sum_{\beta>D'}\lambda_\beta^2$ (see also Eq.2.7), where we assumed that $\sum_{\beta=1}^{D}\lambda_\beta^2 = 1$, and singular values are decreasing with increasing index number. An important remark is at hand: Truncation during a left-right sweep (i.e. a left-orthonormalization sweep) should only be done when the state has been right-orthonormalizated before, without any truncation. This is necessary to have a well defined interpretation of the singular values (see next section on Schmidt decomposition).

The Schmidt decomposition

The Schmidt-decomposition is a tool widely used in quantum information theory ([27]) to investigate entanglement properties of extended quantum systems. Suppose we have

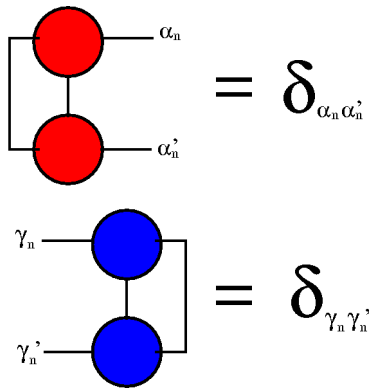

Figure 2.7: Graphical representation of Eq.2.32 (upper figure) and 2.33 (lower figure). Red dots are used for left-normalized matrices, blue dots for right normalized ones.

a many-body quantum state $|\psi\rangle$ living on a Hilbert space S. We now virtually separate S into two disjoint systems A and B. Since S has a product structure ($S = A \otimes B$) the state $|\psi\rangle$ can be expressed using basis-sets of A and B, respectively:

$$|\psi\rangle = \sum_{\{A\}\{B\}} M_{\{A\}\{B\}} \, |\{A\}\rangle \, |\{B\}\rangle \tag{2.41}$$

$\{A\}$ and $\{B\}$ represent the degrees of freedom of systems A and B (i.e. the computational basis, e.g. spin degrees of freedom). $M_{\{A\}\{B\}}$ can be SV-decomposed into

$$M_{\{A\}\{B\}} = \sum_{\beta} U_{\{A\}\beta} \lambda_\beta (V^\dagger)_{\beta\{B\}}. \tag{2.42}$$

Inserting this expression into Eq.2.41 yields

$$|\psi\rangle = \sum_{\beta} \lambda_\beta \underbrace{\left(\sum_{\{A\}} U_{\{A\}\beta} \, |\{A\}\rangle \right)}_{|\beta\rangle^A} \underbrace{\left(\sum_{\{B\}} (V^\dagger)_{\beta\{B\}} \, |\{B\}\rangle \right)}_{|\beta\rangle^B}. \tag{2.43}$$

$|\beta\rangle^A$ and $|\beta\rangle^B$ are called Schmidt states for the bi-partition $A : B$ of system S, and λ_β are the corresponding Schmidt values. The states $|\beta\rangle^A$ and $|\beta\rangle^B$ and the Schmidt values λ_β have certain properties:

$$\begin{aligned} {}^B\langle\beta|\beta'\rangle^B &= \delta_{\beta\beta'} \\ {}^A\langle\beta|\beta'\rangle^A &= \delta_{\beta\beta'} \\ \sum_\beta \lambda_\beta^2 &= 1 \quad , \text{ if } \langle\psi|\psi\rangle = 1. \end{aligned} \tag{2.44}$$

The squares of the Schmidt values λ_β^2 are the eigenvalues of the reduced density matrix $\rho_{A/B}$ obtained after tracing out either system B or system A of the full density matrix

$\rho = |\psi\rangle\langle\psi|$, and the states $|\beta\rangle^A$ and $|\beta\rangle^B$ are the corresponding eigenstates:

$$\rho_A = \mathrm{tr}_B\,|\psi\rangle\langle\psi| = \sum_\beta \lambda_\beta^2\,|\beta\rangle^{A\ A}\langle\beta| \tag{2.45}$$
$$\rho_B = \mathrm{tr}_A\,|\psi\rangle\langle\psi| = \sum_\beta \lambda_\beta^2\,|\beta\rangle^{B\ B}\langle\beta|\,.$$

The actual connection with MPS is now very simple: Suppose you have an MPS in a mixed form

$$\underbrace{(A^{\sigma_1}\dots A^{\sigma_n})_{\alpha_n}}_{|\alpha_n^L\rangle}\,\lambda_{\alpha_n}\,\underbrace{(B^{\sigma_{n+1}}\dots B^{\sigma_N})_{\alpha_n}}_{|\alpha_n^R\rangle} \tag{2.46}$$

where the sums and the matrix indices are suppressed for clearness of notation. The boundary between left and right orthonormalized matrices is at bond connecting sites n and $n+1$. Note that this is the most general mixed form an MPS can acquire. Written out in the under-braced basis, the state has the form

$$\sum_{\alpha_n} \lambda_{\alpha_n}\,|\alpha_n^L\rangle\,|\alpha_n^R\rangle \tag{2.47}$$

which is exactly a Schmidt decomposition of the state for $A = L$ and $B = R$. The Schmidt decomposition is defined only for bipartite splittings, and a straightforward generalization to tripartite or even multi-partite splittings is not known to the author. The Schmidt values λ_{α_n} (or eigenvalues of the reduced density matrices $\rho_{A/B}$) of the bi-partition $A:B$ encode the entanglement between the two system A and B. A measure of entanglement [28] of two systems A, B is the von Neumann entropy S_{vN}:

$$S_{vN} = -\,\mathrm{tr}_{B/A}\Big(\rho_{A/B}\log(\rho_{A/B})\Big) = -\sum_{\alpha_n}\lambda_{\alpha_n}\log(\lambda_{\alpha_n}). \tag{2.48}$$

If A and B were completely unentangled in the computational basis, there would be only one term in the sum in Eq.2.47 and Eq.2.48 ($\lambda_{\alpha_n} = \delta_{0\alpha_n}$), and hence $S_{vN} = 0$. In fact, the entanglement properties of 1d quantum systems lie at the heart of the success of DMRG and MPS in general. For ground states of gapped 1d quantum systems, bi-partite entanglement has been shown to saturate as a function of the system sizes, a property *called boundary law* [28, 13]. These states can be well described by an MPS representation [29] with finite matrix dimension. For gapless phases, where the matrix dimension needed for an accurate description scales polynomially in the size of the system, finite entanglement scaling analysis [30, 31] can be employed to obtain results for the thermodynamic limit.

We now return to the issue of truncation of an MPS. Truncating an MPS at a given bond n connecting sites n and $n+1$ means disregarding a certain number of Schmidt eigenvalues λ_{α_n}. This is equivalent to disregarding the eigenvalues $\lambda_{\alpha_n}^2$ of the reduced density matrices $\rho_{L/R} = \mathrm{tr}_{R/L}(|\psi\rangle\langle\psi|)$, where $\mathrm{tr}_L(\dots)$ means tracing out all sites $i \le n$ (and similar $\mathrm{tr}_R(\dots)$ for $i > n$). The Schmidt eigenvalues of an MPS $|\psi\rangle$ at bond n can be obtained by bringing it into a mixed-orthonormal form about bond n (see Eq.2.46), where all matrices at sites $i \le n$ are left-orthonormal, and all matrices at sites $i > n$

are right-orthonormal. Then, and only then, the matrix living on the bond n (note that in this case there *has* to be a matrix at this bond) is diagonal and contains the Schmidt eigenvalues λ_{α_n}. To truncate a non-orthonormalized MPS $|\psi\rangle$, one first has to do an initializing left- (or right-) orthonormalization sweep *without truncation*, and then can truncate the state durig a following right- (or left-) orthonormalization sweep. This guarantees that one really truncates in the eigenbasis of the reduced density matrix at the corresponding site.

Canonical Matrix Product States

In addition to the left and right normalized forms for MPS there exists the so called *canonical representation* of an MPS. For an arbitrary bi-partition, this representation allows one to immediately obtain the corresponding Schmidt states and Schmidt values, *with no computation involved* . Such a representation assumes the following form (see [10, 11, 9] for details)

$$|\psi\rangle = \sum_{\{\sigma_i\}} \Gamma^{\sigma_1} \lambda^{[1]} \Gamma^{\sigma_2} \lambda^{[2]} \dots \lambda^{[N-1]} \Gamma^{\sigma_N} |\{\sigma_i\}\rangle \,. \tag{2.49}$$

Fig.2.8 shows the graphical representation of such a state. In addition to the usual MPS matrices, there are diagonal matrices $\lambda^{[i]}$ living on every bond connecting sites i and $i+1$. For the proof that *any* many-body state can be brought into such a form, we refer the reader to [9, 10]. $\lambda^{[i]}$ is a diagonal matrix containing the Schmidt values for the bi-partition at bond i, and Γ^{σ_i} are $D \times D$ matrices. These Γ^{σ_i} matrices can be easily obtained, starting from a left/right normalized MPS

$$\begin{aligned} |\psi\rangle &= \sum_{\{\sigma_i\}} A^{\sigma_1} A^{\sigma_2} \dots A^{\sigma_N} |\{\sigma_i\}\rangle \\ |\psi\rangle &= \sum_{\{\sigma_i\}} B^{\sigma_1} B^{\sigma_2} \dots B^{\sigma_N} |\{\sigma_i\}\rangle \end{aligned} \tag{2.50}$$

and using the fact that

$$\begin{aligned} A^{\sigma_i} &= \lambda^{[i-1]} \Gamma^{\sigma_i} \\ B^{\sigma_i} &= \Gamma^{\sigma_i} \lambda^{[i]} \end{aligned} \tag{2.51}$$

(see the braced expressions in Fig.2.8). Thus, $\Gamma^{\sigma_i} = (\lambda^{[i-1]})^{-1} A^{\sigma_i} = B^{\sigma_i} (\lambda^{[i]})^{-1}$ (note that one usually uses pseudo-inversion of the matrices, due to the possibly very small Schmidt-values). Advantages of this representation are that local observables can be calculated without the need of a full contraction of the tensor-network (see below), and that certain algorithms devised for time evolution of many-body MPS can be easily parallelized.

2.4 Matrix Product Operators

In the same manner in which we introduced MPS one can formally define a similar representation for operators, called a Matrix Product Operator (MPO) representation

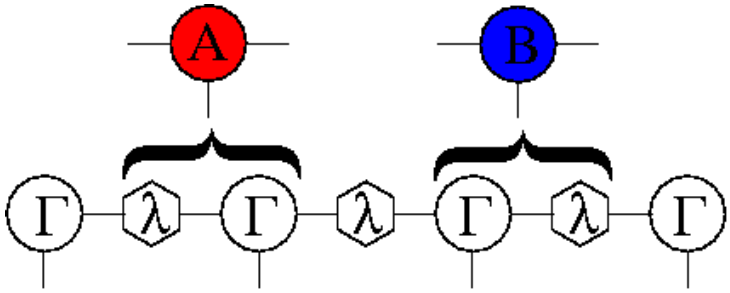

Figure 2.8: Graphical representation of a canonical MPS. On each bond there is a diagonal matrix λ containing the Schmidt eigenvalues of the corresponding bi-partition of the state. The braces show how to construct the left normalized A^σ matrices and the right orthonormalized B^σ matrices from the Γ^σ and λ matrices.

[15, 32] (one of the clearest expositions on MPOs can be found in the review by Schollwöck [9], on which this section is based). Instead of a local basis corresponding to a physical Hilbert-space, at every site one introduces a complete set of operators living on this physical Hilbert space. For spin 1/2 systems, this could for example be the matrices $\{\hat{\sigma}_1 \equiv \mathbb{1}, \hat{\sigma}_x, \hat{\sigma}_y, \hat{\sigma}_z\}$ ($\hat{\sigma}_{x/y/z}$ are the Pauli matrices). Any operator on the many-body Hilbert space can then be (formally) written as

$$\hat{O} = \sum_{\{i_n = x,y,z,1\}} \tilde{M}^{i_1} \dots \tilde{M}^{i_N} \hat{\sigma}_{i_1} \dots \hat{\sigma}_{i_N}. \tag{2.52}$$

Another useful representation can be derived by introducing a representation of $\hat{\sigma}_{i_n}$ in terms of bra/ket vectors:

$$\hat{\sigma}_{i_n} = \sum_{\sigma_n \sigma'_n} h^{i_n}_{\sigma_n \sigma'_n} |\sigma_n\rangle \langle \sigma'_n| \tag{2.53}$$

Inserting this into Eq.2.52, one arrives at

$$\hat{O} = \sum_{\{\sigma_i, \sigma'_i\}} M^{\sigma_1 \sigma'_1} \dots M^{\sigma_N \sigma'_N} |\sigma_1\rangle \langle \sigma'_1| \dots |\sigma_N\rangle \langle \sigma'_N| . \tag{2.54}$$

where $M^{\sigma_n \sigma'_n} = \sum_{i_n} \tilde{M}^{i_n} h^{i_n}_{\sigma_n \sigma'_n}$. Both representation appear frequently in the literature, but in the remainder of this thesis, we will solely use the latter one. $M^{\sigma_n \sigma'_n}$ are again matrices whose dimension K is determined by the "range of interaction" of the operator. As an example, let us see how to obtain the representation of the matrices $M^{\sigma_n \sigma'_n}$ for the XXZ model. We will first state the result, and then show how to derive it. The Heisenberg XXZ Hamiltonian (see also Eq.2.1) is

$$H = \sum_{i=1}^{N-1} \left(\frac{J_{xy}}{2} (S^+_i S^-_{i+1} + S^-_i S^+_{i+1}) + \Delta S^z_i S^z_{i+1} \right) - \sum_i B_i S^z_i \tag{2.55}$$

where $S^\pm = (S^x \pm i S^y)$ and Δ is the exchange anisotropy (the interaction term). The interaction is in this case short ranged, only between nearest neighbors. The term proportional to J_{xy} gives rise to spin-flip processes, and is similar to a kinetic energy term.

The matrices $M^{\sigma_n\sigma'_n}$ for the MPS representation of this operator are given by

$$
\begin{aligned}
M^{\sigma_n\sigma'_n} &= \begin{pmatrix} \mathbb{1} & 0 & 0 & 0 & 0 \\ S^+ & 0 & 0 & 0 & 0 \\ S^- & 0 & 0 & 0 & 0 \\ S^z & 0 & 0 & 0 & 0 \\ -B_n S^z & \frac{J_{xy}}{2} S^- & \frac{J_{xy}}{2} S^+ & \Delta S^z & \mathbb{1} \end{pmatrix} \quad \text{for } n \text{ in the bulk} \\
M^{\sigma_1\sigma'_1} &= \begin{pmatrix} -B_1 S^z & \frac{J_{xy}}{2} S^- & \frac{J_{xy}}{2} S^+ & \Delta S^z & \mathbb{1} \end{pmatrix} \quad \text{for } n = 1 \\
M^{\sigma_N\sigma'_N} &= \begin{pmatrix} \mathbb{1} \\ S^+ \\ S^- \\ S^z \\ -B_n S^z \end{pmatrix} \quad \text{for } n = N
\end{aligned}
\tag{2.56}
$$

where the index-pair $\sigma_n\sigma'_n$ is "hidden" in the operator representation of S^+, S^-, S^z and $\mathbb{1}$. This representation is of course not unique. We will now explain how to obtain such a representation. First of all, one has to realize that every operator (-pair) in H in fact is an operator-*string* with $\mathbb{1}$ operators at all other sites, e.g. $S_i^z = \mathbb{1}_1 \dots S_i^z \mathbb{1}_{i+1} \dots \mathbb{1}_N$. We will now devise a procedure for constructing the MPO-matrices by moving from right to left through these operator strings. This procedure is similar to a Markovian process, where a transition matrix with a certain probability transfers a given state into another one, only that in our case the states will not be from a probability distribution, and there will be no probability associated with the process.

Suppose now there is a reading head moving from right to left along such an operator string, i.e. it starts at site N. At a given site $n \leq N$, the head can distinguish five different states of the string:

$|1\rangle$**:** Down to site n only $\mathbb{1}$s have occurred so far (the string acts non-trivially only on sites $i < n$)

$|2\rangle$**:** Down to site $n+1$ there are only $\mathbb{1}$s, at site n there is an S^+; there is a non-trivial operator somewhere to the left of n

$|3\rangle$**:** Down to site $n+1$ there are only $\mathbb{1}$s, at site n there is an S^-; there is a non-trivial operator somewhere to the left of n

$|4\rangle$**:** Down to site $n+1$ there are only $\mathbb{1}$s, at site n there is an S^z; there is a non-trivial operator somewhere to the left of n

$|5\rangle$**:** Only $\mathbb{1}$s appear to the *left* of site n (the string acts non-trivially only on sites $i \geq n$).

The head initially can be in one of these five different states. Starting from state $|1\rangle$, and moving one site to the left, there are a number of possible transitions:

- $|1\rangle \to |1\rangle$ by $\mathbb{1}$
- $|1\rangle \to |2\rangle$ by S^+
- $|1\rangle \to |3\rangle$ by S^-

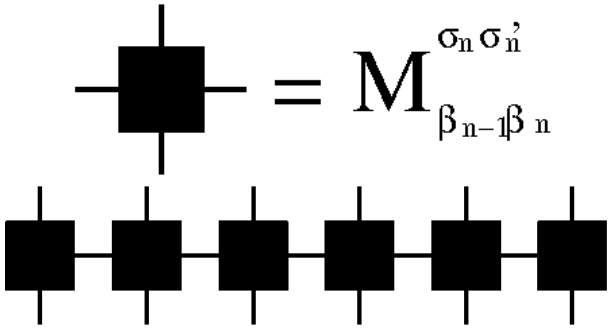

Figure 2.9: Upper figure:Graphical representation of an MPO-matrix. Upper and lower lines correspond to physical indices (σ_n, σ'_n), left and right ones to auxiliary indices (β_{n-1}, β_n). Lower figure: the MPO for open boundary conditions. Connected lines again denote matrix multiplications.

- $|1\rangle \to |4\rangle$ by S^z
- $|1\rangle \to |5\rangle$ by $-B_N S^z$

There are also other transitions when starting from another state. In our case, these are

- $|2\rangle \to |5\rangle$ by $\frac{J_{xy}}{2} S^-$
- $|3\rangle \to |5\rangle$ by $\frac{J_{xy}}{2} S^+$
- $|4\rangle \to |5\rangle$ by ΔS^z
- $|5\rangle \to |5\rangle$ by $\mathbb{1}$.

Filling in the local operators at the corresponding matrix-indices, one thus gets the representation of Eq.2.56. Like for MPS, there is also a graphical representation for MPO-matrices (Fig.2.9) and MPOs.

The case of next-nearest neighbor interactions or next nearest neighbor hoppings can be treated in exactly the same formalism, with the difference that the MPO matrices then contain off-diagonal elements. Of course one has to introduce further states in which the reading head can be. A simple example would be a Heisenberg model with next-nearest neighbor anisotropy Δ':

$$H = \sum_{i=1}^{N-1} \big(\frac{J_{xy}}{2} (S_i^+ S_{i+1}^- + S_i^- S_{i+1}^+) + \Delta S_i^z S_{i+1}^z \big) + \Delta' \sum_{i=1}^{N-2} S_i^z S_{i+2}^z - \sum_i B_i S_i^z . \qquad (2.57)$$

In this case for example the new state corresponds to the situation of a single S^z at the right side, and a $\mathbb{1}$ at the local site. The bulk MPO-matrices for this system assume the

form

$$M^{\sigma_n\sigma'_n} = \begin{pmatrix} \mathbb{1} & 0 & 0 & 0 & 0 & 0 \\ S^+ & 0 & 0 & 0 & 0 & 0 \\ S^- & 0 & 0 & 0 & 0 & 0 \\ S^z & 0 & 0 & 0 & 0 & 0 \\ 0 & 0 & 0 & \mathbb{1} & 0 & 0 \\ -B_n S^z & \frac{J_{xy}}{2} S^- & \frac{J_{xy}}{2} S^+ & \Delta S^z & \Delta' S^z & \mathbb{1} \end{pmatrix} \quad \text{for } n \text{ in the bulk.} \tag{2.58}$$

It is even possible to treat long-ranged interactions of the form $\hat{O}(r_i, r_j) \propto 1/(r_i - r_j)$ by approximating the function $1/(r_i - r_j)$ as a sum of exponentials [32]. This is especially interesting when treating for example electronic systems subject to Coulomb repulsion in the continuum limit [33, 34, 35].

MPOs for bosonic and fermionic systems

Spin systems are one big class of quantum lattice models. Another one are fermionic and bosonic lattice models, among which the most prominent ones are the Bose/Fermi-Hubbard model. For fermionic systems, the correct treatment of the fermionic sign is important when calculating correlation functions. An easy way of implementing this fermionic sign is by introducing string-order operators P [36]. We will illustrate the idea for the case of the Fermi-Hubbard model

$$H = -t \sum_{\sigma i} (c^\dagger_{\sigma i} c_{\sigma i+1} + h.c.) + U \sum_i n_{\uparrow i} n_{\downarrow i} \tag{2.59}$$

where $c_{\sigma i}, c^\dagger_{\sigma i}$ are fermionic annihilation and creation operators, with $\{c_{\sigma i}, c^\dagger_{\sigma' j}\} = \delta_{\sigma\sigma'}\delta_{ij}$. t and U parametrize the kinetic and interaction energy, respectively. The correct treatment of the fermionic sign proceeds as follows: consider an annihilation operator at site i, c_i. We will use the following ordering of the local basis-states: $|0\rangle, |\downarrow\rangle, |\uparrow\rangle, |\uparrow\downarrow\rangle$, where $\uparrow, \downarrow$ represents an up or down electron. To "count" the number of electrons to the left (we choose to start counting from the left) of site i, we introduce parity-operators P_i, which for our chosen ordering of local basis-states assume the form

$$P_i = \begin{pmatrix} 1 & 0 & 0 & 0 \\ 0 & -1 & 0 & 0 \\ 0 & 0 & -1 & 0 \\ 0 & 0 & 0 & 1 \end{pmatrix}. \tag{2.60}$$

Note that $P_i^2 = \mathbb{1}$. Writing annihilation operators c_i as

$$c_i = P_1 \dots P_{i-1} c_i \mathbb{1}_{i+1} \dots \mathbb{1}_N, \tag{2.61}$$

the hopping term at sites i and $i+1$ becomes $c_i^\dagger P_i c_{i+1}$. This is known as a Jordan-Wigner transformation [37]. Interaction terms are not affected. For nearest-neighbor hopping in 1d with open boundary conditions, the fermionic sign in the Hamiltonian

cancels out. When computing correlation functions, including longer ranged hoppings or treating ladder systems the inclusion of the fermionic sign is crucial. The bulk MPO-matrices for the Fermi Hubbard model with correct fermionic sign treatment read

$$M^{\sigma_n\sigma'_n} = \begin{pmatrix} \mathbb{1} & 0 & 0 & 0 & 0 & 0 \\ c^\dagger_\uparrow & 0 & 0 & 0 & 0 & 0 \\ c_\uparrow & 0 & 0 & 0 & 0 & 0 \\ c^\dagger_\downarrow & 0 & 0 & 0 & 0 & 0 \\ c_\downarrow & 0 & 0 & 0 & 0 & 0 \\ Un_\uparrow n_\downarrow & -tc_\uparrow P & -tc^\dagger_\uparrow P & -tc_\downarrow P & -tc^\dagger_\downarrow P & \mathbb{1} \end{pmatrix} \quad \text{for } n \text{ in the bulk.} \tag{2.62}$$

For bosonic degrees of freedom, the local occupation number is unbounded, as a consequence of the commutation relation. This is of course numerically unfeasible, and one has to introduce an upper cutoff, and check that results are independent of the cutoff.

2.5 Calculation of expectation values

A crucial operation is the calculation of expectation values of operators. For operators that can be cast into MPO form, this amounts to the contraction of the full network of MPO and MPS matrices. Using graphical representations of Fig.2.5 and Fig.2.9, an expectation value $\langle \hat{O} \rangle = \langle \Psi | \hat{O} | \Psi \rangle$ assumes the graphical representation shown in Fig.2.10. In our convention, the upper row of dots corresponds to $|\Psi\rangle$, and the lower one to $\langle\Psi|$. Note that matrices of an MPS $|\Psi\rangle$ can in general be complex, and thus the matrices of $\langle\Psi|$ have in general first to be complex conjugated. Also, computational complexity of the contraction depends one the way it is done. Let us look at this in a little bit more detail. MPS matrices are denoted by X^σ, and MPO matrices by $M^{\sigma\sigma'}$. The network is contracted by starting from the left side from the expression

$$E_1 = \sum_{\sigma_1\sigma'_1} X^{\sigma_1} M^{\sigma_1\sigma'_1} \bar{X}^{\sigma'_1} \tag{2.63}$$

or from the right side, starting from

$$F_N = \sum_{\sigma_N\sigma'_N} X^{\sigma_N} M^{\sigma_N\sigma'_N} \bar{X}^{\sigma'_N}. \tag{2.64}$$

These objects are often referred to as E-matrices for obvious reasons (see Fig.2.11, upper panel, leftmost figure). When starting from the left side, we want to add the MPS and MPO matrices of site 2 by matrix multiplication to the E_1 matrix. The best way to do this is to contract the matrices *one by one* into the network. Fig.2.11 shows the graphical representation of these matrix operations. The general formula when adding matrices of site n to E_{n-1} or to F_{n+1} are

$$\begin{aligned} E_n \equiv E^{\beta_n}_{\alpha_n\alpha'_n} &= \sum_{\alpha_{n-1}\sigma_n} X^{\sigma_n}_{\alpha_{n-1}\alpha_n} \sum_{\beta_{n-1}\sigma'_n} M^{\sigma_n\sigma'_n}_{\beta_{n-1}\beta_n} \sum_{\alpha'_{n-1}} E^{\beta_{n-1}}_{\alpha_{n-1}\alpha'_{n-1}} \bar{X}^{\sigma'_n}_{\alpha_{n-1}\alpha'_n} \\ F_n \equiv F^{\beta_{n-1}}_{\alpha_{n-1}\alpha'_{n-1}} &= \sum_{\alpha_n\sigma_n} X^{\sigma_n}_{\alpha_{n-1}\alpha_n} \sum_{\beta_n\sigma'_n} M^{\sigma_n\sigma'_n}_{\beta_{n-1}\beta_n} \sum_{\alpha'_n} F^{\beta_n}_{\alpha_n\alpha'_n} \bar{X}^{\sigma'_n}_{\alpha'_{n-1}\alpha'_n}. \end{aligned} \tag{2.65}$$

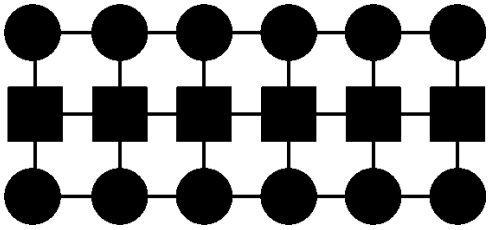

Figure 2.10: Graphical representation of expectation value $\langle\Psi|\,\hat{O}\,|\Psi\rangle$ of an MPO $\hat{O}$.

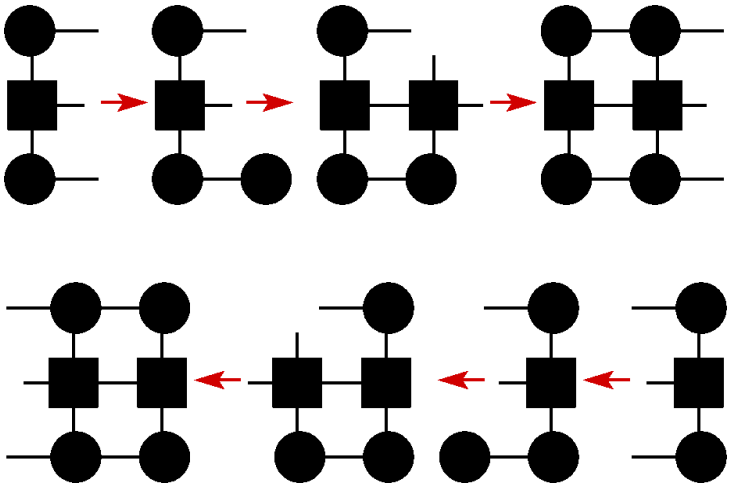

Figure 2.11: Graphical representation of tensor contractions. Upper panel: starting from an E_1 matrix (left side) the MPS and MPO matrices of site 2 are contracted into the network one by one. Using reshape operations to bring the tensors into matrix form, complexity scales $\sim D^3$. Lower panel: the same for the case when starting from the right side of the system.

The order of contraction is indicated by the order of the sums: First, we we contract $\bar{X}^{\sigma'_n}$, then $M^{\sigma_n\sigma'_n}$ and finally X^{σ_n}. All operations in this case scale with $\sim D^3$. So far, we have not imposed any restrictions on the MPS matrices X^{σ_n}. If the operator $\hat{O}$ is local, meaning that it acts non-trivially only on sites m to n, where $m \leq n \leq N$, then imposing left orthonormalization for matrices X^{σ_k}, with $k < m$ and right orthonormalization for matrices X^{σ_l} with $l > n$ simplifies things a lot. In this case, the MPO matrices for sites $k < m$ have dimension one and contain only a single entry, namely $\mathbb{1}$, and similar for $l > n$. The first E_1 matrix at the left side is thus just the identity matrix $\delta_{\alpha_1\alpha'_1}$, and because of that, up to site m, all contractions reduce to a $\delta_{\alpha_k\alpha'_k}$ and can effectively be omitted. Just the same line of arguments also holds for all F_l matrices with $l > n$. This is depicted in Fig.2.12. The black-colored MPO matrices are nontrivial, whereas the other ones have bond dimension $B = 1$ with only a single entry, namely $\mathbb{1}$ (as indicated in the figure).

For the case that all MPS matrices X^σ in the expression for the E_n matrix are *left orthonormal*, we reserve the letter L_n, and similar if all MPS matrices in the expression for the F_n matrix are *right orthonormal*, we use the letter R_n:

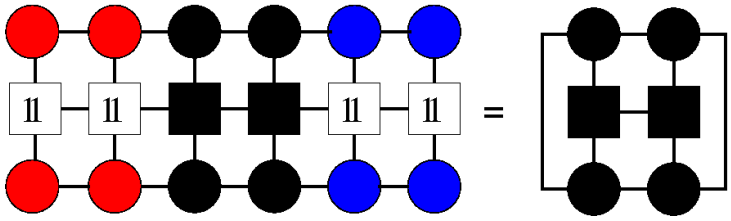

Figure 2.12: Graphical representation of expectation value $\langle\Psi|\hat{O}|\Psi\rangle$ of an MPO $\hat{O}$ which acts only non-trivially on the two central sites (where the MPO matrices are black). The red dots represent left-orthonormalized matrices, the blue dots right orthonormalized ones. Because of the trivial action of the MPO on the outer sites and the normalization of the matrices, one has only to do the contraction as indicated by the right-hand side in the figure.

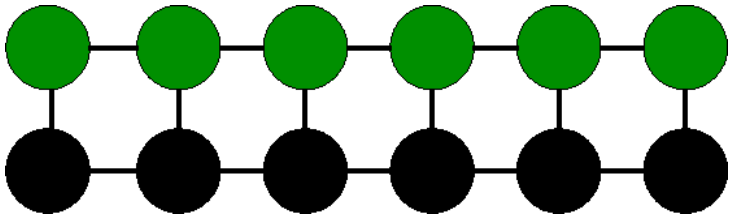

Figure 2.13: Overlap of two different MPS. The states need not have any particular orthonormalization.

$$\begin{aligned} E_n \to L_n \quad & \text{all } X^{\sigma_i} \text{ with } i \leq n \text{ are left orthonormal} \\ F_n \to R_n \quad & \text{all } X^{\sigma_i} \text{ with } i \geq n \text{ are right orthonormal} \end{aligned} \tag{2.66}$$

2.6 Calculation of overlaps

A common operation needed in many applications of matrix product states is the computation of overlaps between different states. Graphically, the overlap between two states is represented in Fig.2.13. The states need not have any particular orthonormalization. The overlap can also be obtained by inserting a layer of identity operators into Fig.2.10.

2.7 DMRG from an MPS perspective

We have already seen that DMRG produces an MPS representation of the groundstate wave function. In fact, DMRG can be entirely rephrased as a variational procedure within the space of matrix product states [9]. The functional which is minimized is the

expectation value of the Hamiltonian H:

$$\mathcal{H}(|\Psi\rangle) = \frac{\langle\Psi| H |\Psi\rangle}{\langle\Psi|\Psi\rangle} \tag{2.67}$$
$$|\Psi\rangle = \sum_{\{\sigma_i\}} \vec{X}^{\sigma_1} X^{\sigma_2} \cdots X^{\sigma_{N-1}} \vec{X}^{\sigma_N} |\{\sigma_i\}\rangle$$
$$\min_{|\Psi\rangle} \mathcal{H} \to |\Psi_0\rangle\,.$$

Of course the number of parameters is still gigantic ($\sim ND^2d$, though importantly *linear* in the system size), and one might ask if this parametrization has bought us anything. In 1d, the good answer is: yes. In the very spirit of the DMRG, the way the problem is solved is by converting the global minimization problem into a local one for every site, and then iterating through all sites until convergence is reached. The minimization is done under the condition of normalization $\langle\Psi|\Psi\rangle = 1$. This condition can be incorporated by use of a Lagrange multiplier μ:

$$\mathcal{H} \to \tilde{\mathcal{H}} = \langle\Psi| H |\Psi\rangle - \mu(\langle\Psi|\Psi\rangle - 1)$$
$$\min_{|\Psi\rangle,\mu} \tilde{\mathcal{H}} \to |\Psi_0\rangle\,. \tag{2.68}$$

To this end, one picks out a single site n and and keeps matrices at all other sites fixed. Eq.2.68 can be written out explicitly. First, let us write out the overlap

$$\langle\Psi|\Psi\rangle = \tag{2.69}$$
$$\sum_{\{\sigma\}\{\alpha,\alpha'\}} \underbrace{\left(X^{\sigma_1}_{\alpha_1}\bar{X}^{\sigma_1}_{\alpha'_1} \ldots X^{\sigma_{n-1}}_{\alpha_{n-2}\alpha_{n-1}}\bar{X}^{\sigma_{n-1}}_{\alpha'_{n-2}\alpha'_{n-1}}\right)}_{\Psi^L_{\alpha_{n-1}\alpha'_{n-1}}} X^{\sigma_n}_{\alpha_{n-1}\alpha_n}\bar{X}^{\sigma_n}_{\alpha'_{n-1}\alpha'_n} \underbrace{\left(X^{\sigma_{n+1}}_{\alpha_n\alpha_{n+1}}\bar{X}^{\sigma_{n+1}}_{\alpha'_n\alpha'_{n+1}} \ldots X^{\sigma_N}_{\alpha_N}\bar{X}^{\sigma_N}_{\alpha'_N}\right)}_{\Psi^R_{\alpha_n\alpha'_n}}.$$

Using the notations of the previous section, Eq.2.68 thus gets (note the $\delta_{\sigma_n\sigma'_n}$ introduced in the expression for the overlap)

$$\tilde{\mathcal{H}} = \sum_{\substack{\beta_n\alpha_n\alpha'_n\sigma'_n \\ \beta_{n-1}\alpha_{n-1}\alpha'_{n-1}\sigma_n}} E^{\beta_{n-1}}_{\alpha_{n-1}\alpha'_{n-1}} X^{\sigma_n}_{\alpha_{n-1}\alpha_n} M^{\sigma_n\sigma'_n}_{\beta_{n-1}\beta_n} \bar{X}^{\sigma'_n}_{\alpha'_{n-1}\alpha'_n} F^{\beta_n}_{\alpha_n\alpha'_n}$$
$$-\mu\Big(\sum_{\substack{\alpha_n\alpha'_n\sigma'_n \\ \alpha_{n-1}\alpha'_{n-1}\sigma_n}} \Psi^L_{\alpha_{n-1}\alpha'_{n-1}} X^{\sigma_n}_{\alpha_{n-1}\alpha_n} \bar{X}^{\sigma'_n}_{\alpha'_{n-1}\alpha'_n} \delta_{\sigma_n\sigma'_n} \Psi^R_{\alpha_n\alpha'_n} - 1\Big). \tag{2.70}$$

To find the extremum (which is usually the minimum) of Eq.2.70 with respect to $X^{\sigma'_n}_{\alpha'_{n-1}\alpha'_n}$, we set the derivative by $\bar{X}^{\sigma'_n}_{\alpha'_{n-1}\alpha'_n}$ to zero. This leads to a generalized eigenvalue problem of the form $h\psi = \mu N\psi$. To ease up notation, we introduce multi-indices $a = (\alpha_{n-1}\alpha_n\sigma_n)$:

$$\nabla_{\bar{X}_{a'}}\tilde{\mathcal{H}} = \sum_a \left(h_{a'a} - \lambda \sum_a N_{a'a}\right) X_a \stackrel{!}{=} 0 \tag{2.71}$$
$$h_{a'a} = \sum_{\beta_{n-1}\beta_n} E^{\beta_{n-1}}_{\alpha_{n-1}\alpha'_{n-1}} M^{\sigma_n\sigma'_n}_{\beta_{n-1}\beta_n} F^{\beta_n}_{\alpha_n\alpha'_n}$$
$$N_{a'a} = \Psi^L_{\alpha_{n-1}\alpha'_{n-1}} \Psi^R_{\alpha_n\alpha'_n} \delta_{\sigma_n\sigma'_n}$$

A major simplification occurs if we impose mixed orthonormalization conditions for the state (see Sec. 2.3.5): if all $X^{\sigma_k} \to A^{\sigma_k}$ for $k < n$ and $X^{\sigma_l} \to B^{\sigma_l}$ for $l > n$, then $\Psi^L_{\alpha_{n-1}\alpha'_{n-1}} \to \delta_{\alpha_{n-1}\alpha'_{n-1}}$ and $\Psi^R_{\alpha_n\alpha'_n} \to \delta_{\alpha_n\alpha'_n}$ and hence $N_{a'a} = \delta_{a'a}$. Note that X^{σ_n} is neither left nor right orthonormal. The final equation one has to solve is thus

$$\sum_{a'} h_{a'a} X_a = \lambda X_a \tag{2.72}$$
$$h_{a'a} = \sum_{\beta_{n-1}\beta_n} L^{\beta_{n-1}}_{\alpha_{n-1}\alpha'_{n-1}} M^{\sigma_n\sigma'_n}_{\beta_{n-1}\beta_n} R^{\beta_n}_{\alpha_n\alpha'_n},$$

where we replaced $E \to L$ and $F \to R$, due to mixed orthonormalization. Solving this system of equations for X still a non-trivial task, but can be efficiently done using large sparse eigensolvers like Lanczos (see Sec.1) or Davidson-Liu . A crucial point is that *$h_{a'a}$ never needs to be explicitly built up.* In fact, one of the great advantages of the MPS parametrization is the resulting product structure of $h_{a'a}$. To obtain high efficiency, the matrix-vector product used in the eigensolver thus has to exploit this structure by *contracting L, R, M and X one by one into the network.* The full optimization problem for a given Hamiltonian H is summarized in the following Tab.2.1.

The way we have presented the algorithm, it differs from the DMRG procedure outlined in the first section in that it optimizes only a single matrix at a time (dubbed "single site DMRG"). The generalization to a two site optimization problem is straightforward. An advantage of the single site method is that it is faster by a factor d^3 per step (d is the local Hilbert space dimension) as compared to the two site approach. On the other hand, the simple minded approach presented shows slower convergence than the two site approach. In the latter, fluctuations between different parts of the system can be built up faster due to the two site variation, where individual particles for example can be exchanged between the two sites. This convergence problem for the single site approach can be overcome by introducing random fluctuations into the DMRG single-site density matrix [38], making the single site approach favorable to the two site one. For most applications in this work the difference in run-time per step is negligible compared to other operations, like time evolution and computation of single particle spectra. For this reason, results presented here were all obtained using a two-site approach for the groundstate computation.

The algorithm presented here is designed for 1d systems with open boundary conditions. Extensions to infinite systems can be done using a variational MPS framework [39], or by applying imaginary time evolution [40]. An efficient incorporation of periodic boundary conditions (pbc) [41, 42] demonstrates the versatility of the MPS formulation of DMRG.

2.8 Operations on MPS

The vector space properties of the underlying many-body Hilbert space carry straightforwardly over to the MPS representation. The most natural operations in this respect are adding states and applying operators to them.

1. Choose a matrix-dimension D and initialize your MPS with random numbers. Bring the state into right-orthonormal form (consisting of B^σ-matrices) (Sec. 2.3.5). Make sure it is normalized: $\langle\Psi|\Psi\rangle = 1$

2. Running from right to left, compute all R_n expressions (see Eq.(2.65) and Eq.(2.66)).

3. Compute the first L_0 object. For the first step, it is just a scalar (with value 1, see again Eq.(2.65) and Eq.(2.66)).

4. **for** n=1:N-1 **do**:

   Solve Eq.2.72 using a suitable eigensolver (e.g. Lanczos, see Sec. 1). After convergence, bring the resulting matrix $X^{\sigma_n}_{\alpha_{n-1}\alpha_n}$ into left orthonormal form using an SVD: $X^{\sigma_n}_{\alpha_{n-1}\alpha_n} \rightarrow A^{\sigma_n}_{\alpha_{n-1}\delta_n}$ (see Eq.2.37). Multiply $\lambda_{\delta_n} V^\dagger_{\delta_n\alpha_n}$ to the right onto the matrix $B^{\sigma_{n+1}}_{\alpha_n\alpha_{n+1}}$ (this yields an improved starting vector for the Lanczos method at the next site [43]). Compute L_n by contracting $A^{\sigma_n}_{\alpha_{n-1}\delta_n}$ to the last L_{n-1} expression (see Eq.(2.65) and Eq.(2.66))

5. **for** n=N:2 **do**:

   Solve Eq.2.72 using a suitable eigensolver (e.g. Lanczos). After convergence, bring the resulting matrix $X^{\sigma_n}_{\alpha_{n-1}\alpha_n}$ into right orthonormal form using an SVD: $X^{\sigma_n}_{\alpha_{n-1}\alpha_n} \rightarrow B^{\sigma_n}_{\delta_{n-1}\alpha_n}$ (see Eq.2.39). Multiply $U_{\alpha_{n-1}\delta_{n-1}}\lambda_{\delta_{n-1}}$ to the left onto the matrix $A^{\sigma_{n-1}}_{\alpha_{n-2}\alpha_{n-1}}$. Compute R_n by contractig $B^{\sigma_n}_{\delta_{n-1}\alpha_n}$ to the last R_{n+1} expression (see Eq.(2.65) and Eq.(2.66))

6. Check if the groundstate energy has converged as compared to the previous sweep. If pre-specified criterion has been reached, stop. Otherwise go to 4. again.

Table 2.1: Pseudo code for variational groundstate search.

2.8.1 Adding Matrix Product States

Adding two arbitrary MPS $|X\rangle, |Y\rangle$, with matrices $X^{\sigma_n}_{\alpha_{n-1}\alpha_n}$ and $Y^{\sigma_n}_{\gamma_{n-1}\gamma_n}$ and bond dimensions D_X and D_Y, respectively, is done by simply forming the direct sum of the two matrices at each site n, i.e. the new state $|Z\rangle = |X\rangle + |Y\rangle$ has matrices

$$Z^{\sigma_n} = X^{\sigma_n} \oplus Y^{\sigma_n} \equiv \begin{pmatrix} X^{\sigma_n} & 0 \\ 0 & Y^{\sigma_n} \end{pmatrix} \tag{2.73}$$

where we have omitted the auxiliary indices of the matrices. The matrices $Z^{\sigma_n}_{\delta_{n-1}\delta_n}$ (with $\delta_n = (\alpha_n\gamma_n)$) have a bond dimension $D_X + D_Y$

2.8.2 Application of operators to Matrix Product States

Consider an operator O in MPO form (see above), with MPO matrices $M^{\sigma_n\sigma'_n}_{\beta_{n-1}\beta_n}$ and MPO-auxiliary dimension $\mathcal{D}$. The product $O|X\rangle$ of O with an MPS $|X\rangle$ with matrices $X^{\sigma_n}_{\alpha_{n-1}\alpha_n}$ yields an MPS $|Y\rangle$ with matrices

$$Y^{\sigma_n} = \sum_{\sigma'_n} M^{\sigma_n\sigma'_n} \otimes X^{\sigma'_n}. \tag{2.74}$$

$Y^{\sigma_n}_{\gamma_{n-1}\gamma_n} = Y^{\sigma_n}_{(\alpha_{n-1}\beta_{n-1})(\alpha_n\beta_n)}$ has a bond dimension of $D_Y = D_X\mathcal{D}$,

The above operations have the unpleasant property of increasing the bond dimension of an MPS. In this sense, MPS of *fixed* bond dimension do *not* form a vector space. Successive operations of the above kind become unfeasible quite quickly. To restore efficiency, the bond dimension of the resulting MPS has to be truncated, as described below.

2.9 Truncation schemes

Truncation of an (un-orthonormalized) MPS $|X'\rangle$ means reducing the bond dimension from D' to $D < D'$. The truncation is done similar to the truncation step in DMRG: at every bond the eigenspectrum of the local reduced density matrix is truncated. There exist several ways of performing such a truncation. The most naive one is to first left-orthonormalize $|X'\rangle$ and then performing a right orthonormalization sweep (see Sec. 2.3.5 on Schmidt decomposition), during which only the D largest eigenvalues are kept at each site, with a scaling $\sim ND'^3$. Although that is the most intuitive way of performing truncation, it exhibits a (in most cases small) systematic error. The reason for this is the fact that truncation is a *non-local* operation, and hence truncations at different bonds *are not independent*. Consider a state that has been brought into mixed orthonormal form about bond n,

$$|\psi\rangle = \sum_{\{\sigma\}} \ldots A^{\sigma_n}\lambda B^{\sigma_{n+1}} \ldots |\{\sigma\}\rangle, \tag{2.75}$$

and assume that there are $D > 1$ Schmidt-values $\lambda_{\alpha_n} \neq 0$. Now we truncate the state down to a *single* Schmidt-value λ_1 (let us consider a spin 1/2 system). This implies, that at the next bond, there can be only *two* independent Schmidt-values. Hence, truncation

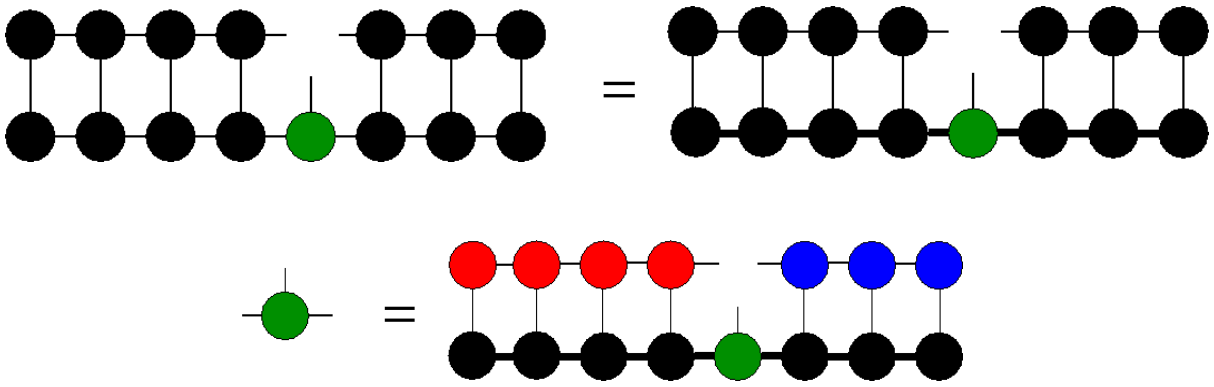

Figure 2.14: *Upper panel:* Graphical representation of the system of linear equations which determines the matrix $X^{\sigma_n}_{\alpha_{n-1}\alpha_n}$ at site n (highlighted as green) of the compressed state $|X\rangle$ (MPS with thin bonds). The uncompressed state is depicted with fat bond-lines (lower MPS on the right side). *Lower panel:* The same equation as in the upper panel, but with $|X\rangle$ brought into mixed orthonormal form about the site n.

at bond n affects the entanglement at bond $n+1$. If truncation at bond n is small, this effect at bond $n+1$ will be small too.

Instead, an optimal truncation scheme can be obtained from a minimization problem: given state $|X'\rangle$ with bond dimension D', one tries to minimize the functional

$$\min_{|X\rangle} || \, |X'\rangle - |X\rangle \, ||_2^2 = \langle X'|X'\rangle + \langle X|X\rangle - \langle X'|X\rangle - \langle X|X'\rangle \tag{2.76}$$

over all MPS $|X\rangle$ with bond dimension $D < D'$. The minimization is rephrased as a variational procedure in the space of MPS matrices X^{σ_n} [44, 9]. Given a random initial guess $|X\rangle$, the minimization is carried out iteratively by locally updating the matrices X^{σ_n}, similar to DMRG. For a random site n, taking the first derivative of Eq.2.76, $\frac{\partial[\langle X'|X'\rangle+\langle X|X\rangle-\langle X'|X\rangle-\langle X|X'\rangle]}{\partial X^{*\sigma_n}_{\alpha_{n-1}\alpha_n}} = \frac{\partial[\langle X|X\rangle-\langle X|X'\rangle]}{\partial X^{*\sigma_n}_{\alpha_{n-1}\alpha_n}} = 0$ yields a system of linear equations for the matrix $X^{\sigma_n}_{\alpha_{n-1}\alpha_n}$. The equations in terms of the matrices X^{σ_n} and X'^{σ_n} look rather complicated (for details see [9]). We will thus jump directly to the graphical representation, given in Fig.2.14. The upper panel in Fig.2.14 shows the system of linear equations which has to be solved. The MPS $|X'\rangle$ with the larger bond dimension D' is plotted with fat lines, and the site which is updated is green. The equation can be solved by e.g. a conjugate gradient method (and variants thereof). The black matrices are kept fixed during the single site update.

The method can be considerably improved by bringing the state $|X\rangle$ into a mixed orthonormal form about the site n. On the left side in the upper panel of Fig.2.14, all contractions to the left and to the right of the green site cancel because of Eqs.2.32 and 2.33. One is left with the much simpler equation in the lower panel of Fig.2.14. The new matrix at site n is thus obtained by contracting the network on the right side in the lower panel of Fig.2.14. Written out in terms of matrices, the lower panel in Fig.2.14 is

$$X^{\sigma_n}_{\alpha_{n-1}\alpha_n} = \sum_{\alpha'_{n-1}\alpha'_n} L_{\alpha_{n-1}\alpha'_{n-1}} X'^{\sigma_n}_{\alpha'_{n-1}\alpha'_n} R_{\alpha_n\alpha'_n}. \tag{2.77}$$

The full optimization is done iteratively by moving back and forth through the state. In the following, we consider a sweep from left to right. After having found the (locally)

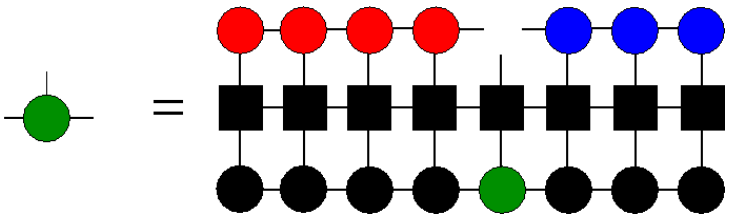

Figure 2.15: Graphical representation of MPO application+truncation, done in a single step. The lower MPS is the original one, the upper one is the compressed state.

optimal $X^{\sigma_n}_{\alpha_{n-1}\alpha_n}$, it is left-orthonormalized, $X^{\sigma_n} \to A^{\sigma_n}$, and the $L_{\alpha_n\alpha'_n}$ is obtained by adding A^{σ_n} and X'^{σ_n} to $L_{\alpha_{n-1}\alpha'_{n-1}}$. $R_{\alpha_{n+1}\alpha'_{n+1}}$ is already known from the previous run, and the procedure can be restarted at site $n+1$. In this fashion, one moves until one reaches the right end. The right-left sweep is done in a similar fashion (see [9]). Convergence is checked by monitoring

$$|| \, |X'\rangle - |X\rangle \, ||_2^2 = 1 - \sum_{\sigma_n} \mathrm{tr}(X^{\sigma_n\dagger} X^{\sigma_n}). \tag{2.78}$$

The performance of this variational compression depends on the quality of the initial guess. A good initial guess can be obtained from the simple SVD compression, which has the drawback that one has to orthonormalize an MPS with a possibly large bond dimensionD'.

Application of an MPO O with bond dimension $\mathcal{D}$ to an MPS $|\Psi\rangle$ with bond dimension D and compression can be done in two ways: either one first applies O to $|\Psi\rangle$ and truncates the resulting state $|X'\rangle$ using one (or both) of the two truncation schemes mentioned above. In the case of simple SVD compression, this scales $\sim N(D\mathcal{D})^3$. One can also do application and variational compression in a single step by inserting an MPO layer instead of the MPS with the fat bonds (see Fig.2.15). This method has a better scaling $ND^3\mathcal{D} + N(D\mathcal{D})^2$ but is more prone to getting stuck in local minimum. For a method with a similar scaling but no sticking problem, we refer the reader to [45]. Again, the method was introduced using single site updates, but extension to a two-site update scheme is straightforward.

The results of this work were obtained by using exclusively the naive approach of first applying the MPO the an MPS and then trucating the resulting state using the naive SVD truncation scbheme.

2.10 Time evolution using MPS

Non-equilibrium dynamics of quantum systems has become an exciting and fast growing field in condensed matter physics. The advent of highly accurate laser techniques for handling ultra cold atoms [46, 47] has given further momentum to the field, and experiments on strongly correlated many-body systems in and out of equilibrium are conducted all over the world, often with spectacular results. An accurate understanding of the results on the other hand is often obscured by the many different and competing energy scales in strongly correlated systems, and the very rare cases of exact analytic results are rightfully

hailed as triumphs in the field which give invaluable insights into the nature of many-body systems. Numerical techniques are hence indispensable tools not only in analyzing experimental data but even as benchmarks for analytic results, where the complexity of the equations itself often admits only restricted classes of solutions to be found [48].

First attempts to exploit the DMRG to do time evolution goes back to 2002, when Cazalilla and Marston [49] first used the truncated DMRG Hamiltonian to carry out the time evolution of a groundstate wave function in a fixed effective basis after performing a quench in the system parameters. This simple minded approach yields reliable results only for short times, and its applicability is hence very limited. The major breakthroughs in the field came in a rapid succession of papers around the year 2004 [50, 51, 11, 10, 52]. In the present work we used the so called Time Evolving Block Decimation (TEBD) method invented by Vidal [10, 11], which will in the following be briefly discussed.

2.10.1 Time Evolving Block Decimation

At the heart of the TEBD algorithm lies the trotterization of the propagator $\hat{U}(\delta t)$ which carries out the time evolution of the system over an infinitesimal (or in practice very small) time step δt (typically $\delta t = 0.05$ for second order expansions, see below). Thus, the method is most suited to deal with short ranged Hamiltonians. For long ranged Hamilton operators, one has to resort to other techniques like Lanczos time evolution [50, 53] or the newly developed time dependent variational principle (tdvp) [54]. In the following, we will consider 1D Hamiltonians with open boundary conditions (obc) of the form

$$H = \sum_{i=1}^{N-1} h_{i,i+1} \tag{2.79}$$

where $h_{i,i+1}$ acts only on site i and $i+1$. An example would again be the Heisenberg Hamiltonian with $h_{i,i+1} = J\vec{S}_i\vec{S}_{i+1}$. The Trotter decomposition starts by grouping the sum into subsets, where terms within a subset commute, and terms between the two subsets need not commute:

$$H = \underbrace{\sum_{e=\text{even}} h_{e,e+1}}_{H_e} + \underbrace{\sum_{o=\text{odd}} h_{o,o+1}}_{H_o}$$
$$[H_e, H_o] \neq 0. \tag{2.80}$$

The propagator $\hat{U}(\delta t') = \exp(-iH\delta t)$ is then decomposed into

$$\begin{aligned} e^{-iH\delta t} &= e^{-iH_e\delta t}e^{-iH_o\delta t} + \mathcal{O}([H_e, H_o]\delta t^2) \quad \text{1st order} \\ e^{-iH\delta t} &= e^{-iH_e\delta t/2}e^{-iH_o\delta t}e^{-iH_e\delta t/2} + \mathcal{O}([H_e, H_o]\delta t^3) \quad \text{2nd order} \end{aligned} \tag{2.81}$$

where the first line is the first order, and the second line is the second order expansion. The individual factors $\exp(-iH_{e/o}\delta t)$ can be decomposed into a product of two-site

operators without any further approximation:

$$e^{-iH_e\delta t} = \prod_{e=even} e^{-ih_{e,e+1}\delta t}$$
$$e^{-iH_o\delta t} = \prod_{o=odd} e^{-ih_{o,o+1}\delta t}. \tag{2.82}$$

To carry out the time evolution over a finite interval t, the interval is divided into L slices ($\delta t = t/L$), and one does L steps with the approximate propagator (for second order time evolution)

$$\hat{U}_a(\delta t) = e^{-iH_e\delta t/2}e^{-iH_o\delta t}e^{-iH_e\delta t/2}. \tag{2.83}$$

Finally, given a state $|\Psi(t=0)\rangle$, the evolved state at time t is thus

$$|\Psi(t)\rangle = \left(\prod_{n=1}^{L}\hat{U}_a(\delta t)\right)|\Psi(0)\rangle\,. \tag{2.84}$$

Note that in this expansion, the intermediate factors $e^{-iH_e\delta t/2}$ from a given $\hat{U}_u$ can be combined with the ones from the previous $\hat{U}_a$ and the next $\hat{U}_a$ into $e^{-iH_e\delta t}$, and thus the only change as compared to a first order expansion is the first and the last $e^{-iH_e\delta t/2}$ in the expansion Eq.(2.84). Of course, before and after a *measurement*, the factors $e^{-iH_e\delta t/2}$ have to be reinserted. The actual application of $\hat{U}_a(\delta t)$ to $|\Psi(0)\rangle$ can be done in different, though related, ways. For this work, we employed the Time Evolving Block Decimation, which has the advantage that it can be easily parallelized. In the TEBD, the initial state $|\Psi\rangle$ is brought into a canonical MPS form. The time evolution over an interval δt brakes down to applying a set of *local* operators or quantum gates $e^{-ih_{i,i+1}\delta t}$ at all pairs of neighboring sites $i, i+1$. The order of these applications is determined by the Suzuki-Trotter decomposition. For the first order expansion $e^{-iH_e\delta t}e^{-iH_o\delta t}$, one first applies all odd gates $\prod_{o=odd} e^{-ih_{o,o+1}\delta t}$, followed by application of all even gates $\prod_{e=even} e^{-ih_{e,e+1}\delta t}$. Within each of these two steps, the order of application does not matter and can in fact be done in parallel. What remains now is the actual procedure of applying a local gate $e^{-ih_{i,i+1}\delta t}$ to a canonical MPS $|\Psi\rangle$. Due to the local nature of the gate and the special form of the MPS, only the matrices $\Gamma^{\sigma_i}, \lambda^{[i]}$ and $\Gamma^{\sigma_{i+1}}$ are affected by the gate. Using the notation $e^{-ih_{i,i+1}\delta t} = g^{\sigma_i'\sigma_{i+1}'}_{\sigma_i\sigma_{i+1}}$, the application of $e^{-ih_{i,i+1}\delta t}$ reads

$$e^{-ih_{i,i+1}\delta t}|\Psi\rangle = \sum_{\alpha_{i-1}\gamma_{i+1}} \underbrace{\sum_{\sigma_i\sigma_{i+1}} g^{\sigma_i'\sigma_{i+1}'}_{\sigma_i\sigma_{i+1}} \left[\lambda^{[i-1]}\Gamma^{\sigma_i}\lambda^{[i]}\Gamma^{\sigma_{i+1}}\lambda^{[i+1]}\right]_{\alpha_{i-1}\gamma_{i+1}}}_{\Theta^{\gamma_{i+1}\sigma_{i+1}'}_{\alpha_{i-1}\sigma_i'}} |\alpha_{i-1}\sigma_i\sigma_{i+1}\gamma_{i+1}\rangle \tag{2.85}$$

where the expression in []-brackets is understood as matrix multiplication (see 2.34 for the definition of $|\alpha_{i-1}\rangle$ and $|\gamma_{i+1}\rangle$). The goal is now to reestablish the canonical form of $e^{-ih_{i,i+1}\delta t}|\Psi\rangle$. This is achieved by invoking an SVD of the matrix $\Theta^{\gamma_{i+1}\sigma_{i+1}'}_{\alpha_{i-1}\sigma_i'}$:

$$\Theta_{(\alpha_{i-1}\sigma_i')(\gamma_{i+1}\sigma_{i+1}')} = U_{(\alpha_{i-1}\sigma_i')\eta}\lambda^{[i]}_{\eta}[V^{\dagger}]_{\eta(\gamma_{i+1}\sigma_{i+1}')} \tag{2.86}$$

where $\lambda_\eta^{\prime[i]}$ are the new Schmidt values at bond i. By rearranging $U_{(\alpha_{i-1}\sigma_i')\eta}$, and dividing the result by $\lambda^{[i-1]}$ from the left, the new matrix $\Gamma^{\sigma_i'}$ is found by

$$\Gamma^{\sigma_i'}_{\alpha_{i-1}\eta} = [\lambda^{[i-1]}_{\alpha_{i-1}}]^{-1} U^{\sigma_i'}_{\alpha_{i-1}\eta} \tag{2.87}$$

and similarly for $\Gamma^{\sigma_{i+1}'}_{\eta\alpha_{i+1}}$

$$\Gamma^{\sigma_{i+1}'}_{\eta\gamma_{i+1}} = [V^\dagger]^{\sigma_{i+1}'}_{\eta\gamma_{i+1}} [\lambda^{[i+1]}_{\gamma_{i+1}}]^{-1}. \tag{2.88}$$

It can easily be checked that these matrices obey the conditions for a canonical MPS. The division by $\lambda^{[i-1]}$ and $\lambda^{[i+1]}$ can be problematic if the Schmidt values become very small, which in some cases can destabilize the algorithm and lead to erratic behavior of observables (which was fortunately not the case for the presented results). This issue has been resolved by Hastings [55] who proposed an update scheme which avoids such explicit divisions.

Because $e^{-ih_{i,i+1}\delta t}$ acts on both sites i and $i+1$, its effect is that in general the *entanglement between the left part containing site i and the right part containing site $i+1$ grows*. As a result, the number of Schmidt values at bond i is larger than before application of $e^{-ih_{i,i+1}\delta t}$, usually by a factor of (at most) d, the local Hilbert space dimension. Successive applications of gates would thus yield exponential growth in computational time and memory consumption. The remedy is to *truncate* the number of Schmidt values, and keep only the D largest ones out of the dD entries in $\lambda_\eta^{\prime[i]}$, in the very spirit of DMRG. In contrast to DMRG, with increasing number of time steps, the result gets increasingly wrong, and from a certain number of iteration steps on is completely off the true results. The total time reachable in typical simulations depends on the problem at hand. Usually, local quenches perform better than global ones due to the slower growth of entanglement entropy [56, 9]. Strong correlations tend to reduce the reachable simulation time due to presence or developing of long ranged spatial correlations. In any case, one has to investigate results for convergence in auxiliary parameters like matrix dimension D and time step δt. A rough measure to estimate the accuracy of your simulations is to monitor the truncated weight $\epsilon_{tw} = \sum_{\eta>D} |\lambda_\eta^{\prime[i]}|^2$ (see also Eq.2.7). Typically, when $\epsilon_{tw} > \mathcal{O}(10^{-4})$, the maximum simulation time for which results are reliable has been reached and simulations can be (or rather should be) stopped.

The scheme can be straightforwardly generalized to the case of next nearest neighbor interaction. In this case, the gate assumes the form $e^{-ih_{i,i+1,i+2}\delta t} = g^{\sigma_i'\sigma_{i+1}'\sigma_{i+2}}_{\sigma_i\sigma_{i+1}\sigma_{i+2}}$, and application to $|\Psi\rangle$ affects now $\Gamma^{\sigma_i}, \lambda^{[i]}, \Gamma^{\sigma_{i+1}}, \lambda^{[i+1]}$ and $\Gamma^{\sigma_{i+2}}$. The resulting tensor $\Theta_{\alpha_{i-1}\sigma_i'\sigma_{i+1}',\sigma_{i+2}',\gamma_{i+2}}$ can again be decomposed by using a sequence of two SVDs by reshaping Θ into a matrix where the corresponding indices have been singled out. Of course, the order of application of the individual three-site gates depends on the choice of Trotter expansion and is not unique.

2.11 Outlook

To cover the full range of applications and developments of MPS is way beyond the scope of this work. We will thus give only a very short survey of the most important applications and developments. MPS methods can be used to calculate static and dynamical properties

of 1d quantum system both at zero and finite temperature [7, 8, 57, 58, 59, 60, 61, 62]. Several methods for efficient time evolution have been proposed [10, 11, 51, 50, 52, 54], MPS methods have been extended to the treatment of continuous field theories [35, 33, 34], and they can even be used to calculate dispersion relations of 1d lattice [63] or continuous [64] field theories. They have strongly contributed to our understanding of the role of entanglement in quantum systems [28], out of which new, efficient methods for correlated quantum systems have been developed [65, 66]. The extension of Tensor Network States (TNS) [67] to higher spatial dimensions [44, 68] is a rapidly expanding field. Recently, the DMRG method has been applied to 2d quantum systems where it settled a longstanding argument about the nature of the groundstate of the spin 1/2 Heisenberg anti-ferromagnet on the Kagome lattice [69, 70]. In summary, MPS and TNS in general are by now the method of choice for 1d systems, they are among the most promising candidates to correlations in $d > 1$ dimensions, and they might well redefine our notion of computability and set completely new standards in computer science.

Chapter 3

Observation of Complex Bound States in the XXZ Model using Local Quantum Quenches

3.1 Introduction

Cold atomic gases [46, 47] provide an ideal testing ground for non-equilibrium many-body quantum physics because the dynamics remain coherent for long times by virtue of the weak coupling to the environment. Recent experiments [71, 72, 73, 74] have opened up the study of an entirely new regime in many particle quantum physics. The "quantum Newton's cradle" experiments of Kinoshita et al [74] drew attention to the importance of dimensionality and conservation laws and prompted a huge number of theoretical analyses on the role played by quantum integrability [75, 76, 77, 78, 79, 80, 81, 82, 83, 84, 85, 86, 87, 88, 89, 90, 91, 92]. A standard protocol for driving a quantum system out of equilibrium is by means of a global quantum quench (QQ) where a system is prepared in the ground state of a given Hamiltonian H_0. At time $t = 0$ an experimentally tuneable parameter that characterizes the Hamiltonian (e.g. a magnetic field) is changed suddenly and one then considers the unitary time evolution of the system by means of the new Hamiltonian H. QQs can be either global or local and we focus on the latter case in the following. The following chapter is devoted to the investigation of quantum quenches in the 1d Heisenberg XXZ-model.

The text of this chapter largely follows the corresponding publication in Physical Review Letters [93], supplemented by additional results and more details on data analysis. The draft for this publication has been written by the author of this thesis. It was then edited by F. H. Essler and H. G. Evertz. All results except the spinon and two-string despersion relation of the Bethe ansatz (solid lines in Fig.3.3) have been obtained by the author.

3.2 Heisenberg model and realization in cold atom experiments

In the following we consider the anisotropic spin-1/2 Heisenberg chain on a lattice with N sites with fixed numbers $N_{\uparrow,\downarrow}$ of up and down spins and open boundary conditions.

$$H(\Delta, B_0) = J \sum_{i=1}^{N-1} S_i^x S_{i+1}^x + S_i^y S_{i+1}^y + \Delta S_i^z S_{i+1}^z - B_0(t) \sum_{i=i_0}^{i_0+m_0-1} S_i^z, \tag{3.1}$$

where $J > 0$ and B_0 is a local magnetic field acting on m_0 consecutive sites starting at position i_0. It is well-known that (3.1) can be mapped to a model of spinless fermions with nearest-neighbor density-density interaction by means of a Jordan-Wigner transformation [37] (see Sec. 2.4) and all of our results are straightforwardly translated into that setting. Originally designed to explain magnetic properties of solids, it has attracted the attention of numerous authors, also because in 1d, it can be solved exactly by means of the Bethe ansatz [94, 95, 96, 97, 98, 99] which has since grown into a large research area of its own. Though a vast amount of literature exists covering the thermodynamic and groundstate properties of this model, results for non-equilibrium properties have long remained elusive due to the complicated nature of the exact solution. Numerical techniques on the other hand had to resort to small system. However, with the advent of efficient numerical approaches like TEBD and tDMRG [11, 10, 51, 50], quenches in the interacting XXZ chain [100, 101, 102, 103, 104, 105, 106, 107, 108] and corresponding conformal field theories [109, 110] in particular and lattice models in general [89, 111, 84, 112, 113, 114, 91, 115] have since been studied intensely. Quite generally, the question of whether or how quantum systems approach an equilibrium distribution after experiencing a strong perturbation is still unclear, and major efforts are made to settle this argument. It is nowadays broadly believed that integrability of quantum system plays an important role and evidence has been gathered that integrable systems in general will not equilibrate due to the strong confinement of phase space, resulting from conservation laws [79, 78].

The study of local QQs in models of the kind (3.1) was initiated in 1970 [116, 117], where the non-interacting case $\Delta = 0$, $m_0 = 1$ was shown to lead to a non-thermal stationary state. Local quenches in different interacting lattice models have since been studied numerically [114, 111, 107, 103, 115] and the ability of engineering strongly correlated lattice models using laser trapping techniques [118] very recently also allowed for experimental investigation of local QQs [119, 120, 16]. Succesfull realizations of Bose-Hubbard [118, 121, 74] and Fermi-Hubbard [122, 123, 124, 125] models have become standard tools in the community. Recent progress even allows now for single site resolution [126, 127, 128] of quantum dynamics of the XXZ-Heisenberg model [129, 120, 16], which was shown to be realizable via a two-species Hubbard model at large interaction strength U [130, 131], of particular interest for our research.

3.3 Bethe ansatz for the Heisenberg model

In 1-d, the Heisenberg model can be solved exactly by means of the Bethe ansatz (in fact, Bethe himself first applied his ansatz to the Heisenberg model). For an introduction to the Bethe ansatz, we refer the reader to [94, 95, 96, 97, 98, 99]. In the following, we will give a short overview of the most important results.

At the heart of the Bethe ansatz lies the fact that in 1-d and for certain pair-potentials, M-body scattering, i.e. scattering of M particles from each other, breaks apart into a sequence of *two-body scattering events* (scattering is then said to be *non diffractive*). The central object of interest in this context is the so called *scattering phase shift* $\theta(k-k')$, obtained from scattering of two particles with momenta k and k' from each other. The effect of the particle-particle interaction is fully encoded into the properties of $\theta(k-k')$. Under the above conditions, one can make the Bethe ansatz for the wave function. In the following, we will present the most important results for the spin-1/2 XXZ Heisenberg magnet, for which the scattering phase shift can be obtained by an elementary calculation [97] (see appendix). The simplest eigenstate of Eq.3.1 is the ferromagetic state with all spins aligned in $|\downarrow\rangle$ direction. This state will serve as reference state from which all excitations can be created via spin-flip operations. Note that for the following discussion it does not matter whether or not $|FM\rangle$ is the ground state of Eq.(3.1), e.g. if $\Delta > 0$ or $\Delta < 0$. In the following discussion, we will also restore periodic boundary conditions again, for the sake of simplicity. Open boundary conditions can in principle also be handled, but are much more cumbersome to incorporate. Excitations with $N_\uparrow$ spin-flips (particles) can be constructed by Bethe's Ansatz and are parametrized by $N_\uparrow$ momenta k_j

$$|N_\uparrow, \mathbf{k}\rangle \;\; = \sum_{x_1<\cdots<x_{N_\uparrow}} \Psi\big(\{k_j\}|\{x_l\}\big) \prod_{n=1}^{N_\uparrow} S^+_{x_n}|\downarrow\rangle. \tag{3.2}$$

The wave function Ψ has the characteristic Bethe Ansatz form

$$\Psi(\{k_j\}|\{x_l\})) = \sum_{\mathcal{P}} A(\mathcal{P}) e^{i\sum_l x_l k_{\mathcal{P}l}} \tag{3.3}$$

where the sum runs over all permutations $\mathcal{P}$ of the indices $(1, 2, \ldots N_\uparrow)$. The amplitudes $A(\mathcal{P})$ can be expressed via the scattering phase shifts. If for example $\mathcal{P}$ and $\mathcal{P}'$ are two permutations where only two momenta k_i and k_j have been exchanged, and all other are the same, then

$$\frac{A(\mathcal{P})}{A(\mathcal{P}')} = -e^{-i\theta(k_i,k_j)}. \tag{3.4}$$

The momenta $\{k_j\}$ are subject to quantization conditions, which for a ring geometry read

$$e^{iNk_j} = \prod_{\substack{l=1\\ l\neq j}} e^{i\theta(k_j,k_l)} = \prod_{\substack{l=1\\ l\neq j}}^{N_\uparrow} -\frac{2\Delta e^{ik_j} - 1 - e^{ik_j+ik_l}}{2\Delta e^{ik_l} - 1 - e^{ik_j+ik_l}} \;,\; j = 1, \ldots, N_\uparrow. \tag{3.5}$$

Taking the logarithm of Eq.(3.5) yields

$$k_j N = 2\pi I_j + \sum_l \theta(k_j, k_l) \tag{3.6}$$
$$\theta(k_j, k_l) = -i \log\left(-\frac{2\Delta e^{ik_j} - 1 - e^{ik_j+ik_l}}{2\Delta e^{ik_l} - 1 - e^{ik_j+ik_l}}\right)$$

often referred to as fundamental equation. The *Bethe quantum numbers* I_j reflect the fact that due to periodicity, Eq.(3.5) is determined only up to modulo 2π, i.e. $e^{ik_j N} = e^{ik_j N \pm 2\pi I_j}$. They assume integer values for an odd number of (bosonic) particles, and half-odd-integers for an even number of particles [97]. A given a set of $\{I_j\}$-quantum numbers yields thus a set of $\{k_j\}$ values. The solution of Eq.(3.6) is in general an involved task. Once a set of $\{k_j\}$ has been found, total energy E and total momentum P of the corresponding state are given by

$$P = \sum_{j=1}^{N_\uparrow} k_j \tag{3.7}$$
$$E = \sum_{j=1}^{N_\uparrow} \epsilon(k_j) = \sum_{j=1}^{N_\uparrow} J\big(\cos k_j - \Delta\big) \tag{3.8}$$

which are remarkably simple formulas! In fact, they are formally the same as for a set of $N_\uparrow$ non-interacting particles. The interaction though is "hidden" in the discretization of the k_j's.

The solutions k_j of Eq.(3.6) can be either real or complex [132, 133, 98]. The former describe scattering states of "magnons", while the latter correspond to bound states. Bound states involving ℓ particles are known as "ℓ-strings" and have wave functions that exhibit exponential decay (which can be slow) with respect to the distances between particles (the name "ℓ-strings" reflects the fact that for such solutions the k_j are equidistantly spread along a line parallel to the imaginary axis, i.e. all k_j have the same finite real part). Their dispersion relations in the thermodynamic limit are [132, 133, 98, 97]

$$\epsilon_\ell(k) = -J\frac{\sin(\nu)}{\sin(\ell\nu)}\big(\cos(\ell\nu) - (-1)^\ell \cos(k)\big) \tag{3.9}$$
$$\Delta = \cos(\nu).$$

Here the total momentum k of ℓ-strings is constrained, e.g. for $|\Delta| < 1$ and $\ell = 2$ we have $|k| > 2\nu$ [134]. For a given value of Δ there generally exists a hierarchy of allowed strings, which was first identified in a seminal work by Suzuki and Takahashi [132, 133, 98]. We note that the energy difference between bound states and scattering continua can generally be very small.

3.4 Local quantum quenches

In the following we will investigate the time evolution of the XXZ-model following a local quantum quench. We will address quenches of different length m_0 (see Eq.3.1),

where model-parameters at m_0 adjacent sites will be changed simultaneously at $t = 0$. In the following we show that quenches with larger $m_0 > 1$ lead to prominent linearly propagating bound states, which in standard condensed matter scenarios have been difficult to discern [108, 135, 136, 137, 138, 139, 140]. We present results for open boundary conditions (obc) [1].

We consider the following quench protocol: we prepare the system in the ground state $|0\rangle$ of the Hamiltonian $H(\Delta, B_0 = \infty)$ (see Eq.3.1). At time $t = 0$ we suddenly switch off the magnetic field B_0 and then consider the time evolution, governed by the Hamiltonian $H(\Delta, B_0 = 0)$, of the following observables

$$\begin{aligned} \langle S^z\rangle(j,t) &\equiv \langle 0|S^z_j(t)|0\rangle \ , \\ P_{\uparrow\uparrow}(j,t) &\equiv \langle 0|P_j(t)P_{j+1}(t)|0\rangle \ , \\ P_{\uparrow\uparrow\uparrow}(j,t) &\equiv \langle 0|P_{j-1}(t)P_j(t)P_{j+1}(t)|0\rangle \ , \end{aligned} \tag{3.10}$$

where $P_j = S^z_j + 1/2$ is the up-spin projection operator on site j. In the following we will consider two different regimes: the first one is the saturated ferromagnet with a magnetization per site m of $-1/2$ (all spins pointing downwards), and the quench corresponds to flipping m_0 spins at consecutive sites. In this case, the problem reduces to a quantum mechanical few-body problem. On the other hand, for magnetizations $-1/2 < m < 0$ the model $H(\Delta, B_0 = 0)$ describes a quantum critical (Luttinger liquid) phase [141] and our local quantum quench involves complex many-body effects and can be thought of as a generalization of the X-ray edge problem. In the following we first consider the simpler, spin-polarized case as this allows us to establish the role played by bound states.

3.4.1 Excitations from the ferromagnetic background

We consider an initial state where at $t = 0$ $m_0 = 3$ spins in the middle of a ferromagnetic spin-chain are simultaneously flipped. Using the exact eigenstates of $H(\Delta, 0)$ we can derive a Lehmann representation for the observables (3.10) after this quench

$$\begin{aligned} \langle\mathcal{O}\rangle(j,t) &= \sum_{\{k_l\},\{p_r\}} \langle 0|m_0,\mathbf{k}\rangle\langle m_0,\mathbf{k}|\mathcal{O}_1|m_0,\mathbf{p}\rangle\langle m_0,\mathbf{p}|0\rangle \\ &\times \ e^{-i\sum_{n=1}^{m_0} t[\epsilon(p_n)-\epsilon(k_n)]-(j-1)[p_n-k_n]]} \ , \end{aligned} \tag{3.11}$$

where the sums are over all Bethe Ansatz states with m_0 momenta. j is the lattice distance from the quench-center. In the case $m_0 = 1$ an elementary calculation (see Eq. 121 in Sec. 2.2) gives $\langle S^z\rangle(j,t) = -\frac{1}{2} + J^2_{j-1}(Jt)$, where $J_n(x)$ is a Bessel function (note that the counting of sites in Eq.3.1 starts with $i = 1$ as compared to Sec.2.2, hence the subscribt $j-1$). Note that as compared to the tight binding case considered in Sec.2.2 the argument of the Bessel function is given by Jt instead of $2Jt$ due to the fact that the spin-hopping term in Eq.3.1 has a factor $J/2$ and not J. For large, fixed j $\langle S^z\rangle(j,t)$ exhibits an oscillatory power-law decay for $Jt \overset{>}{\sim} j$, shows a maximum for $Jt \approx j$ and increases exponentially for $Jt \overset{<}{\sim} j$. A stationary phase approximation shows that the dominant

[1] The boundary conditions do not affect the propagation noticeably until perturbations reaches the boundary.

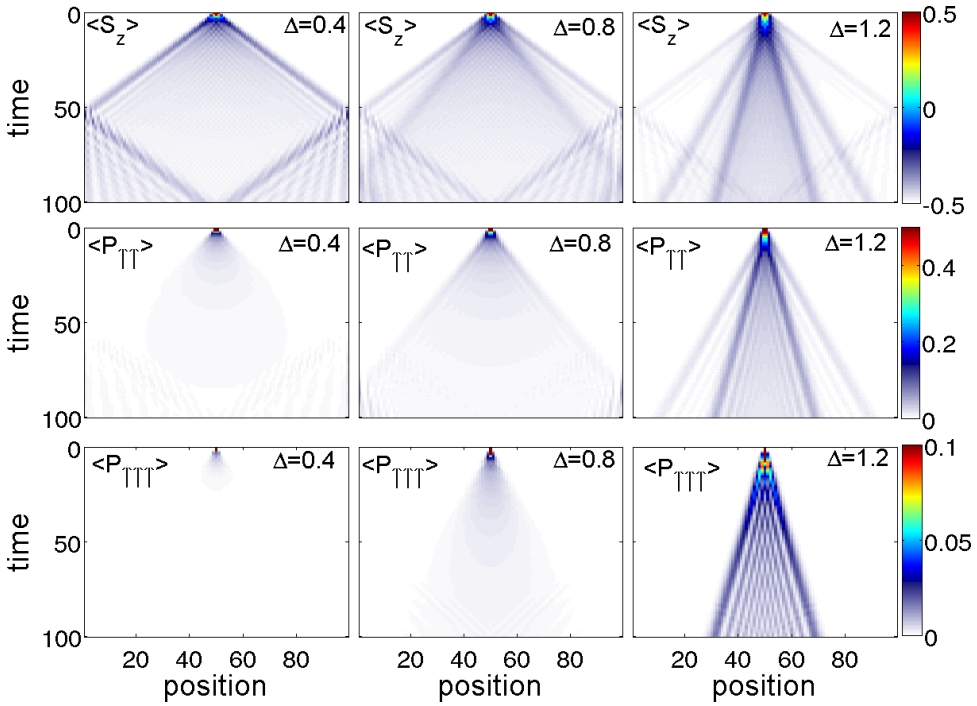

Figure 3.1: Time evolution in the spin polarized case after preparing the system in a initial state with three spin flips in the center of a 101 site chain for different values of Δ. Top row: Space-time plot of $\langle S^z \rangle (x,t)$; middle row: $\langle \mathcal{P}_{\uparrow\uparrow} \rangle (x,t)$, which projects a bond onto $|\uparrow\uparrow\rangle \langle\uparrow\uparrow|$; bottom row: $\langle \mathcal{P}_{\uparrow\uparrow\uparrow} \rangle (x,t)$, which projects three adjacent sites onto $|\uparrow\uparrow\uparrow\rangle \langle\uparrow\uparrow\uparrow|$.

contribution in the Lehmann representation (3.11) for $Jt \approx j$ arises from states with $k \approx \frac{\pi}{2}, \frac{3\pi}{2}$, which propagate with the highest possible velocity $v_{\max} = \max_k \left| \frac{\epsilon(k)}{dk} \right| = J$. The fact that $\langle S^z \rangle (j,t)$ has a maximum at $Jt \approx j$ can be understood qualitatively by noting that the distribution of velocities $\rho_1(v) = \int \delta(v - d\epsilon/dk) dk = \frac{N}{2\pi} \frac{1}{\sqrt{J^2 - v^2}}$ has singularities at the maximum speed $v = \pm J$. The exponential suppression of $\langle S^z \rangle (j,t)$ for $t \lesssim (j/v_{\max})$ gives rise to a horizon effect and is described by the Lieb-Robinson bound [142].

In all other cases $m_0 > 1$, string states $\ell \geq 2$ will contribute to the time evolution of observables and in order to study their influence we have carried out numerical computations using the TEBD [10] (see Sec.2.10.1) Results for $m_0 = 3$ (three neighboring sites with spin up in the initial state) are shown in Fig. 3.1. As a function of the anisotropy Δ we observe three distinct regimes, which are fully consistent with expectations from the Bethe ansatz: (i) for small values of Δ we observe a single wave front in $\langle S^z \rangle (x,t)$, propagating with the maximal magnon velocity $v = J$ (the $m_0 = 1$ case discussed above looks quite similar).

(ii) At $\Delta = 0.8$, a second, slower branch of propagating wave packets emerges both in $\langle S^z \rangle (x,t)$ and in $P_{\uparrow\uparrow}(x,t)$ (we note that these wave fronts, while evident in Fig. 3.1, are not easy to discern in equal time or space slices due to the oscillatory nature of the signal). Its propagation velocity is equal to the maximal 2-string velocity. We have verified by direct evaluation of (3.11) that the second front is associated with 2-strings. Interestingly there

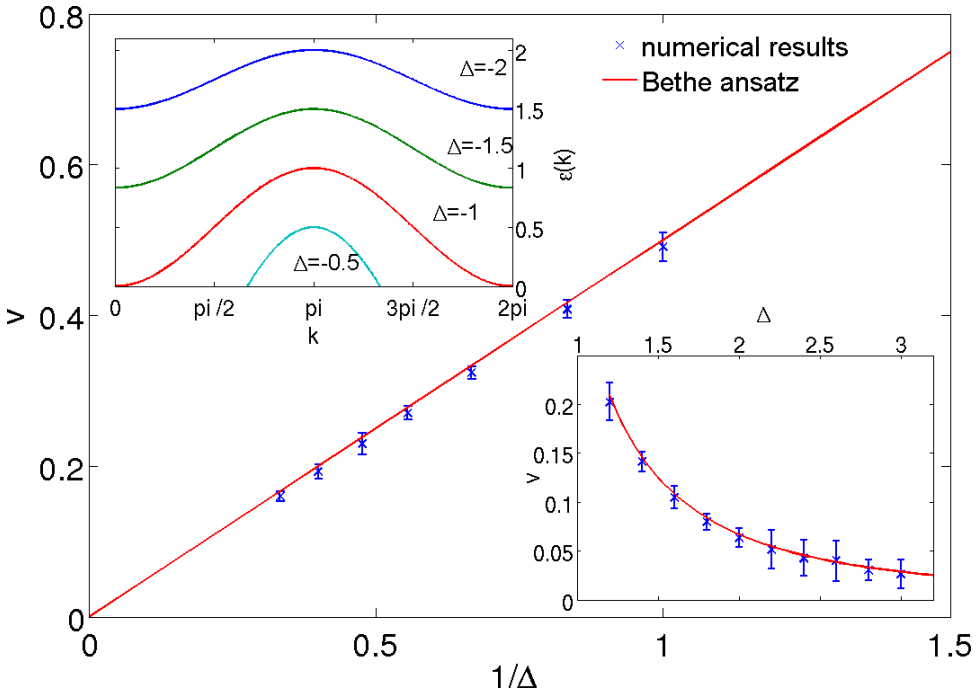

Figure 3.2:

is a threshold in Δ for observing this phenomenon ($\Delta_c \approx \Delta_0 = 1/\sqrt{2}$), while 2-strings exist at any $\Delta \neq 0$. This can be understood by the following argument: the maximal 2-string velocity is $v_{\max,2} = J\sqrt{1-\Delta^2}$ (see upper inset of Fig.3.2) for $0 < \Delta < \Delta_0$ and $v_{\max,2} = \frac{J}{2\Delta}$ for $\Delta_0 < \Delta < 1$, given by the slope of the dispersion at $k = \pi/2$ and $3\pi/2$. On the other hand, the density of states for 2-strings is $\rho_2(v) = 2\Delta/\sqrt{J^2 - (2\Delta v)^2}$, which acquires a singularity *only if* $\Delta \geq 1/\sqrt{2}$. The singularity is related to the fact that the group velocity $v_2(k) = \frac{d\epsilon_2}{dk} = -\frac{1}{2\Delta}\sin(k)$ is constant for $k \approx \pi/2$ and $3\pi/2$. This linear part is on the other hand absent if $\Delta < 1/\sqrt{2}$. It is this singularity which induces a clear signature of propagating 2-strings in both $\langle S^z\rangle(x,t)$ and $P_{\uparrow\uparrow}(x,t)$. (iii) For interaction strengths above $\Delta_{c2} \approx 0.9$ we observe an additional branch in $\langle S^z\rangle(x,t)$, $P_{\uparrow\uparrow}(x,t)$ and in $P_{\uparrow\uparrow\uparrow}(x,t)$. This feature clearly arises from propagating 3-strings and can be understood in complete analogy with the 2-string case discussed above. To confirm our arguments, we compare the Bethe ansatz results for the two- and three-string propagation speeds for different values of Δ with our numerical data (see Fig.3.2 main figure and lower inset).

Finally, let us remark that the above results for excitations above the ferromagnet (or vacuum) remain valid for either sign of anisotropy Δ. This is due to a symmetry valid for initial product states. For a detailed discussion, see Sec.4.3.4.

3.4.2 Results for finite magnetizations

We saw in the previous section that in a ferromagnetic background string states can be observed as prominent features in the time evolution ensuing a local quantum quench. We will now show that the same features can also be observed when the bulk of the system is in a strongly correlated state. In fact, string states exist at any magnetization $m \neq 0$.

As initial state at $t = 0$ we choose the ground state of the model at a fixed magnetization $m \neq 0$ and a local magnetic field $B_0 = \infty$ applied at m_0 consecutive sites (see Eq.3.1). As a result, at $t = 0$ spins at these sites are completely aligned into z-direction. At $t = 0$, the field is switched off and the system is evolved in time. The bulk of the system is in a strongly correlated quantum critical Luttinger liquid phase [141] and our quench protocol described above is closely related to the so called X-ray edge singularity problem in a correlated host [143]. However, the observables relevant to our case are different and cannot be described using methods of boundary conformal field theory [144] as in Ref. [143]. We computed the quenched ground state using the density matrix renormalization group algorithm [5, 17] and the time evolution using the TEBD with matrix dimensions up to 1200. In Fig. 3.3 we present results for $\Delta = 1.2$ and three different magnetizations per site $m = (N_\uparrow - N_\downarrow)/2N = -0.44, -0.26, -0.14$, corresponding to $N_\uparrow = 6, 24, 36$ on a $N = 100$ site chain. We note that this corresponds to the Luttinger liquid phase of the Heisenberg model even though $\Delta > 1$. In all cases we observe two propagating wave fronts (in each direction) in $\langle S^z \rangle(x, t)$. The results for $P_{\uparrow\uparrow}(x, t)$ show that the slower front is associated with excitations that favor neighboring spin flips. In order to interpret these results we follow our analysis of the spin polarized case. It is known from the Bethe ansatz solution that the elementary excitations of the Heisenberg chain at finite magnetization are gapless "spinons" as well as gapped bound states associated with string solutions of the Bethe ansatz equations (3.5). It is then tempting to associate the faster/slower wave fronts with spinon and 2-string excitations respectively, because, just like in the spin polarized case, the latter induce an enhancement in the density of neighboring spin flips as a result of their bound nature. In order to substantiate this expectation we have evaluated the maximal velocities (see Sec.3.4.5) of both spinon and string excitations as functions of the magnetization per site. In Fig. 3.3, lower panel, we present a comparison of these velocities with the ones extracted from the TEBD results in Fig. 3.3 (see Sec. 3.4.5 for details). We see that the results are in excellent agreement.

For magnetizations closer to zero the two-string branch gets more and more washed out, because the momentum range of two-string excitations diminishes and eventually vanishes as the magnetization approaches zero [132, 133, 98] In order to determine whether longer strings also lead to easily recognizable features in observables after a local quench we have analyzed the case $m_0 = 3$ for $\Delta = 1.2$ and magnetization per site $m = -0.2525$. Some results for $\langle S^z \rangle(x, t)$ are shown in Fig. 3.4. We can now identify three branches. The propagation velocities extracted from the TEBD data are $v_1 \approx 1.26 \pm 0.02$, $v_2 \approx 0.702 \pm 0.025$ and $v_3 \approx 0.370 \pm 0.02$ respectively. These values agree with the maximal velocities of spinons, 2-strings and 3-strings calculated from Bethe ansatz, which are $v_{\max} \approx 1.263$, $v_{\max,2} \approx 0.705$ and $v_{\max,3} \approx 0.375$.

3.4.3 Integrability breaking perturbations

In general, string states are not protected kinematically from decaying into scattering states of spinons. Their stability is then a consequence of integrability of the Heisenberg chain and an important question is, whether signatures of bound states survive when integrability breaking perturbations are present. In order to address this issue we have considered two types of perturbation: (i) a next-nearest neighbors interaction and (ii) a spatially varying magnetic field term $\gamma \sum_{j=1}^{N} (j - \frac{N}{2})^2 S_j^z$, (with $\gamma = 8\ 10^{-5}$) which would

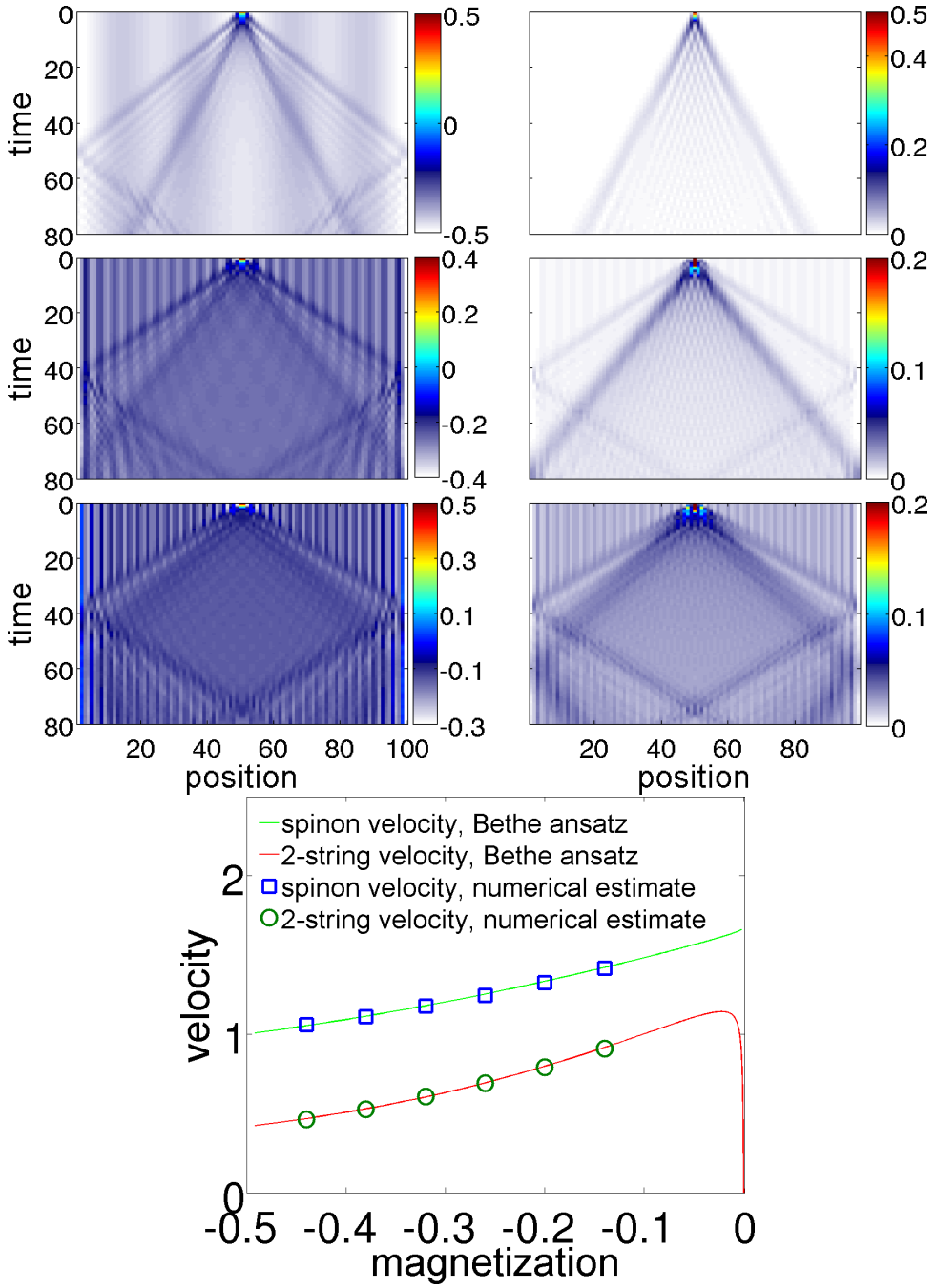

Figure 3.3: *Upper panel:* Two-string propagation at finite magnetization per site m at $\Delta = 1.2$, corresponding to the Luttinger liquid phase of the model. From top to bottom, $m = -0.44$, $m = -0.26$ and $m = -0.14$. The initial state at $t = 0$ is the ground state of (3.1) with an infinite magnetic field term at two sites in the center of the chain (chain length N=100). At $t = 0$, the field is switched off and the state is evolved. The striped patterns visible in all plots are Friedel oscillations due to open boundary conditions. *Lower panel:* Propagation velocity of single-spinon and two-string branch as a function of total magnetization per site m of the system at $\Delta = 1.2$. Green and red curves show single-spinon and two-string velocities as calculated from Bethe ansatz. Blue circles and squares are numerically derived values from real the time simulations. Error-bars are smaller than symbols.

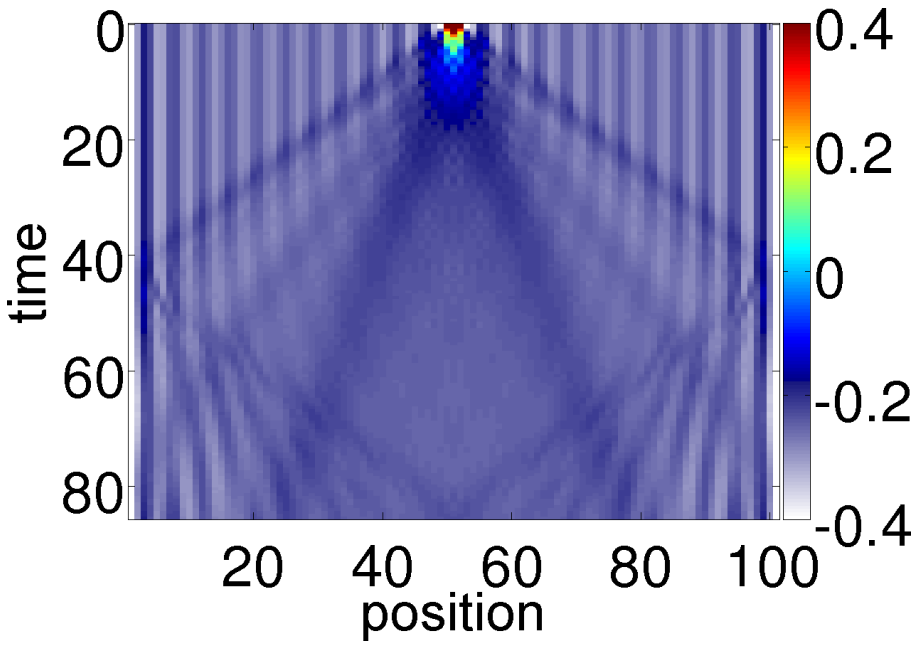

Figure 3.4: Space-time plot of $\langle S^z \rangle$ for a setup similar to Fig. 3.3 with $N = 101$ at total magnetization $m = -0.2525$, $\Delta = 1.2$, with three particles at the chain center at t=0.

model an optical trap in certain realizations of (3.1) based on cold fermionic atoms. In both cases we observe signatures of bound states, indicating that they survive in the form of resonances. We show results for both cases in Fig. 3.5. We note that bound states signatures even exist for $\Delta = 1.0, \gamma = 8\ 10^{-5}$ (not shown).

3.4.4 Evolution of bipartite entanglement

A topic that has recently attracted much interest is entanglement in quantum many-body systems [145, 146]. Classical simulatability of quantum systems can be understood from bi-partite entanglement properties of ground states of 1d quantum many body systems [28]. Groundstates of gapped 1d quantum system are known to be representable by MPS with fairly small bond dimension [147] because they obey an exact area law [28]: For large enough subsystems, the entanglement with its surroundings become size-independent. For non-equilibrium dynamics, it is the growth of entanglement entropy which sets an intrinsic limit on the time scales reachable with time dependent DMRG or MPS methods [10, 11, 51, 50, 9]. For a system in a pure state $|\psi\rangle$, entanglement entropy of a bi-partition $A : B$ is defined as

$$S = -\mathrm{tr}(\hat{\rho}_A \log(\hat{\rho}_A)) \tag{3.12}$$

with $\hat{\rho}_A = \mathrm{tr}_B |\psi\rangle \langle\psi|$ and is a measure of how entangled A and B are. Perales and Vidal [148] investigated the entanglement growth of in the quantum Ising and Mott-insulating Bose Hubbard system after a local QQ with similar methods and observed a saturation-plateau in the entanglement entropy. Especially, for the Ising model in a tilted field, it was observed that bipartite entanglement after a local quench does not truly saturate but shows monotonic (though very small) increase in time.

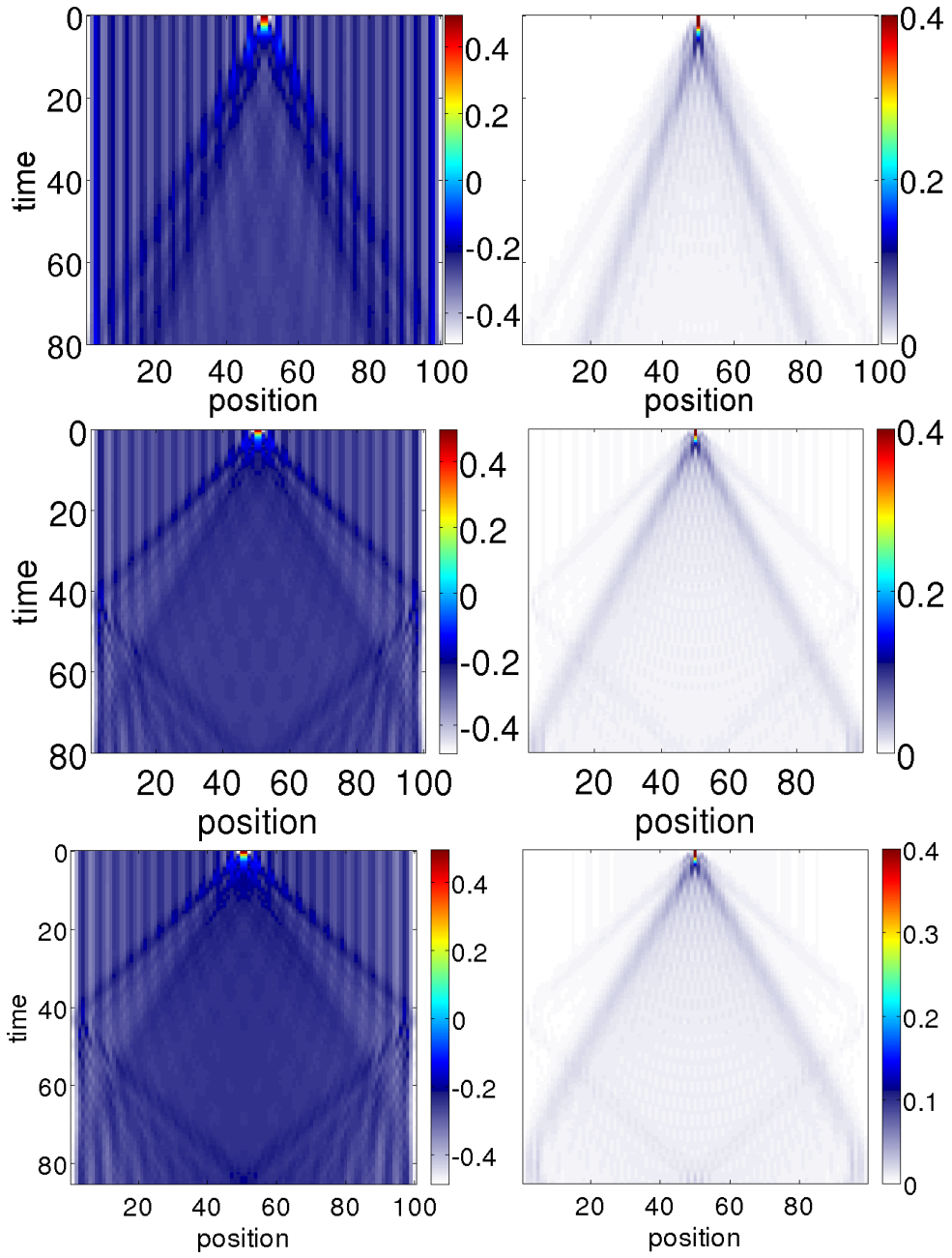

Figure 3.5: *Top panels:* Space-time plot of $\langle S^z \rangle$ and $P_{\uparrow\uparrow}$ for $N = 100$, $m_0 = 2$ at total magnetization $m = -0.26$, $\Delta = 1.2$ and an **extra integrability breaking term** $(J/10)\sum_j \mathbf{S}_j \cdot \mathbf{S}_{j+2}$ added to $H(\Delta, B_0)$. Bound state signatures are seen to persist. Note the increase of propagation speed by approximately a factor of two due to next-nearest neighbor hopping. TEBD parameters: $\chi = 500, dt = 0.05$. *Middle and bottom panels:* Space-time plot of $\langle S^z \rangle$ and $P_{\uparrow\uparrow}$ for $N = 100$, $m_0 = 2$ at total magnetization $m = -0.26$, $\Delta = 1.2$ with an **additional harmonic trap** $\gamma \sum_{j=1}^{N} (j - \frac{N}{2})^2 S_j^z$ with $\gamma = 4\ 10^{-5}$ (middle) and $\gamma = 8\ 10^{-5}$ (bottom) added to $H(\Delta, B_0)$. Simulation parameters were $\chi = 500, dt = 0.05$.

Fig.3.6 a) shows the time evolution of the entanglement entropy for the case of three spins flipped at $t = 0$ from $|0\rangle$ and evolved with $\Delta = 1.2$ as discussed above. The three branches visible in Fig.3.1 can also be observed in the entanglement as a step-like structure [148]. On each plateau the entanglement saturates for long times until the next perturbation crosses from when on a new increase sets in. The saturation values behave such that for higher Δ they decrease, corresponding to the shift of the spectral weight to the two- and three-string states, because for large $\Delta >> 1$, only states with adjacent particles contribute to $|\psi(t)\rangle$ which considerably reduces the relevant Hilbert space.

The picture is quantitatively different when the perturbations travel in a finite density background, Fig.3.6 b). The increase of entanglement caused by the quench is still present, but the step-like structure is more and more washed out for higher densities. Generally, entanglement growth is stronger in this case because of the many more states accessible by the system at finite density. For large t we observe an increase in entanglement growth, possibly logarithmic.

Fig.3.7 shows a more detailed comparison for different m of the entanglement growth at the middle bond of the system (bond 50), where initially two up-spins are located. Shortly after the quench, in all cases we observe a rapid growth of entanglement, almost identical for all magnetizations. For the low density quench $m = -0.44$, the growth levels off abruptly into a slow-growth regime, where it stays almost constant. For high densities ($m >= -0.26$) on the other hand, the initial rapid growth lasts much longer, but shows no kink-like behavior. For very low magnetizations ($m = -0.2, -0.24$) S_{vN} reaches a maximum. The following decrease of entropy is possibly related to the finite size of the system. The dip for $m = -0.14$ coincides with the time when reflections from the boundaries have traveled back to bond 50 (note that signal speed increases with decreasing magnetization m). For intermediate $m = -0.38, -32$, we observe three distinct regimes. The initial rapid growth is followed by an almost linear growth regime, which at $t \approx 60$ levels off into a third regime of much smaller growth.

In Fig.3.7 b), we plot the time evolution of the bipartite entanglement entropy at bond 50 for different Δ, for a quench with $m_0 = 2$ *at zero magnetization* $m = 0$ as a function of $\log(t)$. After the initial sharp increase, we observe a $\log(t)$ like behavior, with oscillations on top. For $\Delta = 0.9$ and 1.0 we plot data for times t small enough so that perturbations have not yet reached the boundaries. For these values of Δ, we observe that finite size effects start to play a role shortly after the perturbations hit the boundary, which lead to deviations of the $\log(t)$ behavior in S_{vN}. With increasing Δ, this effect becomes smaller. Note that the XXZ magnet has a gapless phase for $|\Delta| \leq 1$. Thus correlations are expected to be long ranged, as compared to the gapped phase with a finite correlation length ξ. For $t \geq 3$ (see arrow in Fig.3.7 b) main figure) results were fitted with a linear fit $\alpha \log(t) + \beta$, the inset of Fig.3.7 b) shows the fit parameter α as a function of Δ. The logarithmic growth for $\Delta \leq 1$ is in agreement with results from conformal field theory [109] and numeric [149] calculations. Interestingly, we observe the same behavior for $\Delta > 1$ in which case the system is in a gapped phase and hence conformal field theory cannot be applied. It would be interesting to investigate wether the finite correlation length ξ in this case can be observed as a change in the evolution of the bipartite entanglement.

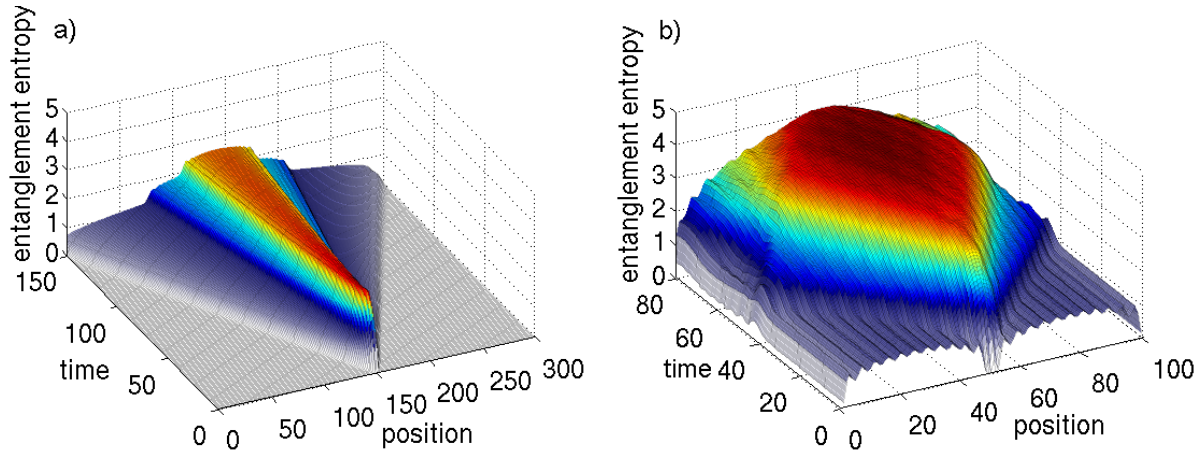

Figure 3.6: a) Time evolution of the entanglement entropy S for $\Delta = 1.2$ for an initial state $|\downarrow \ldots \uparrow\uparrow\uparrow \ldots \downarrow\rangle$ (see Fig.3.1). At $t = 0$, the state is unentangled (pure product state). The three plateaus correspond to the three branches of a single magnon, a two-string and a three-string excitation. Linear increase of the entropy is followed by saturation. b) Time evolution of entanglement entropy for the XXZ anti-ferromagnet, at $m = -0.26$, with initially two up-spins in the middle of the system (see Fig.3.3 middle panels). The $t = 0$ entanglement shows sublinear growth away from the boundaries. Note that at the center the two half chains are not entangled at $t = 0$. For $t > 0$, entropy starts to increase as soon as the perturbation crosses the corresponding bond. For large times the entanglement saturates at a finite value. The step-like structure from a) is washed out but still visible. We verified conovergence of the data keeping up to 100 states (a)) and 2800 states (b)). In b), the difference in entropy between $\chi = 1700$ and $\chi = 2800$ is less than $3 \cdot 10^{-2}$

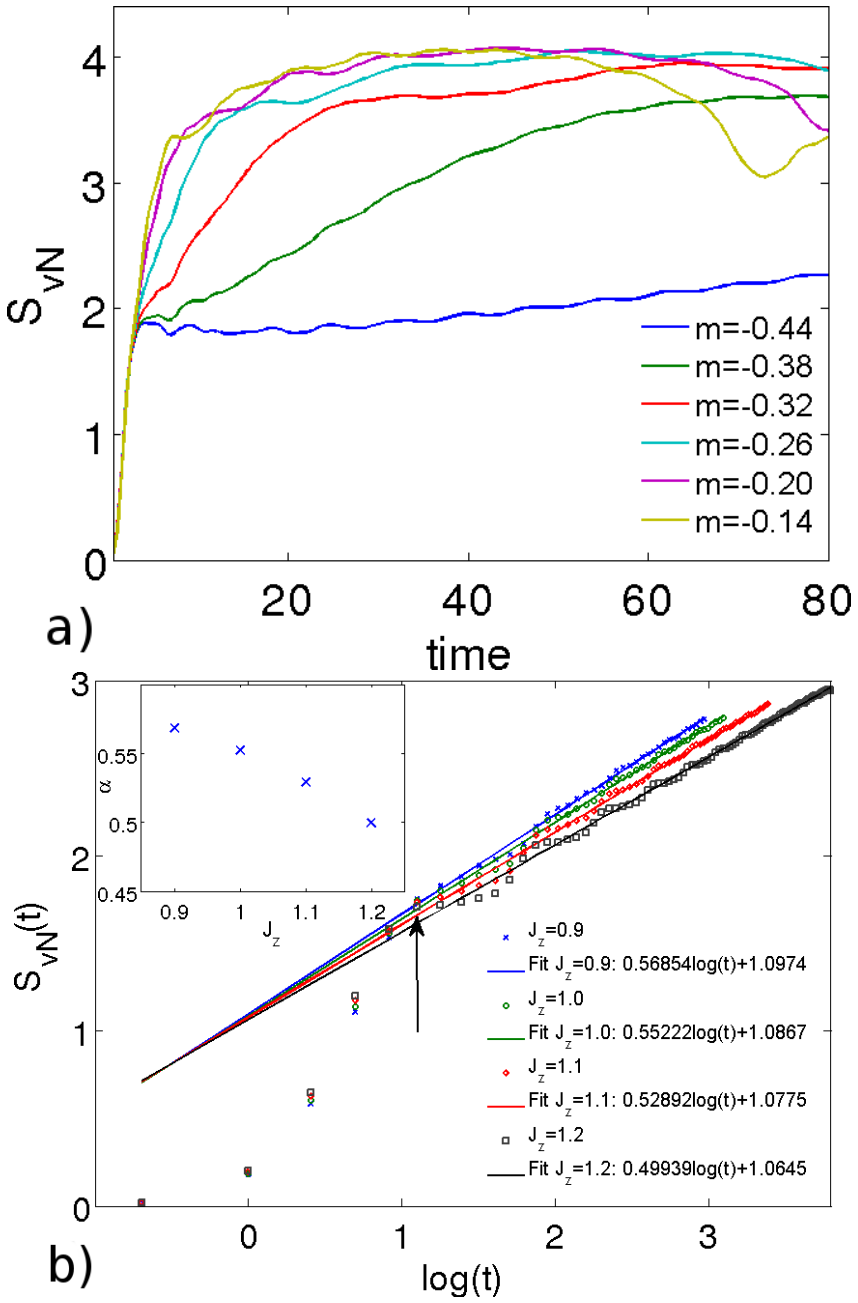

Figure 3.7: a) Von Neuman entropy S_{vN} at bond 50 as a function of time for different magnetizations m following a quench of length $m_0 = 2$ ("two-string quench"). The initial rapid growth is almost independent of m, whereas the in longtime limit for decreasing m, S_{vN} increases. This is not unexpected, since the available phase space growth exponentially with decreasing m, and thus more and more states will become involved in the time evolution. For $m \geq -0.26$, S_{vN} reaches a maximum. This is related to the finite size of the system. For $m = -0.14$, for example, the dip at t$\approx$ 70 coincides with the time when reflections have traveled back to bond 50 (compare also Fig.3.3, lowest two panels). b) Bipartite entanglement vs. $\log(t)$ at bond 50, for a quench with $m_0 = 2$, at $m = 0$ (half filling) and system size $N = 100$, for different interaction strengths Δ. Lines are linear fits to the data points $(\alpha \log(t) + \beta)$. For the fitting, only data points at $t \geq 3$ were used (see arrow). Matrix dimension $\chi = 500$. *Inset:* Fitting parameter α versus interaction strength Δ.

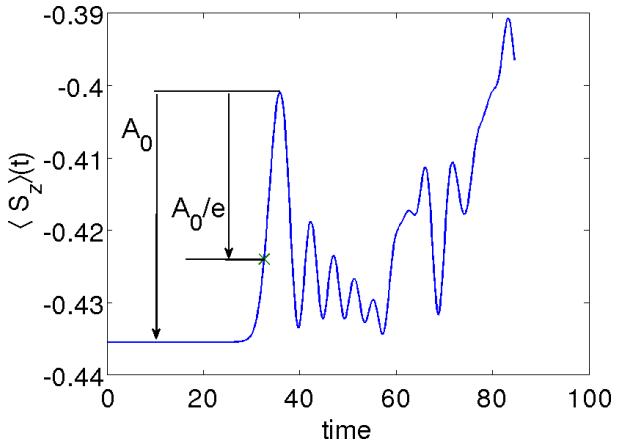

Figure 3.8: $\langle S_z \rangle (t)$ at site $x_i = 15$ for the quench plotted in 3.3 upper panels ($m = -0.44$). To obtain a smoother signal, the data points have been interpolated with cubic splines. To determine the speed of the spinon wave front, we determined the time t_i when the signal at site $x_i = 15$ has increased to $1/e$ of its full height above the background.

3.4.5 Numerical determination of propagation speeds at finite densities

To determine the propagation speed of the spinon and two-string branch for finite magnetizations we used the linear regression method. For a collection of sites x_i, we determined the times t_i at which the signal of spinon/two-string wave-front has increased to $1/e$ of its peak value above the background (the "arrival time of the signal" at site x_i, see Fig.3.8). Note that the width of the front-wave increases as $t^{1/3}$. Hence the the two velocities are in general different by a term $t^{-2/3}$ which vanishes in the limit of long propagation times [150]. We then used the linear regression method to find the most likely straight line connecting these space-time points. The gradient of this line then gives an estimate of the propagation velocities. For the spinon velocities, we used the $\langle S_i^z \rangle (t)$ data to collect the (x_i, t_i) pairs, whereas for the two-string case using data from $P_{\uparrow\uparrow}(j,t)$ turned out to be favorable due to less noise from single-particle propagation. We assumed a read-off error of $\delta t = 1$ for the time, except for $(x_i = 50, t_i = 0)$ (one of the two quenched sites), where we assumed a $\delta t = 0.1$, because at this point the excitation is sure to be there. Due to the finite filling, open boundaries and the magnetic field, the groundstate spin-densities show strong Friedel oscillations. We found that using points x_i at the minima of these oscillations gave best agreement with the analytic propagation velocities. The data used for our fitting routine can be found in Sec.7. The resulting estimates for the spinon and two-string velocities are tabulated in Tab.3.1.

At zero magnetization $m = 0$ ("half filling") string states do not exist. Accordingly, in our numerical simulations, the slower propagation branch which we identified as string excitations, is not visible at $m = 0$. The results for $\langle S^z \rangle (t), P_{\uparrow\uparrow}(t)$ and $S_{vN}(t)$ for $N = 100$, $m = 0$ and $m_0 = 2$ for different interaction strengths $\Delta = 0.9, 1, 1.1$ and 1.2 are plotted in Fig.3.9. From top to bottom we show results for different interaction strengths $\Delta = 0.9, 1.0, 1.1, 1.2$. The speed of the visible branches (obtained from the same method as above) is plotted in Fig.3.10. We observe an increase of the signal velocity with

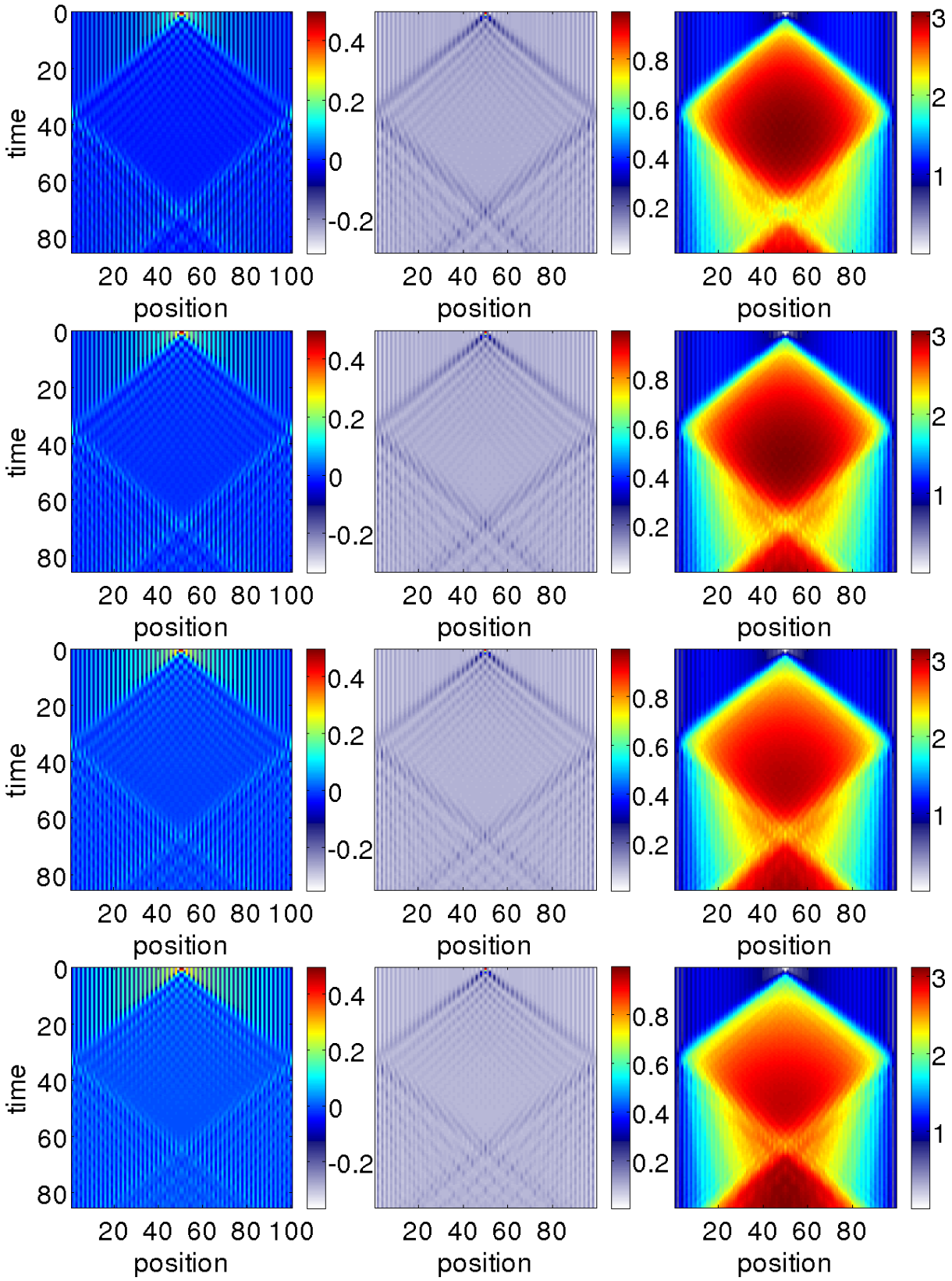

Figure 3.9: Time evolution of an $m_0 = 2$ quench at $m = 0$, $N = 100$. From left to right: $\langle S_z \rangle (t), P_{\uparrow\uparrow}(t), S_{vN}(t)$. From top to bottom: $\Delta = 0.9, 1.0, 1.1, 1.2$.

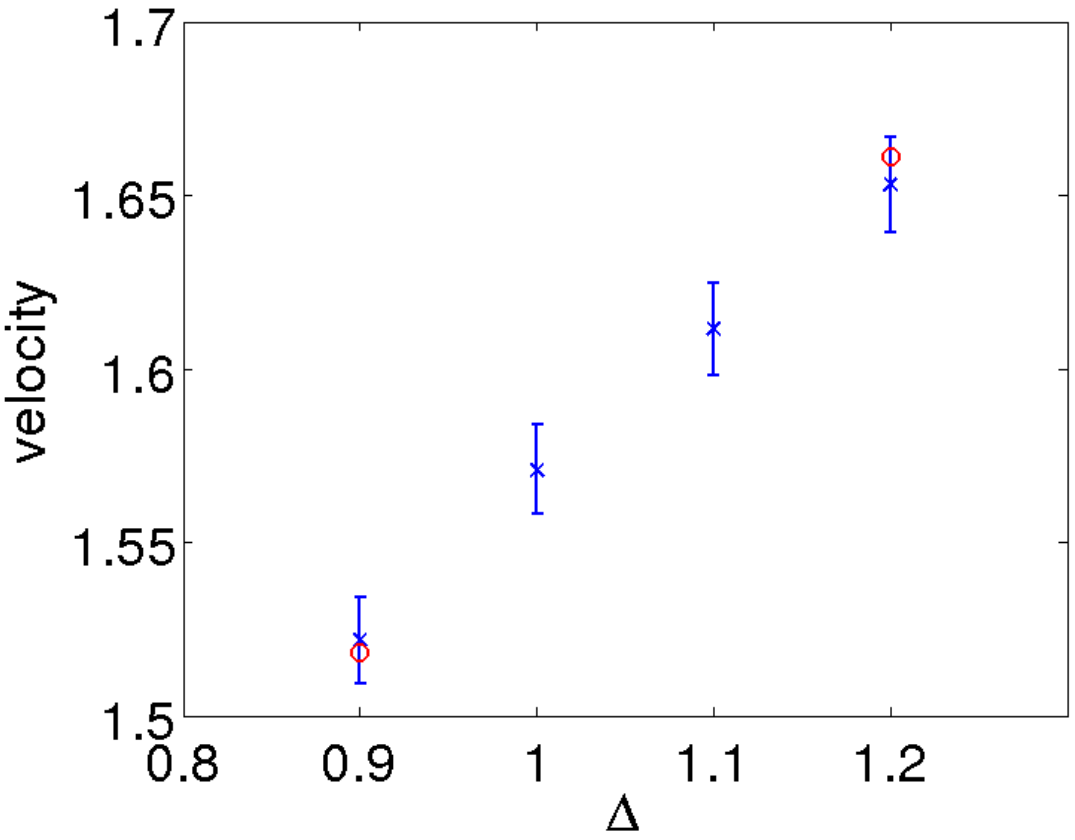

Figure 3.10: Propagation speed of the signal for $m = 0$ and different values of interaction $\Delta = 0.9, 1.0, 1.1, 1.2$ as obtained from TEBD calculations (blue crosses). For comparison we plotted the results from Bethe ansatz for the spinon velocity for $\Delta = 0.9$ and $\Delta = 1.2$.

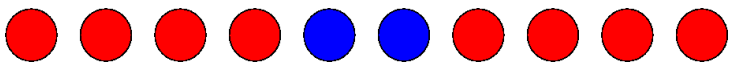

Figure 3.11: Visualization of the experimental setup: Red dots are ^{87}Rb atoms in a $\downarrow$-state, blue ones are ^{87}Rb atoms in a $\uparrow$ state.

magnetization m	spinon velocity	two-string velocity
-0.44	1.049±0.033	0.475±0.013
-0.38	1.110±0.015	0.527±0.009
-0.32	1.178±0.014	0.592±0.007
-0.26	1.248±0.013	0.690±0.017
-0.20	1.327±0.012	0.791±0.026
-0.14	1.424±0.012	0.909±0.020

Table 3.1: Spinon and two-string velocities obtained from linear regression, using the data points of Tab.1 and Tab.2

increasing Δ, in agreement with Bethe ansatz results for the spinon velocity.

3.5 Experimental realization

Very recently our proposal has been realized in a cold atomic gas experiment [16]. The experiment uses ^{87}Rb atoms in two different hyperfine states to realize a two-species Bose Hubbard model with the following Hamiltonian:

$$H_{BH} = -J \sum_{i\sigma} b^{\dagger}_{i\sigma} b_{i+1\sigma} + \sum_{i\sigma\sigma'} \frac{U_{\sigma\sigma'}}{2} n_{i\sigma}(n_{i\sigma'} - \delta_{\sigma\sigma'}) \tag{3.13}$$

where $\sigma = \{\uparrow, \downarrow\}$, and $U_{\sigma\sigma'}$ is a local interaction term between bosons sitting at the same sites. In the case of of large U the Hamiltonian can be mapped to XXZ model, which for the case of $U_{\uparrow\downarrow} = U_{\downarrow\uparrow} = U_{\uparrow} = U_{\downarrow} = U$ yields [130, 131, 16]

$$H = \sum_i \Delta_z S^z_i S^z_{i+1} \pm J_{\perp}(S^x_i S^x_{i+1} + S^y_i S^y_{i+1}) \tag{3.14}$$

with

$$\Delta = 4(\frac{J^2}{U_{\uparrow\downarrow}} - \frac{J^2}{U_{\downarrow}} - \frac{J^2}{U_{\uparrow}}) = -\frac{4J^2}{U} \tag{3.15}$$

$$J_{\perp} = \frac{4J^2}{U_{\uparrow\downarrow}} = \frac{4J^2}{U}. \tag{3.16}$$

At large $U/J \approx 20$, initial states of the type discussed in Sec.3.4.1 with two flipped spins in an elsewise ferromagnetic background correspond in this case to a half-filled Mott-insulator with one boson per site where two adjacent bosons are in a hyperfine state $\uparrow$ and the rest is in the $\downarrow$ state (see Fig.3.11). The experimentalists measured the probability P_{ij} of finding two particles simultaneously at sites i and j, with P_{ij} normalized as

$$\sum_{ij} P_{ij} = 1. \tag{3.17}$$

Simulation results for this quantity and the connected correlation function $C_{ij} = P_{ij} - P_i P_j$ are plotted in Fig.3.12. The simulation parameters are given in the figure caption. For ease of comparison data has been plotted in the same fashion as in Fukuhara et al. [16].

3.6 Conclusions

We have studied local quantum quenches in the anti-ferromagnetic spin-1/2 Heisenberg XXZ chain at different interaction strengths Δ and for different total magnetizations m. We observed that above certain thresholds in the interaction strength Δ, local observables exhibit prominent signatures associated with linearly propagating gapped bound states. Given the difficulty in observing these bound states in scattering experiments on quantum magnets [108, 135, 136, 137, 138, 139, 140], non-equilibrium setups of the kind considered here are an ideal setting for observing them and probing their properties. Our proposed

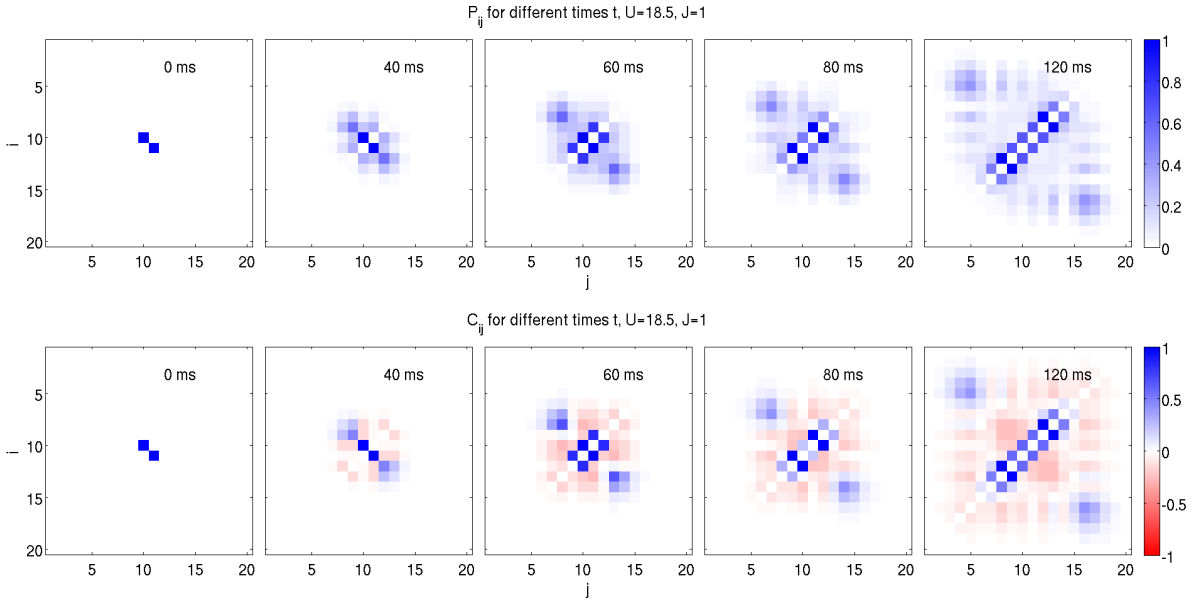

Figure 3.12: *Upper panel:* snapshots of P_{ij} at different times t for an initial state with two $\uparrow$ bosons in the middle of an $N = 10$ sites chain, and exactly one $\downarrow$ boson at all other lattice sites (see Fig.3.11). *Lower panel*: snapshots of $C_{ij} = P_{ij} - P_i P_j$ at different times t. $U/J = 18.5, \chi = 600$, $\uparrow$-cutoff=3, $\downarrow$-cutoff=4. We used a second-order Suzuki-Trotter breakup with $dt = 0.005$.

setup has been realized in a recent experiment by Fukuhara et al. [16] where they used laser trapping techniques of cold bosonic atoms in optical lattices to probe non-equilibrium dynamics with single site resolution [128, 129, 119, 120, 16]. Other recent work has focused on AC driven optical lattices [151] and two-component Bose mixtures [152, 130, 153], where the kind of local perturbation characterizing our initial state could be induced by a focused laser beam.

Chapter 4

Quantum Bowling

4.1 Introduction

This chapter investigates soliton-like excitations and their interactions in different quantum lattice models. The content of this chapter is largely taken from a preprint publication available on arXiv [154]. The preprint was drafted by the author of this thesis and has been edited by M. Haque and H. G. Evertz. All calculations were done by the author.

The investigation of time evolution in non-equilibrium situations is a fast-expanding frontier in quantum many-particle physics. With the development of relevant experimental techniques, e.g. in cold-atom setups [47, 155, 74], situations that were quite academic a decade or two ago have become accessible. The study of coherent non-dissipative dynamics far from equilibrium has received a particular boost.

An emerging theme is the dynamics and interaction of excitations over simple states. For condensed-matter models known and intensively studied for many decades, surprisingly little is known about the dynamical evolution of excitations that are simple but are not eigenstates. Obvious examples are the dynamics of a few interacting particles on lattices, or a few flipped spins in an otherwise ferromagnetic background. In Hubbard models, wide interactions "repulsively bind" on-site pairs and other clusters or combinations of bosons [156]. In models with nearest neighbor couplings like spin chains, bound states ("multi-magnons") exist even at small couplings and their non-equilibrium dynamics has been the subject of recent research [157, 93, 158, 159]. Interacting models and dynamics with single site resolution are now within experimental reach [120, 151, 119, 129, 128, 160, 16]. Collision processes are fundamental for analyzing the physical laws governing the dynamics of classical and quantum systems. A famous classical realization is Newton's cradle, exhibiting the effects of energy and momentum conservation. A quantum version has been realized in cold atom experiments [74].

In this paper we analyze scattering in one-dimensional strongly interacting quantum mechanical lattice models with discrete degrees of freedom using standard precise techniques for coherent many body time evolution [11, 10]. We find intriguing phenomena caused by the discrete quantum nature of the system. We consider three prominent models, spin-polarized fermions, the fermionic Hubbard model, and the Bose Hubbard model. We will first briefly describe the main phenomena, exhibited in Fig. 4.1. Then we analyze the physics behind the observed behavior, arguing that it follows from conservation laws and the discreteness of the models. Finally we discuss a fermionic quantum Newton's

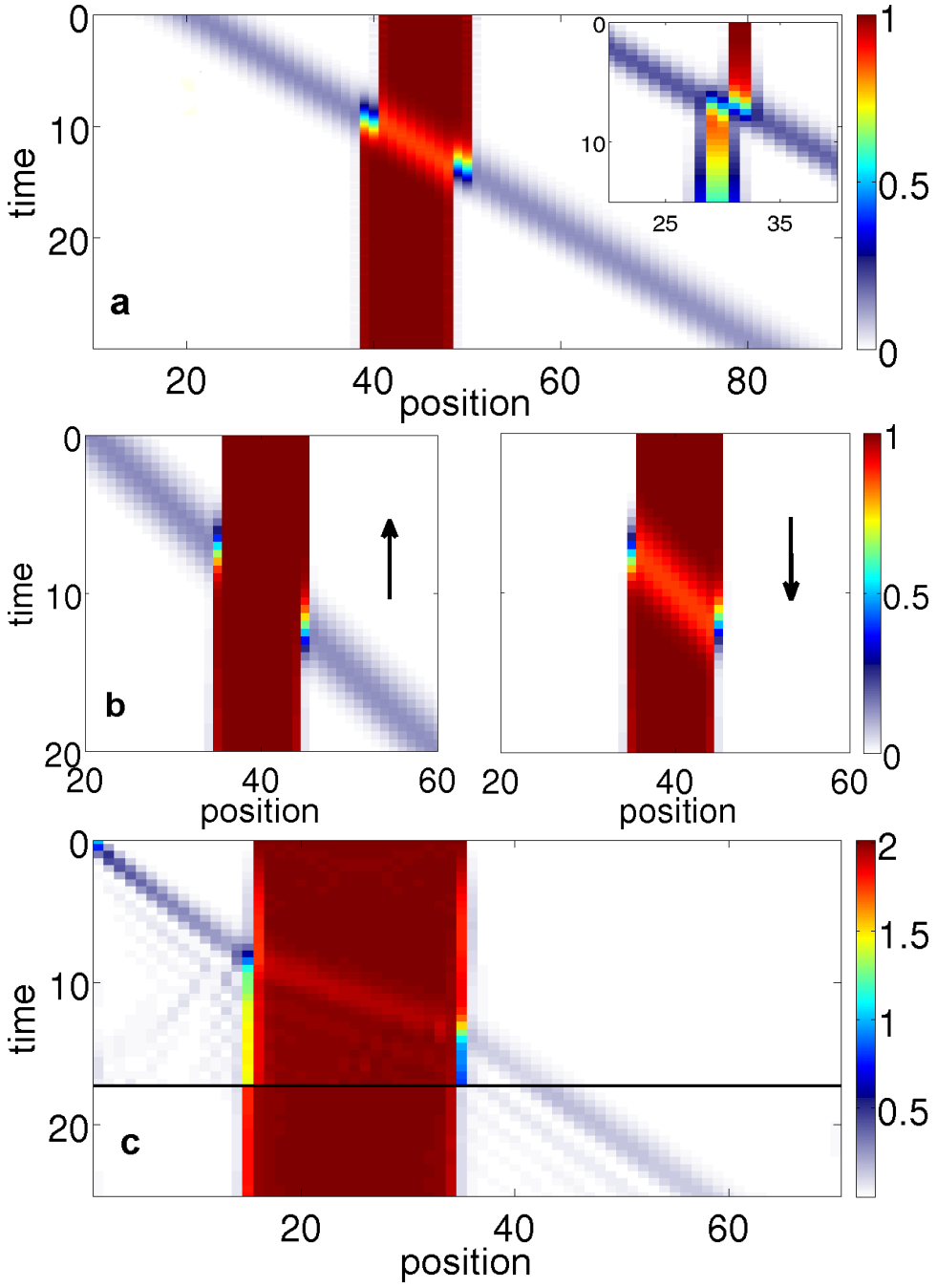

Figure 4.1: Quantum bowling: an incoming single particle in Gaussian shape crosses a wall of bound particles on N consecutive sites. It undergoes particle-hole transmutation and shifts the wall by 2 particles. The figures show particle density $\langle n_i(t)\rangle$. (a) Spin-polarized fermions with $V/t = 10$. The 10-site wall is moved by 2 lattice sites. Inset: A wall of just 2 sites is still moved ($V/t = 20$). (b) Fermi Hubbard model. Left: up-spin density, right: down-spin density. Wall of $N = 10$ doubly occupied sites, $U/t = 100$. (c) Bose Hubbard model. Wall of $N = 18$ doubly occupied sites, $U/t = 30$. The incoming particle is magnon-like. Lower part in (c): density on condition that a particle is present to the right of the wall.

cradle, a meta-material with a tachyonic mode, and other possible applications.

4.2 Main phenomena

The setup of what we call *quantum bowling* consists of an almost stationary "wall" of particles sitting on consecutive sites, on top of an empty lattice. The wall is hit by a single soliton-like particle (Fig. 4.1). The ensuing dynamics are qualitatively independent of details of the initial state or magnitude of the couplings, within a large range. For integrable models [98, 97, 161] (Fig. 4.1a,b), *no back scattering* occurs. Instead, the incoming particle is transmitted as a *hole* through the wall, i.e. there is particle hole transmutation. This situation resembles a many-body version of Klein tunneling [162, 163, 164], even though the dispersion of contributing modes is strongly non-linear and there is no external potential. Strikingly, because of particle number conservation, there are then *two* particles that remain stuck at the front of the wall, instead of the familiar classical result as in Newton's cradle, where just the single incoming particle would be added to the wall. When the transmitted hole exits the wall, it is converted into a particle again, so that two particles vanish from the right side of the wall. For spin-polarized fermions (Fig. 4.1a) a single incoming particle *shifts the whole wall by two sites* to the left, in contrast to the classically expected shift by a single site. The exiting particle itself is shifted to the right. At large coupling, the shift is by two sites and the shape of the wave packet is unchanged by the transmission.

In both Hubbard models (Fig. 4.1b,c), the wall consists of doubly occupied sites, and it is shifted by two particles, namely one doubly-occupied site. Again there is particle hole transmutation. In the Fermi-Hubbard model (Fig. 4.1b), an incoming up-spin fermion becomes a down-spin hole inside the wall. In non-integrable models like the Bose Hubbard model (Fig. 4.1c), there is a finite probability for back scattering. However, the final state is essentially a linear superposition of (i) a back scattering event and (ii) transmission with particle-hole transmutation and wall-shift as described above. Indeed, at large couplings there is very little entanglement between a transmitted particle and the shifted wall, even when the transmitted particle itself is in an entangled Gaussian state. In the following, we will discuss the models individually.

4.3 Spin-polarized fermions.

The dynamics of spin-polarized fermions is governed by the Hamiltonian

$$H_{tV} = t\sum_i \left(c_i^\dagger c_{i+1} + c_{i+1}^\dagger c_i\right) + V\sum_i (n_i - \frac{1}{2})(n_{i+1} - \frac{1}{2}) \tag{4.1}$$

where t and V/t parametrize the kinetic and interaction energy of the fermions on the lattice, respectively, $c_i^\dagger$ and c_i are creation and annihilation operators at site i, and $n_i = c_i^\dagger c_i$. This model is equivalent by a Jordan-Wigner transformation to the 1D spin $\frac{1}{2}$ Heisenberg XXZ model with anisotropy $\Delta = J_z/J_x = V/2t$. We use $t = 1$ as the unit of energy and inverse time for all models, and discuss $V > 2t$. We note that when starting from a product state, results are identical for either sign of U [122], and, by adapting the arguments in ref. [122], for either sign of V/t, i.e. for attractive and repulsive models.

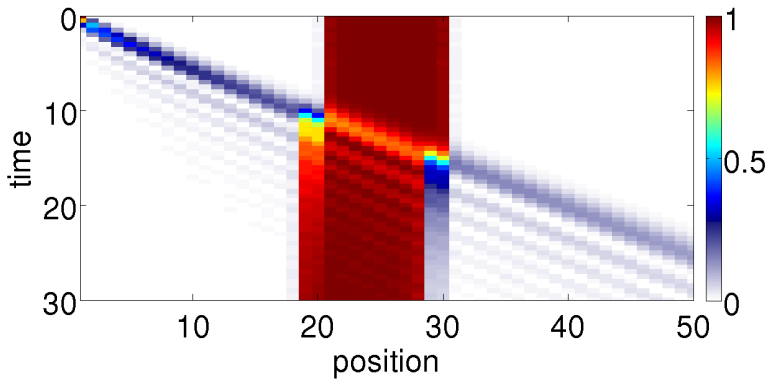

Figure 4.2: Particle density for a single magnon-like excitation hitting a wall of $N = 10$ sites in the spin-polarized fermion model, $V = 10$.

The model is exactly solvable by Bethe ansatz. It contains eigenstates made up of strings of M bound particles in an otherwise empty lattice [159, 93, 157], which become more compact as V/t increases. Their energy is [98]

$$E = 2t(\cosh(M\phi) - \cos K)\sinh\phi/\sinh(M\phi) \tag{4.2}$$

where $\cosh\phi = V/2t$ and K is crystal momentum. Their time evolution is dominated by [93] a maximum velocity $2t\sinh\phi/\sinh(M\phi)$ which decreases like $\frac{2t}{(V/t)^{M-1}}$ for $V \gg 2t$. At large V/t and large M, this velocity becomes exponentially small; M-strings are therefore stable on a very long time scale even when prepared at a fixed position in space.

In the initial state we prepare a "wall", a product state of $N = 10$ consecutive particles on an empty lattice. This is not an eigenstate, but it is instead made up of all subdivisions of N into M-strings. Since smaller strings have larger velocities, they will in time "evaporate" [165] from the wall. At large V/t the dominant contribution [159] is an almost stationary $M = N$ string, followed by the subdivision into $M = 9$ and a single fermion with maximum velocity $2t$.

In the initial state we also prepare a single particle in a Gaussian superposition [166] of width 4 and momentum $-\pi/2$ which moves towards the wall with velocity 2. This particle is created by applying an operator

$$c_G^\dagger \propto \sum_x \exp(-\frac{(x-x_0)^2}{2\sigma^2})\exp(i(x-x_0)k_0)\,c_x^\dagger \tag{4.3}$$

to the state with the initial wall, with momentum $k_0 = -\pi/2$, width $\sigma = 4$, and center position x_0 as visible in the figures, and then normalized to create a single Gaussian shaped particle. Its velocity is $\frac{d\epsilon}{dk}|_{k_0}$, where $\epsilon(k) = -2t\cos(k)$ is the single particle dispersion. With $k_0 = -\pi/2$, the resulting particle travels at velocity $2t$ with almost no dispersion, as seen in the figures. Alternatively, we also created a local particle at the left boundary by applying the creation operator $c_1^\dagger$ at the first left-hand site of the lattice, which may be easier to implement experimentally. Results are shown in Fig. 4.2. The behavior of such an excitation is easiest to understand by considering an empty

lattice with a single particle in the middle at a site $x = 0$ at time $t = 0$ [93]. Since a single particle cannot interact, all models considered in this paper are equivalent to tight binding fermions in this case. The initial state is $|\psi(0)\rangle = |1\rangle_{x=0} = \sum_k |1\rangle_k$. Then $|\psi(t)\rangle = \exp(-iHt)\,|\psi(0)\rangle = \exp(i2t\sum_p \cos p\hat{n}_p)\sum_k |1\rangle_k = \sum_k \exp(i2t\cos k)\,|1\rangle_k$, which can be written as a Bessel function [93]. Each k mode travels with a velocity $v_k = -2t\frac{d\cos k}{dk} = 2t\sin k \leq 2t$. Close to the maximum velocity $v_{max} = 2t$, the most modes contribute, which produces a magnon, a linearly propagating wave distinctly visible in space-time figures. Modes which are further away from $k = \pi/2$ produce additional oscillatory behavior. When starting in the middle of an empty lattice, a left-moving and a right-moving branch ensue, each with an overall probability of 1/2 of containing the particle. When started close to an open boundary, the particle travels only in one direction, away from the boundary, with unit probability. Note that the distinctly visible fastest branch has a velocity $v_{max} = 2t$ at its fastest edge, whereas the location of maximum intensity slowly moves away from the edge sublinearly. After finite times, the average velocity of the peak is therefore slightly smaller than v_{max}, but it converges towards v_{max} for large times. We see that the total intensity of the incoming particle now arrives over time in several waves. Each of them behaves similar to Fig. 4.1a. There is no back scattering, and the probability distribution of the wall converges to a complete shift of 2 sites.

Being integrable, the tV model contains a macroscopic number of conserved quantities, of which particle number $n = \sum_l n_l$, energy E, and energy current (thermal current) $j^E = \sum_l j_l^E$ are especially relevant. The energy current is obtained from a continuity equation for the local energy $h_{l\,l+1} = tc_l^\dagger c_{l+1} + c_{l+1}^\dagger c_l + V(n_l - \frac{1}{2})(n_{l+1} - \frac{1}{2})$ [167]

$$\frac{d}{dt}h_{l\,l+1} = i[H_{tV}, h_{l\,l+1}] = j_l^E - j_{l+1}^E. \tag{4.4}$$

The resulting expression for j_l^E is

$$\begin{aligned} j_l^E \;&= itV(c_{l-1}^\dagger c_l(n_{l+1} - \frac{1}{2}) + (n_{l-1} - \frac{1}{2})c_l^\dagger c_{l+1}) \\ &\quad + it^2 c_{l-1}^\dagger c_{l+1} \;\; + \;\; h.c.\,, \end{aligned}$$

and the MPO representation for the energy current assumes the form

$$j_l^E = \begin{pmatrix} c_{l-1}^\dagger & c_{l-1} & n_{l-1} - \frac{1}{2} \end{pmatrix} \begin{pmatrix} it^2 P_l & 0 & -iVtP_l c_l \\ 0 & it^2 P_l & -iVtP_l c_l^\dagger \\ -iVtc_l^\dagger & -iVtc_l & 0 \end{pmatrix} \begin{pmatrix} P_{l+1}c_{l+1} \\ P_{l+1}c_{l+1}^\dagger n_{l+1} - \frac{1}{2} \end{pmatrix}, \tag{4.5}$$

where

$$P_l = \begin{pmatrix} 1 & 0 \\ 0 & -1 \end{pmatrix} \tag{4.6}$$

takes care of the fermionic commutation relations.

Since the interaction is local, the energy current is conserved separately in spatially disconnected regions. The initial state has a finite right-moving energy current, localized around the incoming particle. In Fig. 4.3 we show the energy current corresponding to Fig. 4.1a). This current is conserved after the particle contacts the wall. Yet the wall is "full" and cannot accommodate an additional particle. Only a *hole* can move through the

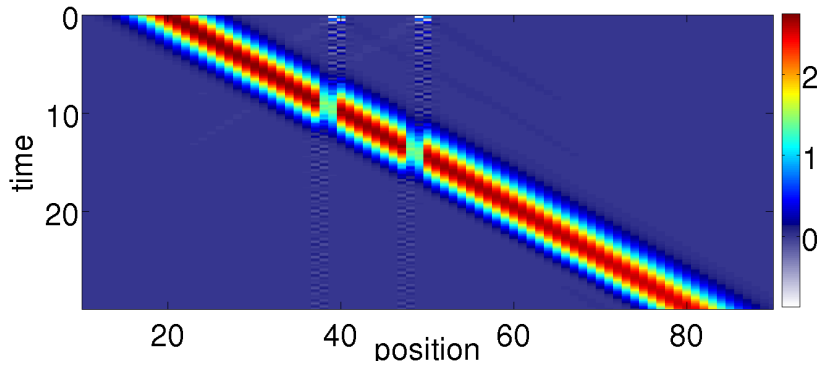

Figure 4.3: Energy current for a Gaussian particle hitting a wall of $N = 10$ sites (parameters of Fig. 4.1a).

wall. Inside the wall the hole possesses the same energy current and the same energy as the incoming particle on the empty lattice because of particle-hole symmetry. However, because of particle number conservation, a particle-hole *pair* must have been created, and there are now *two* particles located to the left of the wall. Because of current conservation and energy conservation, they cannot move: if there was a back scattered particle, it would have additional energy and a left moving energy current, which would have to be compensated by a right moving current from another right moving hole, which would have further additional energy, so that energy conservation would be violated.

When the hole exits the wall, it has to become a particle again, so that two particles are taken away from the right side of the wall. Overall, the wall moves by *two* sites to the left in this quantum mechanical process, contrary to the classical situation.

The particle-hole creation resembles Klein tunneling [162, 163, 164]. However, here we have no external potential, but instead a *many-body* effect. In contrast to Klein tunneling, the dispersion is not linear, but a cosine. When one starts with an initially localized incoming particle. all momenta contribute, yet particle-hole transmutation and the overall features of the transmission process are the same.

An interesting generalization is to hit the wall with a localized two-string instead of a single particle (see Fig. 4.4). In this case, the wall gets shifted by *four* sites. Two-strings in general have lower propagation speed, hence time evolution has to be carried out over a longer period of time.

4.3.1 Small couplings; narrow walls

Particle-hole transmutation and the shift by two sites in the tV model are dictated by conservation laws and the Pauli principle, *not* by especially strong coupling. Indeed, a coupling of e.g. $V/t = 2.2$ ($\Delta = 1.1$) still exhibits the same effects. At such smaller V/t, M-string eigenstates are spatially more extended. In the upper panel of Fig. 4.5, we prepared a wall of $N = 10$ particles and let it evolve for time $100/t$, during which particles evaporated and the wall became wider, closer to a linear combination of M-string eigenstates with mostly large M [159], in a kind of evaporative cooling. The figure clearly shows the evaporation of single particles and of slower $M = 2$ bound strings (note the color-scale cutoff). Apparently, an initially prepared wall of N consecutive particles

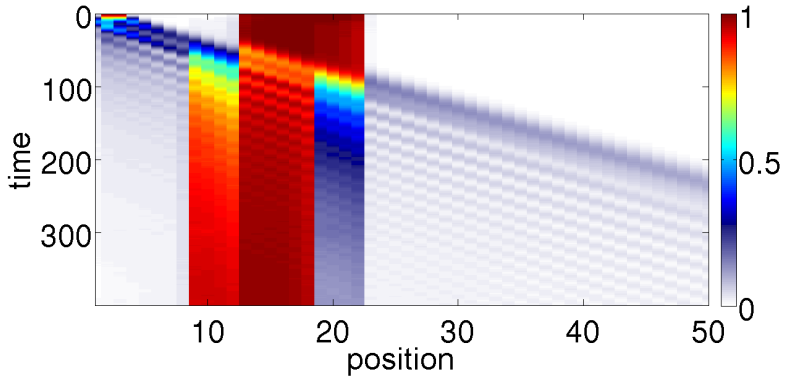

Figure 4.4: Density of spin-polarized fermions for a two-string excitation hitting a wall of 10 particles at $V/t = 10$.

evaporates more than at larger V/t and becomes wider. At time $\tau = 100/t$ we then cut the resulting state to a width of 110 sites and started a Gaussian particle, as visible in middle panel of Fig. 4.5. The lack of back scattering and shift of the wall by 2 sites still occurs at $V/t = 2.2$. For comparison, lowest panel in Fig. 4.5 shows the much smaller scale of evaporation at $V/t = 10$ for the time evolution in Fig. 4.1a.

Amazingly, a wall of only $N = 2$ sites already shows the same phenomena, including a shift by two sites, i.e. by the full wall thickness (Fig. 4.1a, inset).

4.3.2 Role of integrability

Conservation laws are essential for the observed effect. We probe the role of integrability by studying a non-integrable model $H_{V_2} = H_{tV} + V_2 \sum_i n_i n_{i+2}$ (Fig. 4.6), in which the energy current is not conserved. Now there is indeed back scattering. One might suspect the presence of a next-nearest-neighbor coupling to be responsible. However, when one takes H_{tV} and adds the conserved thermal current J^E with next-nearest-neighbor terms,

$$H_\alpha = H_{tV} + \alpha j^E \tag{4.7}$$

another integrable model results, which does *not* show back scattering (Fig. 4.6, inset). This provides strong evidence that integrability is indeed closely connected to the observed lack of back scattering.

It remains an open question whether conservation of n, E, j^E and the restricted local Hilbert space are sufficient to suppress back scattering, or whether full integrability is necessary. It would be very interesting to study a non-integrable model which conserves the above quantities, if such a model exists[168].

4.3.3 Quantum mechanical nature of final state

In the bottom part of Fig. 4.1(c) and Fig. 4.6, the wave function has been projected (and then normalized) onto Fock states in which exactly one particle is present to the right of the wall, i.e. onto the case that the incoming particle was transmitted. Then no reflection is visible in the reflected component and we see that now the wall is shifted by 1 (resp. 2) site.

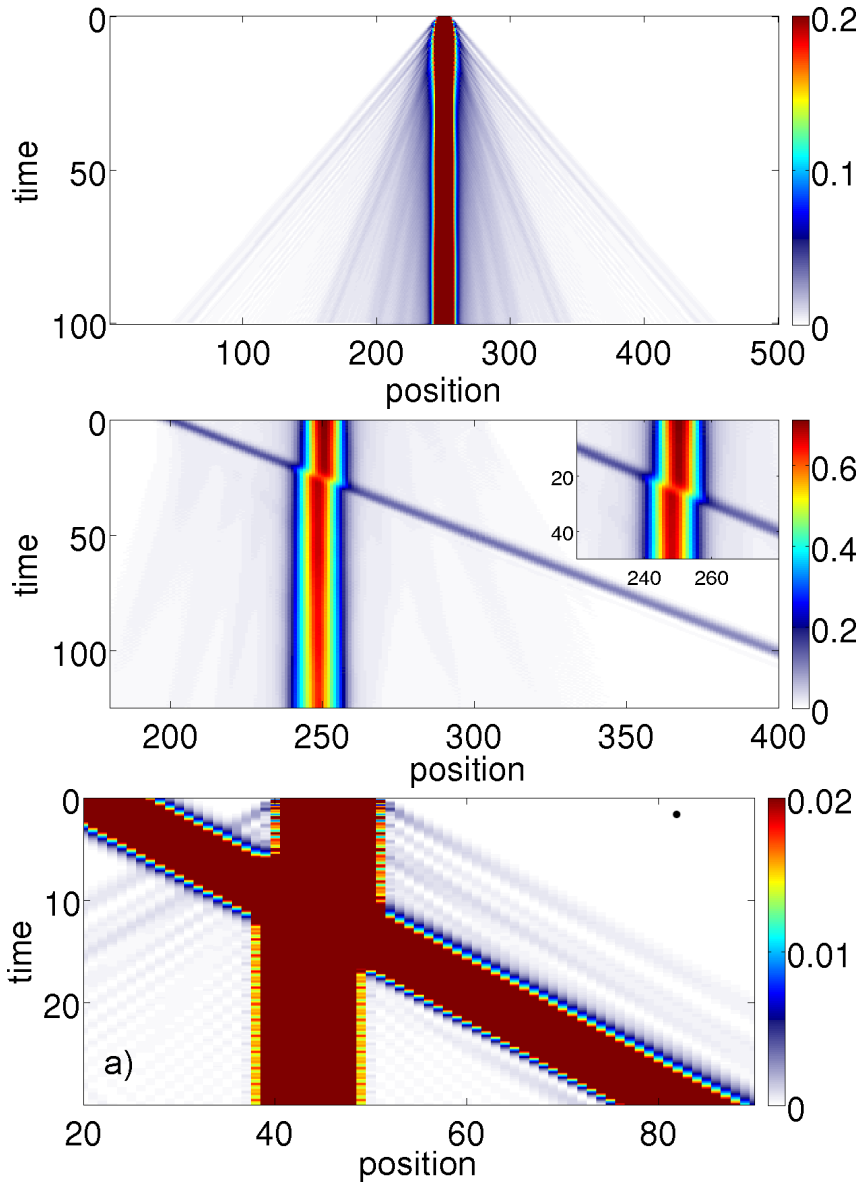

Figure 4.5: *Upper panel:* Particle density for evaporative cooling of a 10-site wall at $V = 2.2$. The vertical scale has been cut off at $n = 0.2$ for better visibility. *Middle panel* Small anisotropy: density of spin-polarized fermions at $V/t = 2.2$ ($\Delta = 1.1$ in the equivalent Heisenberg model); evaporatively cooled initial state. Inset: scattering region at larger scale. *Lower panel:* Particle density at $V/t = 10$ (same as Fig. 4.1a), but with vertical scale cut off at very low $n = 0.02$ to make evaporation of wall visible.

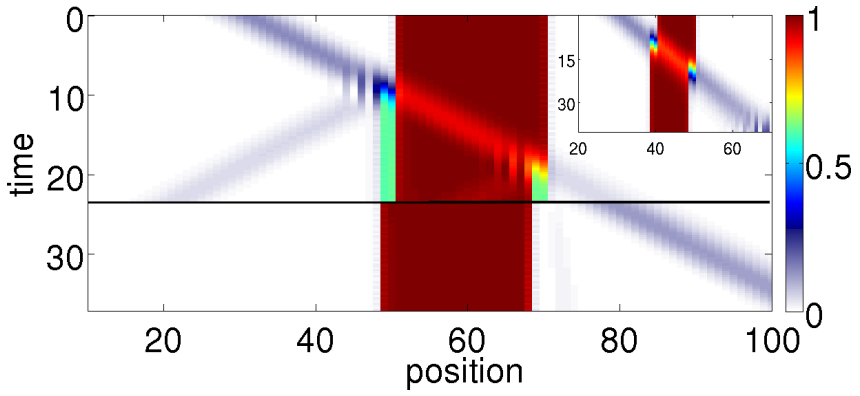

Figure 4.6: Density of spin-polarized fermions with next nearest neighbor interaction. Main figure: Non-integrable model with $V = 10$, $V_2 = 1.2$ and a 10 site wall. Bottom part: density on condition that a particle is present to the right of the wall. Inset: Integrable model eq.4.7 with $V = 10, \alpha = 0.1$ and same wall width.

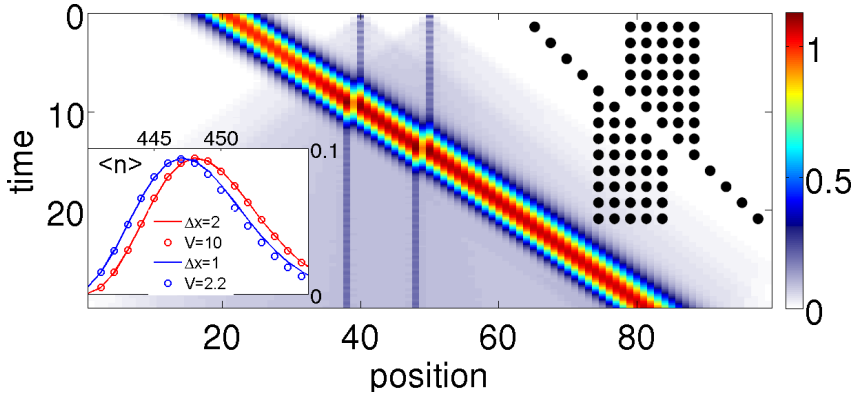

Figure 4.7: Bipartite entanglement entropy S_{AB} for the scattering in Fig. 4.1a. Right inset: semi-classical picture of the time evolution of particles, demonstrating both left-shift of the wall and right-shift of the traveling particle. Space and time directions are as in the main figure. Left inset: spatial density distribution at large x; without wall (shifted right by 2 sites), and after passage through a wall.

Further insight is gained from the bipartite entanglement entropy [145] $S_{AB} = -\mathrm{tr}(\rho_A \log \rho_A)$, where $\rho_A = \mathrm{tr}_B \rho$, and $\rho = |\psi\rangle \langle\psi|$ is the total density matrix. S_{AB} quantifies the number and strength of linear superpositions between A and B. When it is zero, then $|\psi\rangle$ is a product state $|\psi\rangle_A |\psi\rangle_B$. In Fig. 4.7 we show S_{AB} as a function of time and of the position of the subsystem cut. It is dominated by the entanglement inside the traveling Gaussian particle. Additionally, the slight evaporation of the wall is visible as light blue cones emanating from the wall boundaries. Strikingly, the amount of entanglement between the transmitted particle and the wall is hardly larger than on the left hand side of the wall [1] Thus there is no, or very little, entanglement due to the outgoing particle. The outgoing particle, itself in an entangled Gaussian state, is therefore to good precision in a product state with the *shifted* wall.

[1] There is a difference of up to 0.007, which may be caused by earlier scattering with evaporated particles.

One can understand further details from a semi-classical picture (Fig. 4.7, inset) in which the incoming particle is thought of as a single occupied site. Because of energy conservation, the closest that the particle can come to the wall is to a distance of one site; then a particle from inside the wall has to move to the *left*, effectively propagating a hole inside the wall to the right. This picture implies that the propagating signal should experience a shift forward by 1 lattice site both upon entry and upon exit of the wall, thus overall the transmitted particle should be shifted by *two sites* in forward direction. Such a shift is indeed visible in the entropy in Fig. 4.7 and in the energy current. The left inset in Fig. 4.7 shows that at large V/t, the Gaussian signal is moved forward by exactly 2 sites without noticeable change of shape. At small V/t, we observe a smaller shift of about 1.3 sites, and we note that there will have been non-negligible additional scattering events with evaporated particles, which effectively widen the signal.

4.3.4 Interaction inversion symmetry of the Heisenberg chain

In the appendix of ref. [122] it was shown for the fermionic Hubbard model that the time evolution is invariant under the transformation $U \to -U$, for observables invariant under a combined transformation of time reversal and π-boost $c_q \to c_{q+Q}$, which include particle density, and for initial states which only acquire a phase under the combined transformation.

We note that the proof [122] can immediately be generalized. It applies not only to the Hubbard model but also to density-density interactions in general, including the tV-model and the bosonic Hubbard model, and to initial product states. Below we shot that for an initial state with a single particle in a gaussian superposition of local states, it applies when $k_0 \to -k_0$ is also transformed. Therefore all our results apply to both attractive and repulsive models, i.e. they are invariant under $U \to -U$ resp. $V \to -V$ for the initial states used in this work.

In the following section a more explicit and slightly more restricted proof is presented for the case of the anisotropic Heisenberg (or XXZ) model. We consider a system of spins governed by the Heisenberg Hamiltonian

$$H = \sum_i \Delta S_i^z S_{i+1}^z + J(S_i^+ S_{i+1}^- + S_i^- S_{i+1}^+), \tag{4.8}$$

and we will show that for an initial product state, the non-equilibrium dynamics of observables which are invariant under rotation about the z-axis is independent of the sign of the interaction Δ.

Lemma 1. *Take a product state $|\psi_0\rangle = |\sigma_1 \dots \sigma_N\rangle$ of spins σ_n and evolve it in time with H; the expectation values of $\langle S_i^z \rangle(t)$ do not depend on the sign of the anisotropy Δ of the model, i.e $\langle\psi_0| e^{iH(-\Delta)t} S^z e^{-iH(-\Delta)t} |\psi_0\rangle = \langle\psi_0| e^{iH(\Delta)t} S^z e^{-iH(\Delta)t} |\psi_0\rangle$*

Proof: There is a unitary transformation U (rotating every second spin by π about the z-axis) which changes the sign of the hopping: $H(\Delta) \to U^\dagger H(\Delta) U = -H(-\Delta)$. The complete expression for U is a product operator of the form

$$U = \prod_{i=even} \exp(-i\pi S_i^z) = \prod_{i=even} -i\sigma_z \tag{4.9}$$

where we have used $\exp(-i\varphi\vec{n}\vec{S}) = \mathbb{1}\cos(\varphi/2) - i\vec{n}\vec{\sigma}\sin(\varphi/2)$, and set $\hbar = 1$. We start by first applying this bipartite rotation to the time evolution operator:

$$\begin{aligned}\langle\psi_0| e^{iH(-\Delta)t} S_i^z e^{-iH(-\Delta)t} |\psi_0\rangle &= \langle\psi_0| e^{-i(-H(-\Delta))t} S_i^z e^{i(-H(-\Delta))t} |\psi_0\rangle \\ &= \langle\psi_0| U e^{-iH(\Delta)t} U^\dagger S_i^z U e^{iH(\Delta)t} U^\dagger |\psi_0\rangle \\ &= \langle\psi_0| U e^{-iH(\Delta)t} S_i^z e^{iH(\Delta)t} U^\dagger |\psi_0\rangle \\ &= \langle\psi_0| e^{-iH(\Delta)t} S_i^z e^{iH(\Delta)t} |\psi_0\rangle \end{aligned} \tag{4.10}$$

where we used $[S_i^z, U] = 0$. The last equality sign is valid for product states $|\psi_0\rangle$ in the z-basis: looking at $U^\dagger |\psi_0\rangle$ we observe that if $|\psi_0\rangle$ is a product state, then U gives it an over all phase. If on the other hand $|\psi_0\rangle$ is not a product state, then U in general changes it; the two-spin singlet $|s\rangle$ for example is transformed into the two spin triplet with no z magnetization by U. Thus for product states, we can omit U in the equation. The last step is to explain why changing the overall sign of H in the equation in Lemma 1 does not change the evolution of the expectation values. The answer to this is time reversal symmetry. We will first state some facts of time reversal, and then apply it to the equation in Lemma 1.

Let T denote the time reversal operator for a *single particle or a single spin*. Since T reverses time, its effect is to inverse linear and angular momentum as well as spin of a state: $\{\vec{p}, \vec{L}, \vec{S}\} \to \{-\vec{p}, -\vec{L}, -\vec{S}\}$, but $\vec{r} \to \vec{r}$, i.e. positions do not change. Observables O transform under T as

$$O' = TOT^{-1}. \tag{4.11}$$

H in Eq.4.8 is ths obviously time-reversal invariant. T is an *anti-unitary* operator: for a manifestly time-reversal invariant system (like Eq.4.8 or a (non-relativistic) free particle), by its very definition, T has to obey [169, 170]

$$Te^{iHt}T^{-1} \stackrel{!}{=} e^{-iHt}. \tag{4.12}$$

Eq.4.12 can be obtained by either of the following two possibilities:

1. T is unitary and $HT + TH = 0$
2. T is anti-unitary and $HT - TH = 0$.

Clearly, the first one can be ruled out by the demand that T must not reverse the sign of energies. Thus $[T, H] = 0$ is an immediate requirement. The most general ansatz for T is

$$T = GK \tag{4.13}$$

where G is a unitary operator and K is the operator of complex conjugation. The action of T onto states is

$$T(a|a\rangle + b|b\rangle) = \bar{a}T|a\rangle + \bar{b}T|b\rangle. \tag{4.14}$$

If $|a\rangle, |b\rangle$ are real basis vectors, i.e. $|a\rangle = \binom{1}{0}, |b\rangle = \binom{0}{1}$, then K does nothing to them. Let us now find an explicit expression for T for the case of a single spin. As mentioned

above, $T\vec{S}T^{-1} \stackrel{!}{=} -\vec{S}$. Working in the $|\pm z\rangle$-basis, S_x and S_z are real matrices, whereas S_y is purely imaginary. Thus $T = GK$ has to obey the three equations

$$\begin{aligned} S^x G = -GS^x\,, \quad S^z G = -GS^z \\ S^y GK = -GKS^y = GS^y K \rightarrow S^y G = GS^y \end{aligned} \tag{4.15}$$

The last equation suggests the following solution for T:

$$T = e^{-i\pi S^y} K = -i\sigma^y K \tag{4.16}$$

where we set $\hbar = 1$.

The time reversal operator T for a *set of N spins* is given by

$$T = \left(\prod_i -i\sigma_i^y \right) K. \tag{4.17}$$

H in Eq. 4.8 is invariant under T: K takes care of the inversion of S^y, and $\prod_i -i\sigma_i^y$ reversesa S^x and S^y. Evaluation of $Te^{-iHt}T^{-1}$ shows that T reverses time because of the complex conjugation which reverses S^y:

$$\begin{aligned} Te^{-iHt}T^{-1} =& T\sum_n \frac{(-it)^n}{n!} H^n T^{-1} = \sum_n \frac{(it)^n}{n!} T H^n T^{-1} \\ =& \sum_n \frac{(it)^n}{n!} H^n = e^{iHt} \end{aligned} \tag{4.18}$$

where we used $[T, H] = 0$. Now we insert several identities $\mathbb{1} = T^{-1}T$ into Eq. 4.10:

$$\begin{aligned} &\langle \psi_0 | \, T^{-1} T e^{-iHt} T^{-1} T S_i^z T^{-1} T e^{iHt} T^{-1} T \, |\psi_0\rangle \\ &= - \langle \psi_0 | \, T^{-1} e^{iHt} S_i^z e^{-iHt} T \, |\psi_0\rangle \end{aligned} \tag{4.19}$$

where $TS_i^z T^{-1} = -S_i^z$ was used. We will discuss the effect of T on two different classes of states. First, let $|\psi_0\rangle$ be a product state in the $z - basis$. A simple calculation shows that

$$-i\sigma^y \, |\pm z\rangle = \pm \, |\mp z\rangle \, . \tag{4.20}$$

Thus, T flips every spin in $|\psi_0\rangle$ and gives the state a total-spin dependent sign. This sign cancels with the sign of the hermitian conjugate $\langle \psi_0 | \, T^{-1}$. The overall sign in Eq.4.19 then cancels because $T \, |\psi_0\rangle$ has flipped spins as opposed to $|\psi_0\rangle$. The expectation value $\langle S_i^z \rangle (t)$ is thus invariant under $\Delta \rightarrow -\Delta$. Note that for the case of $\langle S_n^x \rangle (t)$ arguments along the same line yield

$$\langle S_n^x \rangle (t) \stackrel{\Delta \rightarrow -\Delta}{\rightarrow} (-1)^{n+1} \langle S_n^x \rangle (t). \tag{4.21}$$

We turn now to the case where the initial state contains a single gaussian-shaped particle with momentum k_0.

Lemma 2. *Let $|\psi_0\rangle$ be a Gaussian state of the form*

$$|\psi_0\rangle = \sum_x \exp(-\frac{(x - x_0)^2}{2\sigma^2}) \exp(i(x - x_0)k_0) \, S_x^+ \, |FM\rangle \tag{4.22}$$

where $|FM\rangle$ is the ferromagnetic state with all spins pointing downwards. The expectation values of $\langle S_i^z \rangle$ are invariant under a combined transformation $\Delta \to -\Delta, k_0 \to -k_0$.

Proof: First we have to discuss the effect of $U^\dagger$ in Eq.4.10 bottom line. Since all states in the expansion Eq. 4.22 have the same number of up and down spins, $U^\dagger$ gives every state the *same* phase, thus this phase can be pulled out of the sum and cancels again with the one from the hermitian conjugate $\langle\psi_0| U$. Hence, we can omit U from Eq. 4.10. Next, we have to turn to the effect of T. The complex conjugate K in T changes $k_0 \to -k_0$ in Eq.4.22, and $\prod_i -i\sigma_i^y$ again flips all spins and gives each state in the expansion the same phase, which again cancels with the one from the hermitian conjugate. The sign in Eq. 4.19 is again compensated. $\langle S_i^z \rangle (t)$ is thus invariant under the simultaneous change of $\Delta \to -\Delta$ and $k_0 \to -k_0$.

4.4 Fermi Hubbard model

The 1D fermionic Hubbard model is specified by

$$H_{fH} = -t \sum_{i\sigma} \left(c_{i\sigma}^\dagger c_{(i+1)\sigma} + h.c. \right) + U \sum_i n_{i\uparrow} n_{i\downarrow} \tag{4.23}$$

where U is the on-site interaction and σ labels spin. It is widely used as a basic model of strongly correlated matter. Its coherent dynamics have recently started to become accessible in cold atom experiments [122].

The initial state in Fig. 4.1(b) contains $N = 10$ consecutive doubly occupied sites. Individually, they are repulsively or attractively bound by large $|U|$. They are however not mutually bound to each other. The outermost sites can therefore decay more easily than in model (4.1), and $|U| \gtrsim 30$ is needed to clearly see the shift over the background. Fig. 4.8 displays scattering for the Fermi Hubbard model, similar to Fig. 4.1b of the main paper, but at smaller coupling $U/t = 30$, where the wall is seen to decay faster. Its shift is still visible in the spatial density distribution before and after the scattering.

Fig. 4.9 shows that, within the precision of our data, the shape of the transmitted particle is independent of U. It is not influenced by additional scattering events with evaporated particles. This indicates that the particle emerges practically unchanged, and without phase shift, from each scattering for a wide range of U values.

The model is integrable and Fig. 4.1 shows no back scattering at all. There is a conserved current [98] (slightly different from the energy current). Again, since the wall is already doubly occupied, only a hole can move through. Due to energy conservation, the number of doubly occupied sites has to be conserved. Therefore a hole of *opposite* spin has to move. Since there is no direct nearest neighbor interaction, in a semi-classical picture the impinging particle can move up to the wall. Therefore, unlike the spinless fermion case, there is no forward jump. Indeed, we observe that transmission through the wall affects neither the shape nor the position of the wave packet.

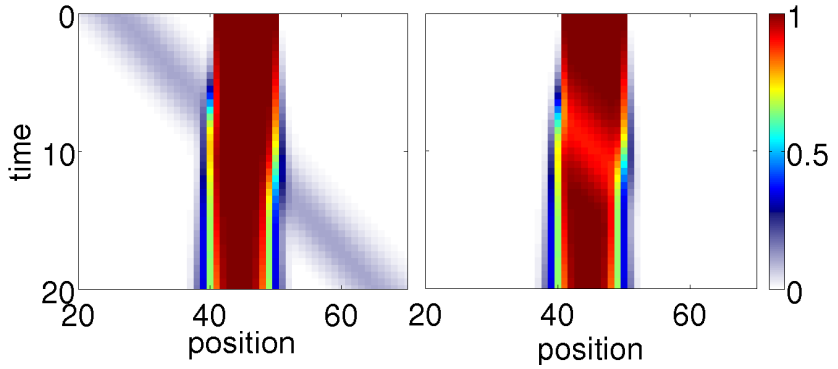

Figure 4.8: Densities in the Fermi Hubbard model at $U = 30$, similar to Fig. 4.1b in the main text. Left: up-spin, right: down-spin. The wall widens over time, but a shift of 1 lattice site (2 particles) is visible in the spatial density distribution.

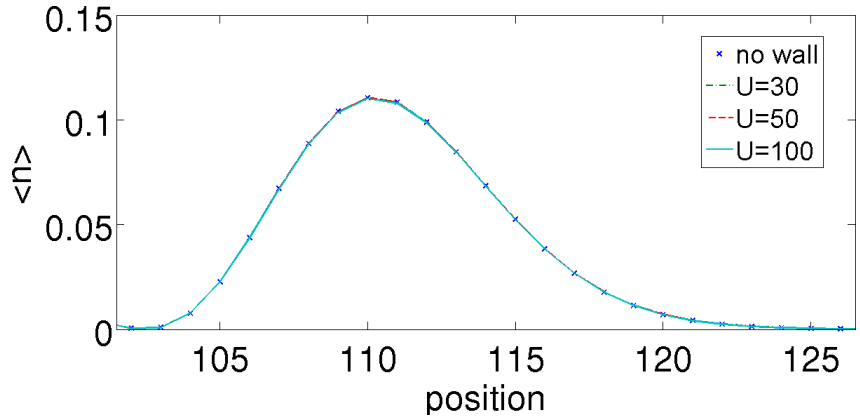

Figure 4.9: Fermi Hubbard model. The spatial density distribution of the transmitted particle is independent of U, and independent of whether there is a wall or not.

4.5 Bose Hubbard model

The dynamics of the Bose Hubbard model

$$H_{bH} = -t \sum_i \left(b_i^\dagger b_{i+1} + h.c. \right) + U \sum_i n_i \left(n_i - 1 \right). \tag{4.24}$$

is now widely realized in experiments with ultra cold atoms in optical lattices [47, 155]. Because of Bose statistics, there is no restriction on local occupation numbers.

The initial state in Fig. 4.1(c) contains $N = 10$ consecutive sites with two bosons each, which are attractively or repulsively bound on each site. For the Bose-Hubbard model, the stability of doubly occupied walls grows with the wall width, as well as with $|U|$, because the pairs can bind to each other when they are on neighboring sites [102, 171, 172].

The Bose-Hubbard model is non-integrable. The scattering result is similar to Fig. 4.6, with partial back scattering. Because of energy conservation, any transmitted incoming signal has to go through the wall as a hole, leaving behind an additional particle and thus one additional doubly occupied single site to the left of the wall. The projected part at the bottom of Fig. 4.1c shows that for these transmitted particles, the wall is indeed again shifted by 1 site, which remains visible for $|U| \gtrsim 10$. Note that inside the wall, the velocity of the hole is twice as high as outside, due to the double occupancy inside the cluster which renormalizes the hopping.

4.6 Applications

We discuss some immediate applications, making use of the wall shifts, the clean nature of scattering in the integrable tV model of spin-polarized fermions (or spin 1/2 Heisenberg chain), and the large stability of walls.

Fermionic quantum Newton's cradle on a lattice.

The continuous space "Quantum Newton's Cradle" [74] is one of the most famous experiments with cold atoms. Here we construct a rather distinct lattice fermionic version by placing the system into an electric field with constant gradient, adding $\sum_j 0.06\, j\, \hat{n}_j$ to eq. (4.1). An incoming Gaussian particle then experiences Bloch oscillations [173], whereas the wall is not affected noticeably due to its high mass. Fig. 4.10 shows the result: a periodic motion very similar to the classical Newton's cradle, except that at each impact, the wall moves by *two* sites instead of one.

Qubits and atomic scale shift register.

When several individual particles hit a wall in succession, the shifts add up quasi-classically, as shown in Fig. 4.11. In effect, the wall position counts the incoming particles, of potential practical interest, e.g. in spintronics applications. Furthermore, when a bound pair of particles impinges on the wall (not shown), it is transmitted inside the wall as a hole pair, shifting the wall by 4 sites after transmission.

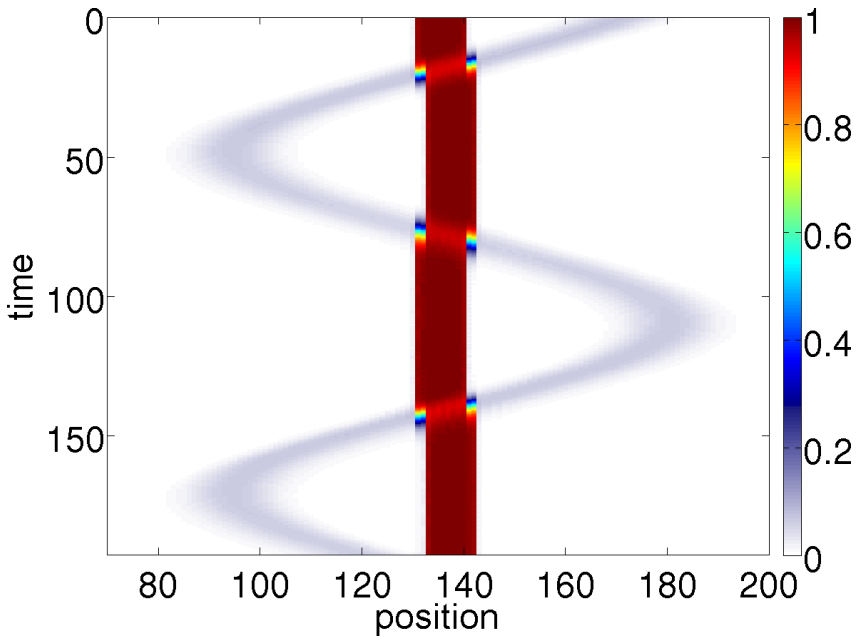

Figure 4.10: A fermionic Quantum Newton's Cradle: density of spin polarized fermions in a linear electric field at $V = 10$, performing Bloch oscillations. Initial Gaussian particle. $V = 10$, 10-site wall.

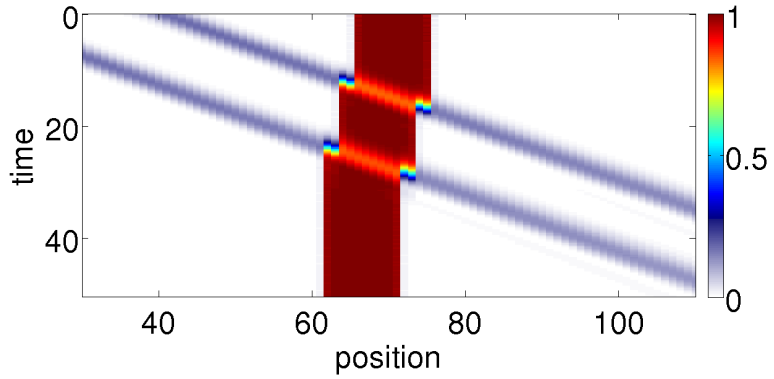

Figure 4.11: Atomic scale signal counter and shift register: each passing particle shifts the wall by 2 sites. (Density of spin-polarized fermions, $V = 10$, 10-site wall.)

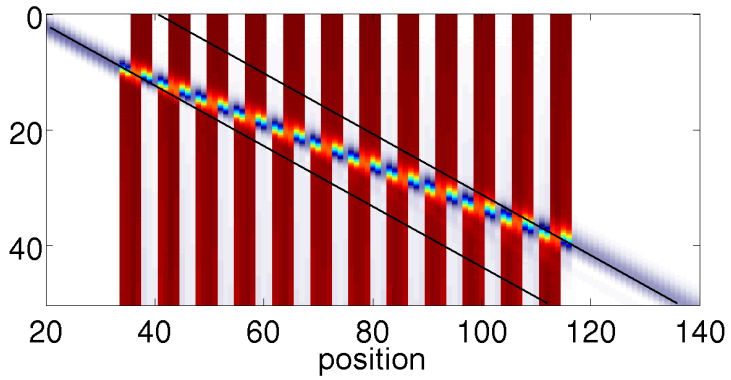

Figure 4.12: Meta-material with "tachyonic" mode: transition of a spin-polarized fermion through a set of 12 equally spaced 4-particle clusters with an intra-cluster distance of 3 sites, at V/t=20. Particle density shown. The forward shift of the traveling particle at each wall leads to an average velocity larger than the velocity of a particle on an empty lattice.

One way to encode a qubit with M-strings is to assign $|0\rangle$ to an M-string in a certain position and $|1\rangle$ to a similar M-string in a different position, ideally non-overlapping. We note that for large values of V/t and M, this qubit will decay only on timescales exponentially small versus the inverse hopping $1/t$.

A sequence of walls and empty space, possibly of various thicknesses, can be interpreted as a sequence of bits. A suitable quantum-mechanical superposition of such sequences can be seen as a sequence of qubits. An incoming single particle would shift the complete sequence of qubits coherently by 2 sites, without becoming entangled, making for a coherent qubit shift register [174].

Meta-material, tachyon.

We have shown above that the transmitted particle is shifted forward by 2 sites (Fig. 4.7, inset). When the particle moves through several walls in succession, as shown in Fig. 4.12, the individual shifts of the traveling particle add up. It moves with an average velocity *higher* than on the empty lattice. If one regards the latter as a "vacuum" with velocity v_0, then the sequential walls act like a meta-material with a tachyonic mode of velocity $v_0 d/(d-2)$, where d is the wall spacing ($d = 7$ in Fig. 4.12). The results in Fig. 4.12 match this expectation precisely.

4.7 Conclusions

We have shown that the quantum mechanical transmission of a particle through a wall of neighboring particles exhibits surprising effects, namely pair creation with particle-hole transmutation and a shift of the wall. In the spin-polarized fermion or Heisenberg case, the wall shifts by *two* sites, and the transmitted particle jumps forward by two sites at large couplings. In addition, and independently, we find that there is no back scattering in the integrable models studied. These effects are due to conservation laws

and the discrete nature of particles. They are therefore robust and, e.g., still occur at small anisotropies $\Delta \gtrsim 1$ in the Heisenberg model and for very narrow walls. The final state is close to a product state of a shifted wall and a transmitted particle of unchanged shape. Applications for spintronics may be possible, like an atomic scale signal counter or coherent shift of qubits. Last, but not least, the phenomena discussed should come within reach experimentally with cold atoms in optical lattices in the foreseeable future.

Chapter 5

Dynamics of Impurity Systems

5.1 Introduction

In following chapter, MPS-techniques are applied to the Single Impurity Anderson Model (SIAM) [175]. We investigated two different regimes. In the first part, MPS techniques are used to obtain groundstate dynamical properties of the model, foremost calculation of the spectral function. For this case we apply and extend the Chebyshev method [59, 176, 177, 178] to obtain highly accurate results. In the second part, we address transport properties of the SIAM and compute the I-V characteristics using real time evolution of a quantum impurity undera finite bias.

5.2 Quantum impurity models

In 1961, Anderson [175] proposed a nowadays famous model to explain the presence or absence of a magnetic moment when metals are doped with certain magnetic ions. The model consists of a local, interacting quantum system in contact with an infinite bath of non-interacting degrees of freedom, typically fermionic. Although ultimately interested in partially filled d-shells Anderson in his work used a simplified model where only two electrons can sit in the "d"-shell (hence apostrophes). The Hamiltonian of the SIAM assumes the form

$$H = \underbrace{\varepsilon_0 \sum_\sigma n_{0\sigma} + U n_{0\downarrow} n_{0\uparrow}}_{H_{imp}} + \underbrace{\sum_{k\sigma} (\varepsilon_k - \mu) n_k}_{H_{bath}} + \underbrace{\sum_{k\neq 0,\sigma} \left(V_k c^\dagger_{0\sigma} c_{k\sigma} + h.c.\right)}_{H_{hyb}}. \tag{5.1}$$

U is an interaction term between electrons, ε_0 is an on-site potential, ε_k is the dispersion of the free electrons in the bath and μ is the chemical potential. The bath and the impurity are *hybridizing* via tunneling matrix elements V_k (see Fig.5.1). The impurity has index 0, the bath states have an index $k \geq 1$. The effect of the bath can be fully described by the spectrum of the so called hybridization function

$$\tilde{\Delta}(\omega) = \pi \sum_k V_k^2 \delta(\omega - \varepsilon_k). \tag{5.2}$$

Being a true many-body model, this system is highly non-trivial. For a linear-dispersion bath, the model can be solved by Bethe ansatz [179], but for more general

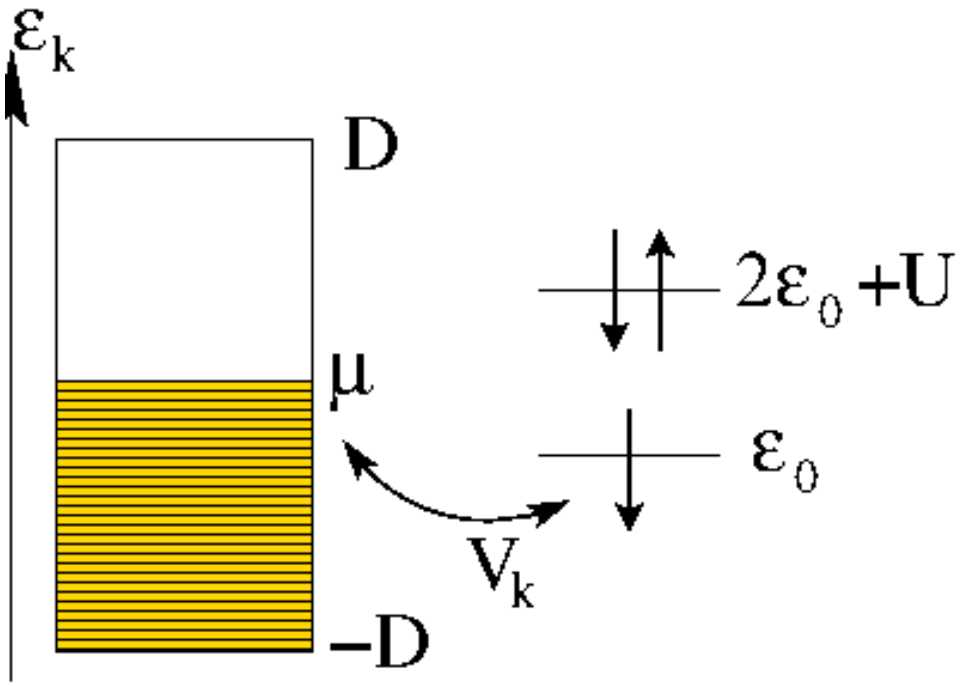

Figure 5.1: Sketch of the single impurity Anderson model. We show a rectangular bath density of states at half filling (left). The electrons can hop from the bath to the impurity via V_k (electrons can hop onto both levels). For $U = -\varepsilon_0/2$, the impurity levels are symmetric about μ.

parameters, one has to resort to numerical techniques. One of the key quantities one is interested in for this model is the impurity Greens function (see Sec.5)

$$G^R_\sigma(\omega) = -i\Theta(t)\left\langle\{c_{0\sigma}(t), c^\dagger_{0\sigma}\}\right\rangle . \tag{5.3}$$

5.2.1 The Resonating Level Model

The non-interacting limit $U = 0$ of Eq.5.1 is an important benchmark for numerical schemes. In the following we will calculate the spectral function $A(\omega)$ for a non-interacting single level coupled to a continuum of non-interacting batch electrons. This model is known as Resonating Level Model (RLM). We will compute the local impurity Greens function and the spectral function by means of equation of motion theory (see Sec.6), following [180]. An alternative discussion can be found in [181]. The full Hamiltonian is given by

$$H = \underbrace{\varepsilon_0 n_0}_{H_{imp}} + \underbrace{\sum_{k\neq 0} \varepsilon_k c^\dagger_k c_k}_{H_{bath}} + \underbrace{\sum_{k\neq 0} (V_k c^\dagger_0 c_k + h.c.)}_{H_{hyb}} \tag{5.4}$$

We have disregarded the spin variable because of the missing interaction between electrons.

We now want to calculate the local Greens function $G_{00}(\omega)$ of the impurity site $l = 0$. This can be done by considering the two cases $l = m = 0$ and $l = k \neq m = 0$ in Eq.165,

with interaction $W = 0$:

$$l = m = 0: \quad (\omega + i\eta - \varepsilon_0)G^R_{00}(\omega) - \sum_{k\neq 0} V_k G^R_{k0}(\omega) = 1 \tag{5.5}$$
$$l = k \neq m = 0: \quad (\omega + i\eta - \varepsilon_k)G^R_{k0}(\omega) - V^*_k G^R_{00}(\omega) = 0$$

(note that for a given k, only $t_{kk} = \varepsilon_k$ and $t_{k0} = t^*_{0k} = V^*_k$ are unequal to zero in Eq.163). The $i\eta$ in Eq.5.5 serve as a reminder of the boundary condition, i.e. if one considers retarded or advanced Greens functions. By inserting $G^R_{k0}(\omega)$ from the second line in Eq.5.5 into the first one, we obtain the following expression for the Greens function $G^R(\omega) \equiv G^R_{00}(\omega)$:

$$G^R(\omega) = \frac{1}{\omega - \varepsilon_0 - \Sigma(\omega)} \tag{5.6}$$
$$\Sigma(\omega) = \sum_k \frac{|V_k|^2}{\omega - \varepsilon_k + i\eta} \tag{5.7}$$

where Σ is the local self-energy of the impurity site and η is a real infinitesimal acting as a regularization parameter. The impurity self-energy $\Sigma(\omega)$ and the hybridization function $\tilde{\Delta}(\omega) = \pi \sum_k |V_k|^2 \delta(\omega - \varepsilon_k)$ are related by the Kramers-Kronig equation

$$\Sigma(\omega) = \frac{1}{\pi} \int_{-\infty}^{\infty} \frac{\tilde{\Delta}(\omega')}{\omega - \omega' + i\eta} dw' \tag{5.8}$$

For a constant bath density of states (DOS) and a constant hybridization $V_k \equiv V$:

$$\rho(\omega) = \begin{cases} 1/(2D), & \omega \in [-D, D] \\ 0 & \text{else} \end{cases} \tag{5.9}$$
$$V_k = V,$$

the integral in Eq.5.8, with the use of Eq.158, yields

$$\Sigma(\omega) = \frac{1}{\pi} \int_{-\infty}^{\infty} \frac{\tilde{\Delta}(\omega)}{\omega - \omega' + i\eta} dw' = \frac{\pi |V|^2 \rho(0)}{\pi} \int_{-D}^{D} \frac{1}{\omega - \omega' + i\eta} dw' \tag{5.10}$$
$$= |V|^2 \rho(0) \left(-i\pi - \ln \left| \frac{1 - \omega/D}{1 + \omega/D} \right| \right) = \Gamma \left(-i - \frac{1}{\pi} \ln \left| \frac{1 - \omega/D}{1 + \omega/D} \right| \right)$$
$$\Gamma = |V|^2 \pi \rho(0)$$

where Γ is called the *hybridization strength* . The spectral function is given by

$$A_\sigma(\omega) = \frac{1}{\pi} \frac{\Gamma}{\left(\omega - \varepsilon_0 + \frac{\Gamma}{\pi} \log \left| \frac{1-\omega/D}{1+\omega/D} \right| \right)^2 + \Gamma^2)}. \tag{5.11}$$

For $D \gg \Gamma$, the log term can be expanded to $\log(\frac{1-\omega/D}{1+\omega/D}) \approx -2\omega/D$, and the spectral function is peaked at $\frac{\varepsilon_0}{1 - 2\Gamma/\pi D}$. If we neglect the log-term the spectral function assumes the form of a Lorentzian of width Γ and the Greens function then simplifies to

$$G(\omega) = \frac{1}{\omega - \varepsilon_0 \pm i\Gamma} \tag{5.12}$$

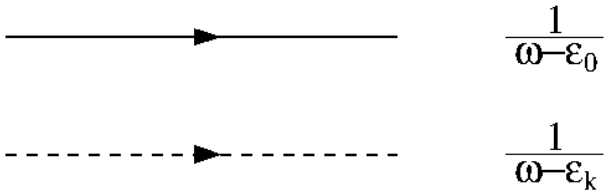

Figure 5.2: Diagrams of the free impurity (upper) and bath (lower) propagator.

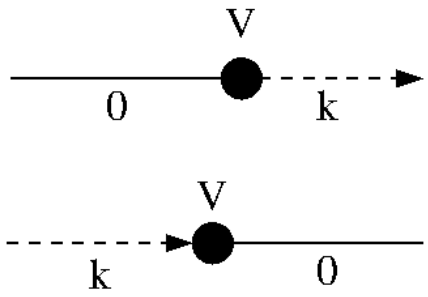

Figure 5.3: Diagrams of the interaction vertices

The case of a non-interacting resonance can be elegantly handled by diagrammatic perturbation theory [180, 182] (see also Sec. 3 and Sec. 4). In Fig.5.2 the free propagators of the impurity and the bath are plotted. The hybridization allows tunneling of the electrons between the impurity and the bath. Fig. 5.4 shows the expansion of the full impurity Greens function. The hybridization term acts as a frequency dependent scatterer. The self energy of this process is plotted in Fig.5.5. The full propagator is obtained using the usual Feynman rules and is plotted in Fig.5.4.

We can now flip the coin and ask for the scattering of the *bath* electrons from the impurity, i.e. the bath-electron propagator $G_b(k', k\omega)$. The Feynman diagram for this process is plotted in Fig.5.6. The translation into a usual mathematical formula is

$$G_b(k', k, \omega) = \delta_{k'k} G_0(k, \omega) + G_0(k', \omega) V^2 G(\omega) G_0(k, \omega). \tag{5.13}$$

From this equation, we can immediately read off the scattering T-matrix

$$T(\omega + i\eta) = V^2 G(\omega + i\eta). \tag{5.14}$$

Scattering theory (see sec.3) relates the T-matrix to the scattering matrix S. Let us assume spherical symmetry of the whole setup, e.g. by assuming a free electron gas that is scattered at a spherical impurity. In this case scattering does not mix states with different orbital quantum numbers l. We will in the following only consider the

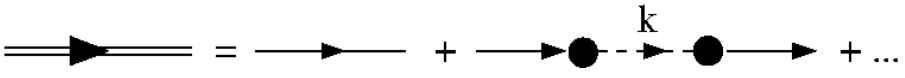

Figure 5.4: Expansion of the full impurity Greens function (double lined arrow) for the Resonating Level Model.

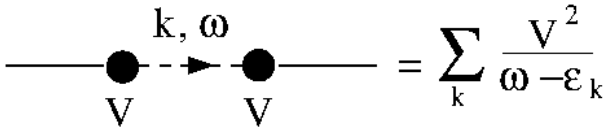

Figure 5.5: Self energy diagram for the impurity Greens function of the Resonating Level Model

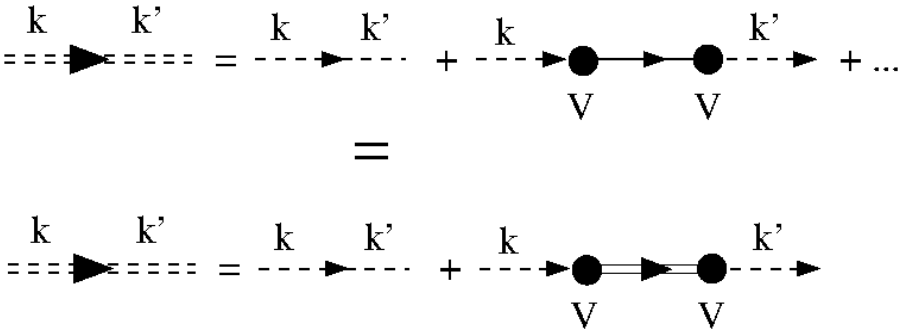

Figure 5.6: Bath-electron propagator

$l = 0, m = 0$ phase shift. In this case S assumes the form

$$S = e^{2i\varphi(\omega)} = 1 - 2i\pi\rho(0)V^2 G(\omega + i\eta) = 1 - 2i\frac{\overbrace{\pi V^2\rho(0)}^{\Gamma}}{\omega - \varepsilon_0 + i\Gamma}. \tag{5.15}$$

By simple algebra we get

$$\varphi(\omega) = \cot^{-1}\Big(\frac{\varepsilon_0 - \omega}{\Gamma}\Big) = \tan^{-1}\Big(\frac{\Gamma}{\varepsilon_0 - \omega}\Big). \tag{5.16}$$

The amount of charge bound in the resonance and the scattering phase shift are related by

$$\langle n_0\rangle = 2\int_{-\infty}^{0}\frac{d\omega}{\pi}\frac{\Gamma}{(\omega - \varepsilon_0)^2 + \Gamma^2} = \frac{2\varphi(\varepsilon_0/\Gamma)}{\pi} \tag{5.17}$$

by an elementary integral (the factor 2 is from spin-degeneracy). This result is called the *Friedel sum rule*. The result for the interacting Anderson model [183] remains the same.

5.2.2 The Anderson Impurity Model

In the presence of an interaction U the Hamiltonian is given by Eq. 5.1 which considerably complicates the computation of the impurity-Greens function. One can again use the equation of motion technique to obtain a set of coupled equations for the impurity Greens function [180]. In the following, the indices l, m, n in Eq. 165 are multi-indices of spin and orbital degrees of freedom, $l \equiv (\nu, \sigma)$, where $\nu \in \{0, k\}$ is either the impurity site 0 or a single particle bath state k. We can again consider two cases $l = (0, \sigma), m = (k, \sigma)$

and $l = (0, \sigma), m = (0, \sigma)$, which yield the coupled equations

$$\begin{aligned}(\omega - \varepsilon_k + i\eta) G^R_{(k\sigma)(0\sigma)}(\omega) &= V_k^* G^R_{(0\sigma)(0\sigma)}(\omega) \\ (\omega - \varepsilon_0 + i\eta) G^R_{(0\sigma)(0\sigma)}(\omega) - \sum_k V_k G_{(k\sigma)(0\sigma)}(\omega) &= 1 + U d_{(0\sigma)(0\sigma)}(\omega) \\ d_{0\sigma}(t) \equiv d_{(0\sigma)(0\sigma)}(t) &= -i\Theta(t) \left\langle \{-[n_{0\uparrow} n_{0\downarrow}, c_{0\sigma}](t), c^\dagger_{0\sigma}\} \right\rangle\end{aligned} \tag{5.18}$$

The expression for $d_{0\sigma}(t)$ can be massaged into

$$d_{0\sigma}(t) = -i\Theta(t) \left\langle \{(c_{0\sigma} n_{0\bar{\sigma}})(t), c^\dagger_{0\sigma}\} \right\rangle \tag{5.19}$$

In the following, we apply *mean field theory*, where the product $n_{0\uparrow} n_{0\downarrow}$ is approximated as

$$n_{0\downarrow} n_{0\uparrow} \approx \langle n_{0\downarrow} \rangle \, n_{0\uparrow} + n_{0\downarrow} \langle n_{0\uparrow} \rangle - \langle n_{0\downarrow} n_{0\uparrow} \rangle \, . \tag{5.20}$$

$d_{0\sigma}(t)$ then simplifies to

$$d_{0\sigma}(t) = -i\Theta(t) \langle n_{0\bar{\sigma}} \rangle \left\langle \{c_{0\sigma}, c^\dagger_{0\sigma}\} \right\rangle = \langle n_{0\bar{\sigma}} \rangle \, G^R_{(0\sigma)(0\sigma)}(t) \tag{5.21}$$

and the set of equation closes. Fourier transforming and then plugging Eq. 5.21 back into Eq. 5.18 then gives

$$\begin{aligned}G^R_{(0\sigma)(0\sigma)}(\omega) &= \frac{1}{\omega - \varepsilon_0 - U \langle n_{0\bar{\sigma}} \rangle - \Sigma(\omega)} \\ \Sigma(\omega) &= \sum_k \frac{|V_k|^2}{\omega - \varepsilon_k + i\eta}.\end{aligned} \tag{5.22}$$

For a flat conduction band $\rho(\omega) = \frac{1}{2}, \omega \in [-D, D]$ and a constant hybridization $V_k = V$, we can use Eq.5.10 to obtain the spectral function

$$A_\sigma(\omega) = \frac{1}{\pi} \frac{\Gamma}{\left(\omega - \varepsilon_0 - \frac{\Gamma}{\pi} \log\left|\frac{1-\omega/D}{1+\omega/D}\right| - U \langle n_{\bar{\sigma}} \rangle\right)^2 + \Gamma^2)}, \tag{5.23}$$

which is again Lorentz-like (see Eq. 5.11), but due to the interaction of the electrons with the mean occupation $\langle n_{\bar{\sigma}} \rangle$ the peak is shifted by $U \langle n_{\bar{\sigma}} \rangle$. Note that $A_\sigma(\omega)$ depends on $\langle n_{\bar{\sigma}} \rangle$. Anderson introduced this model to study the formation of local moments driven by Coulomb interaction. To find the critical U_c, we have to solve the mean-field equations for $\langle n_{0\sigma} \rangle$. The self consistency equation for $\langle n_{0\uparrow} \rangle$ and $\langle n_{0\downarrow} \rangle$ [180] is

$$\begin{aligned}\langle n_{0\sigma} \rangle &= \int_{-D}^{D} d\omega n_F(\omega) A_\sigma(\omega) \\ &= \int_{-D}^{D} \frac{d\omega}{\pi} \frac{\Gamma n_F(\omega)}{\left(\omega - \varepsilon_0 - \frac{\Gamma}{\pi} \log\left|\frac{1-\omega/D}{1+\omega/D}\right| - U \langle n_{\bar{\sigma}} \rangle\right)^2 + \Gamma^2)}.\end{aligned} \tag{5.24}$$

In the wide band limit ($D \gg \Gamma$), the boundaries of the integral can be extended to $D \to \infty$, and the log-term in the denominator can be neglected. At $T = 0$, this yields

$$\langle n_{0\sigma} \rangle = \int_{-\infty}^{0} \frac{d\omega}{\pi} \frac{\Gamma}{(\omega - \varepsilon_0 - U \langle n_{\bar{\sigma}} \rangle)^2 + \Gamma^2)}, \tag{5.25}$$

which is an elementary integral with the solution

$$\langle n_{0\sigma}\rangle = \frac{1}{2} - \frac{1}{\pi}\tan^{-1}\Big(\frac{\varepsilon_0 + U\langle n_{0\bar{\sigma}}\rangle}{\Gamma}\Big). \tag{5.26}$$

We define now magnetization $m \equiv \langle n_{0\uparrow}\rangle - \langle n_{0\downarrow}\rangle$ and density $n \equiv \langle n_{0\uparrow}\rangle + \langle n_{0\downarrow}\rangle$ of the impurity [182], with the mean field equations

$$n = 1 - \frac{1}{\pi}\left(\tan^{-1}\Big(\frac{\varepsilon + \frac{U}{2}(n-m)}{\Gamma}\Big) + \tan^{-1}\Big(\frac{\varepsilon + \frac{U}{2}(n+m)}{\Gamma}\Big)\right) \tag{5.27}$$

$$m = -\frac{1}{\pi}\left(\tan^{-1}\Big(\frac{\varepsilon + \frac{U}{2}(n-m)}{\Gamma}\Big) - \tan^{-1}\Big(\frac{\varepsilon + \frac{U}{2}(n+m)}{\Gamma}\Big)\right). \tag{5.28}$$

At the transition, we have $m = 0^+$, which we plug into Eq.5.27 to obtain

$$\tan\Big(\frac{(1-n)\pi}{2}\Big) = \frac{\varepsilon_0 + \frac{U_c}{2}n}{\Gamma}. \tag{5.29}$$

An expansion of Eq.5.28 around $(\varepsilon_0 + Un/2)/\Gamma$ for small m yields

$$1 = \frac{U_c}{\pi\Gamma}\frac{1}{1+\left(\frac{\varepsilon_0+\frac{U_c}{2}}{\Gamma}\right)^2} = \frac{U_c}{\pi\Gamma}\cos\Big(\frac{(1-n)\pi}{2}\Big). \tag{5.30}$$

Using $n = 1$ at the transition, we thus expect moment formation for $U > U_c = \pi\Gamma$. The total spectral function $A(\omega) = A_\uparrow(\omega) + A_\downarrow(\omega)$ has two peaks at ε_0 and $\varepsilon_0 + U$.

The mean-field approximation is certainly not the whole story when U is comparable to the hybridization energy scale Γ. In the atomic limit $V \to 0$ the spectral function $A_\sigma(\omega)$ shows two δ-peaks at ε_0 and $2\varepsilon_0 + U$. Turning on V one would expect a broadening of these. The single peak of the mean field solution contradicts this expectation. In mean field, the decoupling of the equations of motion happened already at the level of $d_{0\sigma}(t)$. By considering the the EOM for $\partial_t d_{0\sigma}(t)$, and ignoring certain higher order processes, one can improve the result for the spectral function considerably [180]. We will show the calculation for $\sigma = \uparrow$ (the other one is similar):

$$i\partial_t d_{0\sigma}(t) = \delta(t)\langle n_{0\downarrow}\rangle - i\Theta(t)\Big\langle\{-[H_{hyb} + H_{imp} + H_{bath}, n_{0\downarrow}c_{0\uparrow}](t), c^\dagger_{0\uparrow}\}\Big\rangle \tag{5.31}$$

Using the relations

$$\begin{aligned}
[H_{bath}, n_{0\downarrow}c_{0\uparrow}] &= 0\\
[H_{imp}, n_{0\downarrow}c_{0\uparrow}] &= -(\varepsilon_0 + U)n_{0\downarrow}c_{0\uparrow}\\
[H_{hyb}, n_{0\downarrow}c_{0\uparrow}] &= -n_{0\downarrow}\textstyle\sum_k V_k c_{k\uparrow} + \underbrace{\sum_k (\bar{V}_k c^\dagger_{k\downarrow}c_{0\downarrow} - V_k c_{k\downarrow}c^\dagger_{0\downarrow})c_{0\uparrow}}_{\text{neglect}}
\end{aligned}$$

Eq. 5.31 gives

$$i\partial_t d_{0\sigma}(t) = \delta(t)\langle n_{0\downarrow}\rangle + (\varepsilon_0 + U)d_{0\uparrow} + \sum_k \underbrace{(-i\Theta(t))\langle\{(n_{0\downarrow}c_{k\uparrow})(t), c^\dagger_{0\uparrow}\}\rangle}_{f_{k\uparrow}(t)}.$$

A similar consideration for $f_{k\uparrow}(t)$ yields

$$i\partial_t f_{k\uparrow}(t) = \delta(t)\underbrace{\langle\{n_{0\downarrow}c_{k\uparrow}, c_{0\uparrow}^\dagger\}\rangle}_{0} - i\Theta(t)\Big\langle\{[n_{0\downarrow}c_{k\uparrow}, H](t), c_{0\uparrow}^\dagger\}\Big\rangle.$$

With the relations

$$\begin{aligned}
[H_{bath}, n_{0\downarrow}c_{k\uparrow}] &= -c_{k\uparrow}\varepsilon_k \\
[H_{imp}, n_{0\downarrow}c_{k\uparrow}] &= 0 \\
[H_{hyb}, n_{0\downarrow}c_{k\uparrow}] &= -\bar{V}_k n_{0\downarrow}c_{0\uparrow} + \underbrace{\sum_k(\bar{V}_k c_{k\downarrow}^\dagger c_{0\downarrow} - V_k c_{k_\downarrow}c_{0\downarrow}^\dagger)c_{k\uparrow}}_{\text{neglect}}
\end{aligned}$$

and neglecting the under braced expression , the set of equations finally closes to

$$\begin{aligned}
(\omega + i\eta - \varepsilon_0 - U)d_{0\uparrow}(\omega) &= \langle n_{0\downarrow}\rangle + \textstyle\sum_k V_k f_{k\uparrow}(\omega) \\
(\omega + i\eta - \varepsilon_k)f_{k\uparrow}(\omega) &= \bar{V}_k d_{0\uparrow}(\omega)
\end{aligned}$$

where we have performed the Fourier transformation. With the assumption of Eq. 5.9, the occurring sum can be performed (see Eqs. 5.22 and 5.10), and the final result is

$$G_\uparrow^R(\omega) = \tfrac{1-\langle n_{0\downarrow}\rangle}{\omega-\varepsilon_0-\Sigma(\omega)} + \tfrac{\langle n_{0\downarrow}\rangle}{\omega-\varepsilon_0-U-\Sigma(\omega)} \tag{5.32}$$

$$A_\uparrow(\omega) = \tfrac{1}{\pi}\Big(\tfrac{(1-\langle n_{0\downarrow}\rangle)\Gamma}{(\omega-\varepsilon_0-\Re\{\Sigma(\omega)\})^2+\Gamma^2} + \tfrac{\langle n_{0\downarrow}\rangle\Gamma}{(\omega-\varepsilon_0-U-\Re\{\Sigma(\omega)\})^2+\Gamma^2}\Big) \tag{5.33}$$

with $\Sigma(\omega)$ and Γ from Eq. 5.10. The spectral function now shows two Lorentz-like peaks, separated by a distance U, with width Γ. The interpretation is simple: the lower peak at ε_0 corresponds to the process of adding a particle to the empty impurity site, the other one to adding a particle to a partially filled impurity site, which costs an energy U. The first process can also be understood as the probability of being able to remove a $\uparrow$-electron (i.e. adding a *hole*)from the impurity because due to Pauli exclusion, the probability of finding an $\uparrow$-electron at the impurity is 1-$\langle n_{0\downarrow}\rangle$. This *hole* is then propagated backwards in time (this is also consistent with the definition of $G^R(\omega)$, which contains both a particle and hole propagation branch). The two peaks are also referred to as Hubbard satellites. These results also explain the Coulomb-blockade of the zero-bias conductance G. The latter can be calculated from $A(\omega)$ using the Meir Wingreen formula [180].

5.2.3 Kondo effect in the SIAM and its solution with NRG

The interacting Anderson model is intimately related to the so called Kondo (or *s-d*) model [184, 4, 181, 19] of a localized impurity-spin interacting with a bath of free electrons. In fact, the Kondo-Hamiltonian can be obtained from the SIAM by the so called Schrieffer-Wolff transformation [180, 181]. This transformation projects the full SIAM to the subspace where the impurity is only singly occupied (by either a spin up or spin down electron). For large U/Γ, the Kondo model describes the low energy properties of the SIAM. The Kondo Hamiltonian is

$$H_K = \sum_{kk'}\sum_{\alpha\alpha'\in\{\uparrow\downarrow\}}\sum_{i\in\{x,y,z\}} J_i c_{k\alpha}^\dagger \sigma_{\alpha\alpha'}^i c_{k'\alpha'} S^i \tag{5.34}$$

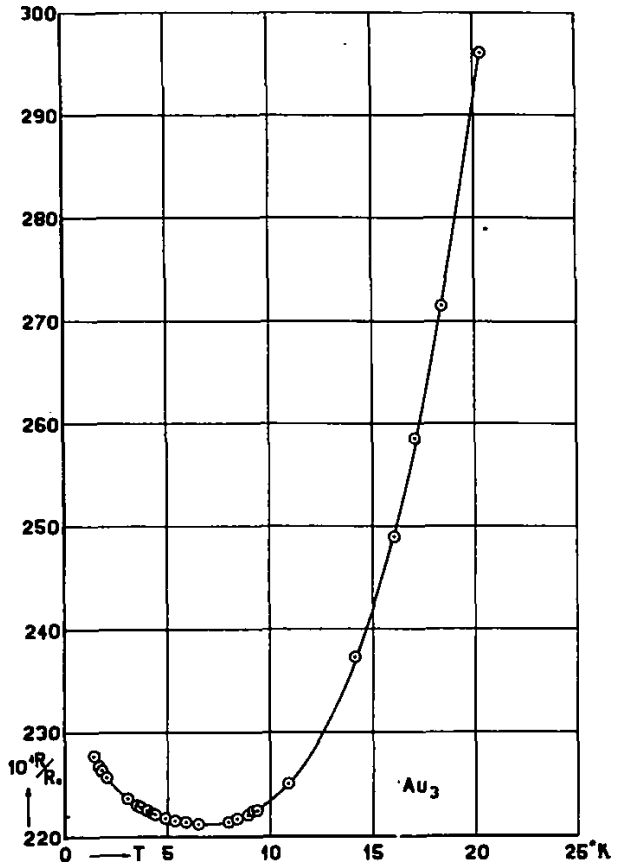

Figure 5.7: Resistance of Au containing Fe and Si impurities as a function of temperature T (taken from W. J. de Haas and G. J. van den Berg [185]).

where $\sigma^i_{\alpha\alpha'}$ are the spin matrices for the electrons, and S_i are the spin operators of the impurity. The Hamiltonian models a local moment immersed into a sea of free electrons, where the electrons at the impurity site are interacting with the local moment of the impurity. Typical materials described by such a Hamiltonian are Cu-Fe, Cu-Mn or Au-Vn, where Fe, Mn or Vn serve as impurities (at very low concentrations of about 0.01%) [19]. Using this model, Kondo [184] was able to explain the anomalous increase of electrical resistivity in metals doped with metallic ions at low temperatures (see Fig.5.7).

This increase was unexpected and could not be explained by electron-phonon scattering or scattering of electrons at localized (single-body) potentials, the first giving a T^5 dependence of the resistivity, the second becoming constant in the $T \to 0$ limit. Kondo realized that the second order perturbation in J_i to the scattering of electrons off the immobile spin-impurity yields a logarithmic correction to the resitivity which diverges as $T \to 0$. This result can be obtained by applying a semiclassical approach to the problem [181]. The Boltzmann equation for the electron-distribution function $f(\mathbf{k})$ in the presence of an electric field $\mathbf{E}$ is

$$\frac{df(\mathbf{k})}{dt} = \frac{\partial \mathbf{k}}{\partial t}\Big(\nabla f(\mathbf{k})\Big) = \mathcal{L}(f(\mathbf{k})) \tag{5.35}$$

where $\mathcal{L}$ is a collision operator which takes into account the scattering of the electrons

due to e.g. impurities. Assuming that

$$\dot{\mathbf{p}} = \hbar \frac{\partial \mathbf{k}}{\partial t} = -e\mathbf{E} \tag{5.36}$$

and using the relaxation time approximation $\mathcal{L}(f(\mathbf{k})) \approx -\frac{f(\mathbf{k})-f_0(\mathbf{k})}{\hbar\tau(\mathbf{k})}$, one can derive the Drude expression for the conductivity

$$\sigma = \frac{ne^2\tau(k_F)}{m} \tag{5.37}$$

where n is the electron density, e is the electronic charge and m is the (effective) mass of an electron. $\tau(k_F)$ is called the *transport lifetime*. The calculation of $\tau(k_F)$ is the essential next step. The result is derived in [181] and is given by

$$\frac{1}{\tau(k)} = 2\pi n_{imp} \int \frac{d\mathbf{k}'}{(2\pi)^3} \delta(\varepsilon_k - \varepsilon_{k'}) |T_{\mathbf{k}\mathbf{k}'}|^2 (1 - \cos(\theta')) \tag{5.38}$$

where θ' is the angle between $\mathbf{k}$ and $\mathbf{k}'$, and the T-matrix is assumed to depend only on θ'. The conductivity is thus expressed as a functional of the matrix elements of the scattering T-matrix. It is now straightforward to insert the perturbation series for T to derive the first and second order corrections to the conductivity. Let us look at this in a little bit more detail. The first thing to note is that we are dealing with the problem on the level of scattering theory. In the appendix we derive (or rather state) the major results of scattering theory. Right now we need the perturbation series for T, given by

$$T = V + VG_0V + VG_0VG_0V + \dots \tag{5.39}$$

In the non-interacting resonating level model above we calculated the exact propagator of the bath electrons, Eq.5.13, using Feynman diagrams. The reason we could get the exact result is essentially that the impurity potential, off which the electrons were scattering, is single-body. Hence there are no internal degrees of freedom. In the case of electrons scattering via Eq.5.34, an incoming electron can flip the impurity spin, and this flipped impurity spin then can interact with another electron, thus there is an effective electron-electron interaction mediated by the spin. When dealing with scattering off single body potentials one can neglect the presence of an (uncorrelated) Fermi sea and treat the scattering of each $|k\rangle$-electron seperately. This is no more valid in this case. That's easiest understood when considering the second order contributions to the T-matrix

$$T^{(2)}_{k\sigma k'\sigma'} \equiv \langle k\sigma | \, H_K G_0(\omega + i\eta) H_K \, |k'\sigma'\rangle \, . \tag{5.40}$$

For simplicity we assume a k-independent coupling $J_i = J$ [181]. For $\sigma = \sigma' = \uparrow$ two

particular contributions which involve spin-flips are

$$J^2 \sum_{k_1 k_1' k_2 k_2'} \langle k' \uparrow | \left(S^- c^\dagger_{k_1 \uparrow} c_{k_1' \downarrow} \frac{1}{\omega + i\eta - H_0} S^+ c^\dagger_{k_2 \downarrow} c_{k_2' \uparrow} \right) | k \uparrow \rangle$$

$$= J^2 \sum_k S^- S^+ \frac{1 - f(\varepsilon_k)}{\omega + i\eta - \varepsilon_k} \tag{5.41}$$

$$J^2 \sum_{k_1 k_1' k_2 k_2'} \langle k' \uparrow | \left(S^+ c^\dagger_{k_1 \downarrow} c_{k_1' \uparrow} \frac{1}{\omega + i\eta - H_0} S^- c^\dagger_{k_2 \uparrow} c_{k_2' \downarrow} \right) | k \uparrow \rangle$$

$$= J^2 \sum_k S^+ S^- \frac{f(\varepsilon_k)}{\omega + i\eta - \varepsilon_k} \tag{5.42}$$

(the impurity state is not explicitly written in the above equations, hence the S^+, S^- are the spin *operators* of the impurity). These two processes involve the same initial and final states of the bath-electrons, but different initial and final states of the impurity. Lets look at Eq.5.41 first. The left plot in Fig.5.8 shows the corresponding Feynman diagram. The upper lines represent the electrons, and the straight bottom line is the impurity spin. An electron in $k \uparrow$ is scattered into an unoccupied state $k_1 \downarrow$ below the Fermi level with opposite spin, and later is then transfered to $k' \uparrow$. In the second process $k_1 \downarrow$ electron is scattered from an occupied level into the state $k' \uparrow$, and the resulting hole is filled by the initial $k \uparrow$ electron. When summing the two contributions, the occupation factors $f(\varepsilon_k)$ and $1 - f(\varepsilon_k)$ (resulting from finite T) *do not cancel out* as an immediate consequence of $[S^+, S^-] = 2S_z \neq 0$. One can evaluate all other $\sigma\sigma'$ contributions and add them up to obtain a correction of third order in J to the transport lifetime $\tau(k_F)$ and the resistivity [181]. The result is a logarithmic divergence as $T \to 0$.

One might suspect that the unphysical logarithmic divergence at $T = 0$ is an artefact of second order perturbation theory as e.g. the diverging ground state energy of an interacting electron gas . Unfortunately, partial resummation of selected diagrams even worsenes the problem [186] as it gives a divergence at a *finite* temperature T_K, known as the Kondo temperature (the divergence being referred to as the Kondo problem). The way out of this dilemma was only found by applying renormalization ideas to the problem, where the first step was done by Anderson [187], who introduced a "poor man's scaling" approach based on perturbative renormalization arguments [181]. This finally led Wilson to develop his famous numerical renormalization group approach to the Kondo model [19].

The poor man's scaling approach is similar in spirit to the Schrieffer-Wolff transformation of the SIAM. Instead of projecting out empty and doubly occupied impurity states one renormalizes the bandwidth D of the bath by projecting out states where electrons are scattered to upper band edge D or holes to the lower band edge $-D$. These fluctuations are then incorporated by renormalized coupling constants

$$\tilde{J}_z = J_z + \delta J_z \tag{5.43}$$
$$\tilde{J}_\pm = J_\pm + \delta J_\pm$$

($J_\pm \equiv J_x/2 = J_y/2$). The resulting flow equations are [181]

$$\frac{dJ_\pm}{d \log D} = -2\rho(0) J_z J_\pm, \frac{dJ_z}{d \log D} = -2\rho(0) J_\pm^2 \tag{5.44}$$

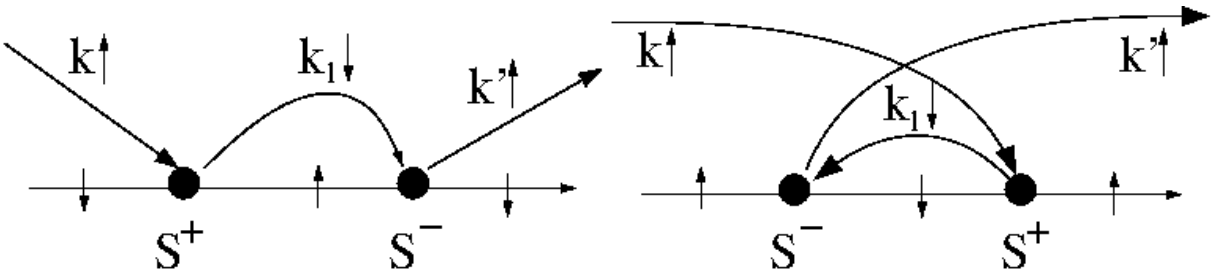

Figure 5.8: Feynman diagrams of the two processes Eq.5.41 (left) and Eq.5.42 (right) (see also [181])

with $dD < 0$. For ferromagnetic models $J_z < 0$ with $|J_z| \geq J_\pm$, the flow is to $J_\pm = 0$. Ferromagnetic couplings with $|J_z| < J_\pm$ and antiferromagnetic couplings $J_z > 0$ flow away from the $J_\pm = 0$ axis to larger and larger $J_\pm$, and eventually the approximations used in the derivation of the flow equations become invalid. In the isotropic case $J_z = J_\pm = J$ the two equation Eq.5.43 are the same, and one can integrate from an initial D, J to a new $\tilde{D}, \tilde{J}$, which yields

$$De^{\frac{1}{2\rho(0)J}} = \tilde{D}e^{\frac{1}{2\rho(0)\tilde{J}}} \sim k_B T_K \tag{5.45}$$

Eq.5.45 is obeyed at all points on the D, J-trajectory (in the weak coupling regime $J\rho(0) \ll 1$) and hence defines an energy scale which is the same for *all models on this trajectory*. Upon reducing D further and further, the coupling $J\rho(0)$ diverges at at some point T_K, at which perturbation theory becomes invalid. Anderson conjectured that this divergence should only appear in the limit $D \to 0$.

The final solution to the problem was found by Wilson. Based on the scaling arguments of Anderson, he invented the numerical renormalization group method (NRG) which enabled him to pursue the scaling of the Hamiltonian down to ever decreasing energy scales. Two major steps finally led to the success: the first one was to map the Kondo system to a chain geometry [181, 19]. The chain geometry suggests a renormalization procedure where a renormalization step is linked with an increase of the system size: one diagonalizes the system for a chain length N, then adds a site, and diagonalizes it again for length $N+1$. To circumvent the problem of exponential increase of Hilbertspace dimension, one could truncate the space at step $N + 1$, where the truncation would be motivated by some renormalization arguments. However, for the generic case of a continuum of bath-states, the parameters of the chain model are all on the same energy scale, independent of the length of the chain, and simple truncation will not converge. Wilson's insight was to use a special discrete representation of the bath. First note that the coupling of the impurity to the bath degrees of freedom can be represented by the bath hybridization function (see Eq.5.2)

$$\tilde{\Delta}_{NRG}(\omega) = \pi \sum_{\mathbf{k}} |V_{\mathbf{k}}|^2 \delta(\omega - \varepsilon_{\mathbf{k}}) \tag{5.46}$$

(we use the convention of the NRG community to put π in front of the sum). Wilson now discretized the hybridization function *logarithmically*

$$x_n^\pm = \pm D\Lambda^{-n}, n \in \{0, 1, 2, \dots\}, \tag{5.47}$$

which reflects the fact that the divergences which occurred in perturbation theory were also logarithmic:

$$\int_{k_BT}^{D} \frac{d\varepsilon}{\varepsilon} = \ln\Big(\frac{k_BT}{D}\Big). \tag{5.48}$$

For this discretization, every subinterval $[x_n^{\pm}, x_{n+1}^{\pm}]$ contributes equally to the above integral, and this incorporates the fact that the higher energy scales are important [181]. The appearance of such terms as Eq.5.48 is a typical problem that arises when there is no characteristic energy scale [19]. For a flat bath DOS with a constant hybridzation, Eq.5.9, the discretization can be done analytically. [4] (apart from an approximation that vanishes in the limit $\Lambda \to 1$). The final step is then to use a tridiagonalization procedure to map the discretized Hamiltonian onto a chain geometry. Our discussion has moved from the SIAM to the Kondo model, but the arguments which lead to the logarithmic discretization are of course valid for both models. Since the focus of this section lies on the SIAM, we now move back to our original model Eq.5.1. The result for the logarithmically discretized SIAM model with a flat bath and constant hybridization V Eq.5.9 is [4]

$$H = \underbrace{\varepsilon_0 \sum_{\sigma} n_{0\sigma} + U n_{0\downarrow} n_{0\uparrow}}_{H_{imp}} + \sqrt{\frac{\xi_0}{\pi}} \sum_{\sigma} (c_{0\sigma}^{\dagger} c_{1\sigma} + h.c.) + \sum_{\sigma n=1}^{\infty} t_n (c_{n\sigma}^{\dagger} c_{n+1\sigma} + h.c.) \tag{5.49}$$

with $\sqrt{\xi_0/\pi} = V/D$ and $t_n/D = \frac{(1+\Lambda^{-1})(1-\Lambda^{-n-1})}{2\sqrt{(1-\Lambda^{-2n-1})(1-\Lambda^{-2n-3})}}\Lambda^{-n/2}$ (we assumed particle hole symmetry; without particle-hole symmetry, there would also be a diagonal term $\sum_{\sigma n} \varepsilon_n c_{n\sigma}^{\dagger} c_{n\sigma}$). Note that this becomes exact only in the limit $\Lambda \to 1$ [4]. The tridiagonalization corresponds to a basis transformation of the conduction electron states. This change of basis turns out to be the crucial point of the procedure. Before discretization, the bath was described by Bloch states. These are completely delocalized over the whole lattice. The discretization + tridiagonalization mapping effectively transforms the description from Bloch states to a more localized basis c_i ($i = 1 \dots$) (Wilson calls it the *Kondo basis* [19]). The c_i obey standard fermionic commutation relation. c_1 is a state which is localized around the impurity. The state c_2 is localized in a layer around the state c_1, c_3 in a layer around c_2, and so on [19, 181]. As i increases, the state c_i is made up of states more and more localized around the fermi energy. As a result, the hoppings t_n/D exhibit *exponential decay* with length n. This feature then makes possible the application of renormalization group ideas to the SIAM [4, 19, 181]. The Hamiltonians for successive lengths N and $N+1$ of the chain obey the recurrence relation

$$H_N = \Lambda^{(N-1)/2}\Big(H_{imp} + \sqrt{\frac{\xi_0}{\pi}} \sum_{\sigma} (c_{0\sigma}^{\dagger} c_{1\sigma} + h.c.) + \sum_{\sigma n=1}^{N-1} t_n (c_{n\sigma}^{\dagger} c_{n+1\sigma} + h.c.)\Big)$$
$$H_{N+1} = \sqrt{\Lambda} H_N + \Lambda^{N/2} \sum_{\sigma} t_N (c_{N\sigma}^{\dagger} c_{N+1\sigma} + h.c.) \tag{5.50}$$

with the H being the limit of the recursion:

$$H = \lim_{N\to\infty} \Lambda^{-(N-1)/2} H_N. \tag{5.51}$$

A detailed exposure of the NRG as applied to the SIAM can be found in [4]. I will briefly state the main steps. Eq.5.50 defines the RG transformation

$$H_{N+1} = R(H_N). \tag{5.52}$$

The algorithm starts by diagonalizing the impurity+first conduction site Hamiltonian H_0

$$H_0 = H_{imp} + \sqrt{\frac{\xi_0}{\pi}} \sum_\sigma (c^\dagger_{0\sigma} c_{1\sigma} + h.c.), \tag{5.53}$$

which yields eigenstates and eigenergies $|E^0_\alpha\rangle, E^0_\alpha$. A representation of $H_1 = \sqrt{\Lambda} H_0 + \Lambda^{1/2} \sum_\sigma t_1 (c^\dagger_{1\sigma} c_{2\sigma} + h.c.)$ can be constructed using the basis $|E^0_\alpha\rangle \otimes |\beta_1\rangle$, with $|\beta_1\rangle \in \{|0\rangle, |\downarrow\rangle, |\uparrow\rangle, |\downarrow\uparrow\rangle\}$. H_1 is then diagonalized to obtain $|E^1_\alpha\rangle, E^1_\alpha$, from which one can construct H_2 in the basis $|E^1_\alpha\rangle \otimes |\beta_2\rangle$ and so on. If not for the exponential growth of number of basis states, one could in principle construct the full eigenbasis in this way. At step N+1, the coupling between sites N and N+1 via t_N acts as a perturbation of order $1/\sqrt{\Lambda}$ to H_N which lifts the four-fold degeneracy of the states $|E^N_\alpha\rangle \otimes |\beta_{N+1}\rangle$ with respect to H_N [19]. To be able to iterate the scheme to large N, at every N one truncates the basis states $|E^N_\alpha\rangle$ to the lowest χ levels of H_N. Typically one keeps $\chi \sim 1000$ states at every step, at values of $\Lambda = 2$ to 2.5 (the limit $\Lambda \to 1$ is beyond reach of the method; in practice, values of 1.5 are considered already quite small). The flow to the fixed-point is checked by monitoring the convergence of the (rescaled) eigenenergies E^N_α. When multiplied with $\Lambda^{-(N-1)/2}$, these energies are approximations to the low-energy eigenspectrum of H.

At this point a remark considering the RG mapping R should be made: When looking at the flow of the energy levels, one needs to look seperately at even and odd N, that is, one looks at the fixed-pointof R^2. The spectra (and hence all other physical quantities) show typical even-odd alternations, originating from the finite size of the system.

What is the meaning of this flow? Let's look at the case of the Kondo model: The Kondo model has two limits in which the physics becomes trivial: at $J = 0$ and at $J = \infty$. In the Kondo problem, the original question was: what is the low-energy behaviour of the impurity in the antiferromagnetic case $J > 0$ (the $J < 0$ case is practically solved by the poor man's scaling approach of Anderson, giving a free spin with an impurity susceptibility of Curie type at $T \to 0$)? Starting from a small $J > 0$ value, and for small iteration number the NRG levels are close to the $J = 0$ case. At some point N of the iteration, the levels however start to move away from the $J = 0$ point towards the $J = \infty$ case, where they are seen to converge to a fixed point. The lowest energy levels of the interacting system thus converge to the eigen energies of the $J = \infty$ case. In the latter, the impurity spin forms a spin-singlet state with a conduction electron. In the case of a small, finite J, the conduction electrons form a "cloud" which screens the impurity spin - the *correlation cloud* [188, 189]. The width of the cloud defines a correlation length ξ. The NRG eigenenergies and eigenstates can be used to calculate e.g. the magnetic impurity susceptibility, which is seen to converge to a finite value with $T \to 0$, as observed in experiment [19, 4]. These considerations are also valid for the SIAM in the limit of large U/Γ.

The logarithmic discretization scheme is the key ingredient for the success of the NRG, but it also poses limitations because some hybridization functions are just not well suited to be discretized in such a fashion. Especially high energy features of the bath

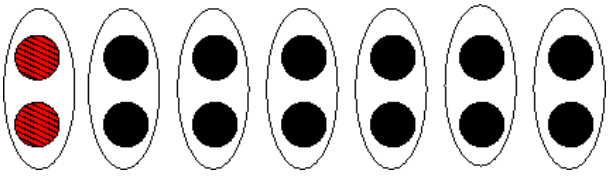

Figure 5.9: Illustration of a two-orbital SIAM. For treatment with NRG, the sites of the two conduction bands (black filled circles) have to be combined into a single, large site (large ellipses).

DOS are badly resolved if Λ is chosen too large, and also for a flat DOS, the mapping is only exact in the limit $\Lambda \to 1$. On the other hand, large values of Λ are required to achieve separation of energy scales which is mandatory for NRG. In NRG as it is applied to the Kondo or Anderson model, one is interested in the low temperature limit where the physics becomes dominated by electrons at the Fermi level, and hence the high energy features can be ignored. A second limitation of NRG is that extension to multiorbital systems comes with an exponential increase in computational cost: solving an n orbital SIAM with n different conduction bands is 4^{n-1} times harder than the original SIAM. The reason is that even if the conduction electrons of different bands do not couple, NRG cannot treat them separately. The n different conduction bands can be discretized separately, but the sites of the different chains have to be treated as one big site (see Fig.5.9 for the case of a two-orbital model).

So far we have considered impurity systems as real physical quantum systems which can be probed in experiments. Advances in theoretical physics have however put impurity systems into a much broader scope. In the so called Dynamical Mean-Field Theory (DMFT) [6] impurity systems are used as auxiliary quantum system to calculate properties of strongly correlated materials. The DMFT is a Greens function based method where the central object is the local impurity Greens function (an outline of the method will be given below). NRG has so far proven to be a powerful solver within the DMFT for single orbital models [190], and it has also been applied to two orbital systems [191]. Applicability of NRG to models with more than two orbitals remains however a challenging task and it is not clear if it can be efficiently used within the framework of DMFT. The purpose of the following work is to establish Matrix Product States techniques as possible impurity solvers for DMFT.

5.3 Dynamical spectral functions of the SIAM using Matrix Product States

The results of the following section have been onbtained in collaboration with Patrik Thunstrm, Frank Verstraete, Karsten Held and Hans Gerd Evertz. The work is available as a preprint version on http://arxiv.org/abs/1403.1209. All calculations and results were obtained by the author of this thesis.

For one-dimensional (1-d) strongly correlated quantum systems, the Density Matrix Renormalization Group (DMRG) [5, 17], and Matrix Product States (MPS) in general [9, 13] have emerged as a powerful tool for calculation of groundstate and excited state prop-

erties. Since its invention, the DMRG has been extended to treat dynamical correlation functions [7, 8] as well as real time evolution [11, 10, 51, 50], and nowadays is considered the method of choice for tackling 1-d quantum systems. In a recent publication [59], MPS techniques have been combined with the Chebyshev expansion method [192] to compute dynamical correlation functions of 1-d quantum system. In the following, we propose efficient extensions to the method and show that it can be easily incorporated into the DMFT cycle.

The first attempt to calculate spectral functions with DMRG involved a continued fraction expansion [193]. The method however fails to produce reliable results for large systems. A major improvement was the introduction of the correction vector (CV) method [7] and its variational formulation [8]. Both methods are known to give highly accurate spectral functions for 1d systems. The method suffers however from two major drawbacks: first, one has to invert a large, non-hermitian and possibly ill-conditioned equation system in a DMRG-like fashion, and second, one has to do full DMRG-like sweeps for every single ω value. A similar approach has also been proposed in [194], where the CV method was used as an impurity solver within Dynamical Mean Field Theory for mulitorbital system.

Recent work [57, 58] reports on major improvement of the continued fraction method by using an MPS parametrization of the Krylov vectors obtained during the Lanzcos method, thus drastically decreasing computational costs as compared to the DDMRG-method while giving results of comparable accuracy to DDMRG. Former approaches using a continued fraction expansion used a fixed effective basis to represent all Lanzcos vectors, whereas in [58], each Lanzcos vector has its own optimized effective basis. This parametrization in terms of MPS proves a powerful and versatile tool, and can in fact be implemented into any Krylov-based method for solving large, sparse eigenvalue problems. In a very recent work by Holzner et al. [59], MPS methods were combined with the Kernel polynomial method (KPM) [176] to obtain highly accurate spectral functions for the isotropic Heisenberg XXX model. Our extensions to the KPM drastically improve achievable spectral resolution at very low cost. The method is applied to the SIAM [175], where we obtain accurate results over a broad parameter range. Finally, we demonstrate the power of the method as a promising impurity solver for Dynamical Mean Field Theory (DMFT) by solving for the Greens function of the Hubbard model on the infinite connectivity Bethe lattice.

5.3.1 The Kernel Polynomial Method: expansion in Chebyshev polynomials

The kernel polynomial method [192, 195, 176] is a numerical method for expanding Greens functions $G(k, \omega)$ and spectral functions $A(k, \omega)$ (see Sec.5 for more details) of (many-body) quantum systems in orthogonal Chebyshev polynomials

$$T_n(\omega) = \cos(n \ \mathrm{acos}(\omega)) \tag{5.54}$$

Very recently it has been extended to the treatment of large interacting 1-d quantum systems by combining it with MPS techniques. The following presents the basic properties of the Kernel Polynomial Method. In mathematical literature, two types of Chebyshev polynomials are used: those of first and those of second kind. We will only need those of the first kind which will hence forth just be called Chebyshev polynomials.

For a quantum system with Hamiltonian H at temperature $T = 0$, the spectral function for the unoccupied part ($A^+(\omega)$) and occupied part ($A^-(\omega)$) of the spectrum has the form

$$A^+(\omega) = \langle\Psi_0| c\delta\big(\omega - (H - E_0)\big)c^\dagger |\Psi_0\rangle\,, \tag{5.55}$$

$$A^-(\omega) = \langle\Psi_0| c^\dagger\delta\big(\omega - (H - E_0)\big)c |\Psi_0\rangle\,, \tag{5.56}$$

where we shifted the (non-degenerate) ground state $|\Psi_0\rangle$ to zero energy; c and $c^\dagger$ are bosonic/fermionic annihilation and creation operators, respectively.

The Chebyshev expansion converges only in the interval $[-1, 1]$, due to the fact the Chebyshev polynomials $T_n(\omega)$ are unbounded as a function of their order n for all $|\omega| > 1$. To resolve features of $A^+(\omega)$ for $|\omega| > 1$, the function has to be rescaled into $[-1, 1]$. The above mentioned divergence of the expansion makes necessary a rescaling of H

$$H \to \tilde{H} \equiv \frac{H - E_0}{a} \tag{5.57}$$

such that the *single particle excitation energies* $\omega \in [-1, 1]$. Henceforth, we assume that H has been properly rescaled to $\tilde{H}$. Inserting a special representation of the Dirac delta function in terms of Chebyshev polynomials

$$\delta(\omega - \tilde{H}) = \frac{1}{\pi\sqrt{1-\omega^2}}\left(1 + 2\sum_{n=1}^{\infty} T_n(\tilde{H})T_n(\omega)\right) \tag{5.58}$$

into Eq.(5.55), one arrives at

$$A^+(\omega) = \frac{1}{\pi\sqrt{1-\omega^2}}\left(\underbrace{\langle\Psi_0|cc^\dagger|\Psi_0\rangle}_{\mu_0^+} + 2\sum_{n=1}^{\infty}\underbrace{\langle\Psi_0| cT_n(\tilde{H})c^\dagger |\Psi_0\rangle}_{\mu_n^+} T_n(\omega)\right). \tag{5.59}$$

The method amounts to computing the expectation values $\mu_n^+ = \langle\Psi_0| cT_n(\tilde{H})c^\dagger |\Psi_0\rangle$ of the n-th Chebyshev polynomial. For manybody systems, this is of course a highly non-trivial task. The KPM yields moments for $\omega > 0$ and $\omega < 0$ *separately*. The full spectral function $A(\omega) = A^+(\omega) + A^-(-\omega)$ is defined over the full ω range and is obtained by combining μ_n^+ and μ_n^-, using $T_n(\omega) = (-1)^n T_n(-\omega)$:

$$\begin{aligned} A(\omega) &= A^+(\omega) + A^-(-\omega) \\ &= \frac{1}{\pi\sqrt{1-\omega^2}}\left([\mu_0^+ + \mu_0^-] + 2\sum_n [\mu_n^+ + (-1)^n\mu_n^-]T_n(\omega)\right) \\ &= \frac{1}{\pi\sqrt{1-\omega^2}}\left(\mu_0 + 2\sum_n \mu_n T_n(\omega)\right) \end{aligned} \tag{5.60}$$

where $\mu_n \equiv \mu_n^+ + (-1)^n\mu_n^-$. Note that the decay of the positive (negative) moments μ_n^+ (μ_n^-) with n is qualitatively different from that of μ_n: The spectral function $A^+(\omega)$ ($A^-(-\omega)$) has a step at the fermi-energy $\omega = 0$, which corresponds to an *algebraic* decay of μ_n^+ (μ_n^-) [196] of order 1 ($\mu_n^+ \propto \frac{1}{n}$). The added moments μ_n on the other hand

corresponds to a smooth analytic spectral function for which the moments converge much faster (exponentially) to zero [196]. This feature is called spectral convergence and will be of importance later on. Given the moments μ_n, the Greens function in the complex plane $z = x + iy$ is obtained from

$$G(z) = \frac{-i}{\sqrt{1-z^2}} \left(\mu_0 + 2 \sum_{n=1}^{\infty} \mu_n \exp(-in \arccos(z)) \right). \tag{5.61}$$

Steps and sharp features of $A(\omega)$ will quite generally lead to ringing artefacts, known as Gibb's oscillations, due to the neccessarily finite expansion order. One usual remedy is to multiply the moments μ_n by damping factors g_n, e.g. $\hat{\mu}_n = \mu_n g_n$, and using $\hat{\mu}_n$ in (5.60). A common choice is Lorentz damping

$$g_n^L(\lambda) = \frac{\sinh\left(\lambda(1 - \frac{n}{K})\right)}{\sinh(\lambda)}. \tag{5.62}$$

Besides removing unwanted oscillations (depending on λ), this also leads to an unwanted reduction of spectral resolution.

Different damping factors g_m can be obtained by introducing different constraints on the expansion of $A(\omega)$ (like causality, smoothness, and so on), and have been extensively discussed in literature [176]. In the followig we will present a different approach to correct Gibb's oscillations by numerically predicting the decay of the moments μ_m, using the linear prediction algorithm [197, 62].

The close relation between the cosine transform and the Chebyshev expansion is revealed when evaluating the latter on a discrete set of abscissas

$$\omega_k = \cos\left(\frac{\pi(k+1/2)}{M}\right), k \in \{0 \cdots M-1\} \tag{5.63}$$

where M is of the order of the expansion order K [176]. These points are actually the roots of the Chebyshev polynomial $T_M(\omega)$. Inserting Eq.(5.63) into the last line of Eq.(5.60), one immediately obtains

$$A(\omega_k) = \frac{1}{\pi\sqrt{1-\omega_k^2}} \left(\mu_0 + 2 \sum_{n=1}^{K} \mu_n \cos\left(\frac{\pi n(k+1/2)}{M}\right) \right), \tag{5.64}$$

and the Chebyshev expansion assumes the form of a cosine expansion on a non-uniform grid of points.

The computation of $\mu_n^+ = \langle \Psi_0 | \, c T_n(\tilde{H}) c^\dagger \, | \Psi_0 \rangle$ involves the Chebyshev recursion relations

$$\begin{aligned} T_0(\tilde{H}) &= \mathbb{1} \\ T_1(\tilde{H}) &= \tilde{H} \\ T_n(\tilde{H}) &= 2\tilde{H} T_{n-1}(\tilde{H}) - T_{n-2}(\tilde{H}) \end{aligned} \tag{5.65}$$

which directly yield a recursion relation for manybody quantum states

$$\begin{aligned} |t_0\rangle &= c^\dagger \, |\Psi_0\rangle \\ |t_1\rangle &= \tilde{H} \, |t_0\rangle \\ |t_n\rangle &= 2\tilde{H} \, |t_{n-1}\rangle - |t_{n-2}\rangle \\ \mu_m^+ &= \langle t_0 | t_m \rangle \, . \end{aligned} \tag{5.66}$$

The moments for the occupied part of the spectrum (μ^-) can be generated by changing $c^\dagger$ to c in the first line of Eq. (5.66). If $\tilde{H}$ has not been properly rescaled, then this recursion relation will diverge. Using product relations of the Chebyshev polynomials, the moments μ^+_{2n} and μ^+_{2n+1} can be calculated from the states $|t_n\rangle$ and $|t_{n+1}\rangle$ using [176]

$$\begin{aligned} \mu^+_{2n} &= 2\,\langle t_n|t_n\rangle - \mu^+_0 \\ \mu^+_{2n+1} &= 2\,\langle t_{n+1}|t_n\rangle - \mu^+_1. \end{aligned} \tag{5.67}$$

If not stated otherwise, results in this paper were obtained using these reconstructed moments (see appendix). The above procedure requires the ability of applying an operator $\tilde{H}$ to a state $|t_m\rangle$ and computing overlaps of the resulting states with a $|t_0\rangle$. As has been shown by Holzner et al. [59], such a procedure can, with minor modifications, straightforwardly be implemented into an MPS framework. Modifications are necessary due to the approximative nature of MPS algorithms and will be discussed in the follwing. The application of an MPO of bond dimension D to an MPS of bond dimension χ (denoted $|\chi\rangle$ in the following) in general leads to an MPS with increased bond dimension $\chi' = D\chi$. Successive applications like in Eq.(5.66) would thus be infeasible. By a variational compression procedure [9] the bond dimension can be reduced from χ' to χ, with the disadvantage of introducing a systematic error into the the compressed state. This systematic error is quantified by the fidelity $\varepsilon = ||\,|\chi\rangle - |\chi'\rangle\,||/||\,|\chi'\rangle\,||$ which measures the relative distance of the compressed and original state. For many systems, ε can be kept at 10^{-6} and smaller with a relatively small bond dimension χ and for relatively large n [59].
When $\tilde{H}$ has not been rescaled over the *full band width* of H, truncation reintroduces modes at energies > 1, again resulting in a rapidly diverging recurrence. To overcome divergence, an energy-truncation scheme has to be used to project out such high energy modes at the price of introducing further systematic errors. Energy truncation is done similar to a DMRG run by sweeping back and forth through the system and at each site projecting out high energy modes by applying a projection operator. This projection operator is obtained by a Lanzcos tri-diagonalization, which yields a set of approximate eigenenergies and eigenstates $|E_n\rangle, E_n$. The projection operator $\mathcal{P}$ projecting out modes with $E_n > 1$ is given by $\mathcal{P} = \mathbb{1} - \sum_{E_n>1}^{D_{max}} |E_n\rangle\langle E_n|$. D_{max} is the number of steps in the Lanzcos procedure and is typically between 10 and 30. For a detailed study on the effect of the D_{max} on the accuracy of the moments μ_m see [59]. We usually used $D_{max} = 5-30$, depending on the rescale parameter a. If the recurrence relation showed divergence, D_{max} was increased until it became stable. The resulting spectra have then to be analyzed for artefacts due to this truncation. An obvious drawback is that, as opposed to groundstate or compression algorithms, energy truncation is not variational in character, hence no notion of optimality can be associated with it, and convergence of the method is not guaranteed.

Expansion of $exp(-\tau H)$

We saw in Section 5.3.1 that, in order to avoid a divergent recurrence scheme, we need to rescale the entire spectrum of H into the interval $I = [-1, 1]$. However, the unavoidable compression of the Chebyshev-MPS $|t_n\rangle$ during the recurrence scheme reintroduce energies $E > \omega_0$ into $|t_n\rangle$, making an additional non-variational energy truncation step necessary. This energy truncation changes $|t_n\rangle$ and is thus a source of systematic error.

Only if H was rescaled over the (a priori unknown) full spectral width, this energy truncation could be omitted, at the cost of drastically increasing the expansion order needed to obtain a given spectral resolution.

On the other hand, any one-to-one mapping $f(H)$ of the spectrum of H into $[-1, 1]$ is sufficient. A very natural first choice for $f(H)$ would be to employ the exponential function, $f(H) = \exp(-\tau(H - E_0))$, where E_0 is the ground state energy. Since the exponential function is bounded, no energy truncation step is needed. Another advantage of this approach is that one can use a Trotter-decomposition of $\exp(-\tau H)$ for sufficiently small τ, which is a standard tool for solving time dependent many-body systems [11, 10, 51]. For small τ, $\exp(-\tau H) \approx 1 - \tau H$, and thus the spectral resolution is approximately constant.

Using the Trotter-Chebyshev expansion for $\exp(-\tau(H - E_0))$ would have some disadvantages. Then the ground state energy of H would have to be shifted by a small amount $\epsilon > 0$, $H \to H - E_0 + \epsilon$. The reason for this is that otherwise spectral weight at $\exp(0) = 1$ (at the boundary of the convergence interval) would leak off into the divergence region $\omega > 1$ due to numerical errors, resulting in a divergent recurrence. The expansion of $\exp(-\tau H)$ requires that a transformation back to the original scale ω is done on the level of the spectral function by plotting $-\tau\tilde{\omega}A(\tilde{\omega})$ vs. $-\ln(\tilde{\omega})/\tau$, where $\tilde{\omega} \in (0, 1)$. Thus relations like Eq.(5.60) can no longer be used to obtain a smooth expansion over the entire ω interval. Instead, the positive and negative branches of $A(\omega)$ have to be calculated separately and then patched to give the full spectral function. A substantial drawback of this procedure is that the linear prediction of the moments becomes less reliable for the two separate patches since both contain a jump at the fermi energy $\omega = 0$.

Instead, we propose to calculate the Chebyshev moments of $\mathbb{1} - \exp(-\tau H)$. Then the spectral function is smooth over the whole expansion interval. As a result, Eq.(5.60) can be used and the full spectral function can be obtained via moments $\mu_n = \mu_n^+ + (-1)^n \mu_n^-$, by plotting $\tau(1 - \tilde{\omega})A(\tilde{\omega})$ vs. $-\ln(1 - \tilde{\omega})/\tau$. The smoothness of $A(\tilde{\omega})$ leads to substantial increase of convergence rate of the μ_n.

5.3.2 Linear prediction

Steps and sharp features of $A(\omega)$ will quite generally lead to ringing artefacts, known as Gibbs oscillations, due to the necessarily finite expansion order of the moments μ_n. The usual remedy [176] is to multiply μ_n by damping factors g_n, i.e., $\hat{\mu}_n = \mu_n g_n$, and using $\hat{\mu}_n$ instead of μ_n in Eq. (5.60). Different damping factors g_m are related to different constraints on the expansion of $A(\omega)$ (likecausality, smoothness, and so on), and have been extensively discussed in the literature [176]. A common choice [176] is Lorentz damping

$$g_n^L(\gamma) = \frac{\sinh\left(\gamma(1 - \frac{n}{K})\right)}{\sinh(\gamma)}, \tag{5.68}$$

where K is the finite number of Chebyshev polynomials employed, and γ is a parameter.

While removing unwanted Gibbs oscillations to an extent depending on γ, this damping also leads to a reduction of spectral resolution. In the following we will present a different approach to correct Gibbs oscillations by numerically predicting the decay of the moments μ_m, using a linear prediction algorithm [197, 62].

Linear prediction is a simple yet powerful tool to predict the behavior of a time series of data points. Given a *training window* of $2T$ data points $\{x_i\}$, $1 \leq i \leq 2T$ at equidistant times t_i, we make the ansatz that the points $x_n,$, $T < n \leq 2T$ can be approximated by a fixed linear combination of the first T data points:

$$x_n \approx \tilde{x}_n \equiv -\sum_{j=1}^{l} a_j x_{n-j}. \tag{5.69}$$

The fixed coefficients $\{a_j\}$ are obtained ("trained") by minimizing the cost function

$$\mathcal{F} = \sum_{n=T+l}^{2T} w_n |\tilde{x}_n - x_n|^2. \tag{5.70}$$

Here, w_n is a weighting function which we choose to be constant, i.e. $w_n = 1/(2T)$. The minimizing condition $\nabla_{\mathbf{a}^*}\mathcal{F} = 0$ yields a set of linear equations, also known as the normal equations:

$$\begin{aligned} &R\mathbf{a} = -\mathbf{r} \qquad\qquad\qquad\qquad\qquad\qquad\qquad\qquad\qquad\qquad (5.71)\\ &R_{ij} = \sum_{n=T+1}^{2T} w_n x^*_{n-i} x_{n-j}, \qquad\qquad r_i = \sum_{n=T+1}^{2T} w_n x^*_{n-i} x_n, \ , \end{aligned}$$

with $1 \leq i, j \leq T$. The coefficients in $\mathbf{a}$ are obtained by inverting the matrix R, i.e., in vector notation $\mathbf{a} = R^{-1}\mathbf{r}$. For reasons of numerical stability of the algorithm, we use a pseudo-inverse with a cutoff δ instead of the full inverse of R. Once the coefficients a_j have been found, the ansatz Eq. 5.69 is generalized and the data points at $T + k$ ($k > 0$) can be predicted as

$$\tilde{x}_{T+k} = \sum_{n=1}^{T} [M^k]_{1\,n}\, x_{T+1-n}\,, \tag{5.72}$$

where

$$M = \begin{pmatrix} -a_1 & -a_2 & -a_3 & \dots & -a_T \\ 1 & 0 & 0 & \dots & 0 \\ 0 & 1 & 0 & \dots & 0 \\ \vdots & \ddots & \ddots & \ddots & \vdots \\ 0 & 0 & \dots & 1 & 0 \end{pmatrix}.$$

Eq. (5.72) can be reexpressed using a diagonal matrix λ containing the eigenvalues λ_i of M,

$$\begin{aligned} M &= U\lambda U^{-1}, \\ b_n &= \sum_{m=1}^{T} U^{-1}_{n\ m} x_{T-m+1}, \\ \tilde{x}_{T+k} &= [U(\lambda)^k \mathbf{b}]_1. \end{aligned} \tag{5.73}$$

From the last line in Eq. (5.73) it is clear that the sequence of predicted data points will diverge if any $|\lambda_i| > 1$. These divergences can arise due to numerical inaccuracies in the

training moments, or when the spectral function has some weight outside the interval $[-1, 1]$. In such cases these eigenvalues can be either set to zero or, as done in the present paper, renormalized to unity by $\lambda_i \to \lambda_i/|\lambda_i|$. The choice should not matter as long as the corresponding coefficient b_i is small.

Eq. (5.73) also shows that linear prediction is best suited to reproduce time series (which may contain oscillations) with an exponentially decaying envelope. It is therefore advantageous to use prediction on the added moments $\mu = \mu^+ + (-1)^n \mu^-$, which will indeed decay exponentially when $A(\omega)$ has no singularities in the expansion interval [196] (see above), rather than on μ^+ and μ^- separately.

5.3.3 Dynamical Mean Field Theory

Dynamical Mean Field Theory (DMFT) [6] is an approximate method to calculate local Greens functions for interacting lattice models in d dimensions. As the name indicates, it is a mean field theory and as such becomes exact only in the limit of large dimensions $d \to \infty$. The general idea behind dynamical mean field theory is very similar in spirit to its static counterpart [6, 198].

The idea behind static mean field theory [180, 199] is to replace the full, interacting lattice Hamiltonian H with a simpler, non-interacting Hamiltonian $H_{eff}(h_j)$ which depends on a set of parameters h_j. h_j is called a Weiss effective field. The textbook example is the classical Ising model

$$H = -J \sum_{\langle ij \rangle} S_i^z S_j^z. \tag{5.74}$$

A mean field decoupling corresponds to replacing the product $S_i^z S_j^z$ with $\langle S_i^z \rangle S_j^z + S_i^z \langle S_j^z \rangle - \langle S_i^z \rangle \langle S_j^z \rangle$. The Weiss mean field h_j corresponds in this case to the mean magnetic moment $m \equiv \langle S_i^z \rangle$ (we assume tranlational invarianve), and the effective Hamiltonian is

$$H_{MF} = -Jdm \sum_i S_i + \frac{JNm^2 d}{2}. \tag{5.75}$$

m is found from the self-consistency condition

$$m \stackrel{!}{=} \frac{1}{Z} \operatorname{tr}(e^{-\beta H_{MF}} S_i) \tag{5.76}$$

where $Z = \operatorname{tr}(e^{-\beta H_{MF}})$.

In DMFT, the central object is the local lattice Greens function $G(\tau - \tau') \equiv G_{ii}(\tau - \tau')$ (and its Fourier transform $G(\omega)$)

$$G_{ii}(\tau - \tau') = \langle \mathcal{T} c_{i\sigma}(\tau) c_{i\sigma}^\dagger(\tau') \rangle \,. \tag{5.77}$$

of an interacting, d-dimensional lattice model. τ can be either real or imaginary time, the latter being commonly used when working at finite temperature in which case $\omega \to i\omega_n = \frac{2\pi i n}{\beta}$ are the Matsubara frequencies. The fundamental concept of DMFT is to mimick the presence of the interacting lattice gas of electrons on the local lattice Greens function by a suitably chosen bath of *free* electrons. This representation is *exact* [198].

The approximation of DMFT enters by assuming that the lattice self energy is purely $\Sigma(k,\omega) \approx \Sigma(\omega)$ is purely local (k-independent). It can be shown that in the limit $d \to \infty$ this assumption becomes *exact* [6, 198], due to the fact the self energy $\Sigma(k,\omega) \overset{d\to\infty}{\to} \Sigma(\omega)$ becomes purely local (k-independent) in this limit. For finite d, this is an approximation. The problem is thus mapped from a d-dimensional lattice problem to an impurity model. The impurity degrees of freedom are fixed by the consistency with the underlying lattice problem. For a single band Hubbard model for example the impurity is a single orbital (s-type) with the four states $|0\rangle, |\downarrow\rangle, |\uparrow\rangle, |\downarrow\uparrow\rangle$, and the mapped problem is thus a Single Impurity Anderson Model (see also Eq.5.1)

$$H = (\varepsilon_0 - \mu)\sum_\sigma n_{0\sigma} + U n_{0\downarrow} n_{0\uparrow} + \sum_{\nu\sigma} \varepsilon_\nu n_\nu + \sum_{\nu=1,\sigma} (V_\nu c^\dagger_{0\sigma} c_{\nu\sigma} + h.c.). \tag{5.78}$$

The task is to find bath-parameters ε_ν and hybridization V_ν such that the impurity Greens function $G_{imp}(\omega)$, i.e. the local Greens function at the site zero of the impurity model, and the local lattice Greens function $G(\omega)$ of the full original model coincide. In a path integral formalism, by integrating out the bath degrees of freedom, one can derive an effective action for the dynamics of the impurity site in terms of $\Delta(i\omega_n)$ (with ω_n the fermionic Matsubara frequencies) [198]

$$\begin{aligned} S_{eff} = -\int_0^\beta d\tau \int_0^\beta d\tau' \sum_\sigma c^\dagger_{0\sigma}(\tau)\mathcal{G}_0^{-1}(\tau-\tau')c_{0\sigma}(\tau') + U\int_0^\beta d\tau n_\uparrow(\tau) n_\downarrow(\tau) \\ \mathcal{G}_0^{-1}(i\omega_n) = i\omega_n + \mu - \varepsilon_0 - \Delta(i\omega_n). \end{aligned} \tag{5.79}$$

$\mathcal{G}_0$ describes the hopping of the electrons from the bath to the impurity and back. The hybridization function $\Delta(i\omega_n)$ is the dynamic analogon of the static Weiss field h_{eff} in the mean field treatment of the Ising model above, and is explicitly given by

$$\Delta(z) \equiv \sum_k \frac{|V_\nu|^2}{z - \varepsilon_\nu} \tag{5.80}$$

where z is a complex number.

The Weiss field $\Delta(i\omega_n)$ and by that the local lattice Greens function $G^R_{latt}(\omega)$ are found from a self-consistency condition which incorporates the mean field . It can be derived from a variational principle [198, 200] of the grand canonical potential $\hat{\Omega}[\Sigma]$, which can be expressed via the Luttinger-Ward functional $\hat{\phi}[G]$ and its Legendre-transform $\hat{F}[\Sigma]$: $\frac{1}{T}\frac{\delta\hat{\Omega}[G]}{\delta\Sigma}|_{\Sigma=\Sigma_{exact}} = 0$.

However, for our case a more heuristic derivation will suffice. In the following we will now work in real time/frequency space with retarded Greens functions. The retarded, k-dependent lattice Greens function $G^R_{latt}(k,\omega)$ of the full original model is

$$G^R_{latt}(\mathbf{k},\omega) = \frac{1}{\omega + \mu + i\eta - \varepsilon_0 - \epsilon(\mathbf{k}) - \Sigma(\mathbf{k},\omega)} \tag{5.81}$$

where $\Sigma(\mathbf{k},\omega)$ is the lattice self energy and $\varepsilon(\mathbf{k})$ is the dispersion of the underlying lattice model $\varepsilon(\mathbf{k}) = \sum_{i,j} t_{ij} e^{i\mathbf{k}(R_i - R_j)}$. The local lattice Greens function is obtained by summing Eq.5.81 over $\mathbf{k}$

$$G^R_{latt}(\omega) = \sum_{\mathbf{k}} G^R(\mathbf{k},\omega). \tag{5.82}$$

The central approximation of DMFT is then to equate the lattice self-energy to the impurity self energy, i.e.

$$\Sigma(\mathbf{k},\omega) \approx \Sigma_{imp}(\omega). \tag{5.83}$$

The impurity self-energy is given by

$$\Sigma_{imp}(\omega) = [\mathcal{G}_0^R(\omega)]^{-1} - [G_{imp}^R(\omega)]^{-1} = \omega + i\eta + \mu - \varepsilon_0 - \Delta(\omega) - [G_{imp}^R(\omega)]^{-1}. \tag{5.84}$$

Put back into Eq.5.81 and Eq.5.82, at the self consistent point $G_{latt}^R(\omega) = G_{imp}(\omega)$ we obtain

$$\begin{aligned} \sum_{\mathbf{k}} \frac{1}{\Delta(\omega) + [G_{imp}^R(\omega)]^{-1} - \varepsilon(\mathbf{k})} &\stackrel{!}{=} G_{imp}^R(\omega) \\ \int d\varepsilon \frac{\rho_0(\varepsilon)}{\Delta(\omega) + [G_{imp}^R(\omega)]^{-1} - \varepsilon} &\stackrel{!}{=} G_{imp}^R(\omega) \end{aligned} \tag{5.85}$$

where in the second line the sum has been replaced by an integral over energies, weighted by the non-interacting density of states $\rho_0(\varepsilon) = \sum_{\mathbf{k}} \delta(\varepsilon - \varepsilon_{\mathbf{k}})$ of the underlying lattice. Eqs.5.85 are implicit equations for $\Delta(\omega)$, since $G_{imp}^R(\omega)$ depends itself on $\Delta(\omega)$ via the impurity problem. The parameters ε_ν and V_ν are usually found by an iterative procedure. Our task is to find couplings V_ν and single particle energies ε_ν constituting a hybridization function

$$\tilde{\Delta}(\omega) \equiv -\frac{1}{\pi}\Im(\Delta(\omega)) = \sum_\nu |V_\nu|^2 \delta(\omega - \varepsilon_\nu) \tag{5.86}$$

which optimally mimicks the effect of the real, interacting lattice onto the local Hubbard site under consideration. The usual initial guess to start the DMFT iteration is $\tilde{\Delta}(\omega) = \rho_0(\omega)$ where $\rho_0(\omega) = \rho_0^+(\omega) + \rho_0^-(-\omega)$ is the DOS of the underlying lattice one is considering, e.g. a semicircle for the Bethe lattice in $d = \infty$ dimensions. Throughout the calculations, this is a fixed quantity. Upon coupling a local site with energy $\varepsilon_0 - \mu$ (μ is the chemical potential) via (the unknown) V_ν to the (unknown) bath states ε_ν, the free impurity propagator $\mathcal{G}_0^R(\omega)$ assumes the form

$$\begin{aligned} [\mathcal{G}_0^R(w)]^{-1} &= \omega + i\eta + \mu - \varepsilon_0 - \Delta(\omega) \\ \Delta(\omega) = \sum_\nu \frac{|V_\nu|^2}{\omega - \varepsilon_\nu + i\eta} &= \int_{-\infty}^{\infty} \frac{\tilde{\Delta}(\omega')}{\omega - \omega' + i\eta} d\omega', \end{aligned} \tag{5.87}$$

where $\Delta(w)$ is the same quantity as $\Sigma(\omega)$ in section 5.2.1 with a different name (to be consistent with literature). To be able to treat this problem numerically with MPS, we have to map it to a lattice, i.e. we have to find the parameters V_ν and ε_ν belonging to $\tilde{\Delta}(\omega)$. In our case we prefer a mapping to a chain geometry, in which case the parameters are now nearest neighbor hoppings t_i inside the chain and a hopping V from the first site of the bath-chain to the impurity. This mapping is done numerically, and the algorithm is described in detail in [4]. For our simulations we employ a linear discretization scheme. There is a small source of confusion here: In NRG related literature, the hybridization function is usually definded $\Delta_{NRG}(\omega) = \pi \sum_\nu |V_\nu|^2 \delta(\omega - \varepsilon_\nu)$ (see for example the review by Bulla et al. [4]), hence $\Delta_{NRG}(\omega) = \pi\tilde{\Delta}(w)$. The discretization procedure described in

[4] is *exactly* the same for $\Delta_{NRG}(\omega)$ and $\tilde{\Delta}(\omega)$. Only the coupling $V_{NRG} = \sqrt{\xi_0/\pi} \overset{\Delta_{NRG}\to\tilde{\Delta}}{\to} V = \sqrt{\xi_0}$ of the impurity to the first bath site is affected by this rescaling, where

$$\xi_0 = \int_{-D}^{D} \tilde{\Delta}(\omega) d\omega \tag{5.88}$$

and $2D$ is the bandwidth of the bath. After having discretized $\tilde{\Delta}(\omega)$ one solves the interacting impurity system for the impurity spectral function $A_{imp}(\omega)$. In general, the Greens function $G^R_{imp}(\omega)$ is obtained using

$$G^R_{imp}(\omega) = \int_{-\infty}^{\infty} \frac{A_{imp}(\omega')}{\omega - \omega' + i\eta} d\omega'. \tag{5.89}$$

Having started from an initial guess $\tilde{\Delta}_{m=0}(\omega) = \rho_0(\omega)$ (m is an iteration index), Eq.(5.85) is in general not satisfied, but one can now iterate the procedure. At step m we can guess for a new hybridization function $\Delta_{m+1}(\omega)$ from

$$\Delta_{m+1}(\omega) - \Delta_m(\omega) = c([G^R_{imp,m}(\omega)]^{-1} - [G^R_{latt,m}(\omega)]^{-1}) \tag{5.90}$$

where $G^R_{latt,m}(\omega)$ is the lattice Greens function

$$G^R_{latt,m}(\omega) = \int d\varepsilon \frac{\rho_0(\varepsilon)}{\Delta_m(\omega) + [G^R_{imp,m}(\omega)]^{-1} - \varepsilon} \tag{5.91}$$

which at the fixed point would just be the same as the previous one. c is a free parameter chosen for good convergence, often $c = 1$ (close to phase transitions using a smaller c can be advantageous to improve on convergence). Note that only the input $\Delta_m(\omega)$ and the measured $G^R_{imp,m}(w)$ appear in Eq.(5.91); one does not need to calculate self energies. The loop is closed by discretizing $\tilde{\Delta}_{m+1}(\omega) = -\frac{1}{\pi}\Im(\Delta_{m+1}(\omega))$ and using the resulting t_i and V as new input to the impurity solver.

In our case we can directly use the Chebyshev moments to obtain the Greens function:

$$G^R_{imp}(z) = \frac{-i}{\sqrt{1-z^2}} \left(\mu_0 + 2 \sum_{n=1}^{\infty} \mu_n \exp(-in \arccos(z)) \right). \tag{5.92}$$

Hence we can omit the Kramers-Kronig transformation Eq.5.89.

An important testbed for impurity solvers is the so called infinite connectivity Bethe lattice, where the local site has an infinite coordination number. The DOS for the free model is a semicircle with a bandwidth $2D$. D is usually taken as the unit of energy. For this model, the upate is particularly simple, namely

$$\Delta_{m+1} = \frac{D^2}{4} G_{imp,m}(\omega) \tag{5.93}$$

instead of Eqs. 5.90 and 5.91

5.3.4 Benchmark: Resonating Level Model

As a first test for our method, we study the SIAM in the non-interacting limit ($U = 0$), also known as the resonating level model (RLM), which is exactly solvable. Each component of our method can therefore be benchmarked separately and the calculated quantities can be compared to exact results. For $U = 0$ the Hamiltonian in Eq. (5.49) contains only quadratic terms, which makes it diagonal in its single-particle eigenbasis. It is therefore easy to perform the recursion relation in Eq. (5.66) for finite systems of moderate size ($N \sim \mathcal{O}(10^2)$) to generate the exact Chebyshev moments to any order.

Furthermore, for an infinite system, the local Greens function and its spectral function $A(\omega)$ can be computed analytically using an equation of motion approach [180]. For a flat density of states of the bath electrons and a constant hybridization V, the exact result is

$$\begin{aligned} A(\omega) &= -\frac{1}{\pi}\mathrm{Im}\left(\frac{1}{\omega - \epsilon_f + \Delta(\omega)}\right) \\ \Delta(\omega) &= \Gamma\left(i + \frac{1}{\pi}\ln\left(\frac{1-\omega/D}{1+\omega/D}\right)\right) \end{aligned} \tag{5.94}$$

where $\Gamma = \pi V^2 \rho(0)$ and $2D$ is the bandwidth of the bath spectral function[190, 180]. The results for the RLM are obtained with a flat conduction electron band with bandwidth $2D = 2$, $\Gamma = 0.005$, and $\epsilon_f = 0$ (particle-hole symmetric point). The moments of this function can be obtained using numerical integration, and will be referred to as $N = \infty$ results.

Linear prediction

We start by comparing the moments obtained by linear prediction with exact moments. In Fig. 5.10(a), 200 moments to the left of the solid, black line were calculated directly from Eq. (5.66), for a $N = 100$ chain. The linear prediction algorithm was trained by predicting the 100 moments between the dashed and the solid line. Subsequently, we predicted 10000 moments. We note that the exact high order moments for the finite $N = 100$ chain would contain drastic finite size effects (essentially from boundary reflections of the signal generated by applying $c^\dagger$). We therefore compare the predicted moments to the exact $N = \infty$ ones. Fig. 5.10(a) shows that the predicted moments are very close to the exact ones, demonstrating the ability of the method to produce accurate results for Chebyshev moments. For the case $\epsilon_f \neq 0$ (not shown), where the decay of the moments is superimposed on oscillations, we get similar accuracy.

Fig. 5.10(b) shows the corresponding spectra. It should be noted that with increasing expansion order K, i.e, including more Chebyshev moments, the energy resolution of the KPM approximation improves like $1/K$. Linear prediction vastly increases the achievable resolution and also removes spurious oscillations that would result from a hard cutoff of the KPM approximation.

MPS-computed moments

We now turn to the MPS-computation of the Chebyshev moments [59]. The RLM is a non-trivial problem to MPS algorithms, even though it is exactly solvable, because of

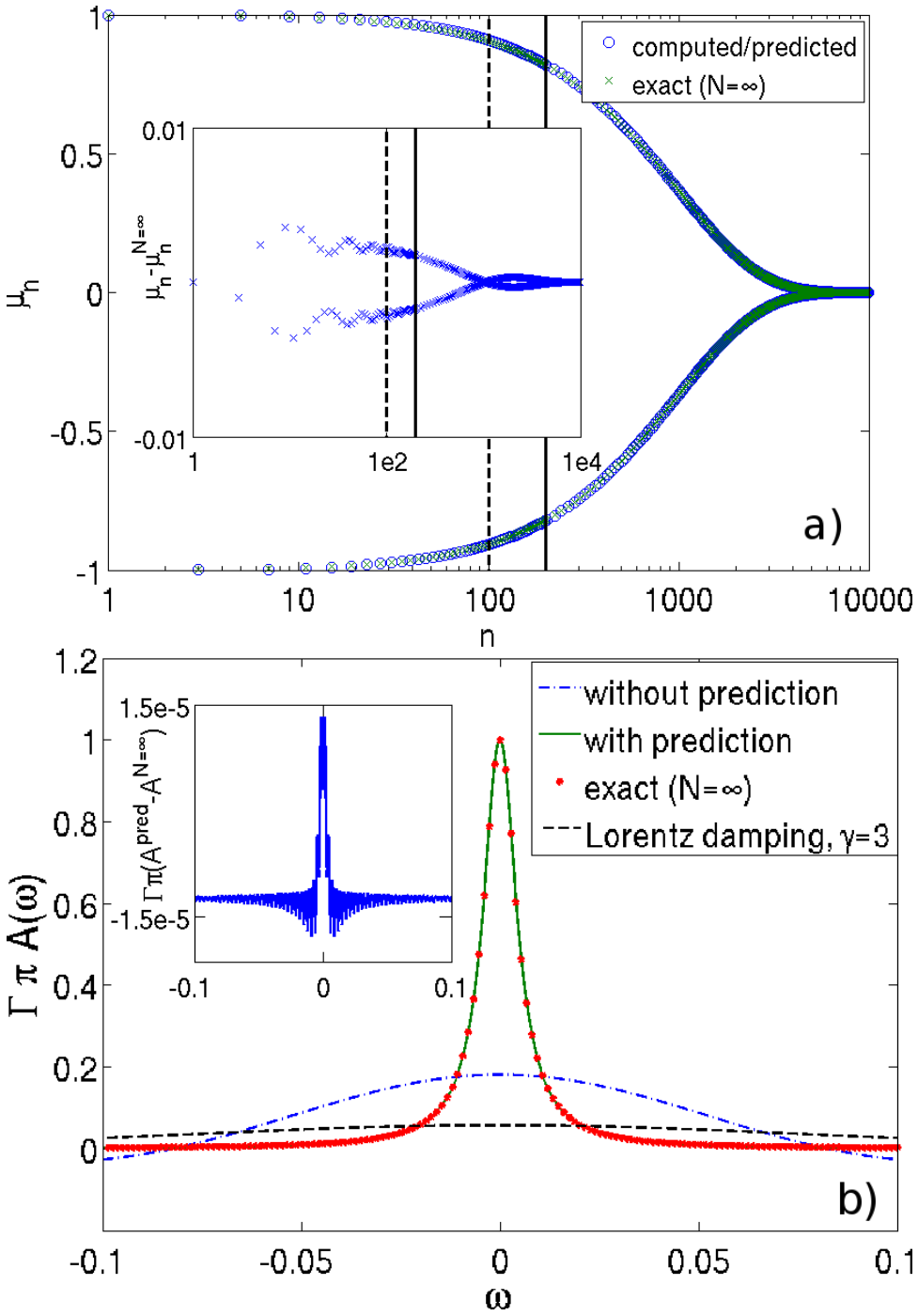

Figure 5.10: (a) Linear prediction using *exact* Chebyshev moments of an $N = 100$ site RLM chain (circles), compared to exact $N = \infty$ moments (crosses). Only even moments are plotted. The prediction was trained on the 100 moments between the two vertical bars. For better visibility, only every 20th moment is plotted at $n > 200$ (note logarithmic scale). The inset shows the difference of the computed/predicted $N = 100$ moments from the exact $N = \infty$ results. (Parameters: $\Lambda = 1.05$, $\Gamma = 0.005$, $\epsilon_f = 0$, $\delta = 10^{-5}$). (b) Spectral function without (dash-dotted blue line) and with (solid green line) linear prediction. The dashed black line shows results obtained with Lorentz damping. The red dots represent the exact $N = \infty$ result (Eq. (5.94), which is very close to the results with linear prediction. The difference is shown in the inset.

non-trivial entanglement between the orbitals of the chain (see Appendix C). Finite entanglement gives rise to compression errors at finite matrix dimension, and also to energy truncation errors (Sec. **??**). These errors can be estimated at each step in the iterative procedure, but to evaluate the overall error, including the effect of error cancellation, one needs the exact Chebyshev moments to compare with. Fig. 5.11(a) shows a comparison of the MPS-computed moments with exact ones ($N = \infty$) for an MPS matrix-dimension of $\chi = 250$, with a rescaling of $a = 5$ and $D_{max} = 20$. The upper inset shows the difference between the exact and MPS-computed moments and the growth of the truncated weight, respectively. For the non-interacting RLM, the MPS method does in fact yield quasi-exact results. The lower panel shows the truncated weight for the first 200 moments.

We then apply the linear prediction to the first 200 MPS-computed moments, and compare the resulting spectrum to the exact result given by Eq. (5.94), shown in Fig. 5.11(b). As in Fig. 5.10(b), with the training moments alone it is not possible to properly resolve the sharp resonance at the Fermi energy. The results are on top of each other, demonstrating that linear prediction based on the MPS-calculation of 200 moments essentially gives exact results for the RLM.

5.3.5 Interacting SIAM

We now turn to the case of finite interaction strength $U > 0$, which renders the solution of Eq. (5.49) a highly non-trivial task. This situation is interesting both from a physical point of view and as a numerically demanding benchmark for our method. The calculations in this section are performed for a semicircular bath DOS with bandwidth $2D \equiv 2$, $\Gamma = 0.5$, and $\epsilon_f = -U/2$ (particle-hole symmetric point) in the regime $U > D$. As a consequence of the large U, there is no conduction electron bath at the energy scale of the Hubbard bands, which results in extremely sharp Hubbard bands. A linear energy discretization corresponding to $N = 120$ sites [4] is used in the calculations throughout this section, unless otherwise stated, to properly resolve all the spectral features. The MPS calculations were performed with $a = 12$, $\chi = 200$, $D_{max} = 25$, and $E_{sweeps} = 5$. For prediction, we used a cutoff $\delta = 10^{-7}$.

MPS-computed moments

In Fig. 5.12 we plot the Chebyshev moments μ_n as obtained from MPS calculations for different values of the interaction strength $U/\Gamma = 2, 4, 6, 8$. For small $U/\Gamma \leq 4$, the moments decay to zero quickly, which indicates a rather featureless spectral function. In such cases, the moments obtained from the MPS calculations already produce a good resolution. For $U/\Gamma > 4$ on the other hand, there is a slower decay, related to the emergence of sharp features in the spectral function [201] (see below); hence the linear prediction can significantly improve the energy resolution for the impurity spectral function. For large values of U/Γ, the ground state of the system exhibits strong spin-fluctuations along the chain, resulting in a strong growth of the site-entanglement (see appendix). **??**). In contrast to the non-interacting limit and to the model studied in Ref.[59], for the SIAM this entanglement can give rise to serious truncation errors.

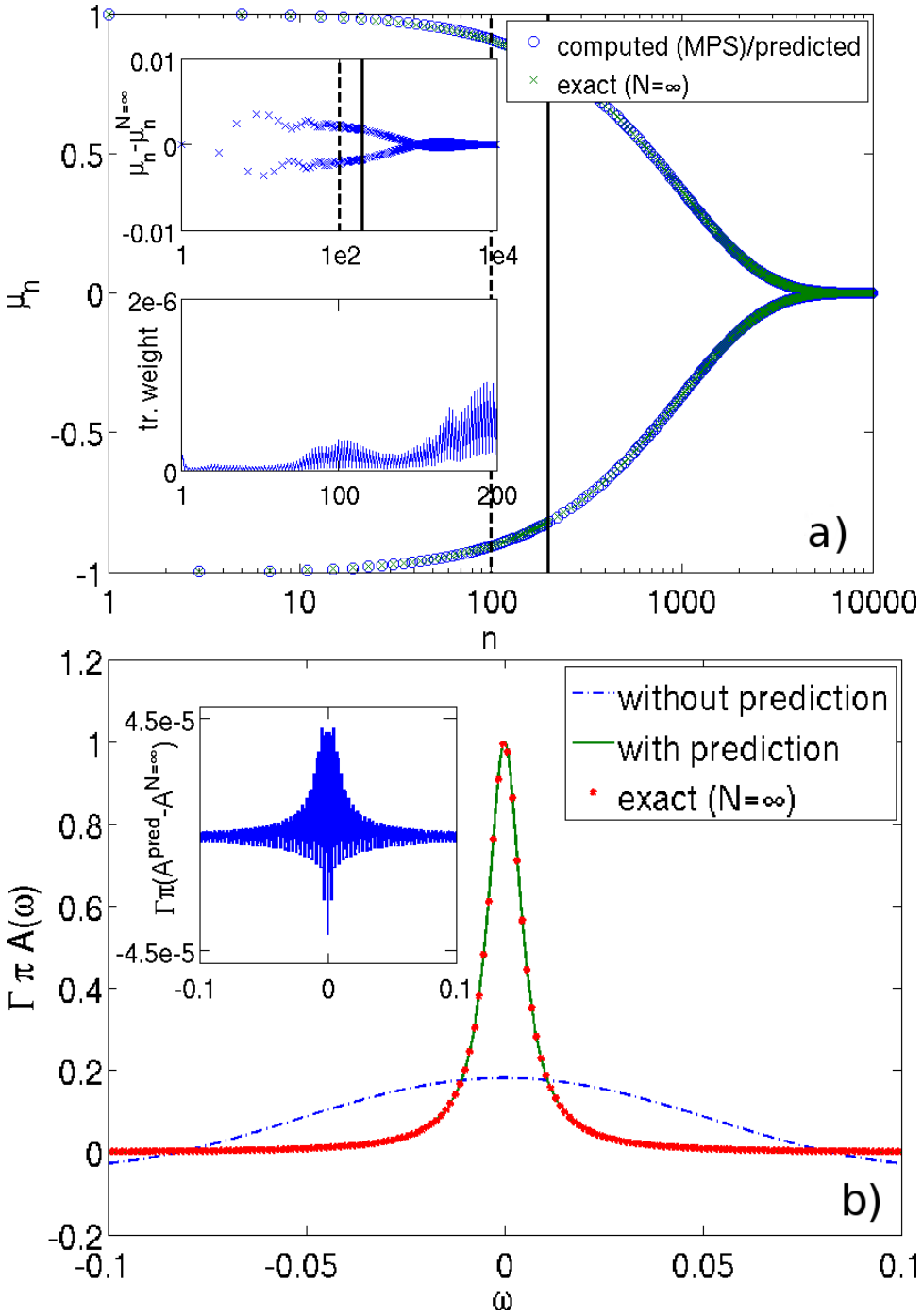

Figure 5.11: Same as Fig. 5.10, but with *MPS computed* Chebyshev moments. (Matrix dimension $\chi = 250$, rescaling $a = 5$, $D_{max} = 20$, $E_{sweep} = 5$) Lower inset in (a): truncated weight of the first 200 MPS-computed moments.

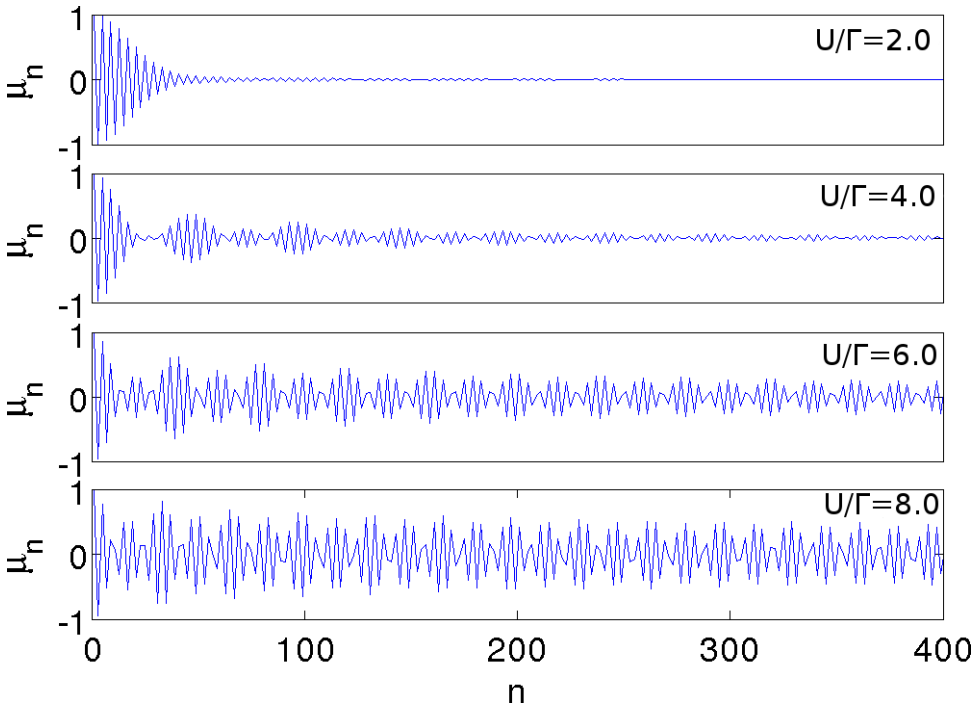

Figure 5.12: MPS-computed Chebyshev moments of the SIAM for $U/\Gamma = 2, 4, 6, 8$. At large U/Γ, the moments show a much slower decay to zero.

Linear prediction

While the training moments obtained from the MPS-calculation of the non-interacting RLM in section 5.3.4 were almost exact, the rapid growth of the truncation errors in the interacting case makes the accurate calculation of high-order moments more difficult and the linear prediction even more important. One also needs to consider the effect of the truncation errors on the moments within the training window of the linear prediction. That is, the information gained by adding an additional training moment is offset eventually by its numerical error which is passed to the linear prediction. When the truncation errors are small, a large training window can employed with excellent result. In Fig. 5.13(a), we compare MPS computed Chebyshev moments (blue line) with the ones obtained by linear prediction (red circles), where we used the first 200 moments (black solid line) to train prediction. Fig. 5.13(b) then shows the spectral function obtained with linear prediction trained on all 400 moments. For comparison, we show the spectrum obtained by using Lorentz damping Eq. (5.62) on the original 400 MPS-computed moments, with damping parameter $\gamma = 3.5$ just high enough to remove all oscillations. The figure clearly demonstrates the increase in spectral resolution achieved by linear prediction.

Comparison with Correction Vector Method (DDMRG)

The correction vector (CV) method [7] and its variational formulation, the DDMRG [8], are considered the methods of choice for high precision calculations of dynamical spectral functions of 1-d quantum system. Their results are assumed to be quasi-exact in many cases. Drawbacks of CV (DDMRG) are an ill-condition matrix inversion which has to

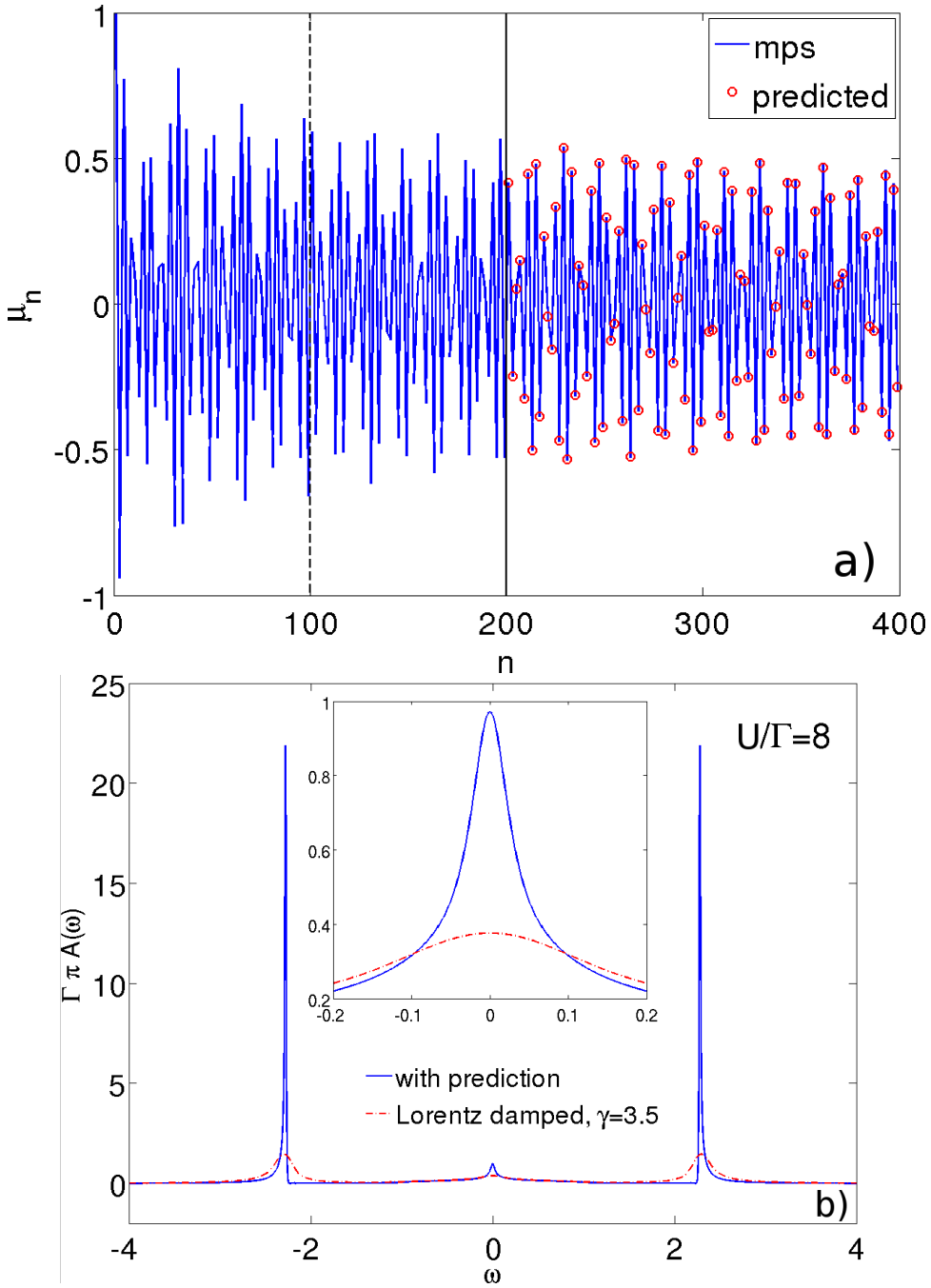

Figure 5.13: (a) Linear prediction using MPS computed Chebyshev moments for the SIAM at $U/\Gamma = 8$, $\Gamma = 0.5$. Moments to the left of the black dashed line were taken as input data; moments between the dashed and the solid line were used as training-data for the linear prediction algorithm. Only the even moments are plotted. $(\delta = 10^{-6}, \chi = 200, N = 120, a = 12, D_{max=25}, E_{sweeps} = 5, n_{comp} = 3)$. (b) The spectral function (blue line) corresponding to 16400 linearly predicted moments generated from all 400 MPS-computed moments shown in (a). This is compared to a Lorentz dampened spectrum using $\gamma = 3.5$ and the 400 MPS moments (red dashed line).

be regularized by a finite (large) broadening of the spectral function, and the need for a separate expensive calculation to be done at each frequency ω. As proof of principle, we benchmark our method against results of the CV (DDMRG) [201] in Fig. 5.14, for $U/\Gamma \in \{2, 4, 6, 8\}$. Results at $U/\Gamma = 8$ are the same as in Fig. 5.13(b).

We observe the development of sharp side peaks (Hubbard satellites) upon increasing U/Γ . The inset of Fig. 5.14 shows a zoom onto the zero-frequency region, where with increasing U a narrowing of the zero-frequency peak at $U/\Gamma = 2$ into a sharp (Kondo) resonance is observed. The agreement with the CV (DDMRG) data [201] for $U/\Gamma = 2, 4$ is excellent. For larger $U/\Gamma = 6, 8$, we observe deviations in the heights of (i) the Hubbard peaks and of (ii) the Kondo resonance. For the latter, the pinning cr¡iterion $\Gamma\pi A(0) = 1$ [181] is satisfied to a higher accuracy using Chebyshev expansion with linear prediction than using a maximum entropy deconvolution of the CV raw data.

Expansion of $\mathbb{1} - e^{-\tau H}$

From the previous discussion, the drawback of the energy truncation scheme [59] is the introduction of a systematic error which depends quite strongly on the choice of auxiliary parameters a, D_{max} and E_{sweeps}. In the this section, we present results for the alternate scheme introduced in section 5.3.1 which employs the expansion of $\mathbb{1} - e^{-\tau H}$. In Fig. 5.15 we compare initial results for $\tau = 0.01$ and a first order Trotter expansion of exp(-τH) against the same DDMRG data as in Fig. 5.14. The results are virtually indistinguishable from those of Fig. 5.14 (except for a very slight difference in the height of the Hubbard peaks), thus validating our new approach. When a second order Trotter decomposition is employed, τ can be increased substantially, and the required numerical effort should become comparable to that of the energy truncation scheme.

Results for logarithmic discretization

In the following we present results for a flat conduction band

$$\rho(\omega) = \begin{cases} 1/(2D), & \omega \in [-D, D] \\ 0 & \text{else} \end{cases} \tag{5.95}$$

using a logarithmic discretization $x_n = \Lambda^{-n}$ for $D = 1$ and a hybridization strength $\Gamma = 0.05$. Fig.5.16 shows the impurity spectral functions for $U/\Gamma = 2, 6, 10, 14$ using a discretization parameter $\Lambda = 1.05$ and a chainlength of $N = 100$ sites. Starting from $U = 0.2$, one observes narrowing of the central conduction peak, accompanied by formation of Hubbard satellites at $\omega \approx U/2$. Please note the different parameter regime as compared to Fig.5.14, where the Hubbard satellites lie well outside the bandwidth of the bath. Now, $U < D$, yielding much broader Hubbard satellites . The inset shows a zoom onto the low-frequency region. Besides the exponential narrowing of the Abrikosov-Suhl resonace, we observe that with increasing U, the pinning criterion is no more obeyed. This is not unexpected, since lifetime of the quasiparticle scales inversely with the resonance width, leading to an exponential increase in the expansion order needed to resolve this resonance. Using prediction increases the achievable resolution, but results of course also depend on the size of the training set. If this set is too small, so that signatures of the resonance are not strong enough to be picked up properly by prediction, it is not fully

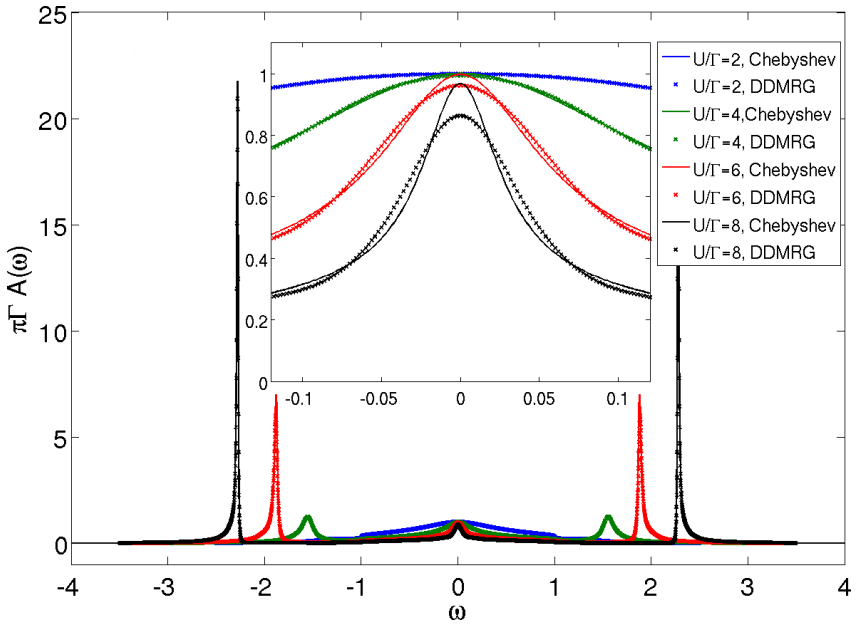

Figure 5.14: Impurity spectral function of the SIAM for different values of the interaction U, $\Gamma = 0.5$. Solid lines: Chebyshev KPM with 400 MPS-computed moments and 16400 further moments from the linear prediction. Symbols: DDMRG results for comparison Inset: magnified region at small frequencies. The vertical order of lines is the same as in the key.

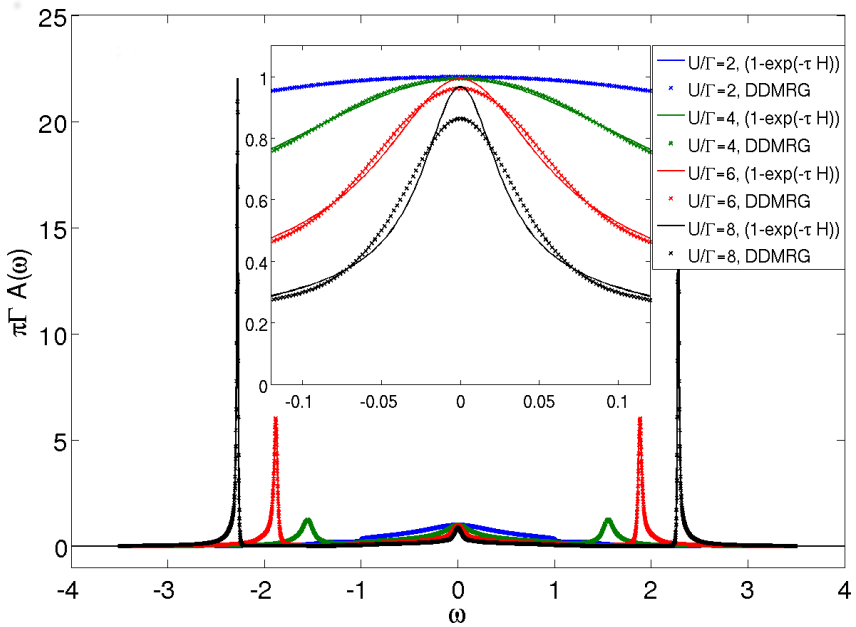

Figure 5.15: Impurity spectral function of the SIAM using a Chebyshev expansion of $\mathbb{1} - \exp(\text{-}\tau H)$ instead of H with a first order Suzuki-Trotter decoupling at $\tau = 0.01, \chi = 300$. U, Γ as in the Fig. 5.14. We used 1000 ($U/\Gamma = 2, 4$), 1200 ($U/\Gamma = 6$) and 1500 ($U/\Gamma = 8$) moments to train the linear prediction ($\delta = 10^{-6}$), and predicted 20000 ($U/\Gamma = 2$), 80000 ($U/\Gamma = 4, 6$) and 120000 ($U/\Gamma = 8$) further moments. *Inset:* Zoom into the zero frequency region of the corresponding main panel.

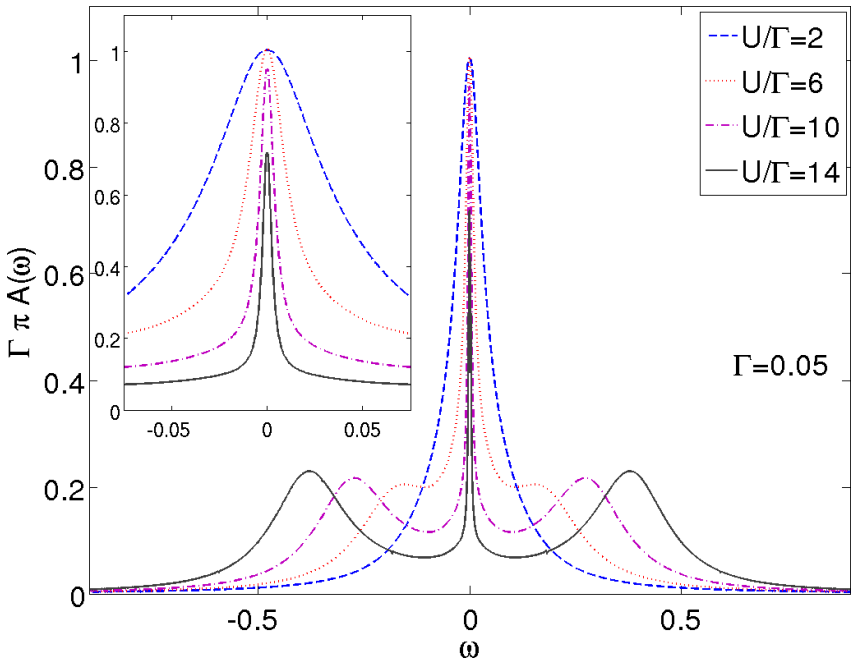

Figure 5.16: *Upper:*Spectral function of the SIAM for different values of interaction parameter $U/\Gamma, \Gamma = 0.05$ at the particle hole symmetric point with flat bath DOS Eq.(5.95) with $D = 1$, obtained from a Chebyshev expansion of H followed by linear prediction for the moments. The rescaling parameter $a = 5$ in all figures, N=100, $\Lambda = 1.05, D_{max} = 30, \chi = 180, E_{sweeps} = 5$. In the central region, one observes an increasing narrowing of the zero-frequency peak which results in the Kondo-resonance. Also clearly visible are the outer Hubbard satellites with peak position at $\approx U/2$. The inset shows a zoom onto the zero frequency region.

resolved by the method. Indeed, the height at $\omega = 0$ is sensitive to parameters like the size of the training window and the cutoff δ for inversion. In some cases, it can vary by 20-30%. We also note that the exact form of the resonance crucially depends on the discretization of the band around $\omega = 0$. If the discretization is too crude, we in general observe an underestimation if the height of the resonance. At $U/\Gamma = 14$, the height is only $\approx 70\%$ of the exact value.

The Hubbard peaks, on the other hand, are not sensitive at all. Importantly, while the precise height at $\omega = 0$ can be sensitive to parameters of the calculation, we observe that the weight of the resonance, i.e. the integral over the resonance peak, is very stable.

One great advantage of MPS-based variational methods over NRG is the freedom of choice of discretization grid. Whereas a logarithmic discretization with rather large $\Lambda \approx 1.5 - 2$ lies at the heart of the success of NRG, MPS-based methods like the one presented here can use *any* discretization grid. Together with the possibility of solving multi-impurity systems without exponential increase in computational complexity, this makes MPS-based methods promising candidates for low T, high resolution impurity solvers for DMFT.

5.3.6 Results for Dynamical Mean Field Theory

Fig.5.17 shows results for different interactions U, at a halfbandwidth $D = 0.25$. For $U/D = 1, 2$, results were obtained for a chainlength of $N = 120$ sites, and a linear discretization of the bath-DOS. For $U/D = 2.5$, we applied a $1-\tanh(n/\tau)$-like discretization increasing number of discretization points around $\omega = 0$ and a linear discretization for large ω (see green crosses in Fig.5.17c). With increasing interaction, we observe a narrowing of the quasiparticle peak at $\omega = 0$, and formation of Hubbard satellites at $\omega \approx u/2$ [202, 203, 190, 204, 205, 206]. At the inner edge, the satellites develop additional structure which has also been observed in earlier works [190, 202, 203, 205].

Entanglement and truncated weight growth

Time scales for MPS simulations are usually limited by growth of site-entanglement between the separate parts of the quantum system. One (non-unique) way of quantifying site-entanglement is the bipartite entanglement entropy $S_{vN} = -\mathrm{tr}_B\left(\rho_B \log \rho_B\right)$ [28], with $\rho_B = \mathrm{tr}_A \rho_{AB}$. ρ_{AB} is the full density matrix of a bipartite quantum system A, B, and tr_A denotes partial trace over all degrees of freedom in part A of the system. Using MPS with a fixed bond-dimension amounts to essentially introducing an upper bound to S_{vN}. The error of this approximation can be quantified by the truncated weight

$$\epsilon_{tw} = 1 - \sum_{i=1}^{\chi} \lambda_i^2 \,, \tag{5.96}$$

where λ_i denote the Schmidt-coefficients [27] belonging to the bipartition $A : B$ (e.g. the simultanious eigenvalues of ρ_A and ρ_B), and χ is the matrix dimension of the MPS-matrices. In our simulations we observed a strong increase of truncated weight which limits the number of computable moments. In Fig. 5.18, we plot the entanglement entropy for the states $|t_n\rangle$ obtained during the Chebyshev expansion of the positive up-spin part of the spectral-function of the SIAM (i.e. $|t_0\rangle = c_\uparrow^\dagger |\Psi_0\rangle$). The left panel shows results for $U = 0, \Gamma = 0.05$ and a semicircular bath DOS with $D = 1$ discretized into N= 120 sites (impurity included). Due to the unfolding, the left side of the plot represents the up spins and the right side the down spins. The added up-spin particle thus travels along the chain and locally increases entanglement around its position. However, after the particle has passed a certain bond, entropy again decreases. Importantly, the signal travels *only in the up-spin branch*, due to the missing entanglement between up- and down spins in the initial ground state $|\Psi_0\rangle$. The truncated weight for this simulation never exceeded 1e-6.

The right panel in Fig. 5.18 shows the same plot for finite $U = 0.5$. Again, we observe a propagating signal, but this time it spreads in both directions, e.g. in the up *and* down spin channel. Furthermore, after passage of the signal at a certain bond, entropy increases and remains at this higher value. Both effects are due to presence of strong correlations in the initial state. Oscillations on top of the signal are due to change in norm of $|t_n\rangle$ during simulation. For $n > 300$ the truncated weight already exceeds a value of 1e-3, and simulation results for $n > 300$ should be considered as unreliable.

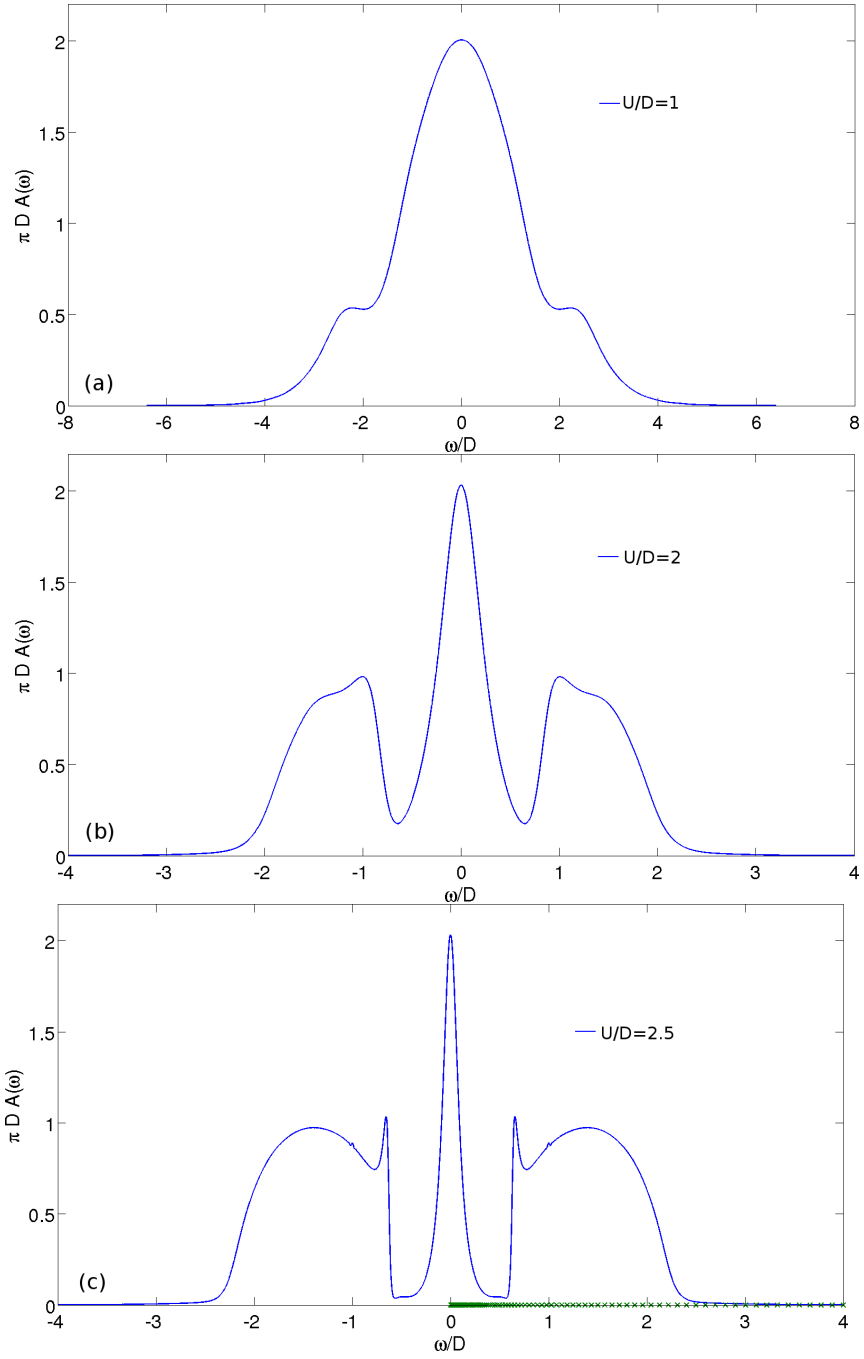

Figure 5.17: Local spectral function of the Hubbard model on the infinite-connectivity Bethe lattice, for different interactions U. With increasing U, formation of Hubbard satellites can be observed. Close to the transition, the Hubbard bands develop additional structure at the inner edges.

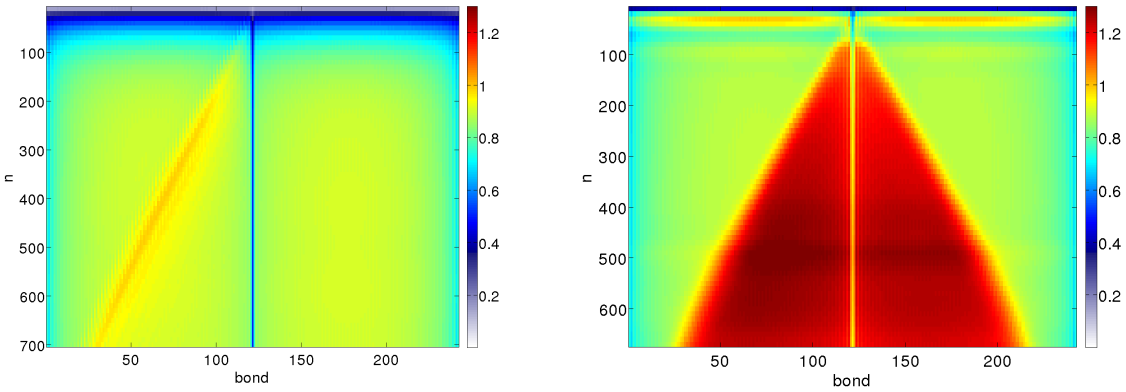

Figure 5.18: Bipartite entanglement at different bonds (x-axis) of the state $|t_n\rangle$ (y-axis) obtained during calculation of the Chebyshev moments for the up-spin, particle branch of the impurity spectral function of the SIAM (e.g. $|t_0\rangle = c_\uparrow^\dagger |\Psi_0\rangle$). Left panel: RLM ($U = 0$); right panel: SIAM for $U = 0.5$. In both plots, $\Gamma = 0.05$, $N = 120, \chi = 300, D_{max} = 5$. (semicircular bath DOS with $D = 1$ and mixed log-linear discretization

5.3.7 Conclusions

We propose two extension of a recently developed matrix product state based method for expanding spectral functions in Chebyshev polynomials [59]. For the usual expansion scheme for Hamiltonians H [59], we use the linear prediction algorithm to extrapolate moments up to high orders, hence significantly improving achievable resolution at practically no cost. This is especially interesting in systems where strong growth of entanglement entropy prevents one from iterating the recursion to high orders, due to increasing truncation effects. We benchmark the method with the exactly solvable resonating level model, where we obtain highly accurate results. We also investigate the Single Impurity Anderson Model and obtain results which compare very well with spectra obtained from the Correction Vector Method [201, 207], albeit at significantly reduced cost. We further apply the method as a high resolution impurity solver within the Dynamical Mean Field Theory [6]. This is in particular interesting since the method works at $T = 0$ temperature and on the real frequency axis. Results confirm the existence of pronounced peaks at the inner edges of the Hubbard bands in the metallic phase of the Hubbard model on the infinte connectivity Bethe lattice. As a second extension, we propose a modified rescaling scheme which employs a Chebyshev expansion of $\exp(-\tau H)$ and $\mathbb{1} - \exp(-\tau H)$, for both of which the energy truncation step [59] can be *completely omitted*, at a comparable spectral resolution. The implementation of the scheme is very similar to standard time evolution algorithm like TEBD [11, 10, 51, 50]. Both methods are promising candidates for high resoluion, low T impurity solvers for DMFT, and extension to multiorbital systems poses no inherent problems (as compared to NRG). One further advantage of the full MPS implementation over the usual Correction Vector Method is the disentangling of groundstate calculation and excited-state-targeting, which might be especially important for multiorbital impurity solvers. An important project for future work would be the incorporation of non-abelian conservation laws like SU(2). Especially for strong interactions $U/\Gamma \geq 20$, this could lead to major improvements in the spectral resolution

due to higher number of computable moments. This is especially relevant for DMFT applications close the phase transitions.

5.4 Current Voltage characteristics of the Single Impurity Anderson Model

Parts of the content of the following chapter have been published in Ref.[208]. Results in the paper were obtained with the Time Evolving Block Decimation algorithm written by the author. Runs were performed by M. Nuss, in collaboration with the author (Martin Ganahl) Hans Gerd Evertz, Enrico Arrigoni and Wolfgang von der Linden. All authors participated in the analysis of the results. The draft for the publication was written by M. Nuss and edited by all authors. The text of the following chapter is written by the the author of the thesis. Figure captions are taken from the publication Ref.[208].

5.4.1 General remarks

Non equilibrium physics of quantum systems has been attracting increasing attention over the past 15 years. This trend is nourished by an increase in experimental control of ultra-cold atoms in optical lattices [74, 73, 122, 120, 16, 119, 128] as well as development of efficient techniques for simulating dynamics of many body quantum system [54, 51, 11, 10, 50, 209, 210, 211, 212, 213]. The question of how many-body interactions influence the dynamics of such quantum system is one of the most challenging problems of today's condensed matter physics. Regarding the ever decreasing size of electronic devices, investigations of charge transport over nano systems is an important and interesting area of research in its own sake. In the following we will investigate the non-equilibrium properties and current-voltage characteristics of a quantum dot with many-body interactions, modeled by a Single Impurity Anderson Model [175]. In the previous chapter we have already discussed the basic physics of this model in equilibrium, which after 50 years of research is nowadays very well understood. On the other hand, the non-equilibrium properties of impurity models are the subject of intense theoretical investigation [214, 215, 216, 217, 218, 219, 220, 221]. The goal of the following work is to obtain quasi steady state currents by evolving different types of initial states into a quasi steady state by use of the Time Evolving Block Decimation (TEBD) [10]. The term "quasi" serves as a reminder that true steady states can only occur in infinite systems. For our simulations, we use a system comprised of two non-interacting tight binding leads and a single Hubbard-like impurity. The leads and the impurity are arranged in a chain geometry, with the impurity in the middle (see Fig. 5.19). The total chain length is L sites. The initial states are obtained using the Density Matrix Renormalization Group (DMRG) [5] algorithm.

5.4.2 Preparation of initial states

In the following we will investigate the current voltage characteristics of a single quantum dot of Hubbard type which is coupled to two non-interacting leads. The leads will serve as electron reservoirs, similar to the classical case. A bias voltage is modeled by setting

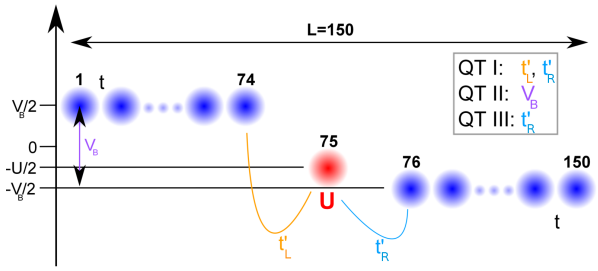

Figure 5.19: Illustration of the three quenches performed for the SIAM: i) QT I: switching on both quantum dot-reservoir tunnelings t'_L and t'_R, ii) QT II: switching the bias voltage V_B and iii) QT III: switching on the dot-lead tunneling t'_R to one lead.

the two leads to two different chemical potentials. The Hamiltonian for such a system is given by (compare with Eq.5.1)

$$H = H_{\text{dot}} + H_{\text{res}} + H_{\text{coup}} \tag{5.97a}$$

$$H_{\text{dot}} = \varepsilon_f \sum_{\sigma} f^\dagger_\sigma f_\sigma + U\, \hat{n}^f_\uparrow \hat{n}^f_\downarrow \tag{5.97b}$$

$$H_{\text{res}} = \sum_{\alpha,\sigma} \left(\varepsilon_\alpha \sum_{i=0}^{L_\alpha - 1} c^\dagger_{i\alpha\sigma} c_{i\alpha\sigma} - t \sum_{\langle i,j \rangle} c^\dagger_{i\alpha\sigma} c_{j\alpha\sigma} \right) \tag{5.97c}$$

$$H_{\text{coup}} = -\sum_{\alpha} t'_\alpha \sum_{\sigma} \left(c^\dagger_{0\alpha\sigma} f_\sigma + f^\dagger_\sigma c_{0\alpha\sigma} \right) , \tag{5.97d}$$

(see Fig. 5.19) where U and ε_f is the interaction strength and on-site chemical potential of the quantum dot, $t'_\alpha, \alpha \in \{\text{L}, \text{R}\}$ is the coupling strength between the quantum dot and the left and right lead. $f^\dagger(f)$ are electron creation (annihilation) operators on the dot. Lead α has intra lead hopping t and on-site chemical potential ε_α. We work at particle-hole symmetry, i.e. at half filling and $\varepsilon_f = -\frac{U}{2}$. We set $t = 1$ and use symmetric couplings $t'_L = t'_R = 0.3162\, t$ (Eq. (5.97d)) for all simulations. This yields a bandwidth of $D = 4\, t$ of the leads and a hybridization strength [181] of $\Delta \equiv \pi\, t'^2_\alpha\, \rho_{\text{reservoir}}(\mu) = \frac{t'^2_\alpha}{t} \approx 0.1\, t$, where the reservoir DOS at the chemical potential is denoted by $\rho_{\text{reservoir}}(\mu)$. Energies are measured in units of Δ ($\hbar, k_B$ and $e = 1$), and we work at temperature $T = 0$. To avoid confusion, we denote real time by τ.

The steady state current corresponding to a bias voltage V_B [222] is obtained using real time evolution with TEBD, with a second order Suzuki-Trotter decomposition ($\delta t = 0.05 t^{-1}$), and matrix dimension of $\chi = 2000$. To this end, we prepare the system in a certain initial state $|\Psi_0\rangle$ and then quench the Hamiltonian parameters to induce the dynamics (see below for details): $\hat{\mathcal{H}}(\mathsf{x}_0) \to \hat{\mathcal{H}}(\mathsf{x})$, with $\mathsf{x}_0 = \{U, t, t'_{p\alpha}, \varepsilon_\alpha\}$. $|\Psi_0\rangle$ is chosen to be the ground state of the initial Hamiltonian $\hat{\mathcal{H}}(\mathsf{x}_0)$ at half filling with total spin-z $S^z = 0$. We investigate three different types of quenches (see Fig. 5.19), to be described below. Note that in each case we have finite filling in *both leads*.

We choose a system of $L = 150$ sites with the quantum dot located at site 75. The bias voltage V_B is applied by setting the on-site energies of the leads to $\varepsilon_L = -\varepsilon_R = \frac{V_B}{2}$. For all quenches, the final parameters are $\mathsf{x} = \{U, t = 1, t'_\alpha = 0.3162\, t, \varepsilon_L = \frac{V_B}{2}, \varepsilon_R = -\frac{V_B}{2}\}$,

with variable U. The initial setup is quench type (QT)-dependent (see Fig. 5.19). In the following, we discuss the three different types of quenches.

QT I: Hybridization quench to both leads $t'_\alpha = 0 \to 0.3162\,t$

For $\tau < 0$ we take $\mathsf{x}_0 = \{U, t, t'_\alpha = 0, \varepsilon_\alpha = \pm V_B/2\}$, i.e. no quantum dot-to-leads coupling. We prepare the ground state of $\hat{\mathcal{H}}(\mathsf{x}_0)$ at half-filling in the left and right lead and a single up-electron on the quantum dot. At $\tau = 0$ the tunneling t'_α is quenched to its finite value and a bias voltage is applied. Note that due to the splitting into three disconnected parts ($t'_\alpha = 0$) of length $N_L = 74, N_M = 1, N_R = 75$ (left, middle right), S^z is not zero on the quantum dot and on the right lead initially.

QT II: Quenching the bias voltage $\varepsilon_\alpha = 0 \to \pm V_B/2$

At $\tau < 0$, $\mathsf{x}_0 = \{U, t, t'_\alpha = 0.3261\,t, \varepsilon_\alpha = 0\}$. The system is prepared in the ground state $|\Psi_0\rangle$ at half filling with overall $S^z = 0$ zero. At $\tau = 0$ the bias voltage is quenched to its desired value. As compared to QT I, this setup has the advantage that no subsystems with finite values of S^z exist in the ground state. Furthermore, correlations between the three regions are already present in the ground state. Note that the initial state is much more complicated than for QT I. This type of quench has also been used by the authors of [218].

QT III: Quenching the hybridization $t'_R = 0 \to 0.3162\,t$ to the right lead

The initial parameters are chosen $\mathsf{x}_0 = \{U, t, t'_L = 0.3261\,t, t'_R = 0, \varepsilon_\alpha = \pm V_B/2\}$, and the system is again solved for the ground state $|\Psi_0\rangle$ at half filling, with each of the two separate chains at half filling, but with an additional $S_z = 1/2$ spin in the left lead. At $\tau = 0$, we quench $t'_R = 0 \to 0.3162\,t$ and evolve $|\Psi_0\rangle$ with the quenched Hamiltonian.

After the quench, the system evolves towards a non-equilibrium steady state, due to the different chemical potentials in the left and right leads. Our main observable is the time evolution of the tunneling current $j(\tau)$ through the dot. The current operator at bond n is given by

$$j_{nn+1}(\tau) = i\,t_n \sum_\sigma \left(c^\dagger_{n\sigma}\, c_{n+1\sigma} - c_{n\sigma}\, c^\dagger_{n+1\sigma} \right) \tag{5.98}$$

where t_n is the hopping matrix element connecting sites n and $n+1$, and $c_{\sigma n}, c^\dagger_{\sigma n}$ are annihilation and creation operators for fermions on site n with spin σ. We use a symmetrized version [218] by averaging over the left and right tunneling current:

$$j(\tau) = \frac{j_{Lf} + j_{fR}}{2} = i\pi t' \sum_\sigma \left(\left(c^{L\dagger}_{0L\sigma} f_\sigma - f^\dagger_\sigma c^L_{0L\sigma} \right) + \left(f^\dagger_\sigma c^R_{0R\sigma} - c^{R\dagger}_{0R\sigma} f_\sigma \right) \right) \tag{5.99}$$

where $c^L_{0L\sigma}, c^{\dagger L}_{0L\sigma}$ denote operators next to the impurity in the left reservoir (number 74 in Fig. 5.19) and $c^R_{0R\sigma}, c^{R\dagger}_{0R\sigma}$ operators next to the impurity in the right reservoir (number

76 in Fig. 5.19). Note that using the (numerical) derivatives

$$j_L(\tau) = \langle \dot{N}_L(\tau) \rangle \tag{5.100}$$

$$j_R(\tau) = \langle \dot{N}_R(\tau) \rangle \tag{5.101}$$

$$N_\alpha = \sum_{i\sigma} n_{i\alpha\sigma} \tag{5.102}$$

is more prone to truncation effects due to the summation over all lattice sites.

The dynamics typically show two regimes: a strong initial increase in current through the quantum dot, accompanied by sinusoidal oscillations, followed by a (possibly slow) relaxation towards a state with finite, constant current through the dot. A true steady state can of course never be reached in our finite system. If the current saturates before perturbations can travel to the boundary and back to the dot, we can speak of a quasi-steady state (which is independent of the system size L except for effects of L on the initial state) and which represents a good approximation to the true steady state.

5.4.3 Transient behavior

The transient response can roughly be divided into three distinct classes: a low, a medium and a high bias regime. Each class shows qualitatively the same behavior for different interactions strengths U/Δ. In the following, we discuss the case $U/\Delta = 12$ (see Fig. 5.20). All three regimes show a common strong initial increase in the current. The initial increase depends on the applied bias voltage V_B. At low bias ($V_B/\Delta \in (0, 18)$), the current plateau [223, 224] is reached quite quickly after this increase (within $\tau \approx \Delta^{-1}$). Increasing V_B ($V_B/\Delta \in (18, 28)$) increases the initial current-peak. The subsequent relaxation to the quasi-steady state is for some model parameters too slow to reach a steady state plateau within accessible simulation time scales. Finally, at high bias ($V_B/\Delta \in (28, 40)$) the initial peak is followed by a fast decrease of the current into a steady state plateau within $\tau \approx \Delta^{-1}$. The data shows, that over a period of $\tau = 3\,\Delta^{-1}$, approximately one particle is transferred from the left reservoir to the right one. All three QT eventually approach the same steady state, although in different ways. A common feature of all three QT's are sinusoidal oscillations in the current. The amplitude of these oscillations however depends on the particular quench, with QT II showing strongest oscillations. QT II also has largest transient current spike, which is one reason for the lower accuracy in determining the steady state for this quench. Quenching the hybridization(s) (QT I or III) yields thus cleaner steady state plateaus as compared to quenching the bias voltage (QT II).

The period τ_C of the current oscillations shows a pronounced U dependence (Fig.5.21 (data points)), which, quite interestingly, compares very well with results from functional renormalization group calculations for an Interacting Resonating Level Model (IRLM) [225] (see Fig.5.21, solid lines) which predict oscillations $\propto \sin(\frac{\tau}{\tau_C})$, with

$$\tau_C(U, V) = \frac{2}{V_B + U}\ . \tag{5.103}$$

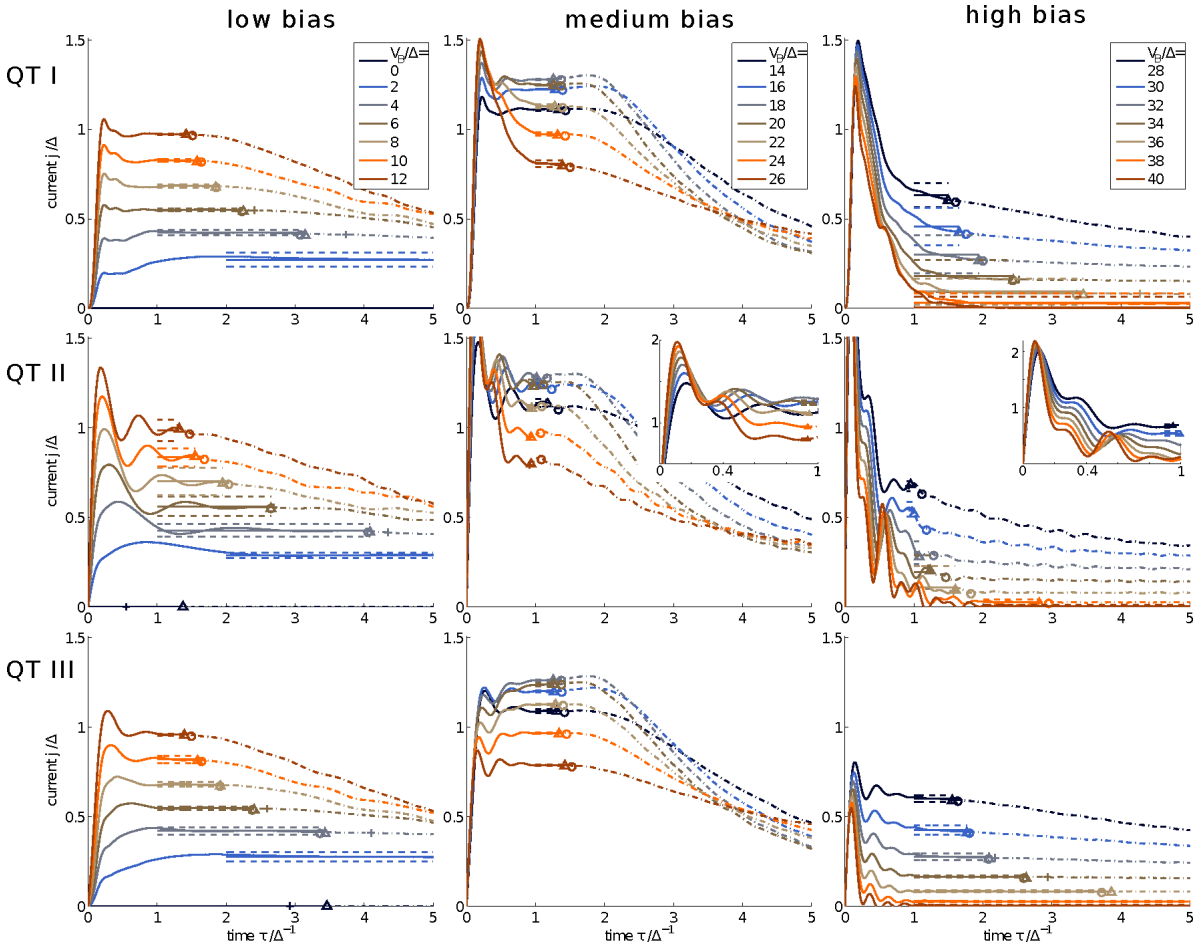

Figure 5.20: Time dependence of the current (Eq. (5.99)) at $U/\Delta = 12$ for the three different QTs and for different bias voltages. The curves are plotted as solid lines up to the last reliable point in the TEBD calculation (see text). Larger times are plotted as dash-dotted lines. Solid horizontal lines are fits to extract the steady state currents. The time domain for these fits starts at $\tau \approx \Delta^{-1}$ and ends at a point which is identified as the last reliable data point (symbols, see text). Dashed horizontal lines indicate the uncertainty. The insets in the mid row show respective zooms onto short time regions, which are not visible in the main part of the figure.

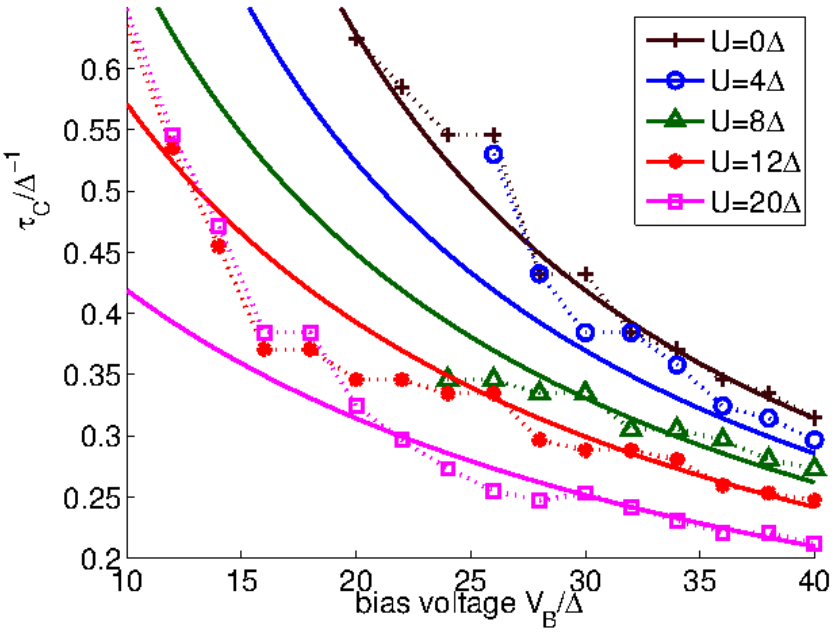

Figure 5.21: Period of the sinusoidal oscillations of the current in QT II for various values of interaction strength $U/\Delta = 0, 4, 8, 12$ and 20 (symbols). Solid lines indicate the predicted form for the interacting resonant level model. [225]

5.4.4 Results for the steady state current

Since we cannot observe a true constant current in our simulations, we define the steady state current by averaging over a suitable time interval $[\tau_S, \tau_E]$ marked in Fig.5.20. τ_S was chosen by hand to lie after the initial peak of the current, and τ_E is taken to be a time when results are not reliable anymore. Beyond τ_E, truncation effects dominate, resulting in decaying current. Whereas transients typically decay over a period of $\tau_S \approx \Delta^{-1}$, the end point of the plateau strongly depends on the parameter region under consideration. We define it by two distinct measures. One is the time $\tau_E^{(1)}$ for which the truncated weight ϵ

$$\epsilon = 1 - \sum_{\gamma=1}^{\chi} \lambda_\gamma^2 \tag{5.104}$$

reaches a threshold of $\epsilon_c = 3 \cdot 10^{-6}$ at any bond (marked by $+$ in Fig. 5.20). The second definition ($\tau_E^{(2)}$ marked by $\circ$ in Fig. 5.20) is given by the time for which two different definitions of the current, namely the expectation value of the current operator (Eq. (5.99)) and the time derivative of the particle number (Eq. (5.100)), deviate by more than $7 \cdot 10^{-4}$, the latter being more susceptible to accumulation of errors. Both times are in good agreement with each other and can be combined into an effective simulation time $\tau_E = \min(\tau_E^{(1)}, \tau_E^{(2)}) + \alpha|\tau_E^{(1)} - \tau_E^{(2)}|$ (marked by triangles in Fig. 5.20). We choose a value of $\alpha = 0.1$. Results do not depend on this particular choice. For the non-interacting case, the time τ_E thus determined agrees with the time when the TEBD current starts

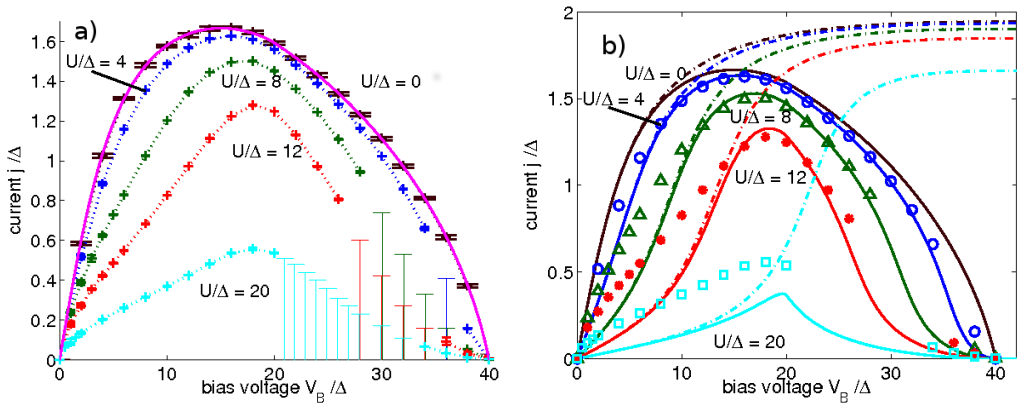

Figure 5.22: *Left panel:* Current-voltage characteristics of the quantum dot. The steady state currents shown are obtained by a fit of the expectation value of the current operator within the steady state plateau. Regions where only a likely upper bound for the steady state current could be obtained are indicated by pedestals (see text). *Right panel:* Comparison of the current-voltage characteristics of a *non interacting*, resonant level device with on-site potential $\varepsilon_f = -\frac{U}{2}$ (solid lines) with the TEBD data for the interacting quantum dot (symbols). Both devices have the same specifications with only the interaction U missing in the first case. The comparison is done for four values of interaction strengths resp. on-site potentials: $\frac{U}{\Delta} = \{4, 8, 12, 20\}$ resp. $\frac{\varepsilon_f}{\Delta} = \{-2, -4, -6, -10\}$ (blue/circles, green/triangles, red/stars, cyan/squares respectively). In addition we show the $U = 0$ result (black/no symbols). The dash-dotted lines indicate data for a non interacting device in the wide-band limit.

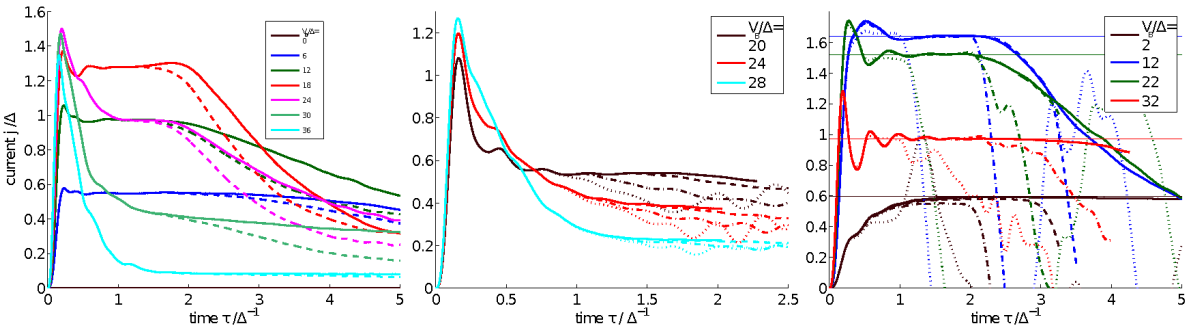

Figure 5.23: Convergence of the current with respect to several auxiliary numerical parameters. Left: Solid lines denote results obtained evaluating the expectation value of the current operator Eq. (5.99), while dashed lines indicate data obtained by evaluating the time derivative of the expectation value of the particle number Eq. (5.100) ($U = 12\,\Delta$, $L = 150$, $\chi_{\mathrm{TEBD}} = 2000$, QT I). Center: Matrix sizes $\chi_{\mathrm{TEBD}} = 250$ (dotted), 500 (dash-dotted), 2000 (dashed) and 4000 (solid) are presented ($U = 20\,\Delta$, $L = 150$, QT I). Right: We show system sizes $L = 20, 40, 60, 80, 100, 120$ and 150 (dotted, dash-dotted, dashed, dash-dash-dot-dotted, long-dash-short-dashed, dash-gap-dashed and solid) at $U = 0$, $L = 150$, $\chi_{\mathrm{TEBD}} = 2000$ for QT I. The constant solid lines indicate the exact steady state currents of the respective thermodynamic system.

to deviate from the exact value. The plateaus typically show oscillations and also small, quench and parameter-dependent drifts. A linear fit within the interval $[\tau_S, \tau_E]$ can be used as a measure of quality of the plateau. If the slope of the fit is too large, we regard the plateau as unreliable. The last reliable value is then treated as an upper bound to the true current (see also Sec. 5.4.5). As threshold for the slope we use a value of $\approx 5 \cdot 10^{-2}\,\Delta$. Each curve in addition was inspected by hand for convergence. The error for the steady state current is estimated to be three times the standard deviation taken over the data points in the fitting interval $[\tau_S, \tau_E]$ (plotted as dashed lines in Fig. 5.20 and Fig. 5.22, (a)). Two important features support the validity of our results: first, the $U = 0$ results match the analytic results nicely, and second, steady state currents are independent of the quench type. Comparing results for different quench types we find QT I and QT III favorable to QT II. For the latter we observe pronounced oscillations which impede reliable extraction of the steady state current, and reachable simulation times are shorter as compared to the other two quenches. Results or the $I - V_B$ characteristic of the interacting quantum dot are shown in Fig. 5.22 (a) for different values of interaction strength $U/\Delta = 0, 4, 8, 12, 20$. Data were obtained using QT I and QT III. In Fig. 5.22 b), we compare results for the steady state of the interacting system with those for $U/\Delta = 0$ case, but with an on-site potential of $\varepsilon_f = -U/2$ in which case the steady state current can be obtained from [226, 227]

$$j = 4\pi t'^4 \int_{-\frac{V_B}{2}}^{\frac{V_B}{2}} d\omega \, \frac{\rho_L(\omega)\rho_R(\omega)}{\Big((\mathrm{g}_L^A(\omega) + \mathrm{g}_R^A(\omega))t'^2 - (\omega - \varepsilon_f)\Big)} \tag{5.105}$$

where $\rho_{L/R}$ denotes the electronic DOS of the (disconnected) left and right lead and $\mathrm{g}_{L/R}^A$ their advanced single particle Green's functions. We show results for finite band width of the leads (solid lines) as well as wide band limit results (dash-dotted lines). Data points are TEBD results. The effect of interaction is to increase the low bias current, attributed to the formation a Abrikosov-Suhl (or Kondo) resonance at zero energy in the dot spectral density, which enhances tunneling of electrons from the left to the right lead via the impurity. The effect increases with increasing interaction U/Δ.

For some values of V_B/Δ and $U\Delta$, reachable simulation times were too short to allow for a conclusive determination of the steady state current. For these values (marked with pedestals) we only can specify an upper bound, given by the last reliable value of the time dependent current (see above). Let us first discuss the $U = 0$ results. The pink solid line is the analytic result for a non-interacting device in the thermodynamic limit and it shows very good agreement with our numerical data. With increasing bias voltage V_B, we observe an expected increase in current. The current however reaches a maximum at $V_B \approx 20$ and then decreases again, which has its origin in the finite bandwidth of the two leads (each one has a semi-circular DOS with width $D = 40\Delta$): the overlap region of the left and right lead DOS diminishes again when increasing V_B, until it is exactly zero for $V_B > 40\Delta$, at which point no current can flow anymore. When turning on U, the general features of a roughly semicircular shape of the current-voltage curve with a maximum, and zero current beyond $V_B > 40$, remain valid. For small V_B however, we observe reduction of the slope, and a flattening of the curvature for intermediate $V_B \approx 10$. The position of the maximum of the current depend on U.

Interestingly, the the onset of slow relaxation coincides with the point where the single

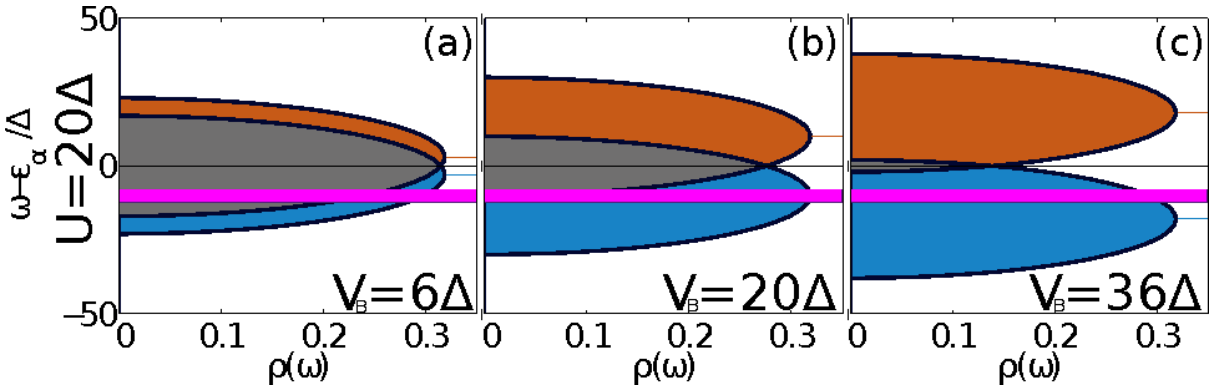

Figure 5.24: Single particle DOS and single particle dot level in a Hubbard-I type picture at $U = 20\,\Delta$, for (a) $V_B = 6\,\Delta$, (b) $V_B = 20\,\Delta$ and (c) $V_B = 36\,\Delta$. The electronic DOS of the left (right) lead is shown in red (blue) and their overlap in brown. The single particle level of the quantum dot is indicated at $-\frac{U}{2}$ in magenta.

particle level $\varepsilon_f = -U/2$ drops out of the overlap region of the lead DOSs (see Fig. 5.24 (bottom)).

There already exists a wealth of literature on the conduction properties of the SIAM, though in most cases restricted to the wide band limit where one assumes a semi-infinite bandwidth. For small V_B, results for finite and infinite bandwidth should however coincide. In Fig.5.25 we compare our results to results from various other studies, namely diagrammatic QMC [228], fourth order Keldysh perturbation theory [229], time-dependent DMRG [214], non equilibrium FRG [230], non equilibrium Cluster Perturbation Theory [231], the non equilibrium Variational Cluster Approach [231, 213], imaginary time QMC [232], iterative summation of real-time path integrals [233] and the linear response result for the Kondo regime $j_{\text{lin}} = 2G_0V_B$.

5.4.5 Kondo effect and relaxation dynamics

At large interaction U/Δ the SIAM exhibits strong Kondo physics [181]. A signature of the Kondo effect is the appearance of an energy scale k_BT_K, where T_K is the Kondo temperature. This energy scale can be identified with the width of the Kondo resonance of the impurity spectral function. The Kondo temperature T_K can be rephrased into a spin-correlation length $\xi_K \propto 2t\sqrt{\frac{2}{U\Delta}}e^{\frac{\pi U}{8\Delta}}$. For large U/Δ, this length scale translates into a dominant time scale for dynamical properties (i.e. the impurity spectral function). In our studies, the correlation length $\xi_K = 50, 200, 900$ and 16000 sites for $U/\Delta = 4, 8, 12$ and 20. Thus, in all cases, except $U/\Delta = 4$, our system was too small to capture the full correlation cloud. The question of what happens to the Kondo effect at bias voltages is still under debate. On the one hand it is argued [234, 235, 236, 237] that for $V_B >> T_K$, which is the case for our simulations, the Kondo effect should be suppressed by the bias voltage and hence Kondo correlations should not be important for these parameters. Other studies conclude that the Kondo peak should split up [238, 239] (with a possible pinning of each peak at the Fermi energy of the corresponding lead), which has also

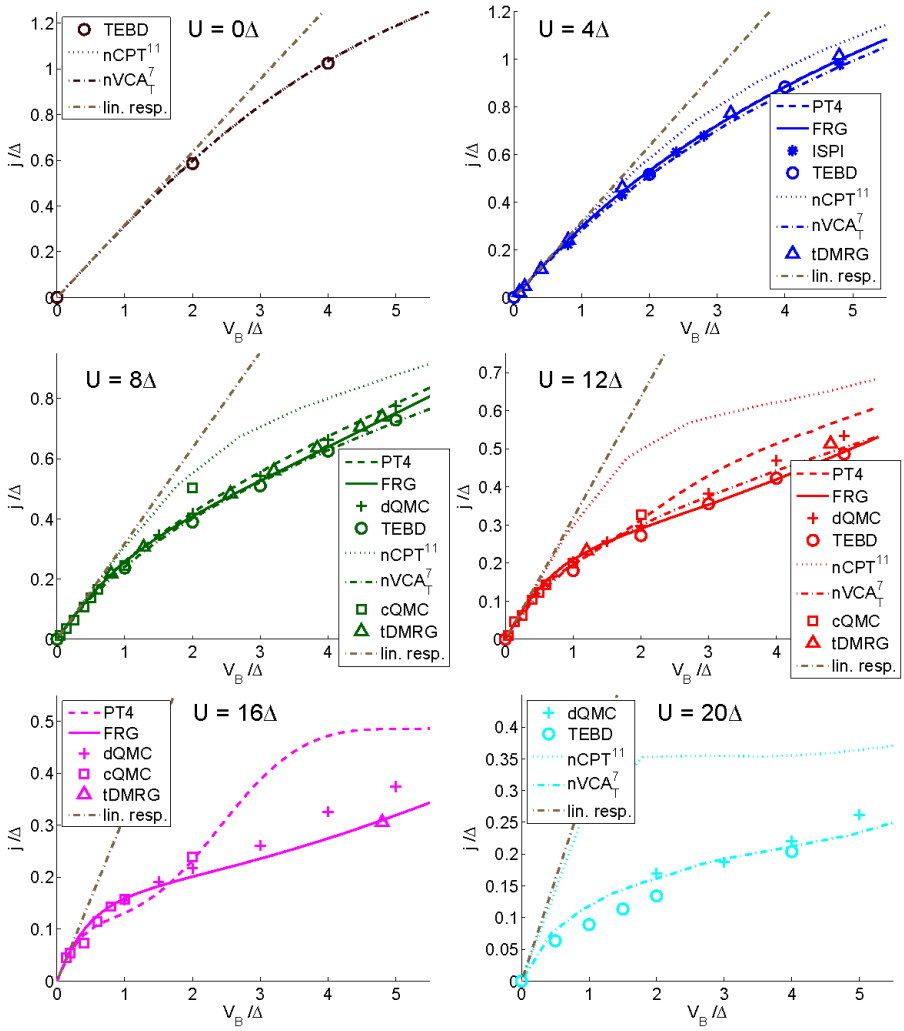

Figure 5.25: Comparison of the current-voltage characteristics of the SIAM obtained with different methods in the low-bias regime. Some of the methods use a wide-band limit and others a semi-circular reservoir DOS which (for equal Δ) become comparable in the low bias region shown. The methods are: 1) diagrammatic QMC for $T = 0$ in the wide-band limit (dQMC), [228] 2) fourth order Keldysh perturbation theory for $T = 0$ in the wide-band limit (PT4), [229] 3) time-dependent DMRG for $T = 0$ using a semi-circular DOS (tDMRG), [214] 4) TEBD for $T = 0$ using a semi-circular DOS (TEBD, this work), 5) non equilibrium FRG for $T = 0$ using a wide-band limit (FRG), [230] 6) non equilibrium Cluster Perturbation Theory for $T = 0$ using a semi-circular DOS (nCPT^{11}), [231] 7) non equilibrium Variational Cluster Approach for $T = 0$ using a semi-circular DOS (nCPT$^{7}_{T}$), [231] 8) imaginary time QMC for $T = 0.2\,\Delta$ in the wide-band limit (cQMC) [232] 9) iterative summation of real-time path integrals for $T = 0.2\,\Delta$ in the wide-band limit (ISPI) [233] and 10) the linear response result for the Kondo regime $j_{\text{lin}} = 2G_0V_B$ (lin. resp.).

been observed in another recent numerical study using variational cluster approach [231]. In our simulations we observe distinct discrepancies of the relaxation times of the spin and charge current: while the charge current is seen to converge in most cases within reachable simulation times, the spin current shows much longer relaxation times and in many cases it is not possible to reach a steady state spin-current [240]. Given the fact that initial states *with* Kondo correlations (QT II) yield the same steady state charge current as initial states without Kondo correlations (QT I and QT III), we conclude that Kondo correlations do not significantly affect the charge current relaxation in the parameter regime under study.

5.4.6 Conclusions

We investigated non-equilibrium properties and current-voltage characteristics of the two-lead Single Impurity Anderson Model. Quasi steady state currents were obtained by quenching the system to a non-eigenstate and subsequently evolving it in real time to a quasi steady state using the Time Evolving Block Decimation algorithm. To this end we investigated three different types of quenches: i) quenching the hybridization with already applied bias voltage, ii) quenching the bias voltage and iii) quenching the hybridization at one side only. For all quenches we find good agreement with existing results. However, transients and especially current oscillations of the quasi steady state plateaus depend strongly on the type of quench. In this respect we find that quench type i) yields the best results due to smallest oscillations and small initial current peaks. We argue that Kondo correlations do not noticeably affect the charge current in the parameter regime under study ($V_B \gg T_K$). In contrast to previous work, we also address the (non-universal) regime $V_B \approx 4t$ of small overlap between the DOS of the left and right leads. For intermediate voltages, we find long relaxation times that do not allow to obtain a quasi stead state.

Future studies might incorporate gate voltages or magnetic fields, typically present in experimental setups, which would allow for simulation of the Coulomb blockade phenomenon. Correlation effects within the leads can also straightforwardly be incorporated [241]. The same technique might also be used to study evolution of correlation functions which could provide interesting insights into the mechanisms of Kondo cloud formation [242, 243]

Appendix

1 The Lanczos algorithm

The most time consuming part in the DMRG algorithm is the approximate diagonalization of the DMRG Hamiltonian with a large sparse eigensolver. For the sake of completeness, the following chapter shall give an short introduction to the Lanczos [244] method, which was used as eigensolver in this work. The Lanczos algorithm [3] is an iterative method to solve for the groundstates (more generally, eigenstates with extremal eigenvalues) of large, sparse (hermitian) matrices, and is widely used in all areas of strong correlation physics. An example is standard DMRG, where one has to find the groundstate of a super-block Hamiltonian within an effective basis. The Lanczos method can be used at zero or finite temperature [245, 246], to calculate Greens functions [247], and to do real time evolution [248]. Recently, MPS methods have been combined with the Lanczos method [57, 58, 53].

Suppose we want to find the groundstate of a Hamiltonian H. A simple minded approach is to start with a random (normalized) initial guess $|x_0\rangle$ (*with finite overlap with the groundstate*), and iterate

$$|\tilde{x}_n\rangle = H\,|x_{n-1}\rangle \tag{106}$$

$$|x_n\rangle = \frac{|\tilde{x}_n\rangle}{\sqrt{\langle\tilde{x}_n|\tilde{x}_n\rangle}}. \tag{107}$$

This is called the Power Method. If H has a single, non-degenerate groundstate $|\psi_0\rangle$ with energy ε_0, then $\lim_{n\to\infty} |x_n\rangle \propto |\psi_0\rangle$:

$$H^n\,|x_0\rangle = H^n \sum_i c_i\,|\psi_i\rangle = \sum_i \varepsilon_i^n c_i\,|\psi_i\rangle = c_0\varepsilon_0^n\left(|\psi_0\rangle + \sum_{i=1}\left(\frac{\varepsilon_i}{\varepsilon_0}\right)^n \frac{c_i}{c_0}\,|\psi_i\rangle\right). \tag{108}$$

For large n, the expression in brackets on the right side is dominated by $|\psi_0\rangle$, since $\left|\frac{\varepsilon_i}{\varepsilon_0}\right| < 1$. One of its major drawbacks is its bad convergence. The basic idea of the Lanczos method is to *orthonormalize* the subspace $\mathcal{K} = \mathrm{span}\{|x_0\rangle, H\,|x_0\rangle, H^2\,|x_0\rangle \ldots H^{M-1}\,|x_0\rangle\}$ (called Krylov space) such that every new vector of the iteration is orthonormal to all previous ones. This can in principle be done by a Gram-Schmidt orthonormalization. For large systems, this can however become quite time consuming. The Lanczos method on the other hand uses an implicit orthonormalization scheme where the new vector is orthonormalized explicitly only to the two previous vectors, and orthonormality to all the others follows implicitly by the hermiticity of H. The procedure starts with a normalized

initial guess $|x_0\rangle = |\tilde{x}_0\rangle / \sqrt{\langle\tilde{x}_0|\tilde{x}_0\rangle}$ and a formal zero-vector $|x_{-1}\rangle = 0$. Vectors with a $\sim$ symbol on top are unnormalized vectors. The Lanczos vectors are then generated according to

$$\begin{aligned} |\tilde{x}_{n+1}\rangle &= H\,|x_n\rangle - \epsilon_n\,|x_n\rangle - k_n\,|x_{n-1}\rangle \\ \epsilon_n &= \langle x_n|H|x_n\rangle \\ k_n &= \langle x_{n-1}|H|x_n\rangle = ||\,|\tilde{x}_n\rangle\,|| \\ |x_{n+1}\rangle &= |\tilde{x}_{n+1}\rangle / \sqrt{\langle\tilde{x}_{n+1}|\tilde{x}_{n+1}\rangle}, \end{aligned} \tag{109}$$

and are all mutually orthonormal. Using the vectors $|x_n\rangle$, we can project H into this subspace $\mathcal{K}$ using the projection operator $\mathcal{P} = \sum_{i=0}^{M-1} |x_i\rangle\langle x_i|$

$$H_M \equiv \mathcal{P}^{-1} H \mathcal{P}. \tag{110}$$

Because of the orthonormality of the $|x_n\rangle$, the projected Hamiltonian assumes a tridiagonal form in this Krylov basis:

$$H_M = \begin{pmatrix} \epsilon_0 & k_1 & 0 & \dots & 0 \\ k_1 & \epsilon_1 & k_2 & & \vdots \\ 0 & k_2 & \epsilon_2 & \ddots & 0 \\ \vdots & & \ddots & \ddots & k_n \\ 0 & \dots & 0 & k_n & \epsilon_n \end{pmatrix}. \tag{111}$$

Convergence is monitored by diagonalizing Eq.(111) every N-th step,

$$U^\dagger H_M U = E, \tag{112}$$

and checking for convergence of the lowest (or highest) eigenvalue in the diagonal matrix E. Due to numerical instabilities (round-off errors), $\langle x_n|x_m\rangle$ is never strictly 0 for $n \neq m$, and thus orthonormality between the states gets lost with increasing iteration number. As soon as k_n drops below a certain threshold (usually $10^{-10} - 10^{-12}$), iteration has to be stopped because it has converged to the groundstate, and continuing the iteration would spoil orthonormality of the Lanczos vectors. The groundstate $|\psi_0\rangle$ in the computational basis is given by

$$|\psi_0\rangle = \sum_{n=0}^{M-1} U_{n0}\,|n\rangle \tag{113}$$

(we assume that entries in E are ordered from small to large).

The Lanczos algorithm for excited states

If the groundstate $|\psi_0\rangle$ of H has been found, an excited state can be obtained from a second Lanczos run where one takes a random vector $|x_0\rangle$ and orthonormalizes it to $|\psi_0\rangle$.

$$|\hat{x}_0\rangle = |x_0\rangle - |\psi_0\rangle\,\langle\psi_0|x_0\rangle\,. \tag{114}$$

The state $|\hat{x}_0\rangle$ is then used as starting vector for the second Lanczos run.

2 Diagonalization of bilinear Hamiltonian's

By definition, a bilinear Hamiltonian has the form

$$H = \sum_{ij=N}^{N} c_i^\dagger t_{ij} c_j$$

We will omit any spin degrees of freedom for simplicity. Such models are generically called non-interacting quantum systems because the system only possesses kinetic energy (given by the hopping matrix elements t_{ij}). A simple diagonalization of t_{ij} immediately gives the spectrum ε_k as

$$\varepsilon_k = \sum_{ij} U_{ik}^* t_{ij} U_{jk} = (U^\dagger t U)_{kk}$$

Creation/annihilation operators $a_k^\dagger / a_k$ of eigenstates are related to real space creation/annihilation operators $c_i^\dagger / c_i$ by the unitary basis transformation U:

$$c_i^\dagger = \sum_k a_k^\dagger U_{ik}^*$$
$$a_k = \sum_i U_{ki} c_i$$

To compute any quantity of interest, for example time dependent correlations, there are two ways to proceed. If one is interested in the $N \to \infty$ limit, then one has to resort to analytical evaluation of the occurring integrals in k-space. Since we want to compare exact results with those obtained from numerical calculations with MPS-methods, we will continue in a different way by numerically diagonalizing the matrix t_{ij} (which is an $N \times N$ matrix), and using the finite matrices U and ε_k to obtain quantities of interest. In the following we will apply this to two different cases: a) the evaluation of the time evolution of local densities after inserting a particle, and b) the evaluation of Chebyshev moments of the single particle spectral function.

2.1 A single particle in a Fermi sea

We will consider the case where a particle is inserted into the groundstate of the system with all levels up to (including) k_F filled with electrons. At $t = 0$, we will then insert a single particle at site i into the system, e.g. apply $c_i^\dagger$ to the ground state. Our initial state thus is

$$|\psi_0\rangle = \frac{c_i^\dagger |0\rangle}{Z} \tag{115}$$

where we introduced a normalization Z (note that $c_i^\dagger$ is not norm-preserving). $|0\rangle$ is the Fermi sea of the half filled system, e.g. $|0\rangle = \prod_{k \leq k_F} a_k^\dagger |vac\rangle$, and $|vac\rangle$ is the real vacuum with no particles present. This state is evolved in time, and we want to compute $\langle n_j(t) \rangle$ for a later time $t > 0$. Using $|\psi(t)\rangle = \exp(-iHt) |\psi_0\rangle$, we get

$$\begin{aligned} Z^2 \langle n_j(t) \rangle &= Z^2 \langle \psi_0 | e^{iHt} c_j^\dagger c_j e^{-iHt} |\psi_0\rangle \\ &= \sum_{k,k'>k_F} \sum_{p,p'} U_{ik'} e^{i\varepsilon'_k t} U_{ik}^* e^{-i\varepsilon_k t} U_{jp}^* U_{ip'} \langle 0 | a_{k'} a_p^\dagger a_{p'} a_k^\dagger |0\rangle \end{aligned} \tag{116}$$

The sum $k, k' > k_F$ is due to the fact the the fermi sea is of course occupied for all $k \leq k_F$. Using the fermionic commutators

$$\{a_k, a_{k'}\} = \{a_k^\dagger, a_{k'}^\dagger\} = 0;$$
$$\{a_k, a_{k'}^\dagger\} = \delta_{kk'}$$

to move all creation operators to the left of all annihilation operators yields

$$a_{k'} a_p^\dagger a_{p'} a_k^\dagger = \delta_{k'p} a_{p'} a_k^\dagger + \delta_{kk'} a_p^\dagger a_{p'} - \delta_{p'k} a_p^\dagger a_{k'} + a_p^\dagger a_k^\dagger a_{p'} a_{k'}. \tag{117}$$

Insertion into Eq.116 shows, that the last two terms vanish due to the annihilation operators in front. By carrying out the summations, one finally obtains

$$\langle n_j(t) \rangle = \sum_{k,k'>k_F} U_{jk} U_{ik}^* U_{ik'} U_{jk'}^* \exp(i(\varepsilon_{k'} - \varepsilon_k)t) + \sum_{k>k_F, p\leq k_F} |U_{ik}|^2 |U_{jp}|^2. \tag{118}$$

The normalization factor is given by

$$Z = \sqrt{1 - \sum_{k<k_F} |U_{ik}|^2}.$$

2.2 A single particle on an empty lattice

In the following we will consider the time evolution of a single particle on a 1d tight-binding lattice with *periodic boundary conditions*. For simplicity we will restrict ourselves to spinless fermions. The tight-binding Hamiltonian is the simplest model for electrons on a lattice and is given by

$$H = -J \sum_{i=0}^{N-1} (c_i^\dagger c_{i+1} + h.c.) \tag{119}$$

where $c_i, c_i^\dagger$ are fermionic annihilation and creation operators at lattice site i (note that counting of sites starts at $i = 0$). The eigenstates $|k\rangle$ and eigenenergies $\varepsilon(k)$ are given by

$$|k\rangle \equiv c_k^\dagger |0\rangle = \Big(\frac{1}{\sqrt{N}} \sum_m e^{ikm} c_m^\dagger \Big) |0\rangle \tag{120}$$
$$\varepsilon(k) = -2J\cos(k), k = \frac{2\pi n}{N}, n \in \{0, 1, \ldots N-1\}.$$

For an initial state $|\psi_0\rangle = c_{i=0}^\dagger |0\rangle = \frac{1}{\sqrt{N}} \sum_k c_k^\dagger$ with a single particle at site $i = 0$, the time dependent density $\langle n_m(t) \rangle$ at site m can be calculated analytically,

$$\begin{aligned}
\langle n_m(t) \rangle &= \frac{1}{N} \sum_{k_1 k_2} e^{im(k_2-k_1)} \langle \psi(t)| c_{k_1}^\dagger c_{k_2} |\psi(t)\rangle \qquad (121)\\
&= \frac{1}{N^2} \sum_{k_1,k_2,q_1,q_2} e^{im(k_2-k_1)+2iJt(\cos(q_1)-\cos(q_2))} \underbrace{\langle 0| c_{q_1} c_{k_1}^\dagger c_{k_2} c_{q_2}^\dagger |0\rangle}_{\delta_{k_1 q_1}\delta_{k_2 q_2}} \\
&= \frac{1}{N^2} \sum_{k_1,k_2} e^{im(k_2-k_1)+2iJt(\cos(k_1)-\cos(k_2))} = \Big[\frac{1}{N}\sum_k e^{i(mk-2Jt\cos(k))}\Big]\Big[\frac{1}{N}\sum_k e^{-i(mk-2Jt\cos(k))}\Big]
\end{aligned}$$

where $|\psi(t)\rangle = e^{-iHt}|\psi_0\rangle$. In the limit of $N \to \infty$ we can replace the sums:

$$\frac{1}{N}\sum_k \to \frac{1}{2\pi}\int_{k=0}^{2\pi} dk \quad \text{with } dk = \frac{2\pi}{N}. \tag{122}$$

For the first braket in the last line of equation Eq.121 we thus get

$$\begin{aligned}\frac{1}{N}\sum_k e^{i(mk-2Jt\cos(k))} &\approx \frac{1}{2\pi}\int_{k=0}^{2\pi} dk e^{i(mk-2Jt\cos(k))} = \frac{1}{2\pi}\int_{k=0}^{2\pi} dk e^{i(mk-2Jt\sin(k-\pi/2))} \\ &\overset{\tilde{k}=k-\pi/2}{=} e^{\frac{im\pi}{2}}\frac{1}{2\pi}\int_{\tilde{k}=-\pi/2}^{\pi/2} d\tilde{k} e^{i(m\tilde{k}-2Jt\sin(\tilde{k}))} = e^{\frac{im\pi}{2}} J_m(2Jt),\end{aligned} \tag{123}$$

where $J_m(2Jt)$ is the m-th Bessel function. The second braket is just the complex conjugate of the first, and hence we obtain

$$\langle n_m(t)\rangle = J_m(2Jt)^2 \tag{124}$$

(note that the Bessel functions $J_m(x) \in \mathbb{R}$).

2.3 Evaluation of Chebyshev moments

Let us now adress the computation of the Chebyshev moments μ_n of the spectral function $A(\omega) = A^+(\omega) + A^-(-\omega)$. The Chebyshev moments of $A^+(\omega)$ (for $A^-(\omega)$ replace $c_i^\dagger$ below with c_i, and $\sum_{k>k_F}$ with $\sum_{k\leq k_F}$) can be computed from the expression

$$\begin{aligned}|t_0\rangle &= c_i^\dagger|0\rangle = \sum_{k>k_F} U_{ik}^* a_k^\dagger|0\rangle \\ \mu_n &= \langle t_0|T^n(H)|t_0\rangle = \sum_{kk'>k_F} U_{ik}^* U_{ik'} T^n(\varepsilon_k) \underbrace{\langle 0| a_k' a_k^\dagger |0\rangle}_{\delta_{kk'}}.\end{aligned}$$

The restriction of $k > k_F$ above is due to the half-filled Fermi sea. Note that by using ε_k in the above equations, we are in fact referring the energies to the real, physical vacuum $|vac\rangle$, not the energy of the half-filled system. This has of course no effect on the spectral function, since shifting the reference energy cannot change the excitation energies from the half-filled Fermi sea. One has however be careful when evaluating $A^+(\omega) + A^-(-\omega)$: In the usual formalism all energies are referenced to the ground-state energy (e.g. the energy of the Fermi sea), and thus hole excitations appear automatically at *negative* energies. That is the reason for the negative sign of the argument of $A^-(-\omega)$. In our case, the hole excitations are still positive, so we actually have to evaluate $A^-(+\omega)$ when using the moments μ_n in a Chebyshev expansion of $A(\omega)$.

3 A short excursion on scattering theory

The goal of this chapter is to introduce the basic notation and ideas of scattering theory which by definition deals with the scattering of free electrons at impurities. We will in

the following however only consider scattering at a single particle potential. A detailed introduction to scattering theory can usually be found in any textbook on basic quantum mechanics [249]. The following section follows closely the lecture notes by Ref.[250, 251]. The general setup is the following: a free particle $|k\rangle$ (i.e. eigenstate to H_0 with ε_k) is incident on a potential V (with a finite range r_0) and is scattered into a state $|k'\rangle$ which is an eigenstate of the full Hamiltonian $H = H_0 + V$, to energy $\varepsilon_{k'}$ ($\varepsilon_{k'}$ and ε_k in general need to be the same, but let's for now suppose they are not). We want thus to solve the equation

$$(H - H_0)\,|k'\rangle = V\,|k'\rangle \tag{125}$$

The formal solution

$$|k'\rangle = |k\rangle + (\varepsilon_k - H_0)^{-1} V\,|k'\rangle = |k\rangle + G_0 V\,|k'\rangle \tag{126}$$

is known as the Lippman-Schwinger equation, and G_0 is the free Greens function. Eq. 126 generates the so called Born series

$$|k'\rangle = (1 + G_0V + G_0VG_0 + G_0VG_0VG_0 + \dots)\,|k\rangle \tag{127}$$

by iteration. The state $|k'\rangle$ is often referred to a scattering state (note that some people use this name for $|k'\rangle - |k\rangle$). At this point it is convenient to define a new operator, called the T-matrix by

$$T \equiv V + VG_0V + VG_0VG_0V + \cdots = V + V(\varepsilon_k - H_0 + i\eta)^{-1}T. \tag{128}$$

ε_k in the denominator of the T-matrix is now associated with a single particle energy, but we can generalize ε_k to any ω.

The major result of scattering theory is that given an incident plane wave $|k\rangle$ in the dim past at $t = -\infty$, the effect of the potential is to give a *scattering phase shift* $\varphi(\varepsilon_k)$ to the outgoing, free wave front in the far future at $t = \infty$, at least far away from the scatterer. The operator that connects the incoming state at $t = -\infty$ and the outgoing state at $t = \infty$ is called the S-matrix, defined as

$$S = \hat{U}(\infty, -\infty) \tag{129}$$

$$\hat{U}(t_1, t_0) = e^{iH_0(t_1 - t_0)} e^{-i(H_0 + V)(t_1 - t_0)} e^{-iH_0(t_1 - t_0)}. \tag{130}$$

The textbook result for $\hat{U}$ in the interaction picture is

$$\hat{U}(t_1, t_0) = \mathcal{T} \exp(-i \int_{t_0}^{t_1} dt' \hat{V}_{t'}(t')) \tag{131}$$

$$\hat{V}_{t'}(t') = e^{iH_0 t'} V(t') e^{-iH_0 t'} \tag{132}$$

where $V(t)$ can explicitly depend on time. We assume that the range of the potential is finite (or equivalently that at $t = -\infty$ and $t = \infty$, the potential is zero), thus S is an operator defined in the space of *free particles*. The following identity can be obtained by expanding the exponential in S and doing the Fourier transformation:

$$\langle k'|\,S\,|k\rangle = \langle k'|k\rangle - 2i\pi\delta(\varepsilon_{k'} - \varepsilon_k)\,\langle k'|\,T\,|k\rangle \tag{133}$$

which is a generalization of Fermi's golden rule to infinite order perturbation theory. The transition probability Γ_{fi} from an initial state $|i\rangle$ to a final state $|f\rangle$ (with $\langle f|i\rangle = 0$) is thus given by

$$\Gamma_{fi} = 2\pi |\langle f| T |i\rangle|^2 \delta(E_f - E_i). \tag{134}$$

This result can be used to do perturbation theory for the conductance of e.g. quantum dots. The quantity $\langle k'| T |k\rangle$ is also proportional to the so called *scattering amplitude*. The δ function allows only outgoing states with the *same energy* as the incoming state. If there is a continuum of states at this energy, we can replace the δ-function by the density of states $\rho(\omega)$ of the non-interacting system at this energy $\varepsilon_k \equiv \omega$, and we get

$$S = 1 - 2i\pi\rho(\omega)T(\omega + i\eta) \tag{135}$$

(we have omitted the states $|k\rangle, |k'\rangle$).

4 Single particle Greens functions

The Greens function method is a symbolic way of solving differential equations like the Schrödinger equation. For $H = H_0 + V$, G and G_0 are simply defined as

$$(E - H_0(r))G_0(r, r', E) = \delta(r - r') \tag{136}$$
$$(E - H(r))G(r, r', E) = \delta(r - r') \tag{137}$$

(H_0 and H are given in real space basis). Given an eigenstate ψ_0 of H_0, i.e.

$$H_0\psi_0 = E\psi_0 \tag{138}$$

we can construct a solution to

$$(E - H_0)\psi(r) = V\psi(r) \tag{139}$$

to the same energy E by

$$\psi(r) = \psi_0(r) + \int dr' G_0(r, r', E)V(r')\psi(r'). \tag{140}$$

The same solution can also be obtained from the full propagator G:

$$\psi(r) = \psi_0(r) + \int dr' G(r, r', E)V(r')\psi_0(r'). \tag{141}$$

If one generates the Born series from Eq.140 in symbolic form

$$\psi(r) = \psi_0(r) + G_0V\psi_0 + G_0VG_0V\psi_0 + \dots \tag{142}$$
$$= \psi_0 + (G_0 + G_0VG_0 + G_0VG_0VG_0 + \dots)V\psi_0 \tag{143}$$

and compares to Eq.141, one obtains the *Dyson equation*

$$G = G_0 + G_0VG_0 + \cdots = G_0 + G_0V(G_0 + G_0VG_0 + \dots) \tag{144}$$
$$G = G_0 + G_0VG = G_0 + G_0TG_0 \tag{145}$$

which is the starting point for diagrammatic perturbation theory.

5 Many-body Greens functions

Greens functions are an invaluable tool for treating strongly correlated materials. Having its origins in the mathematical theory of differential equations, their use ranges from ordinary Maxwell's theory of electrodynamics to high-energy quantum field theory and theory of strongly correlated materials. Greens functions reveal many interesting properties of correlated quantum systems (for example if the system is gapped, or which are the low energy excitations governing low temperature physics). Unfortunately, they are notoriously difficult to calculate, and over the last decades, major efforts in condensed matter theory have been devoted to development of efficient and reliable methods for calculating them. This section introduces the basic concepts of Greens functions, needed in the remainder of this thesis. For a more thorough discussion of the matter, I refer the reader to the standard textbooks [252, 253, 180, 182].

Let H be a generic (many-body) Hamiltonian defined on a lattice with lattice site l. The *causal* single particle Greens function $G_{lm}(t,t')$ at temperature $T=0$ is defined

$$G_{lm}(t,t') = \langle 0|\, \mathcal{T}[c_l(t), c_m^\dagger(t')]_\pm \,|0\rangle \quad \text{causal} \tag{146}$$

$c_l(t)$ is the annihilation operator for a particle at site l in the Heisenberg picture: $c_l(t) = e^{iHt}c_l e^{-iHt}$. The particles can be either bosons or fermions:

$$\begin{aligned} [c_l, c_m^\dagger]_\pm &= \delta_{lm} \\ [c_l, c_m]_\pm = [c_l^\dagger, c_m^\dagger]_\pm &= 0 \end{aligned} \tag{147}$$

where $[a,b]_\pm = ab \pm ba$ is the commutator and anticommutator for negative and positive sign, respectively. $|0\rangle$ is the groundstate of H, and $\mathcal{T}$ is the Wick time-ordering operator. The Greens function comes along in three different flavors, which contain the exact same amount of information: the *causal* Greens function and the so called *advanced* and *retarded* Greens function:

$$G^R_{lm}(t,t') = -i\Theta(t-t')\,\langle 0|\,[c_l(t), c_m^\dagger(t')]_\pm\,|0\rangle \quad \text{retarded} \tag{148}$$

$$G^A_{lm}(t,t') = i\Theta(t'-t)\,\langle 0|\,[c_l(t), c_m^\dagger(t')]_\pm\,|0\rangle \quad \text{advanced,} \tag{149}$$

where $\Theta(t)$ is the Heaviside step-function

$$\Theta(t) = \begin{cases} 0 \text{ for } \ t<0 \\ 1 \text{ for } t \geq 0 \end{cases} \tag{150}$$

$$\lim_{\eta\to 0^+} \Theta(t) = \mp \frac{1}{2i\pi} \int_{-\infty}^{\infty} \frac{e^{\mp i\omega t}}{\omega \pm i\eta} \tag{151}$$

For space-time invariant Hamiltonians (i.e. time independent and translationally invariant), the Greens functions depend only on the coordinate *differences* $(t-t'), (l-m)$, in which case $G_{l-m}(t-t')$ can be Fourier transformed to energy-momentum space:

$$G_{l-m}(t-t') = \frac{1}{N}\sum_k e^{ik(l-m)} \frac{1}{\sqrt{2\pi}} \int d\omega G(k,\omega) e^{i\omega(t-t')} \tag{152}$$

$$G(k,\omega) = \frac{1}{\sqrt{2\pi}} \int dt e^{-i\omega t}\,\langle 0|\,[c_k(t), c_k^\dagger(0)]_\pm\,|0\rangle$$

$$c_k(t) = \frac{1}{N}\sum_l e^{ikl} c_l(t)$$

The *spectral function* is defined from the Greens function through the following relations:

$$A(k,\omega) = A^+(k,\omega) + A^-(k,-\omega) = \mp\frac{1}{\pi}\Im(G^{R/A}(k,\omega)) \tag{153}$$

$$A^+(k,\omega) = -\frac{1}{\pi}\Im(G(k,\omega)), \omega > 0 \tag{154}$$

$$A^-(k,-\omega) = -\frac{1}{\pi}\Im(G(k,\omega)), \omega < 0 \tag{155}$$

or in compact form

$$G(k,\omega) = \int_0^\infty \left[\frac{A^+(k,\omega')}{\omega - \omega' + i\eta} + \frac{A^-(k,\omega')}{\omega + \omega' - i\eta}\right] d\omega' \tag{156}$$

which should be understood as $\lim_{\eta\to 0}$. It has poles in both, the upper and lower half plane.

In terms of retarded and advanced Greens functions, the spectral function is defined by

$$G^{R/A}(k,\omega) = \int_{-\infty}^{\infty} \frac{A(k,\omega')}{\omega - \omega' \pm i\eta} d\omega'. \tag{157}$$

Using the Dirac-identity

$$\frac{1}{w - w' \pm i\eta} = \mathcal{P}\frac{1}{\omega - \omega'} \mp i\pi\delta(\omega - \omega') \tag{158}$$

the spectral functions is obtained from the retarded Greens function via

$$A(k,\omega) = -\frac{1}{\pi}\Im(G^R(k,\omega)) \tag{159}$$

The function $A(k,\omega)$ thus fully determines G, G^R and G^A. The spectral density function can be interpreted as the number of quantum many-body states in the energy range $[\omega, \omega + d\omega]$ and is normalized to unity:

$$\int d\omega A(k,\omega) = 1 \tag{160}$$

It can be probed in experiments using photon-emission spectroscopy (ARPES).

6 Equation of motion theory for many-body Greens functions

The equation of motion of Greens function [180] can often be used to calculate the Greens function from a coupled set of equations. For a generic retarded Greens function

$$G^R_{AB}(t) = -i\Theta(t)\left\langle [A(t), B]_\pm \right\rangle \tag{161}$$

with A, B arbitrary operators, differentiation of Eq. 161 yields

$$i\partial_t G^R_{AB}(t) = \delta(t)\,\langle [A(t), B]_\pm \rangle - i\Theta(t)\big\langle \big[\,[A,H](t), B\big]_\pm \big\rangle \tag{162}$$

where H is the Hamilton operator of the system.

In the following, consider a Hamiltonian $H = H_0 + W$, where

$$H_0 = \sum_{lm} t_{lm} c^\dagger_l c_m \tag{163}$$

is quadratic in creation and annihilation operators, and W contains particle-particle interactions. The equation of motion for $G^R_{lm}(t) = -i\Theta(t)\,\langle [c_l(t), c^\dagger_m]_\pm \rangle$ is obtained by differentiating Eq.148 and using $i\partial_t c(t) = -[H, c(t)]$:

$$i\partial_t G^R_{lm}(t,t') - \sum_n t_{ln} G^R_{nm}(t,t') = \delta(t-t')\delta_{lm} - i\Theta(t-t')\,\big\langle \big[-[W, c_l(t)], c^\dagger_m(t')\big]_\pm \big\rangle \tag{164}$$

The Fourier transformation to frequency ω is done by replacing $\partial_t \to -i\omega + \eta$, where η is a regularization parameter that serves as a reminder of the boundary condition of the Greens function (i.e. if it is a retarded ($\eta > 0$ or an advanced $\eta < 0$) Greens function, see also Eq.150), and using that the Fourier transform of $\delta(t)$ is the identity:

$$\begin{aligned}
&(\omega + i\eta) G^R_{lm}(\omega) - \sum_n t_{ln} G^R_{nm}(\omega) = \delta_{lm} + D_{lm}(\omega) \qquad (165)\\
&D_{lm}(\omega) = -i \int_{-\infty}^{\infty} d(t-t') e^{i(\omega+i\eta)(t-t')} \Theta(t-t')\,\big\langle \big[-[W, c_l](t), c^\dagger_m(t')\big]_\pm \big\rangle\,.
\end{aligned}$$

$D_{lm}(\omega)$ is a higher order Greens function, which itself obeys an equation of motion ($[W, c_l](t) \equiv e^{-iHt}[W, c_l]e^{iHt}$). In the generic case, this chain of equations is infinite. An approximate solution is often obtained by ignoring higher order terms, which leads to a closed set of equations. In other cases, the set of equations is seen to close exactly. One such example is the non-interacting resonating level model.

7 Numerical determination of spinon and two-string velocities

In Sec.3.4.5 we described how to obtain an estimate for the spinon and two-string velocities from our numerical simulations. For completeness the following tables show the input data for our fit.

-0.44	-0.38	-0.32	-0.26	-0.2	-0.14
(15, 32.61)	(1,44.41)	(1,41.89)	(1,39.84)	(1,37.15)	(1,33.87)
(18, 29.86)	(11,34.99)	(6,37.66)	(5,36.00)	(4,36.14)	(4,32.17)
(21, 27.11)	(20,27.05)	(12,32.17)	(10,32.59)	(7,32.68)	(6,33.02)
(24, 24.14)	(29,18.61)	(18,26.93)	(14,29.19)	(11,29.84)	(9,29.61)
(27, 21.39)	(39,9.68)	(24,21.70)	(18,25.78)	(15,25.99)	(12,27.06)
(30, 18.42)	(50,0.00)	(30,16.71)	(23,21.73)	(18,24.16)	(15,24.50)
(33, 15.46)		(36,11.72)	(27,18.53)	(21,21.92)	(18,21.94)
(36, 12.71)		(42,6.48)	(31,15.13)	(25,18.47)	(21,19.39)
(39, 9.95)		(50,0.00)	(36,10.86)	(28,16.44)	(23,19.39)
(42, 6.99)			(40,7.67)	(32,12.99)	(26,17.04)
(45, 4.02)			(44,4.69)	(35,11.17)	(29,14.70)
			(50,0.21)	(39,7.51)	(32,12.36)
				(42,5.68)	(35,9.80)
				(50,0.20)	(37,10.01)
					(40,7.46)
					(43,5.11)
					(50,0.21)

Table 1: Space time points used to fit the propagation speed for *spinon-branch* with linear regression, for different magnetizations $m = -0.44, -0.38, -0.32, -0.26, -0.2, -0.14$.

-0.44	-0.38	-0.32	-0.26	-0.2	-0.14
(10,81.80)	(7,82.04)	(1,83.29)	(8,59.86)	(16,41.21)	(3,51.34)
(14,77.33)	(16,64.34)	(6,74.56)	(12,53.90)	(20,35.93)	(5,49.21)
(18,69.45)	(25,47.38)	(12,64.09)	(16,49.64)	(23,31.67)	(6,49.64)
(22,60.93)	(34,29.92)	(18,54.11)	(21,41.33)	(27,27.41)	(11,40.48)
(26,52.19)	(43,12.22)	(24,43.39)	(25,35.15)	(30,22.94)	(50,0)
(30,42.82)	(50,0)	(30,33.17)	(29,29.40)	(33,19.29)	
(34,33.87)		(36,22.94)	(34,22.16)	(37,14.82)	
(38,25.56)		(42,12.97)	(38,15.98)	(40,7.51)	
(42,17.47)		(50,0)	(42,10.44)	(50,0)	
(46,8.73)			(50,0)		

Table 2: Space time points used to fit the propagation speed for *two-string-branch* with linear regression, for different magnetizations $m = -0.44, -0.38, -0.32, -0.26, -0.2, -0.14$.

Bibliography

[1] W. M. C. Foulkes et al. "Quantum Monte Carlo simulations of solids". *Reviews of Modern Physics* 73 (2001), pp. 33–83. URL: http://link.aps.org/doi/10.1103/RevModPhys.73.33.

[2] Emanuel Gull et al. "Continuous-time Monte Carlo methods for quantum impurity models". *Reviews of Modern Physics* 83 (2011), pp. 349–404. URL: http://link.aps.org/doi/10.1103/RevModPhys.83.349.

[3] Wolfgang von der Linden. *Numerical Treatment of Many-Body Problems*. URL: http://itp.tugraz.at/LV/wvl/NBVP/.

[4] Ralf Bulla, Theo A. Costi, and Thomas Pruschke. "Numerical renormalization group method for quantum impurity systems". *Reviews of Modern Physics* 80 (2008), p. 395. URL: http://link.aps.org/doi/10.1103/RevModPhys.80.395.

[5] Steven R. White. "Density matrix formulation for quantum renormalization groups". *Physical Review Letters* 69 (1992), p. 2863. URL: http://link.aps.org/doi/10.1103/PhysRevLett.69.2863.

[6] Antoine Georges et al. "Dynamical mean-field theory of strongly correlated fermion systems and the limit of infinite dimensions". *Reviews of Modern Physics* 68 (1996), pp. 13–125. URL: http://link.aps.org/doi/10.1103/RevModPhys.68.13.

[7] Till Kühner and Steven R. White. "Dynamical correlation functions using the density matrix renormalization group". *Physical Review B* 60 (1999), pp. 335–343.

[8] Eric Jeckelmann. "Dynamical density-matrix renormalization-group method". *Physical Review B* 66 (2002), p. 045114. URL: http://link.aps.org/doi/10.1103/PhysRevB.66.045114.

[9] Ulrich Schollwöck. "The density-matrix renormalization group in the age of matrix product states". *Annals of Physics* 326 (2011), pp. 96–192. URL: http://www.sciencedirect.com/science/article/pii/S0003491610001752.

[10] Guifre Vidal. "Efficient Classical Simulation of Slightly Entangled Quantum Computations". *Physical Review Letters* 91 (2003), p. 147902. URL: http://link.aps.org/abstract/PRL/v91/e147902.

[11] Guifre Vidal. "Efficient Simulation of One-Dimensional Quantum Many-Body Systems". *Physical Review Letters* 93 (2004), p. 040502. URL: http://link.aps.org/abstract/PRL/v93/e040502.

[12] U. Schollwöck. "The density-matrix renormalization group". *Reviews of Modern Physics* 77 (2005), p. 259. URL: http://link.aps.org/abstract/RMP/v77/p259.

[13] F. Verstraete, V. Murg, and J.I. Cirac. "Matrix product states, projected entangled pair states, and variational renormalization group methods for quantum spin systems". *Advances in Physics* 57 (2008), pp. 143–224. URL: http://www.tandfonline.com/doi/abs/10.1080/14789940801912366.

[14] Reinhard M Noack and Salvatore R. Manmana. "Diagonalization- and Numerical Renormalization-Group-Based Methods for Interacting Quantum Systems". *cond-mat/0510321* (2005). URL: http://arxiv.org/abs/cond-mat/0510321.

[15] Ian P. McCulloch. "From density-matrix renormalization group to matrix product states". en. *Journal of Statistical Mechanics: Theory and Experiment* 2007 (2007), P10014. URL: http://iopscience.iop.org/1742-5468/2007/10/P10014.

[16] Takeshi Fukuhara et al. "Microscopic observation of magnon bound states and their dynamics". en. *Nature* 502 (2013), pp. 76–79. URL: http://www.nature.com/nature/journal/v502/n7469/full/nature12541.html.

[17] Steven R. White. "Density-matrix algorithms for quantum renormalization groups". *Physical Review B* 48 (1993), p. 10345. URL: http://link.aps.org/abstract/PRB/v48/p10345.

[18] S. R. White and R. M. Noack. "Real-space quantum renormalization groups". *Physical Review Letters* 68 (1992), pp. 3487–3490. URL: http://link.aps.org/doi/10.1103/PhysRevLett.68.3487.

[19] Kenneth G. Wilson. "The renormalization group: Critical phenomena and the Kondo problem". *Reviews of Modern Physics* 47 (1975), pp. 773–840. URL: http://link.aps.org/doi/10.1103/RevModPhys.47.773.

[20] Andreas Lüscher and Andreas M. Läuchli. "Exact diagonalization study of the antiferromagnetic spin-12 Heisenberg model on the square lattice in a magnetic field". *Physical Review B* 79 (2009), p. 195102. URL: http://link.aps.org/doi/10.1103/PhysRevB.79.195102.

[21] Susumu Yamada et al. "Ultra Large-scale Exact-diagonalization for Confined Fermion-Hubbard Model on the Earth Simulator: Exploration of Superfluidity in Confined Strongly-Correlated Systems". *Journal of the Earth Simulator* 7 (2007), pp. 23–35.

[22] Stefan Rommer and Stellan Östlund. "Class of ansatz wave functions for one-dimensional spin systems and their relation to the density matrix renormalization group". *Physical Review B* 55 (1997), p. 2164. URL: http://link.aps.org/abstract/PRB/v55/p2164.

[23] Stellan Östlund and Stefan Rommer. "Thermodynamic Limit of Density Matrix Renormalization". *Physical Review Letters* 75 (1995), pp. 3537–3540. URL: http://link.aps.org/doi/10.1103/PhysRevLett.75.3537.

[24] I. P. McCulloch and M. Gulacsi. "The non-Abelian density matrix renormalization group algorithm". en. *EPL (Europhysics Letters)* 57 (2002), p. 852. URL: http://iopscience.iop.org/0295-5075/57/6/852.

[25] Andreas Weichselbaum. "Non-abelian symmetries in tensor networks: a quantum symmetry space approach". *arXiv:1202.5664* (2012). URL: http://arxiv.org/abs/1202.5664.

[26] Ian Affleck et al. "Rigorous results on valence-bond ground states in antiferromagnets". *Physical Review Letters* 59 (1987), pp. 799–802. URL: http://link.aps.org/doi/10.1103/PhysRevLett.59.799.

[27] Michael A. Nielsen and Isaac L. Chuang. *Quantum Computation and Quantum Information*. Cambridge University Press, 2000.

[28] J. Eisert, M. Cramer, and M. B. Plenio. "Colloquium: Area laws for the entanglement entropy". *Reviews of Modern Physics* 82 (2010), pp. 277–306. URL: http://link.aps.org/doi/10.1103/RevModPhys.82.277.

[29] M. Fannes, B. Nachtergaele, and R. F. Werner. "Finitely correlated states on quantum spin chains". en. *Communications in Mathematical Physics* 144 (1992), pp. 443–490. URL: http://link.springer.com/article/10.1007/BF02099178.

[30] B. Pirvu et al. "Matrix product states for critical spin chains: Finite-size versus finite-entanglement scaling". *Physical Review B* 86 (2012), p. 075117. URL: http://link.aps.org/doi/10.1103/PhysRevB.86.075117.

[31] Frank Pollmann et al. "Theory of Finite-Entanglement Scaling at One-Dimensional Quantum Critical Points". *Physical Review Letters* 102 (2009), p. 255701. URL: http://link.aps.org/doi/10.1103/PhysRevLett.102.255701.

[32] B. Pirvu et al. "Matrix product operator representations". en. *New Journal of Physics* 12 (2010), p. 025012. URL: http://iopscience.iop.org/1367-2630/12/2/025012.

[33] E. M. Stoudenmire et al. "One-dimensional Continuum Electronic Structure with the Density Matrix Renormalization Group and Its Implications For Density Functional Theory". *Physical Review Letters* 109 (2012). URL: http://arxiv.org/abs/1107.2394.

[34] Jutho Haegeman et al. "Calculus of continuous matrix product states". *Physical Review B* 88 (2013), p. 085118. URL: http://link.aps.org/doi/10.1103/PhysRevB.88.085118.

[35] F. Verstraete and J. I. Cirac. "Continuous Matrix Product States for Quantum Fields". *Physical Review Letters* 104 (2010), p. 190405. URL: http://link.aps.org/doi/10.1103/PhysRevLett.104.190405.

[36] S. Caprara. "Density-matrix renormalization group for fermions: Convergence to the infinite-size limit". *Nuclear Physics B* 493 (1997), pp. 640–650. URL: http://ftubhan.tugraz.at/han/996/www.sciencedirect.com/science/article/pii/S0550321397001429.

[37] P. Jordan and E. Wigner. "Über das Paulische Äquivalenzverbot". 47 (1928), p. 631.

[38] Steven R. White. "Density matrix renormalization group algorithms with a single center site". *Physical Review B* 72 (2005), p. 180403. URL: http://link.aps.org/doi/10.1103/PhysRevB.72.180403.

[39] I. P McCulloch. "Infinite size density matrix renormalization group, revisited". *0804.2509* (2008). URL: http://arxiv.org/abs/0804.2509.

[40] Guifre Vidal. "Classical Simulation of Infinite-Size Quantum Lattice Systems in One Spatial Dimension". *Physical Review Letters* 98 (2007). URL: http://prl.aps.org/abstract/PRL/v98/i7/e070201.

[41] F. Verstraete, D. Porras, and J. I. Cirac. "DMRG and periodic boundary conditions: a quantum information perspective". *cond-mat/0404706* (2004). URL: http://arxiv.org/abs/cond-mat/0404706.

[42] Peter Pippan, Steven R. White, and Hans Gerd Evertz. "Efficient matrix-product state method for periodic boundary conditions". *Physical Review B* 81 (2010), p. 081103. URL: http://link.aps.org/doi/10.1103/PhysRevB.81.081103.

[43] Steven R. White. "Spin Gaps in a Frustrated Heisenberg Model for CaV4O9". *Physical Review Letters* 77 (1996), p. 3633. URL: http://link.aps.org/doi/10.1103/PhysRevLett.77.3633.

[44] F. Verstraete and J. I. Cirac. "Renormalization algorithms for Quantum-Many Body Systems in two and higher dimensions". *arXiv:cond-mat/0407066* (2004). URL: http://arxiv.org/abs/cond-mat/0407066.

[45] E. M. Stoudenmire and Steven R. White. "Minimally entangled typical thermal state algorithms". en. *New Journal of Physics* 12 (2010), p. 055026. URL: http://iopscience.iop.org/1367-2630/12/5/055026.

[46] Immanuel Bloch, Jean Dalibard, and Sylvain Nascimbene. "Quantum simulations with ultracold quantum gases". en. *Nature Physics* 8 (2012), pp. 267–276. URL: http://www.nature.com/nphys/journal/v8/n4/abs/nphys2259.html.

[47] M. Lewenstein, A. Sanpera, and V. Ahufinger. *Ultracold Atoms in Optical Lattices: Simulating quantum many-body systems*. Oxford University Press, 2012.

[48] Rok Zitko, Jernej Mravlje, and Kristjan Haule. "Ground State of the Parallel Double Quantum Dot System". *Physical Review Letters* 108 (2012), p. 066602. URL: http://link.aps.org/doi/10.1103/PhysRevLett.108.066602.

[49] M. A. Cazalilla and J. B. Marston. "Time-Dependent Density-Matrix Renormalization Group: A Systematic Method for the Study of Quantum Many-Body Out-of-Equilibrium Systems". *Physical Review Letters* 88 (2002), p. 256403. URL: http://link.aps.org/doi/10.1103/PhysRevLett.88.256403.

[50] Steven R. White and Adrian E. Feiguin. "Real-Time Evolution Using the Density Matrix Renormalization Group". *Physical Review Letters* 93 (2004), p. 076401. URL: http://link.aps.org/abstract/PRL/v93/e076401.

[51] A. J. Daley et al. "Time-dependent density-matrix renormalization-group using adaptive effective Hilbert spaces". *Journal of Statistical Mechanics: Theory and Experiment* 2004 (2004), P04005. URL: http://iopscience.iop.org/1742-5468/2004/04/P04005?fromSearchPage=true.

[52] Peter Schmitteckert. "Nonequilibrium electron transport using the density matrix renormalization group method". *Physical Review B* 70 (2004), p. 121302. URL: http://link.aps.org/doi/10.1103/PhysRevB.70.121302.

[53] Juan Jose Garcia-Ripoll. "Time evolution algorithms for Matrix Product States and DMRG". *cond-mat/0610210* (2006). URL: http://arxiv.org/abs/cond-mat/0610210.

[54] Jutho Haegeman et al. "Time-Dependent Variational Principle for Quantum Lattices". *Physical Review Letters* 107 (2011), p. 070601. URL: http://link.aps.org/doi/10.1103/PhysRevLett.107.070601.

[55] M. B. Hastings. "Light Cone Matrix Product". *0903.3253* (2009). URL: http://arxiv.org/abs/0903.3253.

[56] Adrian E. Feiguin. "The Density Matrix Renormalization Group and its timedependent variants". *AIP Conference Proceedings*. Vol. 1419. AIP Publishing, 2011, pp. 5–92. URL: http://scitation.aip.org/content/aip/proceeding/aipcp/10.1063/1.3667323.

[57] P. E. Dargel et al. "Adaptive Lanczos-vector method for dynamic properties within the density matrix renormalization group". *Physical Review B* 83 (2011), p. 161104. URL: http://link.aps.org/doi/10.1103/PhysRevB.83.161104.

[58] P. E. Dargel et al. "Lanczos algorithm with matrix product states for dynamical correlation functions". *Physical Review B* 85 (2012), p. 205119. URL: http://link.aps.org/doi/10.1103/PhysRevB.85.205119.

[59] Andreas Holzner et al. "Chebyshev matrix product state approach for spectral functions". *Physical Review B* 83 (2011), p. 195115. URL: http://link.aps.org/doi/10.1103/PhysRevB.83.195115.

[60] F. Verstraete, J. J. Garcia-Ripoll, and J. I. Cirac. "Matrix Product Density Operators: Simulation of Finite-Temperature and Dissipative Systems". *Physical Review Letters* 93 (2004), p. 207204. URL: http://link.aps.org/doi/10.1103/PhysRevLett.93.207204.

[61] Michael Zwolak and Guifre Vidal. "Mixed-State Dynamics in One-Dimensional Quantum Lattice Systems: A Time-Dependent Superoperator Renormalization Algorithm". *Physical Review Letters* 93 (2004), p. 207205. URL: http://link.aps.org/doi/10.1103/PhysRevLett.93.207205.

[62] Thomas Barthel, Ulrich Schollwöck, and Steven R. White. "Spectral functions in one-dimensional quantum systems at finite temperature using the density matrix renormalization group". *Physical Review B (Condensed Matter and Materials Physics)* 79 (2009), pp. 245101–6. URL: http://link.aps.org/abstract/PRB/v79/e245101.

[63] Jutho Haegeman et al. "Variational matrix product ansatz for dispersion relations". *Physical Review B* 85 (2012), p. 100408. URL: http://link.aps.org/doi/10.1103/PhysRevB.85.100408.

[64] Damian Draxler et al. "Particles, Holes, and Solitons: A Matrix Product State Approach". *Physical Review Letters* 111 (2013), p. 020402. URL: http://link.aps.org/doi/10.1103/PhysRevLett.111.020402.

[65] Guifre Vidal. "Class of Quantum Many-Body States That Can Be Efficiently Simulated". *Physical Review Letters* 101 (2008), p. 110501. URL: http://link.aps.org/doi/10.1103/PhysRevLett.101.110501.

[66] G. Vidal. "Entanglement Renormalization". *Physical Review Letters* 99 (2007). URL: http://link.aps.org/doi/10.1103/PhysRevLett.99.220405.

[67] Roman Orus. "A Practical Introduction to Tensor Networks: Matrix Product States and Projected Entangled Pair States". *arXiv:1306.2164 [cond-mat, physics:hep-lat, physics:hep-th, physics:quant-ph]* (2013). URL: http://arxiv.org/abs/1306.2164.

[68] F. Verstraete et al. "Criticality, the Area Law, and the Computational Power of Projected Entangled Pair States". *Physical Review Letters* 96 (2006), p. 220601. URL: http://link.aps.org/doi/10.1103/PhysRevLett.96.220601.

[69] Simeng Yan, David A. Huse, and Steven R. White. "Spin-Liquid Ground State of the S = 1/2 Kagome Heisenberg Antiferromagnet". en. *Science* 332 (2011), pp. 1173–1176. URL: http://www.sciencemag.org/content/332/6034/1173.

[70] Stefan Depenbrock, Ian P. McCulloch, and Ulrich Schollwöck. "Nature of the Spin-Liquid Ground State of the S=1/2 Heisenberg Model on the Kagome Lattice". *Physical Review Letters* 109 (2012), p. 067201. URL: http://link.aps.org/doi/10.1103/PhysRevLett.109.067201.

[71] Markus Greiner et al. "Collapse and revival of the matter wave field of a BoseEinstein condensate". en. *Nature* 419 (2002), pp. 51–54. URL: http://www.nature.com/nature/journal/v419/n6902/abs/nature00968.html.

[72] S. Hofferberth et al. "Non-equilibrium coherence dynamics in one-dimensional Bose gases". en. *Nature* 449 (2007), pp. 324–327. URL: http://www.nature.com/nature/journal/v449/n7160/abs/nature06149.html.

[73] S. Trotzky et al. "Probing the relaxation towards equilibrium in an isolated strongly correlated one-dimensional Bose gas". en. *Nature Physics* 8 (2012), pp. 325–330. URL: http://www.nature.com/nphys/journal/v8/n4/full/nphys2232.html.

[74] Toshiya Kinoshita, Trevor Wenger, and David S. Weiss. "A quantum Newton's cradle". en. *Nature* 440 (2006), pp. 900–903. URL: http://www.nature.com/nature/journal/v440/n7086/abs/nature04693.html.

[75] Jacek Dziarmaga. "Dynamics of a quantum phase transition and relaxation to a steady state". *Advances in Physics* 59 (2010), pp. 1063–1189. URL: http://www.tandfonline.com/doi/abs/10.1080/00018732.2010.514702.

[76] Anatoli Polkovnikov et al. "Colloquium: Nonequilibrium dynamics of closed interacting quantum systems". *Reviews of Modern Physics* 83 (2011), pp. 863–883. URL: http://link.aps.org/doi/10.1103/RevModPhys.83.863.

[77] Austen Lamacraft and Joel Moore. "Potential insights into non-equilibrium behavior from atomic physics". *arXiv:1106.3567 [cond-mat]* (2011). URL: http://arxiv.org/abs/1106.3567.

[78] Marcos Rigol et al. "Relaxation in a Completely Integrable Many-Body Quantum System: An Ab Initio Study of the Dynamics of the Highly Excited States of 1D Lattice Hard-Core Bosons". *Physical Review Letters* 98 (2007), p. 050405. URL: http://link.aps.org/doi/10.1103/PhysRevLett.98.050405.

[79] Marcos Rigol, Vanja Dunjko, and Maxim Olshanii. "Thermalization and its mechanism for generic isolated quantum systems". *Nature* 452 (2008), pp. 854–858. URL: http://dx.doi.org/10.1038/nature06838.

[80] Pasquale Calabrese and John Cardy. "Time Dependence of Correlation Functions Following a Quantum Quench". *Physical Review Letters* 96 (2006), p. 136801. URL: http://link.aps.org/doi/10.1103/PhysRevLett.96.136801.

[81] Pasquale Calabrese and John Cardy. "Quantum quenches in extended systems". en. *Journal of Statistical Mechanics: Theory and Experiment* 2007 (2007), P06008. URL: http://iopscience.iop.org/1742-5468/2007/06/P06008.

[82] Pasquale Calabrese and John Cardy. "Evolution of entanglement entropy in one-dimensional systems". en. *Journal of Statistical Mechanics: Theory and Experiment* 2005 (2005), P04010. URL: http://iopscience.iop.org/1742-5468/2005/04/P04010.

[83] M. A. Cazalilla. "Effect of Suddenly Turning on Interactions in the Luttinger Model". *Physical Review Letters* 97 (2006), p. 156403. URL: http://link.aps.org/doi/10.1103/PhysRevLett.97.156403.

[84] S. R. Manmana et al. "Strongly Correlated Fermions after a Quantum Quench". *Physical Review Letters* 98 (2007), p. 210405. URL: http://link.aps.org/doi/10.1103/PhysRevLett.98.210405.

[85] M. Cramer et al. "Exact Relaxation in a Class of Nonequilibrium Quantum Lattice Systems". *Physical Review Letters* 100 (2008), p. 030602. URL: http://link.aps.org/doi/10.1103/PhysRevLett.100.030602.

[86] T. Barthel and U. Schollwöck. "Dephasing and the Steady State in Quantum Many-Particle Systems". *Physical Review Letters* 100 (2008), p. 100601. URL: http://link.aps.org/doi/10.1103/PhysRevLett.100.100601.

[87] Guillaume Roux. "Quenches in quantum many-body systems: One-dimensional Bose-Hubbard model reexamined". *Physical Review A* 79 (2009), p. 021608. URL: http://link.aps.org/doi/10.1103/PhysRevA.79.021608.

[88] Davide Fioretto and Giuseppe Mussardo. "Quantum quenches in integrable field theories". en. *New Journal of Physics* 12 (2010), p. 055015. URL: http://iopscience.iop.org/1367-2630/12/5/055015.

[89] Corinna Kollath, Andreas M. Läuchli, and Ehud Altman. "Quench Dynamics and Nonequilibrium Phase Diagram of the Bose-Hubbard Model". *Physical Review Letters* 98 (2007), p. 180601. URL: http://link.aps.org/doi/10.1103/PhysRevLett.98.180601.

[90] Giulio Biroli, Corinna Kollath, and Andreas M. Läuchli. "Effect of Rare Fluctuations on the Thermalization of Isolated Quantum Systems". *Physical Review Letters* 105 (2010), p. 250401. URL: http://link.aps.org/doi/10.1103/PhysRevLett.105.250401.

[91] Davide Rossini et al. "Long time dynamics following a quench in an integrable quantum spin chain: Local versus nonlocal operators and effective thermal behavior". *Physical Review B* 82 (2010), p. 144302. URL: http://link.aps.org/doi/10.1103/PhysRevB.82.144302.

[92] Pasquale Calabrese, Fabian H. L. Essler, and Maurizio Fagotti. "Quantum Quench in the Transverse-Field Ising Chain". *Physical Review Letters* 106 (2011), p. 227203. URL: http://link.aps.org/doi/10.1103/PhysRevLett.106.227203.

[93] Martin Ganahl et al. "Observation of Complex Bound States in the Spin-1/2 Heisenberg XXZ Chain Using Local Quantum Quenches". *Physical Review Letters* 108 (2012), p. 077206. URL: http://link.aps.org/doi/10.1103/PhysRevLett.108.077206.

[94] Michael Karbach and Gerhard Müller. "Introduction to the Bethe ansatz I". *cond-mat/9809162* (1998). URL: http://arxiv.org/abs/cond-mat/9809162.

[95] Michael Karbach, Kun Hu, and Gerhard Müller. "Introduction to the Bethe ansatz II". *cond-mat/9809163* (1998). URL: http://arxiv.org/abs/cond-mat/9809163.

[96] Michael Karbach, Kun Hu, and Gerhard Muller. "Introduction to the Bethe Ansatz III". *cond-mat/0008018* (2000). URL: http://arxiv.org/abs/cond-mat/0008018.

[97] Bill Sutherland. *Beautiful Models*. Wolrd Scientific Publishing Co. Pte. Ltd., 2004.

[98] Minoru Takahashi. *Thermodynamics of One-Dimensional Solvable Models*. Cambridge University Press, 1999.

[99] V. E. Korepin, N. M. Bogoliubov, and A. G. Izergin. *Quantum Inverse Scattering Method and Correlation Functions*. Cambridge University Press, 1997.

[100] Jarrett Lancaster and Aditi Mitra. "Quantum quenches in an XXZ spin chain from a spatially inhomogeneous initial state". *Physical Review E* 81 (2010), p. 061134. URL: http://link.aps.org/doi/10.1103/PhysRevE.81.061134.

[101] Dominique Gobert et al. "Real-time dynamics in spin-1/2 chains with adaptive time-dependent DMRG". *cond-mat/0409692* (2004). URL: http://arxiv.org/abs/cond-mat/0409692.

[102] David Petrosyan et al. "Quantum liquid of repulsively bound pairs of particles in a lattice". *Physical Review A* 76 (2007), p. 033606. URL: http://link.aps.org/doi/10.1103/PhysRevA.76.033606.

[103] S. Langer et al. "Real-time study of diffusive and ballistic transport in spin-(1/2) chains using the adaptive time-dependent density matrix renormalization group method". *Physical Review B (Condensed Matter and Materials Physics)* 79 (2009), pp. 214409–11. URL: http://link.aps.org/abstract/PRB/v79/e214409.

[104] Jie Ren and Shiqun Zhu. "Quench dynamics of entanglement in an open anisotropic spin-12 Heisenberg chain". *Physical Review A* 81 (2010), p. 014302. URL: http://link.aps.org/doi/10.1103/PhysRevA.81.014302.

[105] Lea F. Santos and Aditi Mitra. "Domain wall dynamics in integrable and chaotic spin-1/2 chains". *Physical Review E* 84 (2011), p. 016206. URL: http://link.aps.org/doi/10.1103/PhysRevE.84.016206.

[106] Robin Steinigeweg et al. "Coherent Spin-Current Oscillations in Transverse Magnetic Fields". *Physical Review Letters* 106 (2011), p. 160602. URL: http://link.aps.org/doi/10.1103/PhysRevLett.106.160602.

[107] Stephan Langer et al. “Real-time energy dynamics in spin-1/2 Heisenberg chains [ballistic in both phases]”. *1107.4136* (2011). URL: http://arxiv.org/abs/1107.4136.

[108] Rodrigo G. Pereira, Steven R. White, and Ian Affleck. “Exact Edge Singularities and Dynamical Correlations in Spin-1/2 Chains”. *Physical Review Letters* 100 (2008), p. 027206. URL: http://link.aps.org/doi/10.1103/PhysRevLett.100.027206.

[109] Pasquale Calabrese and John Cardy. “Entanglement and correlation functions following a local quench: a conformal field theory approach”. en. *Journal of Statistical Mechanics: Theory and Experiment* 2007 (2007), P10004. URL: http://iopscience.iop.org/1742-5468/2007/10/P10004.

[110] Jean-Marie Stephan and Jerome Dubail. “Local quantum quenches in critical one-dimensional systems: entanglement, the Loschmidt echo, and light-cone effects”. en. *Journal of Statistical Mechanics: Theory and Experiment* 2011 (2011), P08019. URL: http://iopscience.iop.org/1742-5468/2011/08/P08019.

[111] A. Kleine et al. “Spin-charge separation in two-component Bose gases”. *Physical Review A* 77 (2008), p. 013607. URL: http://link.aps.org/doi/10.1103/PhysRevA.77.013607.

[112] A. J. Daley et al. “Measuring Entanglement Growth in Quench Dynamics of Bosons in an Optical Lattice”. *Physical Review Letters* 109 (2012), p. 020505. URL: http://link.aps.org/doi/10.1103/PhysRevLett.109.020505.

[113] J. Schachenmayer et al. “Entanglement Growth in Quench Dynamics with Variable Range Interactions”. *Physical Review X* 3 (2013), p. 031015. URL: http://link.aps.org/doi/10.1103/PhysRevX.3.031015.

[114] C. Kollath, U. Schollwöck, and W. Zwerger. “Spin-Charge Separation in Cold Fermi Gases: A Real Time Analysis”. *Physical Review Letters* 95 (2005), p. 176401. URL: http://link.aps.org/doi/10.1103/PhysRevLett.95.176401.

[115] K. A. Al-Hassanieh et al. “Excitons in the One-Dimensional Hubbard Model: A Real-Time Study”. *Physical Review Letters* 100 (2008), p. 166403. URL: http://link.aps.org/doi/10.1103/PhysRevLett.100.166403.

[116] D. B. Abraham et al. “Thermalization of a Magnetic Impurity in the Isotropic XY Model”. *Physical Review Letters* 25 (1970), pp. 1449–1450. URL: http://link.aps.org/doi/10.1103/PhysRevLett.25.1449.

[117] D. B. Abraham et al. “Dynamics of a local perturbation in the XY model”. *Stud. Appl. Math.* 50 (1971), p. 121.

[118] D. Jaksch et al. “Cold Bosonic Atoms in Optical Lattices”. *Physical Review Letters* 81 (1998), pp. 3108–3111. URL: http://link.aps.org/doi/10.1103/PhysRevLett.81.3108.

[119] Marc Cheneau et al. “Light-cone-like spreading of correlations in a quantum many-body system”. en. *Nature* 481 (2012), pp. 484–487. URL: http://www.nature.com/nature/journal/v481/n7382/full/nature10748.html.

[120] Takeshi Fukuhara et al. “Quantum dynamics of a mobile spin impurity”. en. *Nature Physics* 9 (2013), pp. 235–241. URL: http://www.nature.com/nphys/journal/v9/n4/full/nphys2561.html.

[121] Markus Greiner et al. “Quantum phase transition from a superfluid to a Mott insulator in a gas of ultracold atoms”. en. *Nature* 415 (2002), pp. 39–44. URL: http://www.nature.com/nature/journal/v415/n6867/full/415039a.html.

[122] Ulrich Schneider et al. “Fermionic transport and out-of-equilibrium dynamics in a homogeneous Hubbard model with ultracold atoms”. en. *Nature Physics* 8 (2012), pp. 213–218. URL: http://www.nature.com/nphys/journal/v8/n3/full/nphys2205.html.

[123] Lucia Hackermüller et al. “Anomalous Expansion of Attractively Interacting Fermionic Atoms in an Optical Lattice”. en. *Science* 327 (2010), pp. 1621–1624. URL: http://www.sciencemag.org/content/327/5973/1621.

[124] Niels Strohmaier et al. “Observation of Elastic Doublon Decay in the Fermi-Hubbard Model”. *Physical Review Letters* 104 (2010), p. 080401. URL: http://link.aps.org/doi/10.1103/PhysRevLett.104.080401.

[125] Robert Jördens et al. “A Mott insulator of fermionic atoms in an optical lattice”. en. *Nature* 455 (2008), pp. 204–207. URL: http://www.nature.com/nature/journal/v455/n7210/full/nature07244.html.

[126] Waseem S. Bakr et al. “A quantum gas microscope for detecting single atoms in a Hubbard-regime optical lattice”. en. *Nature* 462 (2009), pp. 74–77. URL: http://www.nature.com/nature/journal/v462/n7269/full/nature08482.html.

[127] Jacob F. Sherson et al. “Single-atom-resolved fluorescence imaging of an atomic Mott insulator”. en. *Nature* 467 (2010), pp. 68–72. URL: http://www.nature.com/nature/journal/v467/n7311/abs/nature09378.html.

[128] Christof Weitenberg et al. “Single-spin addressing in an atomic Mott insulator”. en. *Nature* 471 (2011), pp. 319–324. URL: http://www.nature.com/nature/journal/v471/n7338/full/nature09827.html.

[129] Jonathan Simon et al. “Quantum simulation of antiferromagnetic spin chains in an optical lattice”. en. *Nature* 472 (2011), pp. 307–312. URL: http://www.nature.com/nature/journal/v472/n7343/full/nature09994.html.

[130] L.-M. Duan, E. Demler, and M. D. Lukin. “Controlling Spin Exchange Interactions of Ultracold Atoms in Optical Lattices”. *Physical Review Letters* 91 (2003), p. 090402. URL: http://link.aps.org/doi/10.1103/PhysRevLett.91.090402.

[131] Ehud Altman et al. “Phase diagram of two-component bosons on an optical lattice”. en. *New Journal of Physics* 5 (2003), p. 113. URL: http://iopscience.iop.org/1367-2630/5/1/113.

[132] Minoru Takahashi and Masuo Suzuki. “One-Dimensional Anisotropic Heisenberg Model at Finite Temperatures”. en. *Progress of Theoretical Physics* 48 (1972), pp. 2187–2209. URL: http://ptp.oxfordjournals.org/content/48/6/2187.

[133] Michael Fowler and Xenophon Zotos. "Quantum sine-Gordon thermodynamics: The Bethe ansatz method". *Physical Review B* 24 (1981), pp. 2634–2639. URL: http://link.aps.org/doi/10.1103/PhysRevB.24.2634.

[134] Martin Ganahl. *Simulation of Spin Transport in One Dimensional Quantum Heisenberg Spin 1/2 Systems in Real Time (Diplomarbeit)*. 2010.

[135] Jean-Sebastien Caux and Jean Michel Maillet. "Computation of Dynamical Correlation Functions of Heisenberg Chains in a Magnetic Field". *Physical Review Letters* 95 (2005), p. 077201. URL: http://link.aps.org/doi/10.1103/PhysRevLett.95.077201.

[136] Jean-Sebastien Caux, Rob Hagemans, and Jean Michel Maillet. "Computation of dynamical correlation functions of Heisenberg chains: the gapless anisotropic regime". en. *Journal of Statistical Mechanics: Theory and Experiment* 2005 (2005), P09003. URL: http://iopscience.iop.org/1742-5468/2005/09/P09003.

[137] Rodrigo G. Pereira, Steven R. White, and Ian Affleck. "Spectral function of spinless fermions on a one-dimensional lattice". *Physical Review B* 79 (2009), p. 165113. URL: http://link.aps.org/doi/10.1103/PhysRevB.79.165113.

[138] Masanori Kohno. "Dynamically Dominant Excitations of String Solutions in the Spin-1/2 Antiferromagnetic Heisenberg Chain in a Magnetic Field". *Physical Review Letters* 102 (2009), p. 037203. URL: http://link.aps.org/doi/10.1103/PhysRevLett.102.037203.

[139] Aditya Shashi et al. "Nonuniversal prefactors in the correlation functions of one-dimensional quantum liquids". *Physical Review B* 84 (2011), p. 045408. URL: http://link.aps.org/doi/10.1103/PhysRevB.84.045408.

[140] Adilet Imambekov, Thomas L. Schmidt, and Leonid I. Glazman. "One-dimensional quantum liquids: Beyond the Luttinger liquid paradigm". *Reviews of Modern Physics* 84 (2012), pp. 1253–1306. URL: http://link.aps.org/doi/10.1103/RevModPhys.84.1253.

[141] Thierry Giamarchi. *Quantum Physics in One Dimension*. Clarendon Press, Oxford, 2004.

[142] Elliott H. Lieb and Derek W. Robinson. "The finite group velocity of quantum spin systems". *Communications in Mathematical Physics* 28 (1972), pp. 251–257. URL: http://projecteuclid.org/euclid.cmp/1103858407.

[143] I. Affleck and A. W. W. Ludwig. "The Fermi edge singularity and boundary condition changing operators". en. *Journal of Physics A: Mathematical and General* 27 (1994), p. 5375. URL: http://iopscience.iop.org/0305-4470/27/16/007.

[144] J. L. Cardy. "Boundary conditions, fusion rules and the Verlinde formula". *Nucl. Phys.* B324 (1989), p. 581.

[145] Luigi Amico et al. "Entanglement in many-body systems". *Reviews of Modern Physics* 80 (2008), p. 517. URL: http://link.aps.org/doi/10.1103/RevModPhys.80.517.

[146] J. I. Latorre and A. Riera. "A short review on entanglement in quantum spin systems". *Journal of Physics A: Mathematical and Theoretical* 42 (2009), p. 504002. URL: http://iopscience.iop.org/1751-8121/42/50/504002/?ejredirect=.iopscience.

[147] F. Verstraete and J. I. Cirac. "Matrix product states represent ground states faithfully". *Physical Review B* 73 (2006), p. 094423. URL: http://link.aps.org/doi/10.1103/PhysRevB.73.094423.

[148] Alvaro Perales and Guifre Vidal. "Entanglement growth and simulation efficiency in one-dimensional quantum lattice systems". *Physical Review A* 78 (2008), p. 042337. URL: http://link.aps.org/doi/10.1103/PhysRevA.78.042337.

[149] Viktor Eisler and Ingo Peschel. "Evolution of entanglement after a local quench". en. *Journal of Statistical Mechanics: Theory and Experiment* 2007 (2007), P06005. URL: http://iopscience.iop.org/1742-5468/2007/06/P06005.

[150] V. Zauner et al. "Time Evolution within a Comoving Window: Scaling of signal fronts and magnetization plateaus after a local quench in quantum spin chains". *arXiv:1207.0862 [cond-mat, physics:quant-ph]* (2012). URL: http://arxiv.org/abs/1207.0862.

[151] Yu-Ao Chen et al. "Controlling Correlated Tunneling and Superexchange Interactions with ac-Driven Optical Lattices". *Physical Review Letters* 107 (2011), p. 210405. URL: http://link.aps.org/doi/10.1103/PhysRevLett.107.210405.

[152] A. B. Kuklov and B. V. Svistunov. "Counterflow Superfluidity of Two-Species Ultracold Atoms in a Commensurate Optical Lattice". *Physical Review Letters* 90 (2003), p. 100401. URL: http://link.aps.org/doi/10.1103/PhysRevLett.90.100401.

[153] G. Thalhammer et al. "Double Species Bose-Einstein Condensate with Tunable Interspecies Interactions". *Physical Review Letters* 100 (2008), p. 210402. URL: http://link.aps.org/doi/10.1103/PhysRevLett.100.210402.

[154] M. Ganahl, M. Haque, and H. G. Evertz. "Quantum Bowling: Particle-hole transmutation in one-dimensional strongly interacting lattice models". *arXiv:1302.2667 [cond-mat]* (2013). URL: http://arxiv.org/abs/1302.2667.

[155] Immanuel Bloch, Jean Dalibard, and Wilhelm Zwerger. "Many-body physics with ultracold gases". *Reviews of Modern Physics* 80 (2008), pp. 885–964. URL: http://link.aps.org/doi/10.1103/RevModPhys.80.885.

[156] K. Winkler et al. "Repulsively bound atom pairs in an optical lattice". en. *Nature* 441 (2006), pp. 853–856. URL: http://www.nature.com/nature/journal/v441/n7095/abs/nature04918.html.

[157] Masudul Haque. "Self-similar spectral structures and edge-locking hierarchy in open-boundary spin chains". *Physical Review A* 82 (2010), p. 012108. URL: http://link.aps.org/doi/10.1103/PhysRevA.82.012108.

[158] Anton Wöllert and Andreas Honecker. "Solitary excitations in one-dimensional spin chains". *Physical Review B* 85 (2012), p. 184433. URL: http://link.aps.org/doi/10.1103/PhysRevB.85.184433.

[159] Jorn Mossel and Jean-Sebastien Caux. "Relaxation dynamics in the gapped XXZ spin-1/2 chain". en. *New Journal of Physics* 12 (2010), p. 055028. URL: http://iopscience.iop.org/1367-2630/12/5/055028.

[160] M. Endres et al. "Observation of Correlated Particle-Hole Pairs and String Order in Low-Dimensional Mott Insulators". en. *Science* 334 (2011), pp. 200–203. URL: http://www.sciencemag.org/content/334/6053/200.

[161] O. A. Castro-Alvaredo and B. Doyon. "Bi-partite entanglement entropy in integrable models with backscattering". en. *Journal of Physics A: Mathematical and Theoretical* 41 (2008), p. 275203. URL: http://iopscience.iop.org/1751-8121/41/27/275203.

[162] Tobias Salger et al. "Klein Tunneling of a Quasirelativistic Bose-Einstein Condensate in an Optical Lattice". *Physical Review Letters* 107 (2011), p. 240401. URL: http://link.aps.org/doi/10.1103/PhysRevLett.107.240401.

[163] R. Gerritsma et al. "Quantum Simulation of the Klein Paradox with Trapped Ions". *Physical Review Letters* 106 (2011), p. 060503. URL: http://link.aps.org/doi/10.1103/PhysRevLett.106.060503.

[164] M. I. Katsnelson, K. S. Novoselov, and A. K. Geim. "Chiral tunnelling and the Klein paradox ingraphene". en. *Nature Physics* 2 (2006), pp. 620–625. URL: http://www.nature.com/nphys/journal/v2/n9/abs/nphys384.html.

[165] F. Heidrich-Meisner et al. "Quantum distillation: Dynamical generation of low-entropy states of strongly correlated fermions in an optical lattice". *Physical Review A* 80 (2009), p. 041603. URL: http://link.aps.org/doi/10.1103/PhysRevA.80.041603.

[166] T. Ulbricht and P. Schmitteckert. "Is spin-charge separation observable in a transport experiment?" *EPL (Europhysics Letters)* 86 (2009), p. 57006. URL: http://iopscience.iop.org/0295-5075/86/5/57006/?ejredirect=.iopscience.

[167] X. Zotos, F. Naef, and P. Prelovsek. "Transport and conservation laws". *Physical Review B* 55 (1997), pp. 11029–11032. URL: http://link.aps.org/doi/10.1103/PhysRevB.55.11029.

[168] M. P. Grabowski and P. Mathieu. "Integrability test for spin chains". en. *Journal of Physics A: Mathematical and General* 28 (1995), p. 4777. URL: http://iopscience.iop.org/0305-4470/28/17/013.

[169] Kurt Gottfried and Tung-Mow Yan. *Quantum Mechanics: Fundamentals*. en. Springer, 2003. ISBN: 9780387955766.

[170] Michael Edward Peskin and Daniel V. Schroeder. *An Introduction To Quantum Field Theory*. en. Westview Press, 1995. ISBN: 081334543X.

[171] David Petrosyan et al. "Erratum: Quantum liquid of repulsively bound pairs of particles in a lattice [Phys. Rev. A 76, 033606 (2007)]". *Physical Review A* 77 (2008), p. 039908. URL: http://link.aps.org/doi/10.1103/PhysRevA.77.039908.

[172] Ricardo A. Pinto, Masudul Haque, and Sergej Flach. "Edge-localized states in quantum one-dimensional lattices". *Physical Review A* 79 (2009), p. 052118. URL: http://link.aps.org/doi/10.1103/PhysRevA.79.052118.

[173] Ramaz Khomeriki et al. "Interaction-induced fractional Bloch and tunneling oscillations". *Physical Review A* 81 (2010), p. 065601. URL: http://link.aps.org/doi/10.1103/PhysRevA.81.065601.

[174] A. Lengwenus et al. "Coherent Transport of Atomic Quantum States in a Scalable Shift Register". *Physical Review Letters* 105 (2010), p. 170502. URL: http://link.aps.org/doi/10.1103/PhysRevLett.105.170502.

[175] P. W. Anderson. "Localized Magnetic States in Metals". *Physical Review* 124 (1961), pp. 41–53. URL: http://link.aps.org/doi/10.1103/PhysRev.124.41.

[176] Alexander Weie et al. "The kernel polynomial method". *Reviews of Modern Physics* 78 (2006), pp. 275–306. URL: http://link.aps.org/doi/10.1103/RevModPhys.78.275.

[177] Alexander Braun and Peter Schmitteckert. "Numerical evaluation of Greens functions based on the Chebyshev expansion". *arXiv:1310.2724 [cond-mat]* (2013). URL: http://arxiv.org/abs/1310.2724.

[178] Ronny Thomale, Stephan Rachel, and Peter Schmitteckert. "Tunneling spectra simulation of interacting Majorana wires". *Physical Review B* 88 (2013), p. 161103. URL: http://link.aps.org/doi/10.1103/PhysRevB.88.161103.

[179] A.M. Tsvelick and P.B. Wiegmann. "Exact results in the theory of magnetic alloys". *Advances in Physics* 32 (1983), pp. 453–713. URL: http://www.tandfonline.com/doi/abs/10.1080/00018738300101581.

[180] Hendrik Bruus and Karsten Flensberg. *Many-Body Quantum Theory in Condensed Matter Physics*. Oxford University Press, 2006.

[181] A. C. Hewson. *The Kondo Problem to Heavy Fermions*. Cambridge University Press, 1993.

[182] Piers Coleman. *Introduction to Many Body Physics*. 2013.

[183] David C. Langreth. "Friedel Sum Rule for Anderson's Model of Localized Impurity States". *Physical Review* 150 (1966), pp. 516–518. URL: http://link.aps.org/doi/10.1103/PhysRev.150.516.

[184] Jun Kondo. "Resistance Minimum in Dilute Magnetic Alloys". en. *Progress of Theoretical Physics* 32 (1964), pp. 37–49. URL: http://ptp.oxfordjournals.org/content/32/1/37.

[185] W. J. De Haas and G. J. Van Den Berg. "The electrical resistance of gold and silver at low temperatures". *Physica* 3 (1936), pp. 440–449. URL: http://www.sciencedirect.com/science/article/pii/S0031891436800093.

[186] Alexey A. Abrikosov. "On the Anomalous Temperature Dependence of the Resistivity of Non-magnetic Metals with a Weak Concentration of Magnetic Impurities". *Physics* 2 (1965), p. 5.

[187] P. W. Anderson, G. Yuval, and D. R. Hamann. "Exact Results in the Kondo Problem. II. Scaling Theory, Qualitatively Correct Solution, and Some New Results on One-Dimensional Classical Statistical Models". *Physical Review B* 1 (1970), pp. 4464–4473. URL: http://link.aps.org/doi/10.1103/PhysRevB.1.4464.

[188] Andreas Holzner et al. "Kondo screening cloud in the single-impurity Anderson model: A density matrix renormalization group study". *Physical Review B* 80 (2009), p. 205114. URL: http://link.aps.org/doi/10.1103/PhysRevB.80.205114.

[189] Laszlo Borda. "Kondo screening cloud in a one-dimensional wire: Numerical renormalization group study". *Physical Review B* 75 (2007), p. 041307. URL: http://link.aps.org/doi/10.1103/PhysRevB.75.041307.

[190] Rok Zitko and Thomas Pruschke. "Energy resolution and discretization artifacts in the numerical renormalization group". *Physical Review B* 79 (2009), p. 085106. URL: http://link.aps.org/doi/10.1103/PhysRevB.79.085106.

[191] Th Pruschke and R. Bulla. "Hunds coupling and the metal-insulator transition in the two-band Hubbard model". en. *The European Physical Journal B - Condensed Matter and Complex Systems* 44 (2005), pp. 217–224. URL: http://link.springer.com/article/10.1140/epjb/e2005-00117-4.

[192] R.N. Silver and H. RöDer. "Densities of States of Mega-Dimensional Hamiltonian Matrices". *International Journal of Modern Physics C* 05 (1994), pp. 735–753. URL: http://www.worldscientific.com/doi/abs/10.1142/S0129183194000842?prevSearch=%5BContrib%3A+Silver%5D&searchHistoryKey=.

[193] Karen A. Hallberg. "Density-matrix algorithm for the calculation of dynamical properties of low-dimensional systems". *Physical Review B* 52 (1995), R9827–R9830. URL: http://link.aps.org/doi/10.1103/PhysRevB.52.R9827.

[194] Robert Peters. "Spectral functions for single- and multi-impurity models using density matrix renormalization group". *Physical Review B* 84 (2011), p. 075139. URL: http://link.aps.org/doi/10.1103/PhysRevB.84.075139.

[195] R. N. Silver and H. Röder. "Calculation of densities of states and spectral functions by Chebyshev recursion and maximum entropy". *Physical Review E* 56 (1997), pp. 4822–4829. URL: http://link.aps.org/doi/10.1103/PhysRevE.56.4822.

[196] John P. Boyd. *Chebyshev and Fourier Spectral Methods*. DOVER Publications, Inc. 31 East 2nd Street Mineola, New York 11501, 2000.

[197] Steven R. White and Ian Affleck. "Spectral function for the S=1 Heisenberg antiferromagetic chain". *Physical Review B* 77 (2008), p. 134437. URL: http://link.aps.org/doi/10.1103/PhysRevB.77.134437.

[198] Antoine Georges. "Strongly Correlated Electron Materials: Dynamical Mean-Field Theory and Electronic Structure". *arXiv:cond-mat/0403123* (2004). URL: http://arxiv.org/abs/cond-mat/0403123.

[199] Subir Sachdev. *Quantum Phase Transitions*. Cambridge University Press, 2011.

[200] Michael Potthoff. "Non-perturbative construction of the Luttinger-Ward functional". *arXiv:cond-mat/0406671* (2004). URL: http://arxiv.org/abs/cond-mat/0406671.

[201] Carsten Raas, Götz S. Uhrig, and Frithjof B. Anders. "High-energy dynamics of the single-impurity Anderson model". *Physical Review B* 69 (2004), p. 041102. URL: http://link.aps.org/doi/10.1103/PhysRevB.69.041102.

[202] Michal Karski, Carsten Raas, and Götz S. Uhrig. "Single-particle dynamics in the vicinity of the Mott-Hubbard metal-to-insulator transition". *Physical Review B* 77 (2008), p. 075116. URL: http://link.aps.org/doi/10.1103/PhysRevB.77.075116.

[203] Daniel J. Garcia, Karen Hallberg, and Marcelo J. Rozenberg. "Dynamical Mean Field Theory with the Density Matrix Renormalization Group". *Physical Review Letters* 93 (2004), p. 246403. URL: http://link.aps.org/doi/10.1103/PhysRevLett.93.246403.

[204] Ziga Osolin and Rok Zitko. "Pade approximants for improved finite-temperature spectral functions in the numerical renormalization group". *arXiv:1302.3334* (2013). URL: http://arxiv.org/abs/1302.3334.

[205] Satoshi Nishimoto, Florian Gebhard, and Eric Jeckelmann. "Dynamical density-matrix renormalization group for the MottHubbard insulator in high dimensions". *Journal of Physics: Condensed Matter* 16 (2004), pp. 7063–7081. URL: http://iopscience.iop.org/0953-8984/16/39/038.

[206] M. Jarrell. "Hubbard model in infinite dimensions: A quantum Monte Carlo study". *Physical Review Letters* 69 (1992), pp. 168–171. URL: http://link.aps.org/doi/10.1103/PhysRevLett.69.168.

[207] C. Raas and G. S. Uhrig. "Spectral densities from dynamic density-matrix renormalization". *The European Physical Journal B - Condensed Matter and Complex Systems* 45 (2005), pp. 293–303. URL: http://www.springerlink.com/content/v229h813x46hj732/abstract/.

[208] Martin Nuss et al. "Steady-state and quench-dependent relaxation of a quantum dot coupled to one-dimensional leads". *Physical Review B* 88 (2013), p. 045132. URL: http://link.aps.org/doi/10.1103/PhysRevB.88.045132.

[209] Frithjof B. Anders. "Steady-State Currents through Nanodevices: A Scattering-States Numerical Renormalization-Group Approach to Open Quantum Systems". *Physical Review Letters* 101 (2008), p. 066804. URL: http://link.aps.org/doi/10.1103/PhysRevLett.101.066804.

[210] Frithjof B. Anders and Avraham Schiller. "Real-Time Dynamics in Quantum-Impurity Systems: A Time-Dependent Numerical Renormalization-Group Approach". *Physical Review Letters* 95 (2005), p. 196801. URL: http://link.aps.org/doi/10.1103/PhysRevLett.95.196801.

[211] P. Schmidt and H. Monien. "Nonequilibrium dynamical mean-field theory of a strongly correlated system". *arXiv:cond-mat/0202046* (2002). URL: http://arxiv.org/abs/cond-mat/0202046.

[212] J. K. Freericks, V. M. Turkowski, and V. Zlatic. "Nonequilibrium Dynamical Mean-Field Theory". *Physical Review Letters* 97 (2006), p. 266408. URL: http://link.aps.org/doi/10.1103/PhysRevLett.97.266408.

[213] Michael Knap, Wolfgang von der Linden, and Enrico Arrigoni. "Nonequilibrium steady state for strongly correlated many-body systems: Variational cluster approach". *Physical Review B* 84 (2011), p. 115145. URL: http://link.aps.org/doi/10.1103/PhysRevB.84.115145.

[214] F. Heidrich-Meisner, A. E. Feiguin, and E. Dagotto. "Real-time simulations of nonequilibrium transport in the single-impurity Anderson model". *Physical Review B* 79 (2009), p. 235336. URL: http://link.aps.org/doi/10.1103/PhysRevB.79.235336.

[215] K. A. Al-Hassanieh et al. "Adaptive time-dependent density-matrix renormalization-group technique for calculating the conductance of strongly correlated nanostructures". *Physical Review B* 73 (2006), p. 195304. URL: http://link.aps.org/doi/10.1103/PhysRevB.73.195304.

[216] Sam T. Carr, Dmitry A. Bagrets, and Peter Schmitteckert. "Full Counting Statistics in the Self-Dual Interacting Resonant Level Model". *Physical Review Letters* 107 (2011), p. 206801. URL: http://link.aps.org/doi/10.1103/PhysRevLett.107.206801.

[217] E. Boulat, H. Saleur, and P. Schmitteckert. "Twofold Advance in the Theoretical Understanding of Far-From-Equilibrium Properties of Interacting Nanostructures". *Physical Review Letters* 101 (2008), p. 140601. URL: http://link.aps.org/doi/10.1103/PhysRevLett.101.140601.

[218] F. Heidrich-Meisner et al. "Nonequilibrium electronic transport in a one-dimensional Mott insulator". *Physical Review B* 82 (2010), p. 205110. URL: http://link.aps.org/doi/10.1103/PhysRevB.82.205110.

[219] F. Heidrich-Meisner et al. "Transport through quantum dots: a combined DMRG and embedded-cluster approximation study". en. *The European Physical Journal B* 67 (2009), pp. 527–542. URL: http://link.springer.com/article/10.1140/epjb/e2009-00036-4.

[220] Shunsuke Kirino et al. "Time-Dependent DMRG Study on Quantum Dot under a Finite Bias Voltage". *Journal of the Physical Society of Japan* 77 (2008), p. 084704. URL: http://jpsj.ipap.jp/link?JPSJ/77/084704/.

[221] A. Branschädel, G. Schneider, and P. Schmitteckert. "Conductance of inhomogeneous systems: Real-time dynamics". en. *Annalen der Physik* 522 (2010), 657678. URL: http://onlinelibrary.wiley.com/doi/10.1002/andp.201000017/abstract.

[222] A. Kawabata. "Electron conduction in one-dimension". en. *Reports on Progress in Physics* 70 (2007), p. 219. URL: http://iopscience.iop.org/0034-4885/70/2/R02.

[223] M. Einhellinger, A. Cojuhovschi, and E. Jeckelmann. "Numerical method for nonlinear steady-state transport in one-dimensional correlated conductors". *Physical Review B* 85 (2012), p. 235141. URL: http://link.aps.org/doi/10.1103/PhysRevB.85.235141.

[224] Ned S. Wingreen, Antti-Pekka Jauho, and Yigal Meir. "Time-dependent transport through a mesoscopic structure". *Physical Review B* 48 (1993), pp. 8487–8490. URL: http://link.aps.org/doi/10.1103/PhysRevB.48.8487.

[225] S. Andergassen et al. "Renormalization group analysis of the interacting resonant-level model at finite bias: Generic analytic study of static properties and quench dynamics". *Physical Review B* 83 (2011), p. 205103. URL: http://link.aps.org/doi/10.1103/PhysRevB.83.205103.

[226] Yigal Meir and Ned S. Wingreen. "Landauer formula for the current through an interacting electron region". *Physical Review Letters* 68 (1992), pp. 2512–2515. URL: http://link.aps.org/doi/10.1103/PhysRevLett.68.2512.

[227] Hartmut J. W. Haug and Antti-Pekka Jauho. *Quantum Kinetics in Transport and Optics of Semiconductors*. Springer-Verlag GmbH, 1996. ISBN: 3540616020.

[228] Philipp Werner et al. "Weak-coupling quantum Monte Carlo calculations on the Keldysh contour: Theory and application to the current-voltage characteristics of the Anderson model". *Physical Review B* 81 (2010), p. 035108. URL: http://link.aps.org/doi/10.1103/PhysRevB.81.035108.

[229] Tatsuya Fujii and Kazuo Ueda. "Perturbative approach to the nonequilibrium Kondo effect in a quantum dot". *Physical Review B* 68 (2003), p. 155310. URL: http://link.aps.org/doi/10.1103/PhysRevB.68.155310.

[230] Severin G. Jakobs, Mikhail Pletyukhov, and Herbert Schoeller. "Nonequilibrium functional renormalization group with frequency-dependent vertex function: A study of the single-impurity Anderson model". *Physical Review B* 81 (2010), p. 195109. URL: http://link.aps.org/doi/10.1103/PhysRevB.81.195109.

[231] Martin Nuss et al. "Steady-state spectra, current, and stability diagram of a quantum dot: A nonequilibrium variational cluster approach". *Physical Review B* 86 (2012), p. 245119. URL: http://link.aps.org/doi/10.1103/PhysRevB.86.245119.

[232] Andreas Dirks et al. "Imaginary-time quantum many-body theory out of equilibrium. II. Analytic continuation of dynamic observables and transport properties". *Physical Review B* 87 (2013), p. 235140. URL: http://link.aps.org/doi/10.1103/PhysRevB.87.235140.

[233] S. Weiss et al. "Iterative real-time path integral approach to nonequilibrium quantum transport". *Physical Review B* 77 (2008), p. 195316. URL: http://link.aps.org/doi/10.1103/PhysRevB.77.195316.

[234] L. Mühlbacher, D. F. Urban, and A. Komnik. "Anderson impurity model in nonequilibrium: Analytical results versus quantum Monte Carlo data". *Physical Review B* 83 (2011), p. 075107. URL: http://link.aps.org/doi/10.1103/PhysRevB.83.075107.

[235] Mikhail Pletyukhov, Dirk Schuricht, and Herbert Schoeller. "Relaxation versus Decoherence: Spin and Current Dynamics in the Anisotropic Kondo Model at Finite Bias and Magnetic Field". *Physical Review Letters* 104 (2010), p. 106801. URL: http://link.aps.org/doi/10.1103/PhysRevLett.104.106801.

[236] Mikhail Pletyukhov and Herbert Schoeller. "Nonequilibrium Kondo model: Crossover from weak to strong coupling". *Physical Review Letters* 108 (2012), p. 260601. URL: http://link.aps.org/doi/10.1103/PhysRevLett.108.260601.

[237] A. Rosch, J. Kroha, and P. Wölfle. "Kondo Effect in Quantum Dots at High Voltage: Universality and Scaling". *Physical Review Letters* 87 (2001), p. 156802. URL: http://link.aps.org/doi/10.1103/PhysRevLett.87.156802.

[238] S. De Franceschi et al. "Out-of-Equilibrium Kondo Effect in a Mesoscopic Device". *Physical Review Letters* 89 (2002), p. 156801. URL: http://link.aps.org/doi/10.1103/PhysRevLett.89.156801.

[239] R. Leturcq et al. "Probing the Kondo Density of States in a Three-Terminal Quantum Ring". *Physical Review Letters* 95 (2005), p. 126603. URL: http://link.aps.org/doi/10.1103/PhysRevLett.95.126603.

[240] Guy Cohen et al. "Numerically exact long-time magnetization dynamics at the nonequilibrium Kondo crossover of the Anderson impurity model". *Physical Review B* 87 (2013), p. 195108. URL: http://link.aps.org/doi/10.1103/PhysRevB.87.195108.

[241] Adrian Feiguin et al. "Nonequilibrium Transport through a Point Contact in the =5/2 Non-Abelian Quantum Hall State". *Physical Review Letters* 101 (2008), p. 236801. URL: http://link.aps.org/doi/10.1103/PhysRevLett.101.236801.

[242] M. Medvedyeva, A. Hoffmann, and S. Kehrein. "Spatiotemporal buildup of the Kondo screening cloud". *Physical Review B* 88 (2013), p. 094306. URL: http://link.aps.org/doi/10.1103/PhysRevB.88.094306.

[243] Shreyoshi Ghosh, Pedro Ribeiro, and Masudul Haque. "Real-space structure of the impurity screening cloud in the Resonant Level Model". *arXiv:1309.0027 [cond-mat]* (2013). URL: http://arxiv.org/abs/1309.0027.

[244] C. Lanczos. *An iteration method for the solution of the eigenvalue problem of linear differential and integral operators*. English. National Bureau of Standards, 1950. URL: http://archive.org/details/jresv45n4p255.

[245] Markus Aichhorn et al. "Low-temperature Lanczos method for strongly correlated systems". *Physical Review B* 67 (2003), p. 161103. URL: http://link.aps.org/doi/10.1103/PhysRevB.67.161103.

[246] J. Jaklic and P. Prelovsek. "Lanczos method for the calculation of finite-temperature quantities in correlated systems". *Physical Review B* 49 (1994), pp. 5065–5068. URL: http://link.aps.org/doi/10.1103/PhysRevB.49.5065.

[247] R. Haydock, V. Heine, and M. J. Kelly. "Electronic structure based on the local atomic environment for tight-binding bands. II". *Journal of Physics C: Solid State Physics* 8 (1975), pp. 2591–2605. URL: http://iopscience.iop.org/0022-3719/8/16/011/cites.

[248] Tae Jun Park and J. C. Light. "Unitary quantum time evolution by iterative Lanczos reduction". *The Journal of Chemical Physics* 85 (1986), pp. 5870–5876. URL: http://scitation.aip.org/content/aip/journal/jcp/85/10/10.1063/1.451548.

[249] J. J. Sakurai. *Modern Quantum Mechanics*. Addison-Wesley Publishing Company, 1994.

[250] Michael G. Moore. URL: http://www.pa.msu.edu/~mmoore/852.html.

[251] Alexander Altland. *Advanced Quantum Mechanics*. URL: http://www.thp.uni-koeln.de/alexal/teaching.html.

[252] Wolfgang Nolting. *Grundkurs Theoretische Physik 7*. Springer-Verlag Berlin Heidelberg, 2005. ISBN: 3-540-24117-5.

[253] Gerald D. Mahan. *Many-Particle Physics*. Plenum Press New York (Plenum Publishing Corporation,) 1990.

Acknowledgements

Science is a winding path through a maze of unpredictable turns and countless dead ends; at its heart, it is driven by creativity, curiosity and the exciting prospect of something completely unexpected to cross your way; and it crucially depends on the right environment. It is my pleasure to thank all the people at the institute of for theoretical physics at the Graz university of technology to make it such a great place to work at and conduct research!

Dear Hans Gerd, I owe you the first and deepest thanks for your aid and assistance, your enthusiasm for physics and for keeping up the spirit during our late night arxiv-submission sessions; for giving me the freedom to follow my own ideas; for all your time you invested in reiterating our results; for your advice and your support; for always having time for discussions, even when students were waiting for their exams; and of course for accepting my thesis. Thank you for this great time! My second thanks goes to our computeradmin Andi who was unfortunate enough to occupy the office just opposite to mine. I am infinitely indebted to him for enduring my incredibly stupid questions on linux shell commands and for making my working station work so smoothly; for helping me out with my notebook problems; and for his expert's advice on shell scripting and python programming which always came along with a full set of printed out introductions and tutorials. My third thanks goes to Brigitte for all her efforts in administrating the institute. Without her, a smooth flow would be inconceivable.

My heartiest thanks go to the members of the many-body group at the institute for theoretical physics: Markus, for our frequent morning-boulder-sessions which were always great, for our skiing trips to the Grazer Bergland, and most importantly, for his invaluable advice on so many questions regarding physics and also other things, and his ability to break things down to the core of the matter. Martin, for making it such a pleasure to collaborate on quantum physics, and for the incredible effort put in analyzing tons and tons of data, and for our memorable visit of the Deutsche Raumfahrtausstellung at the back of beyond in Germany. And of course for setting up (and winning!) the great empty-the-dish-washer competition! Christoph, for silently enduring the torture of so many discussion between Martin and me on quantum impurity problems and other stuff. Toni, for his company in this unforgettable night on the balcony of our apartment in Sestri. Thanks also to my office mates Georg and Daniel, and Robert, Max, Simon and Werner for many amusing discussions. Enrico, for always having an open door when I had another question on condensed matter physics, be it in or out of equilibrium, and for the great time he and Markus and me had on the famous Kragelschinken (and the Plöschkogel), and of course Wolfgang, who as head of our institute only made all this possible.

A special thanks goes to all those people who left the institute during my work:

Valentin, for the great time we had when sharing an office in Graz and flying paper planes out of the window, for leaving a great book on the cumbersome culture of Japan on his office desk, and for his seemingly never ending positivity. Michael, for sharing his programming skills with me and helping me out when I was stuck with a problem.

The last and most important thanks goes to my friends, to my family and to Antonia! Without their support, this would surely not have been possible!

I thank all of you for this great time here in Graz! Its hard to imagine that it could have been any better.